

University of Nottingham
UK | CHINA | MALAYSIA

Faculty of Engineering
Department of Mechanical, Materials and Manufacturing Engineering

Experimental and Numerical Investigations of deformation and fracture mechanisms in Double-Sided Incremental Forming

Wenxuan Peng
Wenxuan.Peng@nottingham.ac.uk

Supervisors
Dr. Hengan Ou
&
Prof. Adib Becker

Thesis submitted to the University of Nottingham for the degree of

Doctor of Philosophy

September 2021

ABSTRACT

Incremental sheet forming (ISF) is a novel sheet forming technology, which has had a rapid development in the last two decades. ISF and the Single Point Incremental Sheet Forming (SPIF) processes have considerable advantages of low cost, high flexibility and adaptability in manufacturing small batch and customized products for automotive, medical and aerospace applications. The general ISF process only requires the use of a Computer Numerical Control (CNC) milling machine to control a semi-spherical tool traveling along a pre-defined toolpath to form a blank sheet on a dedicated fixture. Through continuous deformation by layers, the blank workpiece is incrementally deformed to the desired shape. However, there are shortcomings in terms of formability and accuracy in SPIF process as reported in literature. As a result, several variants are proposed and developed to overcome these SPIF limitations.

Double-Sided Incremental Forming (DSIF) is a new variant of advanced ISF processes, developed from a flexible die concept, by using an additional tool to follow the main or master tool movement on the other side of the formed sheet to provide local support. The additional tool support improves the deformation stability and helps to achieve improved formability and accuracy as compared to SPIF whilst it keeps the same benefits of conventional ISF processes.

This thesis reports work on the deformation and fracture mechanisms of SPIF and DSIF processes through experimental investigation and Finite Element (FE) simulation. The accurate predictions were achieved by a modification of shear mechanisms in damage modelling, as well as the correct estimation for machine deflection during experiments.

The methodologies were initially validated in using two bespoke testing methods, Tension under Cyclic Bending (TCB) and Tension under Cyclic Bending and Compression (TCBC) tests as they resemble the local bending and tension features of SPIF and DSIF processes. Experimental validation was carried out by using a bespoke TCB and TCBC test rig with grade 1 pure Ti samples. The additional compression in TCBC captures the key features of formability improvement in DSIF process. The analytical model and FE results

showed the bending effect induced the local deformation feature, where the local stress state was the key to fracture occurrence.

To predict fracture under TCB and TCBC conditions, a Lode angle parameter and stress triaxiality based new shear modified Gurson-Tvergaard-Needleman (GTN) damage model was developed and implemented through ABAQUS VUMAT user subroutine in FE simulations. As validated in TCB and TCBC simulations, an accurate prediction to the elongation-to-fracture with an error less than 10% was achieved. The results suggest the relatively high stress triaxiality due to pure tension in reverse-bending stage is the determinative factor causing fracture initiation at the surface contacting with the bending roller.

In SPIF and DSIF testing of AA5052 material with a pneumatic support tool, a particular case of formability reduction was observed due to an "over-bending" phenomenon. This proactive compensation approach could result in tool misplaced when the machine deflections occur. To quantify the effect of machine deflections in ISF processing, a general approach based on Homogeneous Transformation Matrix (HTM) was proposed to simulate the tool positioning errors during practical SPIF and DSIF tests of grade 1 pure Ti. The comparison between the part profiles from experimental and FE results indicated a significant improvement of accuracy in geometry prediction.

By implementing the developed machine stiffness estimation approach and the modified GTN model in FE simulations of SPIF and DSIF processes with grade 1 pure Ti sheets, the formed geometry and fracture depth can be correctly predicted. For the first time, the cyclic local bending was identified as a common deformation feature in both TCB/ TCBC and SPIF/ DSIF. The additional compression reduces the shear and delays the damage initiation and hence improves the formability improvement in TCBC and DSIF as compared to their counterparts of TCB and SPIF respectively. However, three-dimensional bending in SPIF and DSIF increases stress triaxiality that moves the location of fracture initiation to the surface of non-contact region to the master tool. In conclusion, local bending and additional support tool induces different stress states by combinations

of tension, shear and compression, results in the discrepancies between SPIF and DSIF in terms of damage evolution and process formability being achieved.

LIST OF PUBLICATIONS

1. Peng, W., Ou, H., & Becker, A. (2019). Double-sided incremental forming: A review. *Journal of Manufacturing Science and Engineering*, *141*(5).
2. Peng, W., Li, M., Lu, B., Chen, J., Becker, A., & Ou, H. (2019). Experimental and finite element investigation of over-bending phenomenon in Double-Sided Incremental Forming (DSIF) of aluminum sheets. *Procedia Manufacturing*, *29*, 59-66.

ACKNOWLEDGEMENTS

Firstly, I would like to sincerely acknowledge my supervisors, Dr. Hengan Ou and Prof. Adib Becker for their expertise, invaluable guidance and unreserved support from my first day of PhD study to the completion of my thesis writing. It would be impossible for me to finish my PhD without their advice and encouragement.

Then, I would like to thank Prof. Jun Chen, Dr. Bin Lu and Dr. Meng Li of Department of Plasticity Technology, Shanghai Jiao Tong University, China for the support of a series of ISF tests; Mr. Renhao Wu, Mr. Xuepeng Zhan and Ms. Xinmei Liu for helping to arrange proper test sessions and assistance of machine operation.

My sincere thanks go to Dr. Gatea Shakir of Faculty of Engineering, University of Kufa, for the great helps with the GTN model and ABAQUS related works and discussion. I also appreciate Prof. Hui Long and Dr. Ai Sheng of the Department of Mechanical Engineering, the University of Sheffield, UK for performing TCB and TCBC tests and having valuable discussions of the fracture mechanisms in DSIF and TCBC processes.

Special thanks are given to technicians in laboratories and central workshops, especially to Mr. Jason Young, Mr Ken Wilson and Mr. Andy Plummer, for their kind help in components manufacture, machine optimization and experiment works.

I would also give thanks to my research colleagues, particularly during this unexpected, even continuing COVID-19 pandemic. This is also for anyone caring and helping me in this pandemic. Many thanks go to my roommate, Dr. Tengtuo Zhu, who made my PhD life to be little a bit more special.

Finally, I gratefully present my acknowledgement to my parents, Mr. Xiuming Peng and Ms. Lingjie Jiang. They never stop to support my education and life even from thousands of miles away. This is always my faith and strength to overcome any hardness. I am eternally grateful.

LIST OF ABBREVIATIONS AND SYMBOLS

ADSIF	*Accumulative Double-Sided Incremental Forming*
ASIF	*Asymmetric Incremental Sheet Forming*
BUT	*Bending Under Tension*
CBT	*Cyclic Bending and Tension*
CGA	*Circle Grid Analysis*
CNC	*Computer Numerical Control*
DOST	*Drop of Stress Triaxiality*
DSIF	*Double-Sided Incremental Forming*
EBSD	*Electron Back Scatter Diffraction*
FE	*Finite Element*
FLC	*Forming Limit Curve*
FLD	*Forming Limit Diagram*
GFLD	*Generalized Forming Limit Diagram*
GTN model	*Gurson-Tvergaard-Needleman model*
HTM	*Homogeneous Transformation Matrix*
ISF	*Incremental Sheet Forming*
SPIF	*Single Point Incremental Forming*
SEM	*Scanning Electron Microscope*
TPIF	*Two-Point Incremental Forming*
TCB	*Tension under Cyclic Bending*

TCBC	*Tension under Cyclic Bending and Compression*
PEEK	*Polyether ether ketone*
A	*Area of cross-section*
$[A]$	*Rotation matrix*
A, B, n	*Johnson-Cook model parameters*
a	*Radius of contact area with the support tool*
$[C_T]$	*Coordinate transformation matrix*
D, D_{shear}	*Total and the shear damage variables*
d	*Step size, step depth*
E	*Young's modulus*
E'	*Modulus of elasticity in plane strain condition*
F_c	*Compression force*
$[F]$	*Flexibility matrix*
$[f]$	*Force vector*
$\dot{f}$	*Total void volume fraction rate*
$\dot{f}_{growth}$	*Void volume fraction rate of hydrostatic stress*
$\dot{f}_{nucleation}$	*Void volume fraction rate of void nucleation*
f_c	*Critical void volume fraction*
f_f	*Final void volume fraction*
G	*Shear modulus*
I	*Second moment of area*

J_3	*Third stress invariant*
$[K]$	*Stiffness matrix*
$[L]$	*Beam length vector*
l_0, l	*Length of the raw material and its arc length after deformation*
M	*Moment*
$[m]$	*Moment vector*
p	*Position in through thickness direction*
m	*Position of elastic limit in through thickness direction*
n_c	*Total number of contact times*
P_s	*Local contact stress by Hertz contact theory*
$[P]$	*Relative position matrix*
$[p]$	*Vector of relative positions*
p_{dc}	*Ratio between the relative tool angle and the desired forming angle*
p_d	*Relative position to the contact centre*
Q	*First moment of area*
q_1, q_2, q_3	*GTN model constants*
$\varepsilon_0, q_4, q_5, q_6, n_s, k_s, k_w$	*Material fracture strain surface parameters*
ε_N	*Mean value of the normal distribution of the nucleation strain*
S_N	*Standard Deviation for void nucleation*
f_N	*Volume fraction of void nucleation*
R	*Radius of tool roller*

R_S	*Radius of the support roller*
$[R]$	*Transformation matrix for the location of stiffness components*
r_1, r_2	*Master and support tool radii*
S	*Yield stress under current stress state*
S_i	*Coordinate system based on the i_{th} component*
$T, \Delta T$	*Tension and the tension increment*
$[T]$	*Force and moment transformation matrix*
t_0, t	*Initial thickness and current thickness*
W_{ext}, W_b, W_t	*Total external work, work by bending and work by tension, respectively*
$\dot{W}_{ext}, \dot{W}_b, \dot{W}_t$	*Total external power, power by bending and power by tension, respectively*
β	*Current forming angle*
ϕ	*Desired forming angle*
ϕ_{dc}	*Relative angle between the master and support tools*
$\Delta\phi_{dc}$	*Angle of double-contact arc with centre of the master tool*
κ	*Double-contact state indicator*
$\varepsilon_\phi, \varepsilon_\theta, \varepsilon_t$	*Strain in meridional, circumferential and thickness direction*
$\varepsilon_{eq}/\bar{\varepsilon}$	*Equivalent plastic strain*
$\Delta\bar{\varepsilon}/\ \dot{\bar{\varepsilon}}_M^p$	*Equivalent plastic strain rate*
$\dot{\varepsilon}_{kk}^p$	*Trace of the plastic strain rate tensor*

$\sigma_\phi, \sigma_\theta, \sigma_t$	*Stresses in meridional, circumferential and thickness direction, respectively*
σ_Y	*Yield stress*
σ_{eq}	*von Mises stress*
σ_{kk}	*Hydrostatic stress*
τ	*Shear stress*
$[\Delta\delta]$	*Linear deflection vector*
ρ	*Distance from tool centre to central surface*
η	*Stress triaxiality*
$\eta_{lim}^{(-)}, \eta_{lim}^{(+)}$	*Stress triaxiality limits of the boundary of fracture strain surface*
ξ	*Lode angle parameter*
ν	*Poisson's ratio*
μ	*Friction coefficient*
θ	*Tangential contact angle*
θ_L	*Lode angle*
$[\Delta\theta]$	*Vector of angular deflection*

CONTENTS

1 INTRODUCTION 1

1.1. Overview of Incremental sheet forming (ISF) and Double-sided incremental forming (DSIF) 1

1.1.1. Incremental Sheet Forming (ISF) 1

1.1.2. Double-Sided Incremental Forming (DSIF) 2

1.2. Research challenges 5

1.2.1. Forming method 5

1.2.2. Process modelling 5

1.3. Research aims and objectives 6

1.4. Research methodology 7

1.5. Thesis structure 8

2 LITERATURE REVIEW 10

2.1. Introduction 10

2.2. Comparison between SPIF and DSIF 10

2.3. Testing equipment in DSIF 13

2.4. Formability in DSIF 16

2.4.1. Definition 16

2.4.2. Influential factors to the formability of DSIF 18

2.4.3. Electrical-assisted heating in DSIF 20

2.5. Toolpath design in DSIF 22

2.5.1. Accumulative-DSIF Strategy 22

2.5.2. Compensation-based toolpath 23

2.5.3. Feature-based toolpath strategy 27

2.6. Simulation of the DSIF process 30

2.6.1. Constitutive models 31

2.6.2. FE strategies with reduced CPU time 31

2.6.3. Applications of FE simulation in DSIF 32

2.7. Deformation mechanisms of DISF 33

2.7.1. Tension under cyclic bending and compression 34

2.7.2. Deformation mechanisms in DSIF 35

2.7.3. Deformation mechanisms in ADSIF 37

2.8. Discussion and Conclusions 39

2.8.1. Formability 40
2.8.2. Toolpath strategies in DSIF 41
2.8.3. Simulations for DSIF 42
2.8.4. Deformation mechanisms in DSIF 42
2.9. Challenges of DSIF research 43

3 DEFORMATION AND FRACTURE MECHANISMS OF TENSION UNDER CYCLIC BENDING (TCB) AND TENSION UNDER CYCLIC BENDING AND COMPRESSION (TCBC) TESTS 45

3.1. Introduction 45
3.2. Theoretical analysis of TCB and TCBC tests 48
3.2.1. General case of deformation 48
3.2.2. TCBC case 52
3.2.3. Strain evolution in bending and unbending process 53
3.2.4. The effect of bending depth 59
3.3. Damage evolution under low stress triaxiality 61
3.4. Modified GTN model 65
3.4.1. Original GTN model 66
3.4.2. Shear mechanism 67
3.4.3. Lode angle effect 70
3.4.4. Modified void evolution function 73
3.4.5. Modified shear mechanisms 74
3.4.6. Equivalent fracture strain locus function 75
3.4.7. Implementation of the new modified GTN model 77
3.5. Experimental testing 79
3.6. Validation of the new modified GTN model 82
3.6.1. Benchmark test of a single element 82
3.6.2. FE simulation of uniaxial tensile test 87
3.6.3. FE models for TCB and TCBC 88
3.7. Results and discussion 89
3.7.1. Experimental results 89
3.7.2. FE results 93
3.8. Discussion 105
3.8.1. The effect of localised bending 106

3.8.2. The effect of compression 107
3.8.3. The through-thickness effect 108
3.8.4. Limitations of the new modified shear GTN model 109
3.8.5. The link between TCB/TCBC and ISF processes 110
3.9. Conclusions 112

4 MACHINE TOOL STIFFNESS AND ITS IMPACT ON DSIF PROCESS ... 115

4.1. Introduction 115
4.2. A general approach of machine stiffness quantification 117
4.2.1. Transformation matrix of coordinates 118
4.2.2. Transformation matrix of forces and moments 121
4.2.3. Simplified beam models of ISF machine stiffness 122
4.2.4. Quantification of the overall deflection of an ISF machine system 127
4.3. Theoretical analysis of the effect of machine deflection in DSIF 129
4.4. Experimental testing 132
4.4.1. ISF tests for Al5052 of truncated cone shape 132
4.4.2. ISF tests for grade 1pure Ti of hyperbolic cone shape 133
4.5. Finite element simulation 133
4.5.1. FE modelling of DISF processes with and without a support tool 133
4.5.2. Calibration of DSIF machine stiffness using FE simulation 136
4.5.3. FE simulation of DSIF with machine tool stiffness 138
4.6. Results and discussion 140
4.6.1. "Over-bending" in DSIF with pneumatic support 140
4.6.2. Stiffness model and implementation in ISF simulation 144
4.6.3. Experimental results and FE stiffness validations for SPIF and DSIF processes 148
4.7. Conclusions 153

5 MODELLING OF DEFORMATION AND DUCTILE FRACTURE IN SPIF AND DSIF 155

5.1. Introduction 155
5.2. Theoretical analysis of deformation in SPIF and DSIF processes 156
5.2.1. Local deformation and contact parameters in the i_{th} contact period 156
5.2.2. Local strain development in ISF process 159

5.2.3. Local stresses in ISF processes 160
5.2.4. Damage evolution by a simplified GTN model 163
5.2.5. Effects of process parameters in SPIF and DSIF 166
5.3. Finite element simulation 171
5.3.1. Tool path modification for machine compliance 171
5.3.2. Finite element models 172
5.4. Results 174
5.4.1. Fracture depths and geometries 174
5.4.2. Equivalent strain and damage distributions 176
5.4.3. The effect of different tool settings 179
5.4.4. Localised deformation and damage 181
5.4.5. Local stress state evolution during tool and workpiece contact 187
5.4.6. Deformation mechanisms in SPIF and DSIF 189
5.5. Discussion 192
5.5.1. Similarity and differences between TCB/TCBC and SPIF/DSIF 192
5.5.2. Influence of tool and workpiece contact in FE simulations 194
5.5.3. The limitations of the presented analytical model 196
5.5.4. The deformation and fracture mechanisms in SPIF and DSIF 197
5.6. Conclusions 199

6 CONCLUSIONS AND FUTURE WORK 202

6.1. Introduction 202
6.2. Conclusions 202
6.2.1. TCB and TCBC processes 202
6.2.2. Machine and tool stiffness modelling in DSIF 203
6.2.3. Deformation and fracture mechanisms in DSIF process 204
6.3. Thesis novelty and contributions to knowledge 205
6.4. Future work 206
6.4.1. TCB and TCBC testing 206
6.4.2. Machine stiffness and tools configuration in FE model 207
6.4.3. DSIF process 207

REFERENCES 209

TABLE OF FIGURES

Figure. 1.1 Illustrations of incremental sheet forming. 2

Figure. 1.2 Schematics of (a). SPIF (b). TPIF and (c). DSIF 2

Figure. 1.3 Schematics of (a) conventional DSIF toolpath, and (b) accumulative DSIF (ADSIF) toolpath [8]. 4

Figure 2.1 Equivalent plastic strain contour plot of (a) SPIF (b) DSIF, and thickness distribution in (c) SPIF and (d) DSIF process of 45° pyramids [11] 13

Figure 2.2 Developed DSIF testing method and bespoke machines (a) DSIF using turning machine (IIT Kanpur, 2006 [49]) (b) Robotic arms DSIF (Ruhr-University, 2011 [57]) (c) bespoke DSIF machine (IIT Kanpur, 2010 [49]) (d) scaled dedicated DSIF machine (IITH [18]) (e) bespoke DSIF machine (Shanghai Jiaotong University [58]) (f) DSIF on C-clamp (Northwestern unidersity, 2008 [50]) (g) bespoke DSIF machine (Northwestern unidersity, 2012 [43]), and (h) parallel robotic structure DSIF machine (Northwestern unidersity, 2020 [56]) 15

Figure. 2.3 An illustration of the sin law and squeeze factor in DSIF 17

Figure. 2.4 Material deformation via different supporting forces and tool shift: (a) 240 N without tool shift, (b) 240 N with tool shift, (c) 480 N without tool shift, and (d) 480 N with tool shift *[14]* 19

Figure. 2.5 (a) Schematic of toolpath variables, and (b) Definition of stable angle *[61]* 20

Figure. 2.6 (a) Two electrical connection modes in DSIF, and (b) improved geometry accuracy in electrically assisted DSIF *[13]* 21

Figure. 2.7 Comparison of geometries of components made by ADSIF, DSIF and SPIF with wall angles (a) 40° and (b) 50° *[43]* 23

Figure. 2.8 Schematic of applying the correction through the reference CAD model *[16]* 25

Figure. 2.9 (a) Toolpath and sheet deflection, (b) steps of how compensation applied, and (c) partition of profile based on features *[44]* 26

Figure. 2.10 Illustration of squeezing and reverse bending strategies for anti-spingback purpose *[58]* 27

Figure. 2.11 (a) Contour plot of Z-forces predicted via FE simulation, and (b) Classification of tool movement based on tool movement and contour [96] 29

Figure. 2.12 The desired and final product fabricated via the mixed toolpath strategy [76] 30

Figure. 2.13 Schematic of TCBC process 35

Figure. 2.14 Comparison plots of equivalent strain versus stress triaxiality in (a) DSIF , and (b) SPIF *[14]* 36

Figure. 2.15 (a) Element layers through thickness, and (b) sections separation by forming depth for different forming stages in FE model for both SPIF and ADSIF *[8]*.. 38

Figure. 2.16 Schematics of (a). simplified ADSIF model, and (b). variables D and S in ADSIF *[15, 62]* 39

Figure 3.1 Schematics of (a) TCB (b) TCBC (c) SPIF and (b) DSIF processes. 45

Figure 3.2 General local bending for TCB and TCBC: (a) deformation regions by contact condition, and (b)stress and tension equilibrium 49

Figure 3.3 Strain diagram and stress diagram for typical bending and tension process, divided into bending and reverse-bending stages 50

Figure 3.4 (a) Geometry of local bending area and (b) Schematic of force and moment equilibrium 54

Figure 3.5 Through thickness distribution of (a) normalised shear stress, (b) stress triaxiality and (c) representative material damage during bending process in TCB and TCBC 59

Figure 3.6 Material damage evaluation based on stress triaxiality when equivalent strain equal to 1, (a) normalised compression stress, (b) normalised bending depth in TCB, (c) normalised bending depth in TCBC, and damage increments as a function of the ratio of bending depth and roller radius (d) TCB, and (e) TCBC 61

Figure 3.7 Void behaviours of (a) growth (b) coalescence (c) shear and (d) closure..... 62

Figure 3.8 Approximation of fracture loci in the (a) 2D plane of equivalent fracture strain and stress triaxiality, and (b) 3D space of equivalent fracture strain, stress triaxiality and Lode parameters (reproduced by testing data of A710 steel from Wierzbicki et al. [133]) 64

Figure 3.9 Typical void growth behaviours of various (a) stress triaxiality and (b) Lode angles in RVE model when stress triaxiality at $1/3$ [142, 146] 65

Figure 3.10 Illustration of generally used Lode angle and parameters as a function of the third invariant of deviatoric stress ξ 70

Figure 3.11 Equivalent fracture strain loci in a space of stress triaxiality and Lode angle parameter in (a) material with Lode dependence i.e. A710 steel, and (b) material with weak dependence i.e. 1045 steel (reproduced with test data from [27, 133]) 71

Figure 3.12 Shear mechanisms weight functions in space of stress triaxiality and Lode parameter from (a) Xue [121], (b) Nahshon-Hutchinson [120], (c) Zhou's modified Nahshon-Hutchinson [122], (d) Malcher modified Nahshon-Hutchinson [152], and (e) Dæhli's modification using RVE [146] 73

Figure 3.13 Effective regions of void collapse and coalescence of dependent lode angle and stress triaxiality when the initial void volume fraction $f_0 = 0.01$ [134]. 75

Figure 3.14 A new normalised fracture strain locus for Pure Ti Grade 1. 77

Figure 3.15 (a) Tensile test equipment with instron machine and DIC system (b) TCBC testing rig. 80

Figure 3.16 (a) TCBC test set-up and parameters (compression, bending depth) during process and (b) dimension of specimen design 81

Figure 3.17 Boundary conditions for: (a) uniaxial tension, (b) Pure shear and (c) tension under compression 83

Figure 3.18 Fracture loci illustrated in the plane of Equivalent strain to fracture and stress triaxiality for aluminium alloy 2024-T351 (Reproduced based on experimental data from Bao and Wierzbicki [130] and Bai and Wierzbicki [27], and numerical model assessment from Malcher et al. [154]) 84

Figure 3.19 (a) Ratio of equivalent stress and yielding stress, (b) void volume fraction and (c) damage evolution by equivalent strain from GTN model with the modification of Nahshon-Hutchinson's and Zhou's shear mechanisms by single element simulation under uniaxial tension. 85

Figure 3.20 (a) Ratio of equivalent stress and yielding stress, (b) shear damage and (c) total damage evolution by equivalent strain from GTN model with Xue's and the modified Zhou's shear mechanisms by single element simulation under pure shear states. 86

Figure 3.21 (a) Ratio of equivalent stress and yielding stress, (b) void volume fraction and (c) damage evolutions by equivalent strain from GTN model with the modification of Nahshon-Hutchinson's, Xue's and Zhou's shear mechanisms by single element simulation under uniaxial tension and tension combined compression conditions..... 87

Figure 3.22 Finite element model of TCBC with mesh and rollers set configuration. 89

Figure 3.23 True stress-strain curves for material pure Ti grade 1 at various strain rates. 90

Figure 3.24 Completed samples for comparison in uniaxial tensile, TCB and TCBC tests. 91

Figure 3.25 Maximum elongations obtained under various bending depths and compression forces in TCB and TCBC (note: zero compression force refers to TCB test condition)..... 92

Figure 3.26 Tensile forces comparison from uniaxial tensile, TCB and TCBC tests for Pure Ti 0.7mm 93

Figure 3.27 Load-displacement curve comparison by experimental data and FE prediction..... 94

Figure 3.28 Plastic strain distribution in (a) TCB and (b)TCBC 95

Figure 3.29 Distribution of damage variable in (a)TCB and (b)TCBC..... 96

Figure 3.30 Von mises stress (MPa) distribution and stages classification in the local deformation region for TCB and TCBC process 97

Figure 3.31 Maximum principle logarithmic strain distribution in TCBC numerical result, with location selection in longitudinal and through-thickness directions..... 98

Figure 3.32 Comparisons of FE plastic strain development in longitude direction between TCB and TCBC processes at (a) section 1, (b) section 2, (c) section 3, and (d) section 4..... 99

Figure 3.33 Increases of plastic stain (a) TCB and (b) TCBC, and damage (c) TCB and (d) TCBC during a single contact period 101

Figure 3.34 Comparison of stress indicators development during a single contact period: Stress triaxiality in (a) TCB and (b) TCBC, and Lode angle parameters in (c)TCB and (d)TCBC 102

Figure 3.35 Stress state path plotted on the conceptual plane constructed by stress triaxiality and Lode angle parameter (a)TCB and (b)TCBC 104

Figure 3.36 Strain paths of TCB and TCBC based on elements in section 2 108

Figure 3.37 Von Mises stress distribution through thickness under 20% and 50% thickness reduction cases in (a) TCB and (b) TCBC 109

Figure 4.1 Influence of slave tool shifting in DSIF processes (a) geometries, and (b) formability in space of fracture depth and compressive force [14]. 116

Figure 4.2 Schematic of three orthogonal axes milling machine structure and simplification in incremental sheet forming. 118

Figure 4.3 An example of the coordinate system transformation matrix 120

Figure 4.4 An example of force and moment transformation matrix 122

Figure 4.5 Cantilever beam model for simplified one-end connection component 125

Figure 4.6 Simplified gantry-type beam model 126

Figure 4.7 Gantry-type incremental sheet forming machine (AMINO DLNC-PC ISF machine, 2014 [175]) 127

Figure 4.8 Flow chart to establish a machine structure-based deflection prediction model. 129

Figure 4.9 Forces and tools' relative positions in local deformation area in DSIF: (a). Ideal condition, and (b). "Over-bending" 130

Figure 4.10 FE model schematics for DSIF processes with pneumatic support: (a) Assembly, (b) Modification of toolpath, and (c) FE mesh strategy. 135

Figure 4.11 Equivalent strain distribution in FE modelling for DSIF Al5052-O sample with pneumatic support 136

Figure 4.12 Schematic and coordinate system of DSIF machine 137

Figure 4.13 (a) FE mesh and (b) machine deflections under loading of DSIF machine. 137

Figure 4.14 (a) FE Mesh and (b) machine deflections under loading of frame fixture. 138

Figure 4.15 (a) Schematic of implementing stiffness matrix by connector element in DSIF simulation, and (b) Mesh strategy for DSIF simulations. 140

Figure 4.16 Parts formed with or without the supporting force. 141

Figure 4.17 Overall geometry profiles and thickness distribution along with the radius direction (a) 45 deg cones, and (b) 60 deg cones 142

Figure 4.18 Comparison of geometry and thickness result from FEA and experiments 143

Figure 4.19 (a) Machine structure and main components division (b) simplified model for dedicated DSIF machine. 145

Figure 4.20 Change of tool displacements in (a) x-axis, (b) y-axis and (c) z-axis with applied load at 4 tool positions. 146

Figure 4.21 Illustrations of force-displacement curves in 6 different loading positions on frame fixture used in ISF testing. 147

Figure 4.22 Pure Ti grade 1 samples of hyperbolic shape produced by (a)SPIF and (b)DSIF processes 148

Figure 4.23 Comparison of profiles from desired shape, experimental testing, FE with rigid tool and FE with stiffness model in SPIF process (a) geometry profiles, and (b) deviations between experiment, and FE models with and without machine stiffness configuration. 149

Figure 4.24 Equivalent strain contour plots for (a) FE model using rigid tool definition, and (b) FE model applied stiffness matrix in SPIF process. 150

Figure 4.25 Comparison of profiles from the desired shape, experimental testing, FE with rigid tool and FE with stiffness model in DSIF process (a) geometry profiles, and (b) deviations between experiment, FE models with and without machine stiffness configuration. 151

Figure 4.26 Comparison of profile errors from DSIF testing and detected tool deflection in FE simulation in DSIF 152

Figure 4.27 Equivalent strain contour plots for (a) FE model using rigid tool definition, and (b) FE model applied stiffness matrix in DSIF process 153

Figure 5.1 Schematics of the whole deformation processes of materials in SPIF and DSIF process. 157

Figure 5.2 Schematic of analytical model: local deformation regions divided by forming passes in DSIF process. 159

Figure 5.3 Flowchart for the analytical model for SPIF and DSIF associated with shear modified GTN model. 165

Figure 5.4 Stress triaxiality by equivalent strain curve from the analytical model of SPIF and DSIF processes. 167

Figure 5.5 Damage evolution by the development of the equivalent strain 168

Figure 5.6 The equivalent fracture strain development by (a) step size, (b) master tool radius, (c) master tool radius under fixed ratio $\boldsymbol{d/r1}$ and (d) the relative position of tools in DSIF process. 170

Figure 5.7 Influence of relative tool position to process formability in DSIF (reproduced from [14]) 170

Figure 5.8 Tool modelling with and without implementation of machine stiffness tested in FE simulation. 172

Figure 5.9 Predictions to maximum forming depth by different tool modification strategies with the modified GTN model 175

Figure 5.10 Comparisons of predicted profiles by FE simulations with different tool strategies (a). SPIF, and (b). DSIF 176

Figure 5.11 Experimental and FE simulated results with fracture depth comparison from the modified GTN model for (a) SPIF, and (b)DSIF 177

Figure 5.12 Contour plot of equivalent plastic strain at fracture in (a) SPIF (b) DSIF processes, and (c) strain at contact region 178

Figure 5.13 Comparison of average and maximum reaction acceleration during FE simulation among different tool strategies 180

Figure 5.14 Comparison of equivalent strain and damage development from earliest fracture elements in FE models applied with tools with flexibility of machine stiffness (Case B) or the deflected toolpath (Case C) calculated by experimental measured forming forces. 181

Figure 5.15 Schematic showing investigated element sections along the deformed component wall for sections 1-4 182

Figure 5.16 The comparison of equivalent plastic strain evolutions for sections 1-4 through 4 element layers 184

Figure 5.17 The comparison of damage evolution for sections 1-4 through 4 element layers 186

Figure 5.18 Development of local stress triaxiality in a single contact cycle in section 2: (a) SPIF. and (b) DSIF. 188

Figure 5.19 The development of stress triaxiality and corresponding damage increment of the concave element in the last 3 local deformation cycles before the end of forming in Section 2. 189

Figure 5.20 Stress paths in a local deformation cycle of (a) SPIF and (b) DSIF in the plane of stress triaxiality and lode angle parameters. 191

Figure 5.21 Fracture limit curves from numerical and experimental Nakajima and SPIF tests [97] 194

Figure 5.22 Schematics of two contact pair algorithms in ABAQUS/Explicit (a) finite-sliding formulation, and (b) small sliding formulation. 196

Figure 5.23 The damage development by equivalent strain from analytical model and FE simulations (a) SPIF, and (b) DSIF 197

Figure 5.24 Comparison of through thickness shear stress in FE simulations for SPIF and DSIF processes. 198

LIST OF TABLES

Table 3.1 Types of classical tests and corresponding stress triaxiality and Lode angle parameters for fracture strain surface calibration of pure Ti grade 1 (extracted and processed from [27, 97, 159]) 76

Table 3.2 Experimental designs and maximum elongation results for Pure Ti grade 1 82

Table 3.3 Material and GTN model parameters for grade 1 pure Ti used in FE simulations [23] 89

Table 4.1 Experimental testing parameters (PS=Pneumatical support) 133

Table 4.2 The dedicated DSIF machine divisions and calibrated parameters for stiffness estimation 144

Table 5.1 Material and GTN model parameters being used for grade 1 pure Ti. 164

Table 5.2 Process parameters applied in ISF analytical model 166

Table 5.3 FE simulations parameters for both SPIF and DSIF 174

CHAPTER 1 INTRODUCTION

1.1. Overview of Incremental sheet forming (ISF) and Double-sided incremental forming (DSIF)

1.1.1. Incremental Sheet Forming (ISF)

The general definition of the incremental forming may be referred to a number of sheet and bulk forming processes such as spinning or rolling, incremental sheet forming (ISF). Also known as Single Point Incremental Forming (SPIF) initially reported by Mason and Appleton in 1984 [1, 2], ISF is specifically designated to sheet forming processes, in which a simple hemispheric tool is normally used to form a metal sheet into the desired shape by moving along a pre-defined toolpath by using CNC machines or industrial robots . Figure 1.1 shows a schematic of the ISF process, which includes three key elements, i.e. (i) a simple hemispherical forming tool; (ii) blank holder and (iii) backing plate [3]. The sheet is clamped on the periphery and the trajectory of the tool is defined by a succession of spiral contours, which determines the geometry and accuracy of the formed products. The main advantages of ISF processes include its "dieless" feature, easy adaptation and simple structure of the tool system as compared to many conventional sheet forming processes, which require the use of a complex press and dedicated die or tool systems. The flexibility and low set-up cost allow ISF to be implemented for the manufacturing of low-volume, high-value and customised parts [4]. For instance, a limited number of replacement parts have been made by Honda with Amino through the ISF process [1]. Nevertheless, the ISF technology is generally considered to have considerable potential in aerospace, automotive, medical and other industrial fields.

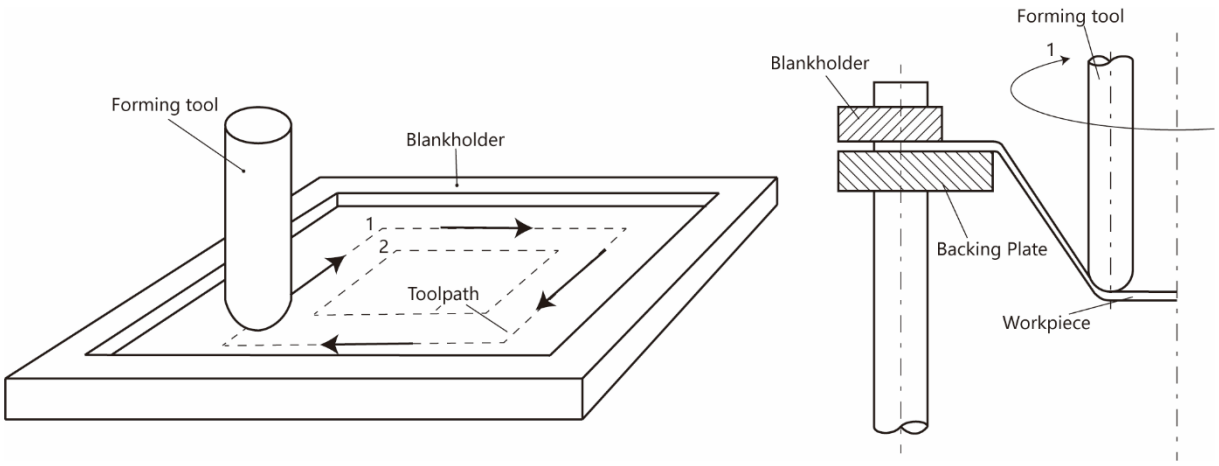


Figure. 1.1 Illustrations of incremental sheet forming.

In recent years, many variants such as Two-Point Incremental Forming (TPIF) and Double-Sided Incremental Forming (DSIF) have been proposed. As shown in Figure 1.2, the classification of the variants of ISF processes is based on the method of applying supporting forces. The SPIF uses only one tool traveling along a pre-defined toolpath on one side of the forming sheet (Figure. 1.2(a)), whilst TPIF uses an extra full or partial die on the other side of the workpiece to increase forming stability (Figure. 1.2(b)). The DSIF process replaces the full or partial die with a flexible supporting tool following a specified trajectory as illustrated in Figure. 1.2(c). These ISF variants improve the formability and accuracy in comparison with the conventional SPIF process. Especially, the DSIF process keeps both die-less feature and flexibility that attracts increasing research interests and efforts for industrial applications in recent years [5].

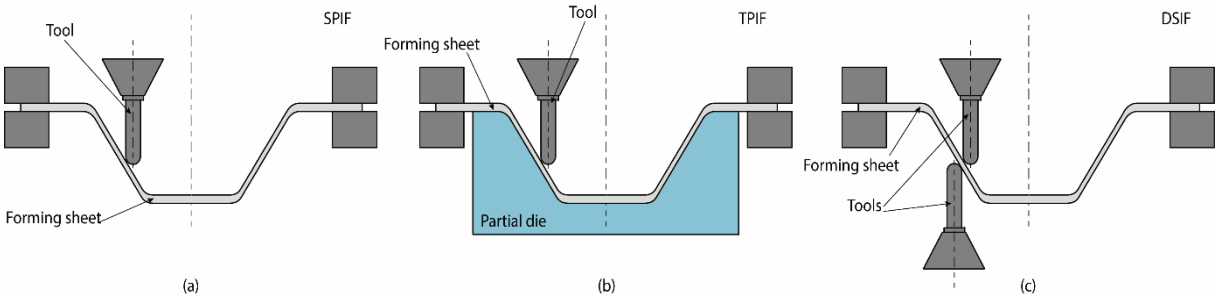


Figure. 1.2 Schematics of (a). SPIF (b). TPIF and (c). DSIF

1.1.2. Double-Sided Incremental Forming (DSIF)

DSIF was initially studied by Maidagan et al. [6] and Meier et al. [7] in 2007. It

aims to apply a backup force for the better control of the localised deformation and improvement of the formability and accuracy. In the DSIF process, the tool on the top side of the workpiece is generally named as the master tool mainly generating localised deformation, whilst the tool on the bottom side is named as the support tool or slave tool offering a supporting force. The toolpath of the support tool is derived from the trajectory of the top tool incorporated with the wall angle and thickness of the workpiece at the contact point. In DSIF, two variants can be classified by the tool moving direction in the radial orientation, i.e. conventional DSIF with an out-to-in toolpath (Figure 1.3a) and Accumulative Double-Sided Incremental Forming (ADSIF) with an in-to-out toolpath (Figure 1.3b). In the conventional DSIF process, the tools move continuously from the maximum fringe of the workpiece towards the centre. The tool steps along the negative Z direction with an incremental depth ΔZ and then forms the material in the horizontal X-Y plane at the current Z depth. In the ADSIF process, the tools start from the minimum annulus of the clamped sheet and simultaneously move down by an incremental depth ΔZ. Both the master and support tools travel on the X-Y plane and keep at a constant Z= -ΔZ. Generally, ADSIF is regarded as a specific toolpath strategy of DSIF. However, it is worthwhile to discuss and compare the ADSIF with SPIF and DSIF due to its some unique features for enhanced formability, accuracy and deformation mechanism [8].

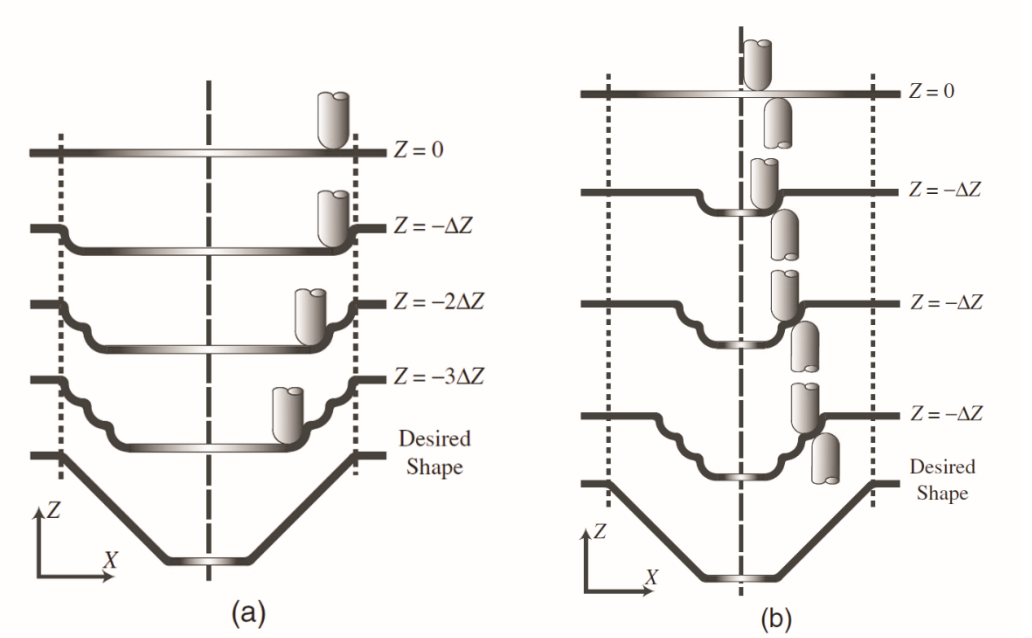


Figure. 1.3 Schematics of (a) conventional DSIF toolpath, and (b) accumulative DSIF (ADSIF) toolpath [8].

There are a number of advantages that grant the DSIF process to be a valuable solution to a small batch of sheet metal manufacture process:

- High flexibility to produce parts of customised design [9].
- Low manufacture cost due to die-less feature [10].
- Improved formability and accuracy over the conventional ISF method [11].
- Adaptability to electrically assisted forming for hard-to-form materials [12, 13].

On the other hand, the double-contact characteristic in DSIF brings additional requirements and drawbacks:

- Non-trivial requirements for equipment by using either a dedicated DSIF machine [14, 15] or two robotic arms [16].
- A specific strategy for toolpath planning to avoid the support tool losing contact during forming process [16-18].
- Inferior accuracy to conventional stamping process due to spingback.
- Limited forming angles which is hard to approach 90° of parts [19].

Further research and development to utilise its advantages and to overcome

current drawbacks would enable the DSIF process to become a more robust forming approach for rapid prototyping of sheet metal parts with enhanced accuracy, formability and versatility. Further improvement for formability and applicability requires a better understanding to the deformation and fracture mechanisms in DSIF process.

1.2. Research challenges

As a novel variant under development of ISF technologies, the DSIF not only inherits the capability of customisation and die-less feature of ISF but also presents improved formability and geometric accuracy over the conventional ISF processes. However, further applications of DSIF face challenges in two aspects: the understanding to the forming method, such as machine deflections and the loss of contact problem, and the process modelling, including the material deformation and fracture behaviours during double contacts under DSIF processing conditions.

1.2.1. Forming method

The effect of process parameters and machine compliances in DSIF process is a challenging research question yet to be answered. Ai et al. [20, 21] developed tension under cyclic bending and compression (TCBC) test as a means to capture key DSIF features, the same as the tension under cyclic bending (TCB) test by Emmens et al. [22] to SPIF . These test methods aimed at creating a standardised and measurable experimental approach to repeat the formability improvement by incremental forming with and without compression, to quantify the effect of forming parameters and investigate the deformation mechanisms in SPIF and DSIF processes. However, the level of correlation between TCB/TCBC and SPIF/DSIF in terms of deformation and fracture mechanisms is yet to be established. Further research would help develop a better understanding of both the TCB and TCBC as well as the SPIF and DSIF processes.

1.2.2. Process modelling

There has been inadequate effort made to numerically predict the ductile fracture behaviour in DSIF processes, although the effectiveness of micro-mechanics based models

such as the GTN model has been proven in SPIF studies [23-26]. Therefore, utilisation or development of new micro-mechanics based damage models for accurate prediction of fracture in DSIF processes is highly desirable, which would contribute to a better understanding of the complex mechanisms of deformation and fracture, such as local bending and compression. The proven model in SPIF processes would help further the development of numerical modelling for DSIF processes closer to practical implementation.

1.3. Research aims and objectives

In considering the aforementioned challenges, the investigation into the deformation and fracture mechanisms in SPIF and DSIF processes is the core aims of this PhD research. The investigation attempts to establish the commonality for the formability improvement through modelling of the local bending deformation in TCB/ TCBC and SPIF/ DSIF using both analytical and numerical methods. To address the question of the effect machine systems in DSIF, the PhD work also aims to develop a general approach for quantification of ISF machine stiffness and its implementation in FE simulations of SPIF and DSIF processes. To achieve these aims, the research objectives of this PhD project are to:

1. Establish an analytical model to describe the local deformation and its propagation through tool movement in TCB and TCBC processes. The effect of forming parameters can be evaluated and validated through experimental tests.
2. Examine the effectiveness of a new shear modified GTN model in numerical fracture prediction with grade 1 pure Ti material in TCB and TCBC processes. Develop a FE model applied with the verified shear modified GTN model to predict the fracture for SPIF and DSIF processes.
3. Develop a generic method for the quantification of ISF machine stiffness with considerations of the machine structure and tool position. Investigate the impact of machine and tool deflections to the formability of SPIF and DSIF processes.

4. Improve the understanding of deformation mechanisms in ISF processes and investigate the similarities and differences between the TCB/ TCBC and SPIF/ DSIF.

1.4. Research methodology

The research methodology is focused on the design and completion of a series of tasks planned to achieve the proposed objectives:

1. Due to the nature of SPIF and DSIF processes, the GTN damage model with new shear mechanisms is developed to distinguish the shear and compression stress states under low stress triaxiality, and then calibrate the damage evolution accordingly.
2. The TCB and TCBC experiments with grade 1 pure Ti are carried out to capture the formability improvement under continuous bending and compression, with different sets of forming parameters, such as the bending depth, sheet thickness and compressive forces. The elongations to fracture are used as formability indicator. Two methods are applied respectively to investigate the deformation mechanisms in TCB and TCBC processes: 1) a theoretical derivation based on local strain evolution and stress state under contact for qualitative evaluation of formability by using a conventional ductile damage criterion proposed by Bai and Wierzbicki [27]; 2) a new shear modified GTN model is developed and implemented in FE simulation using ABAQUS Explicit package and VUMAT user subroutine to predict the fracture occurrences in TCB and TCBC processes.
3. Experimental and numerical investigations are conducted to evaluate the formability of grade 1 pure Ti and AA5052 alloy in SPIF and DSIF processes. By comparing the formed and designed geometries, a specific phenomenon of geometric errors for DSIF process are found and reported as “over-bending”. The reasons of this discrepancy were attributed to the effect of machine deflections where the related influential factors are analysed and discussed. Then, the following FE simulations are carried out under the dedicated boundary condition to repeat the geometries obtained in experiments as a validation of the proposed evaluation of forming inaccuracy.

4. A generic method for machine stiffness quantification is developed based on the similarity between general Cartesian-structure ISF machine and multi-axis CNC machine. A case study is conducted on a dedicated DSIF machine. The derived stiffness model is applied to FE simulations of DSIF processes to examine the improvement of predicted geometric accuracy.
5. To investigate the feasibility of fracture prediction in both SPIF and DSIF processes, the developed shear modified GTN model is implemented in SPIF and DSIF using both analytical evaluation and FE simulations. The deformation and fracture mechanisms are captured based on the FE results.

1.5. Thesis structure

The thesis is presented in six chapters and organised by research objectives as follows:

Chapter 1 gives an introduction to the fundamental concepts of conventional SPIF and DSIF processes. This includes the application fields, advantages and current challenges which require further research, the aims and objectives that define the basic scope of this thesis. This is followed by a summary of the methodologies used and contributions made of this PhD thesis.

Chapter 2 presents a detailed literature review involving the state-of-the-art development of DSIF processes from the points of views of formability, hardware, toolpath planning, simulations, and deformation mechanisms. This leads to the discussions and recommendations of valuable research topics in the future studies.

Chapter 3 focuses on the experimental and numerical investigations on TCB and TCBC processes, which are implemented to validate the developed shear modified GTN damage model. The chapter starts with an analytical model to assess the effect of forming parameters, followed by a comparison with the results from TCB and TCBC parametric tests using grade 1 pure Ti. A particular attention is paid to the FE simulations applied with the new shear modified GTN model to predict the elongations to fracture in TCB and

TCBC processes. Based on FE results, the mechanisms of formability improvement, local deformation and fracture are discussed.

Chapter 4 presents a generic method for machine-tool stiffness quantification and concentrates on the effect of machine deflections to the formed geometry and formability in DSIF process. A general derivation of establishing machine stiffness matrix is introduced with a case study of the dedicated DSIF machine. Then a case of formability reduction by machine deflections is analysed and repeated in FE simulations. In addition, the derived machine stiffness matrix is incorporated in FE models to simulate the in-process geometric inaccuracy in SPIF and DSIF processes.

Chapter 5 summarises the developed shear modified GTN damage model and estimated machine stiffness to predict the fracture in SPIF and DSIF process with grade 1 pure Ti. An analytical model is proposed to capture the stress and stain development in ISF processes. The methods of applying the machine-tool stiffness in FE model and its effects to prediction of forming accuracy are discussed. The detailed deformation and fracture mechanisms are explained and compared between the SPIF and DSIF processes. Based on this conclusion, the relationship between TCB/ TCBC and SPIF/ DSIF is also discussed in detail.

The main conclusions based on thesis work are summarised in Chapter 6. This leads to an outline of recommended future works in the DSIF research field.

CHAPTER 2 LITERATURE REVIEW

2.1. Introduction

Incremental sheet forming (ISF), also known as Single Point Incremental Forming (SPIF), is a novel sheet forming process with high flexibility and cost efficiency. With advantages of adaptability to conventional 3-axis milling machine and robotic system, the minimum requirement of the tool and dies makes ISF process to be flexible to various forming shapes and easy to be employed on existing equipment. However, in the past research and applications, SPIF process is yet to be sufficient for the wider applications because of technical challenges such as inadequate accuracy and low formability to hard-to-form materials. Thus, a number of variants were developed, in which Double-sided Incremental Forming (DSIF) process considerable potentials to overcome the shortcomings of SPIF without the loss of flexibility and die-less feature. The purpose of this chapter is to introduce the current development of DSIF, including comparison with SPIF in terms of toolpath design, formability and material deformation mechanisms. This leads to a discussion on research methods of FE simulation and comparative study of simplified processes as well as identified research gaps in the field of DSIF and recommendations for further research.

2.2. Comparison between SPIF and DSIF

As a mainstream in the ISF field, extensive studies have been carried out on the aspects of SPIF concerning accuracy, toolpath strategy, deformation and failure mechanisms. There are many published reviews of SPIF on its history, the improvements and limitations compared with the conventional sheet forming processes and the deformation and failure mechanisms [1, 22, 28-30] as well as the advantages of SPIF include high flexibility, low set-up cost and improved formability [28, 29]. However, the SPIF process is also limited by the slow forming speed, insufficient accuracy, rough surface finishing and small achievable wall angle [29]. A number of reviews focus on

specific aspects of ISF processes such as the effects of the process parameters [31], hardware [32], asymmetric incremental sheet forming (AISF) [33], toolpath strategies [34] and FEA research [30]. Future prospects were also suggested in terms of the mechanisms studies, prediction by FE simulations and the extension of small scale production and industrial applications [30].

Whilst notable advances have been made in SPIF processes, specific limitations of SPIF have also been identified by various studies through experimental or theoretical analysis. The localised deformation under ISF process results in the high dependence of the geometrical accuracy on the stability of the deformation occurring around the contact region [35]. The springback effect and the artificial dynamic oscillations in contact area is also reported as a main resource of error [8, 28]. The optimisation of toolpath and the application of the support tool are commonly used to overcome the drawbacks of SPIF. In terms of the optimisation of toolpath, the starting point, direction of tool movement and the gap between circulars are optimised and tested to be effective [36, 37]. Techniques like FE simulation and closed-loop feedback control system were combined with the toolpath design and successfully enhanced the geometrical accuracy and homogeneity of the parts produced [38, 39]. In terms of the additional support, the TPIF process with the use of a partial die is confirmed to help reduce the springback upon the unloading in SPIF, and thereby the formability and accuracy are improved [3, 40, 41].

DSIF also brings comparative benefits by using an additional tool support, instead of a partial or full die used in the TPIF process, to achieve improved formability and accuracy to the SPIF process. DSIF was studied by Meier, et al. [7] as a truly “die-less” TPIF method and was tested and compared with SPIF through a robotic system. A simply truncated cone was produced separately by SPIF and DSIF processes. The thickness deviation results show that the cone fabricated by DSIF has more homogeneous error dispersion than using SPIF. According to the comparison between SPIF and DSIF from published papers [42, 43], the additional support tool can effectively

reduce the geometrical deviation. The die-less feature makes DSIF an economical solution to resolve the current problems in SPIF.

A full comparative investigation using both experiment and FE simulation was conducted by Knight and Lasunon [11] looking into the stress and strain condition, thickness and part profile. A shallow square-sided pyramid with 38 mm dimension for open width, 4.6 mm for depth was chosen as the desired shape in both experimental and analytical trials. The material was AA5052 alloy and two wall angles were tested to evaluate the performance of both processes to the distinct angles. It is observed from contour plots (Figures 2.1a and b) that the peak value of the equivalent strain in SPIF was higher than that of DSIF when forming the same shape; on aspect of thickness (Figures 2.1c and d), the sheet thinning from SPIF process was greater than that by DSIF, and the thinning concentrates in the corner in SPIF when it happens in the wall area in DSIF [11]. Therefore, the failure is more likely to occur in the wall region in DSIF instead of the corners from SPIF. The contrast of minimum thickness values indicates an advantage of DSIF process that can be utilised to produce parts with sharper edges and steeper wall angle as compared to SPIF process.

The deformation instability, which limits the accuracy and formability of SPIF process is imporved by the implemention of the support tool in DSIF. However, the support tool was found to lose contact with the workpiece at an early stage of the process in both experimental test and FE simulation conducted by Maidagan, et al. [6], suggesting that the process may be degenerated to SPIF. The thickness distribution suggested the unexpected sheet thinning, which differed from the prediction used in the support tool trajectory generation, could be a general cause of losing contact. Besides, the deflections caused by insufficient machine tool stiffness and sheet spring-back were noticed and believed as one of the major reasons resulting loss of contact [44]. These facts confirm that the control of the support tool to avoid loss of contact is a key challenge in DSIF research. Thus, the prediction of deviations during process and countermeasures are important questions to maintain the improved formability in DSIF,

which is very different from the SPIF process.

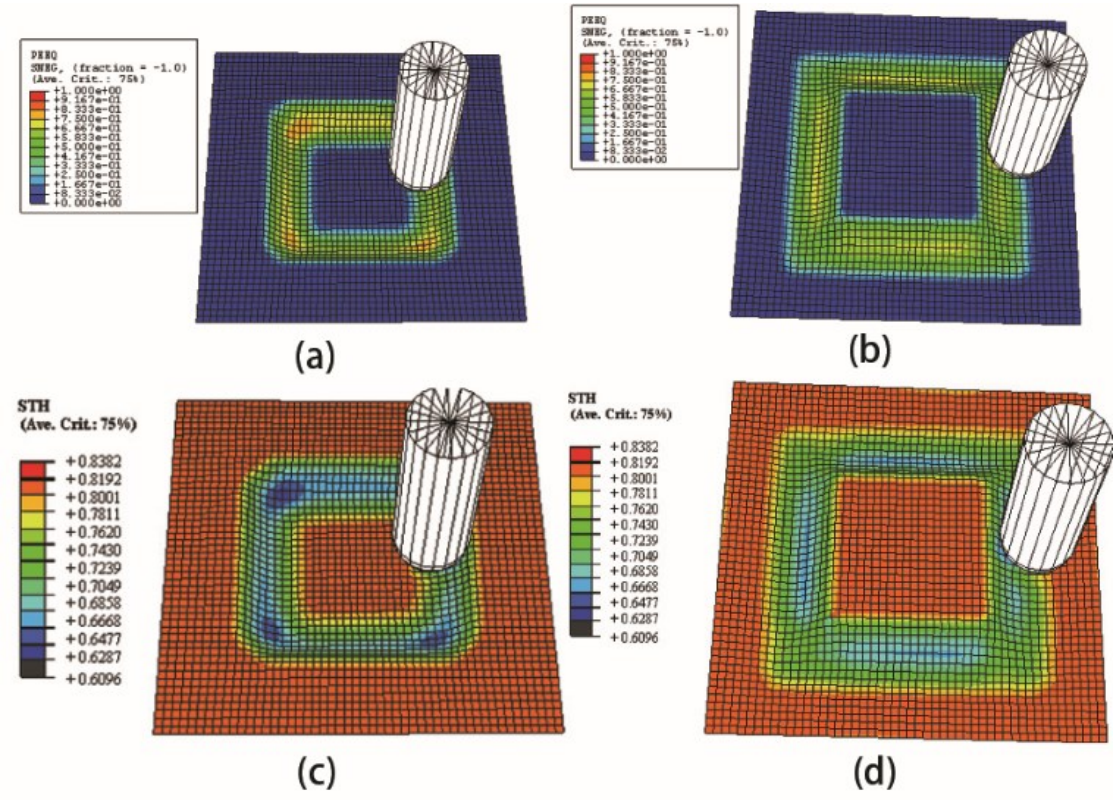


Figure 2.1 Equivalent plastic strain contour plot of (a) SPIF (b) DSIF, and thickness distribution in (c) SPIF and (d) DSIF process of 45° pyramids [11]

In both SPIF and DSIF processes, the sheet is clamped and formed by the movement of specific tools. Most of the advantages of SPIF are inherited by DSIF, such as high flexibility and no requirement of dies. DSIF shows the potential to surmount the formability limits and low geometric accuracy in SPIF [11, 45]. The value of plastic strains and the extent of sheet thinning concentration in SPIF are higher than that in DSIF, which means a lowered possibility of failure occurrence in DSIF than that of SPIF. Therefore, the aforementioned studies show a clear advantage of the DSIF over SPIF in a number of key attributes under general ISF processing conditions.

2.3. Testing equipment in DSIF

The concern for machine design rises with the increasing research interest for DSIF

in the past decades by multiple research groups because of the increased complexity of the machines used for DSIF. Unlike SPIF process where a conventional 3-axis CNC machine would be sufficient to complete the SPIF or TPIF processes [46-48], a 5 or 6 axis machine system plus a clamping fixture is necessary for the DSIF process to be carried out. The machine structure and control system determine the stiffness of machine tool and directly impact to the amount of deflection under forming forces. As a result, sufficient level of control that keeps the accuracy of relative positions between the master and support tools and adequate system stiffness are important considerations to minimise the effect of machine tool deflections to the geometry of formed parts.

The machine systems implemented in previous DSIF research are summarised in Figure 2.2. Figure 2.2a shows an early attempt with synchronised tools on a turning centre preformed in Indian Institute of Technology Kanpur (IITK) [49]. A similar work using C-frame for DSIF concept was conducted in Northwestern university as shown in Figure 2.2f [50]. Meier et al. [7, 51] developed robot based DSIF method (Figure 2.2b) which utilised the high controllability and flexibility but limited by the stiffness of manipulator systems. IITK (Figures 2.2c, d [49]), Shanghai Jiao Tong University (Figure 2.2e [14]) and Northwestern University respectively (Figure 2.2g [50]) designed bespoke DSIF machines placing two individually controlled three axis forming tool positioning systems to operate two tools on both sides of workpieces. However, the machine compliance was a challenge for these machines which led to a series of studies for toolpath compensation and optimisation [18, 52-54]. There was also effort to improve the stiffness of DSIF machine system to eliminate the tool positional error from the source. The research group in Northwestern University deigned a tri-pyramid robot structure DSIF machine [55] to enhance the load capacity and robustness. This is followed by the real-time kinematic calibration to achieve sufficient accuracy for incremental forming test [56].

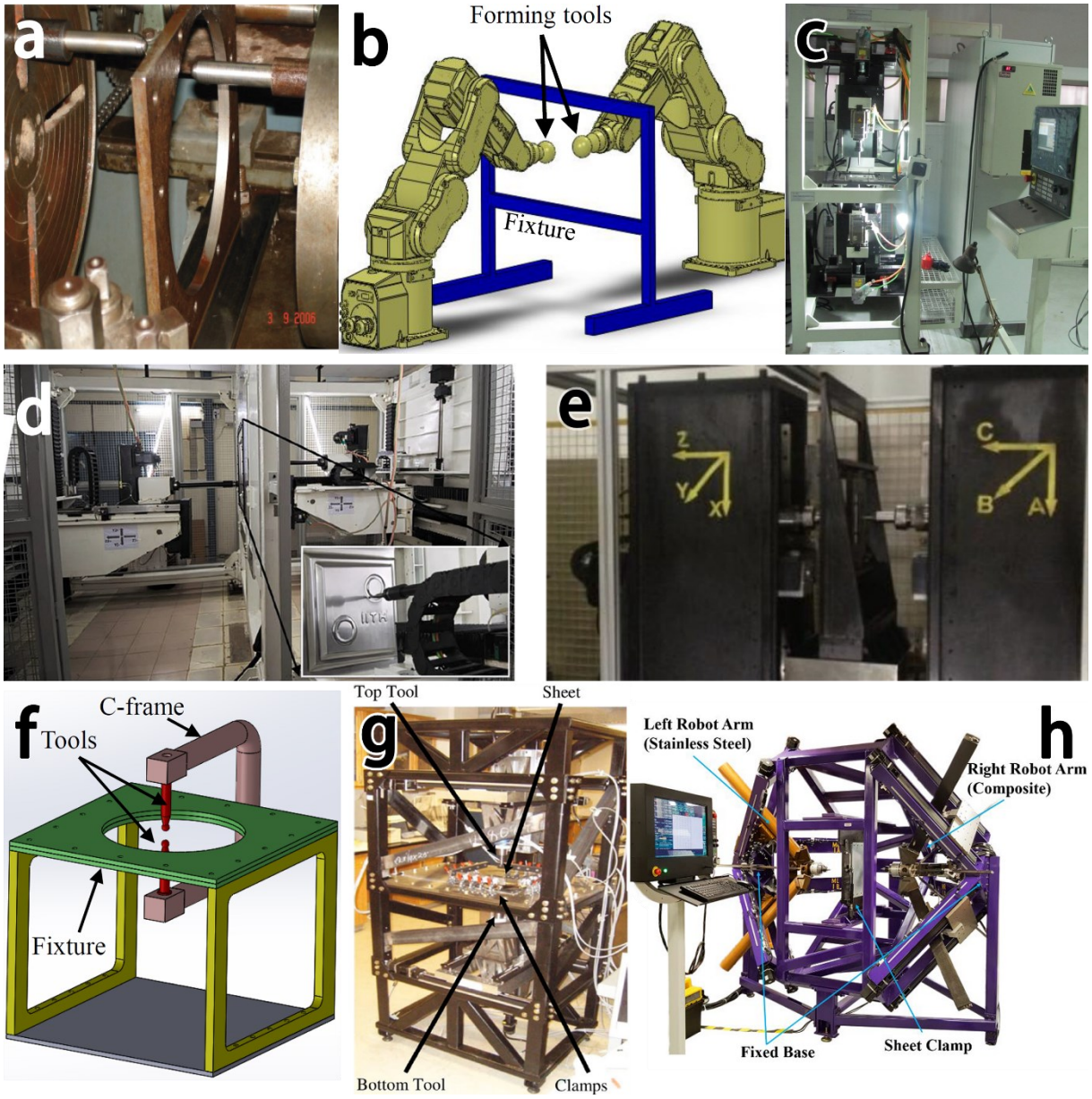


Figure 2.2 Developed DSIF testing method and bespoke machines (a) DSIF using turning machine (IIT Kanpur, 2006 [49]) (b) Robotic arms DSIF (Ruhr-University, 2011 [57]) (c) bespoke DSIF machine (IIT Kanpur, 2010 [49]) (d) scaled dedicated DSIF machine (IITH [18]) (e) bespoke DSIF machine (Shanghai Jiaotong University [58]) (f) DSIF on C-clamp (Northwestern unidersity, 2008 [50]) (g) bespoke DSIF machine (Northwestern unidersity, 2012 [43]), and (h) parallel robotic structure DSIF machine (Northwestern unidersity, 2020 [56])

As a novel sheet forming method requiring dedicated equipment, the development of DSIF machines highlights the need of solutions to two key questions. When the master tool executes a contouring movement, the travel of the support tool requires

synchronisation to maintain proper squeezing between the tools and workpiece. Two individual positioning systems are demanded for tools travelling on both sides, manipulated by a dedicated control system designed with capability of collaborations among axes [10]. Alternatively, a mechanical duplication device for the secondary tool was used in the early stage [59]. On the other hand, the requirement of positional accuracy owns a strong dependency on the stiffness of machine system as well. As the machine positioning error was noticed in the recent years, the compensation based on experimental data using machine learning techniques [53, 56] became a common choice to improve the forming accuracy. In contrast, there is a lack of sufficient research on machine stiffness [18] and optimisation of machine structure [55] in DSIF processing.

2.4. *Formability in DSIF*

2.4.1. Definition

The term of formability in sheet forming process is used to describe the ability to enable sheet deformation without material failure. Similar to the SPIF process, the formability of DSIF can be described by the maximum achievable wall angle α_{max} according to the sine law as shown in Equation (2.1):

$$t_f = t_0 \sin(90° - \alpha) \tag{2.1}$$

where t_f and t_0 are the final and initial wall thickness, respectively, and α is the wall angle as shown in Figure 2.3 *[60]*. Using the sine law, the wall thickness can be uniquely determined by wall angle α. Considering the potential squeezing effect brought by the support tool, another parameter called squeeze factor s, suggested by Malhotra, et al. *[42]*, was used to estimate the extent of an artificial squeezing effect applied on the thickness in the contact region as defined in Equation (2.2), where $t_f^{squeezed}$ is the current thickness of squeezed wall:

$$t_f^{squeezed} = s \cdot t_f \tag{2.2}$$

The squeeze factor s demonstrates the ratio of the final formed thickness to the thickness predicted by the sine law. According to the sine law, the sheet thickness decreases and the chance of failure rises when the wall angle increases. Thus the maximum achievable wall angle α_{max} is regarded as the most common indicator for the formability of the DSIF process and has been widely implemented in comparative study [43] and parametric investigation [61, 62].

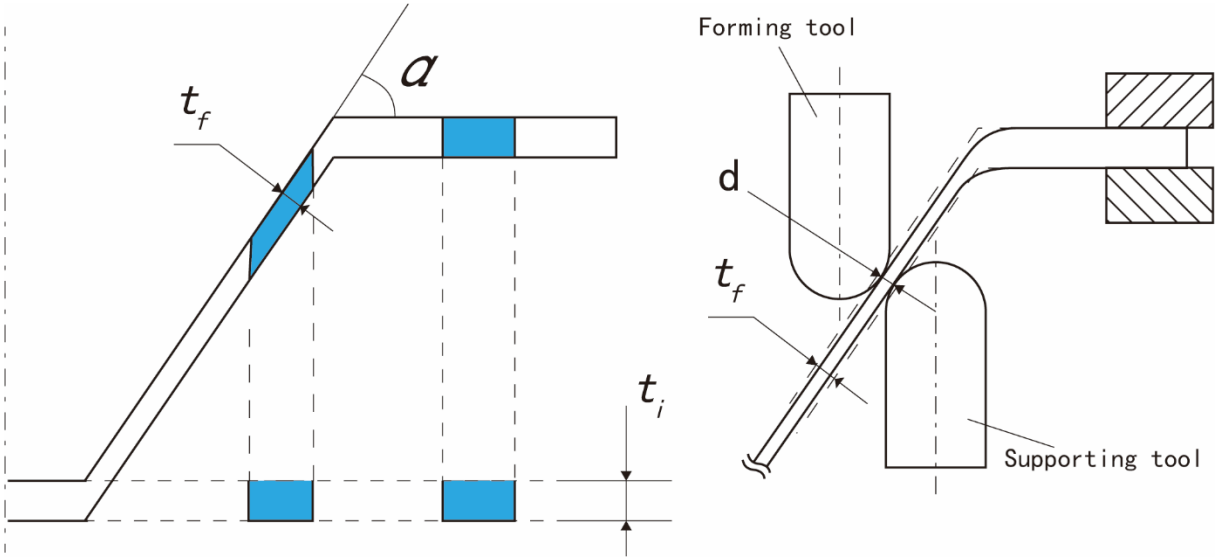


Figure. 2.3 An illustration of the sin law and squeeze factor in DSIF

The indicators of formability in ISF can also be used in DSIF, especially for analytical studies. Lu et al. [14] used the stress triaxiality, which is previously used to evaluate the contribution of deformation mode combined with stretching, squeezing and shearing in the ISF processes, as an indicator of the enhanced formability of the DSIF process. Based on the traditional forming limit diagram (FLD) [22], Allwood and Shouler [63] proposed a generalised forming limit diagram (GFLD), which took the normal stresses and through-thickness shear into consideration to match the nature of the deformation mechanisms of DISF. The general methods for the evaluation of process formability can be used to support the analytical research of DSIF [8] although specific procedure or approach for adaptation and implmentation is still to be fully researched and validated.

2.4.2. Influential factors to the formability of DSIF

The DSIF process inherits the localised deformation feature of the general ISF processes and hence the formability also depends on process parameters such as tool rotations, feed rate and step size [31]. One unique process factor in DSIF is the relative tool position as it controls the compression and the direction of local bending. Lu et al. [14] implemented a series of experiments with dedicated support tool mounted on a pneumatic actuator in order to investigate the effect of tool shift and compressive stress in DSIF. Figure 2.4 showed how the effect of tool shift and compression were estimated via checking the deformation of pre-drilled holes in through-thickness direction. Based on the observation of results, the stretching in meridional direction is considered to have a dominant effect in the deformation of DSIF. The other factors are the compression in the radial direction and slight through thickness shear in the tool movement direction. The compressive stress shows a positive effect to the formability. However, excessive supporting forces generating too much squeezing pressure reduce the formability in DSIF. Similarly, the tool shift has a positive effect on the enhancement of formability and would change the position of fracture occurrence. This approach was successfully used to form pure titanium cranioplasty plate for medical application [64].

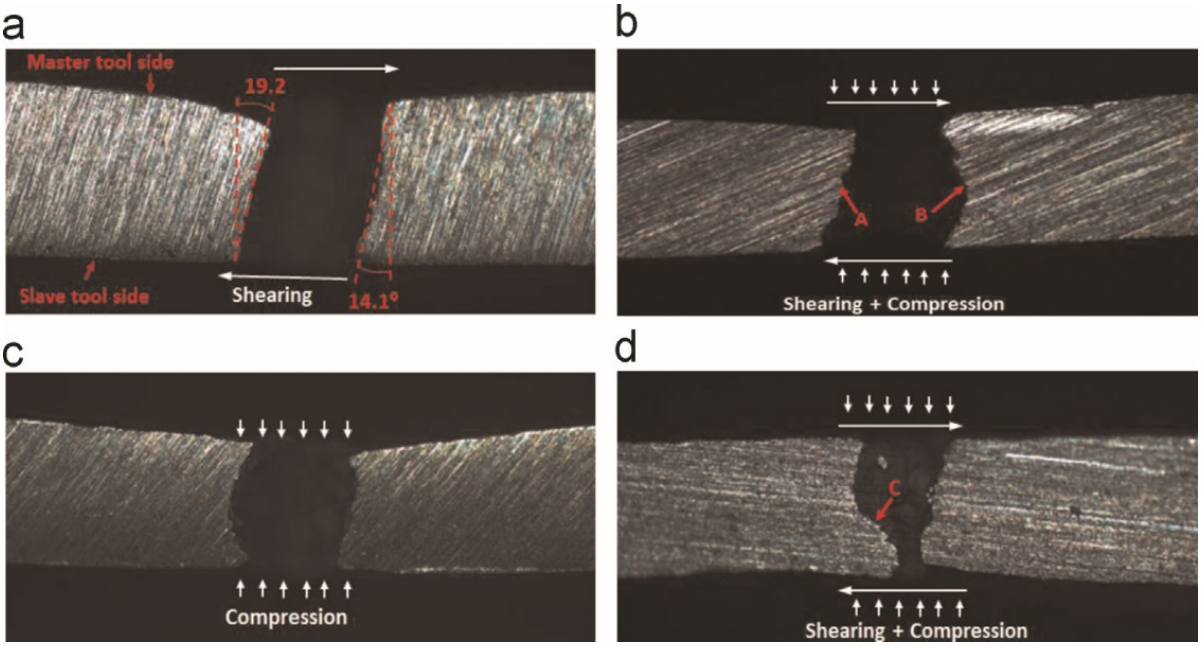


Figure. 2.4 Material deformation via different supporting forces and tool shift: (a) 240 N without tool shift, (b) 240 N with tool shift, (c) 480 N without tool shift, and (d) 480 N with tool shift *[14]*

Ren, et al. [61] processed a parametric study using FE simulation to investigate the influential factors on formability in the ADSIF process. As shown in Figure 2.5a, the tool gap T_g and the position angle θ were chosen as the variables, and the stable wall angle was measured as the criterion of formability (Figure 2.5b). It is found that the dominant influential factor is switched between T_g and θ depending on the extent of the squeeze effect. When squeezing is the dominant deformation mode during the process ($T_g \leq 0.7$), T_g has the leading effect on the stable angle; when bending is the main deformation mode ($T_g \geq 1$), θ is the dominant factor instead of T_g; when the process is in the competing region ($0.7 < T_g < 1$), there are implicit influential factors of process formability. This result may be partially explained by the force transfer due to the changes of T_g. When $T_g < 1$, the forming force increases dramatically with the T_g decreasing. Also, θ affects the bending instead of squeezing and makes the transition from the current wall angle into a stable wall angle. Therefore, keeping the process under the competing or bending-dominant region ($T_g > 0.7$) and increasing the position angle θ is recommended to control the squeezing effect, as well as the forming force, in an appropriate range to reach

the maximum formability in ADSIF forming. However, this conclusion may not be applicable to the conventional DSIF process due to significant differences between the ADSIF and DSIF processes, which are discussed in Section 5 on deformation mechanisms.

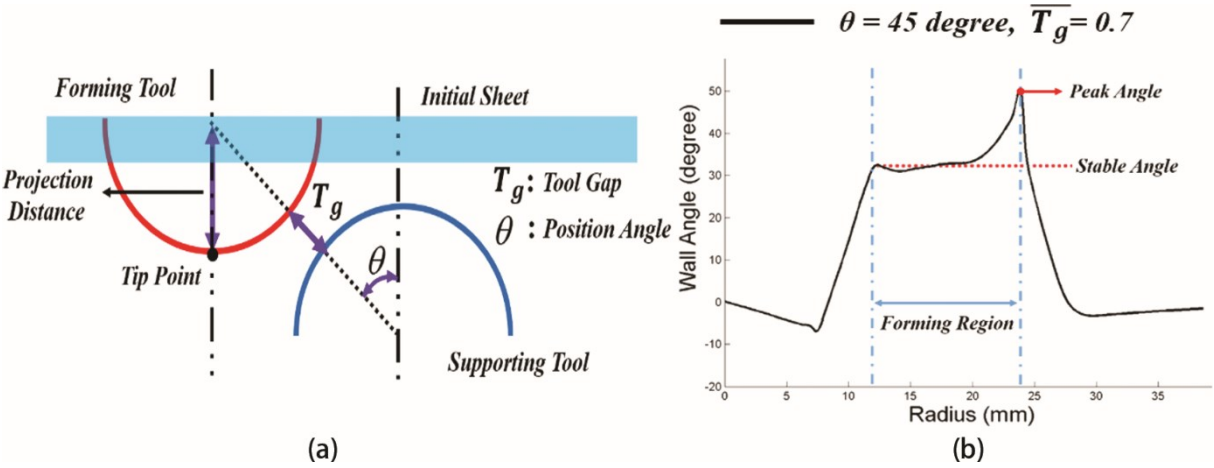


Figure. 2.5 (a) Schematic of toolpath variables, and (b) Definition of stable angle *[61]*

2.4.3. Electrical-assisted heating in DSIF

Several trials were reported for various materials being tested in ISF inclusive of composite or high-strength materials. Preliminary studies for composite materials focused on the formability and failure mechanics of polymers [65] or metal-polymer/foam/fibre [66-68] by SPIF process. Specifically, for medical use, the application of PEEK material in ISF was one focus in resent studies and faced challenges of heating method [69]. Davarpanah et al. [70] presented a series of experiments for thermoplastics using SPIF, conversational DSIF and ADSIF processes to give a comprehensive assessment. The results showed an agreement with previous tests using metal sheet that the DSIF process postpones or avoids the occurrence of fracture on polymer sheet as well. The SEM images demonstrated less void growth in the parts of polymer made by DSIF, which leads to discussion that the heating generated by the additional tool causes the formability improvement, instead of the compression effect when forming sheet metals.

For hard-to-form materials, heating is a generally used solution to increase the formability of materials in the ISF processes. There are various methods developed for heating-assisted ISF including mounting heating equipment (e.g. hot air blowers [71],

heater band [72] and laser generator [47]), friction stir heat [73, 74] and electric heating [75, 76]. Xu, et al. [13] investigated electrically assisted DSIF in forming an AZ31B magnesium alloy. Two modes of electrical connection were discussed. Figure 2.6a shows the set-up of electrical assisted DSIF process. An air cylinder and rolling-ball tool were used to eliminate loss of contact and electrical discharging phenomenon. In contrast to the electrical SPIF process, the forming feasibility, geometric accuracy, and surface finishing were improved (Figure 2.6b). Valoppi, et al. [12] conducted an electrically-assisted ADSIF process to form Ti6Al4V alloy. The electric current was applied directly to two forming tools and the value of electric current was the main variable to control the temperature during the process. In the results, the formability improvement was apparent as almost all specimens fabricated with the electrically assisted ADSIF could achieve a larger depth than the normal ADSIF process without cracks. However, the best achieved depth was obtained in the case of applying 50 A current. The negative effect appeared when the applied current value increased above 50 A. The reason could be the decrease of forming force and the release of the internal stresses due to the thermal effects during the process. A specific advantage of heat assisted DSIF over SPIF is potentially the local heating effect by tool rotation friction or direct resistance heating from both sides of the workpiece to allow more even heating and greater controllability under ISF deformation conditions.

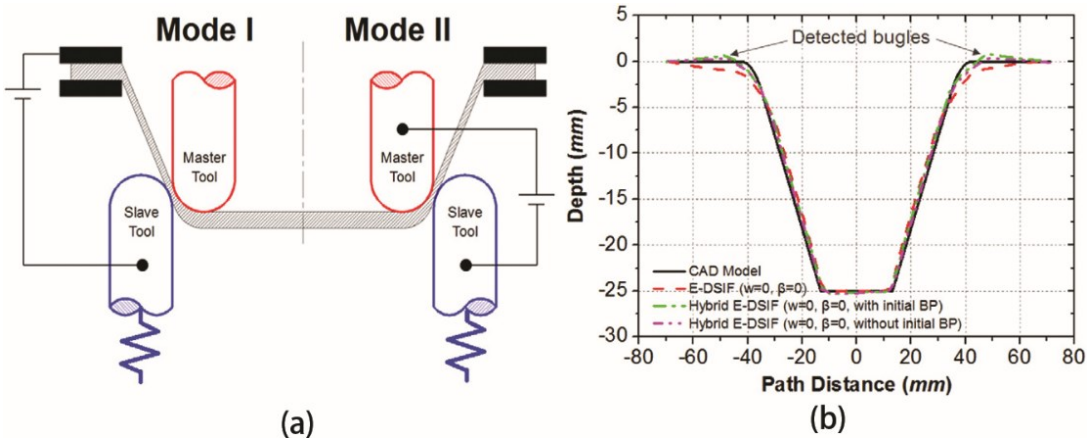


Figure. 2.6 (a) Two electrical connection modes in DSIF, and (b) improved geometry accuracy in electrically assisted DSIF *[13]*

2.5. Toolpath design in DSIF

The local deformation characteristic of ISF process determines tools trajectory as the most influential factor to finished geometry, which leads toolpath design and optimisation becoming the mainstreams of DSIF research. The key questions to be solved through toolpath design are insufficient geometrical accuracy and loss of contact. The basic principle of toolpath design is the sine law, which is consistent with conventional ISF. The toolpaths can be classified into two options: the traditional out-to-in DSIF and the specific in-to-out ADSIF strategies. Several prediction and compensation strategies are applied based on DSIF and ADSIF processes. The advantages and limitations of each strategy are discussed.

2.5.1. **Accumulative-DSIF Strategy**

ADSIF requires a novel toolpath that uses two tools forming the sheet via an initially single incremental depth and horizontal in-plane motion. ADSIF has two main differences from the conventional DSIF strategy: (i) the tools are moving from minimum annulus to the fringe; (ii) after the first step, tools are positioned at $Z = -\Delta Z$ level without any movement in vertical axis throughout the process. A significant advantage of ADSIF is that two tools maintain contact with the forming sheet and mechanically avoid the loss of contact throughout the whole process.

The constant contact leads to the improved formability and geometrical accuracy in the ADSIF process as compared with the conventional DSIF and SPIF processes [77]. The ADSIF concept was originally introduced and tested by Malhotra, et al. [43]. Two cones with wall angles of 40° and 50° were formed to test the forming limit and precision with the reference parts made by SPIF and DSIF for comparison. As test results illustrated in Figure 2.7, the smaller geometric deviations and thickness inconsistency were observed from parts produced by ADSIF instead of SPIF or conventional DSIF. When forming a cone with 50° draw angle, fracture occurs in the processes except ADSIF (Figure 2.7). On the other hand, a small incremental depth is required in the ADSIF process to sustain the high

accuracy and results in considerable time for completion. Additionally, the achievable wall angle is hard to exceed much more than 50° [19].

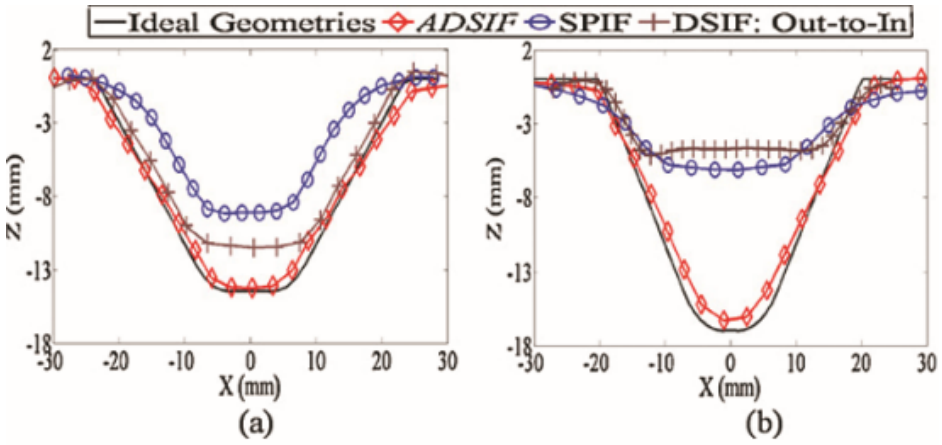


Figure. 2.7 Comparison of geometries of components made by ADSIF, DSIF and SPIF with wall angles (a) 40° and (b) 50° [43]

Although the long forming time and the limitation of forming wall angles in ADSIF prevent it to be a full replacement of conventional DSIF, the improved formability and quality by ADSIF still attract attention for further studies. Toolpath optimisation and combination with out-to-in DSIF toolpath are verified to be beneficial for the enhancement of formability and profile accuracy [77]. Other numerical analysis reveals the unique deformation mechanism in ADSIF of enhanced shearing and bending effect in contrast to dominant stretching and bending effect in conventional DSIF processes [8, 62]. In summary, the ADSIF is a noteworthy strategy and has a considerable potential of applications.

2.5.2. Compensation-based toolpath

Toolpath compensation is one strategy to accurately predict the machine tool deflection during the process and counteract the springback effect through the optimisation of tools trajectory. Accurate prediction or in-situ measurement with adjustment algorithm to the deflection during the process is the key challenge in the optimisation of tools trajectory. In the study of SPIF, the tools deflection was realised and optimised especially in ISF by robotic systems based on stiffness theory [78, 79]. For sheet

springback, analytical models were established to estimate the error between the formed and the ideal geometry [80-82]. FE simulation was implemented with satisfactory accuracy before the part was made, which contributed to predictive model training and toolpath correction [39, 83, 84]. There were studies focusing on parametric investigation with digital image correlation (DIC) obtained data from experimental tests, using regression algorithm or even neural network training methods against the complexity of machine inaccuracy and material elastic recovery [85-89]. However, real-time closed loop control was barely applied and studied in ISF [38].

For DSIF processes, the additional tool brings both controllability and interferences. The studies for compensation- based toolpath strategy in DSIF were accordingly inherited from the methods used in traditional ISF fields. Meier, et al. [16] presented experiments of model-based and sensor-based strategies in robotic forming. Figure 2.8 shows how an adjustment vector, derived from the deviation obtained by simulation results and CAD model, was defined as a key parameter for toolpath revision. In terms of the sensor-based method, actual geometry is obtained through a 3D surface scanner and projected onto the reference CAD model in the direction of the adjustment vector with the aim of plotting counter points of the next forming run. For the model-based strategy, the process is simulated through an FE model with adjustment made based on the geometric errors obtained from the simulation result. Both strategies were verified to be able to reduce the deviations with results showing a significant reduction of deviation from ±1 mm to ±0.25 mm using the sensor-based strategy, and 0.7 mm in z-direction with 1 mm in y-direction using the model-based strategy. To improve the performance of the model-based approach, the springback effect should be taken into account in the FE model.

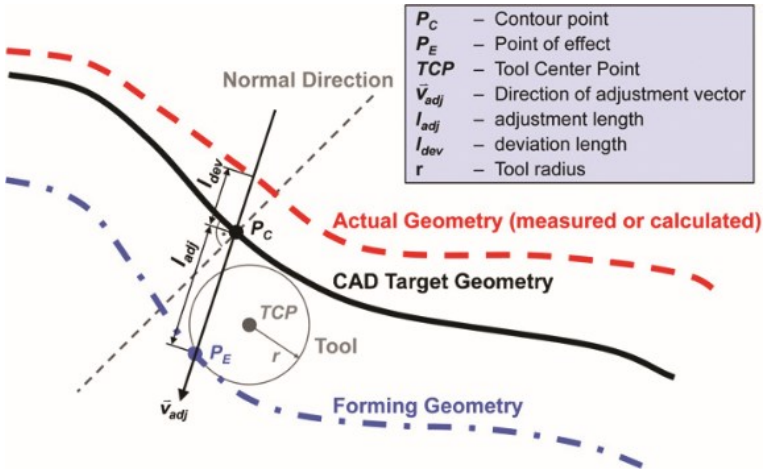


Figure. 2.8 Schematic of applying the correction through the reference CAD model *[16]*

Rakesh, et al. [44] developed another toolpath strategy which takes the deformation of tools and sheet responses by the forming forces into consideration. The adjustment vector was made up by sheet and tool deflection separately calculated by the predicted forming forces, as shown in Figure 2.9a. The sheet and tool deflections were calculated from forming forces by plate theory and tool stiffness model. The geometry obtained in the first iteration of FE simulation was compared with the desired shape to predict the deflections and to generate the compensated toolpath (Figure 2.9b). To optimise the forming process of varying wall angle or asymmetric component, the desired profile was divided by geometric features to predict forming forces more precisely (Figure 2.9c). Based on the results of several tests with different shapes and features, it can be confirmed that the deflection-compensated toolpath strategy can enhance the geometrical accuracy of DSIF as the measured maximum error is less than 0.5 mm. The maximum deviation can be kept under 0.6 mm in the fringe region after component being trimmed. Praveen et al. [18] extended the scope of application to large sheet size, introducing membrane theory as perfection of sheet deflection. The machine stiffness was given as a force-displacement map obtained by experimental measurements. As the algorithm tested by a free-form geometry with various sizes and features (component opening from 150mm- 610mm), the maximum error was controlled within 0.8mm.

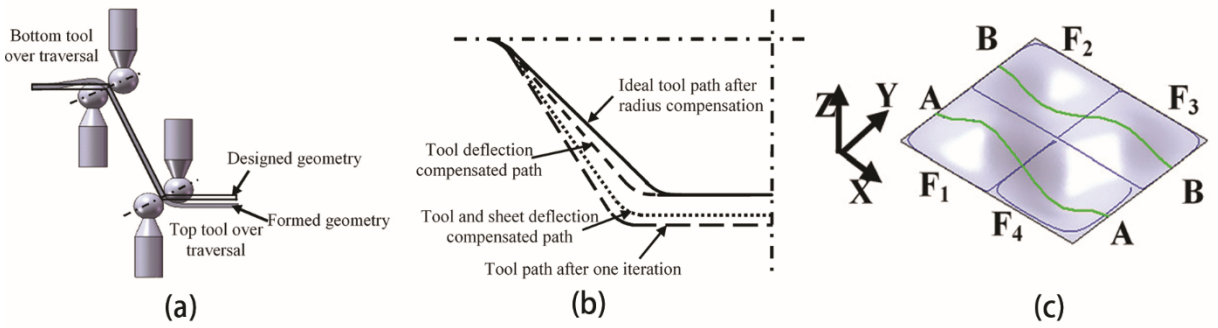


Figure. 2.9 (a) Toolpath and sheet deflection, (b) steps of how compensation applied, and (c) partition of profile based on features *[44]*

Another approach to compensate for tool deflection was proposed by Ren, et al. [90] who developed a closed-loop algorithm to eliminate the inaccuracy from the tool deformation and the system error from motor drivers or controllers. A model coupled with the stiffness of the forming tools, machine and the sheet metal under squeezing was established to derive the system response from force to displacement. Therefore, the loss of contact can be avoided, and the state of stresses is under control by monitoring the reaction force on the supporting tool. In the tests, the produced asymmetric and complex parts proved the effectiveness of this algorithm towards maintaining the contact between tools and sheet as well as the enhancement on the formability and geometric accuracy.

Wang et al. [58] proposed a novel strategy to reduce the springback in the DSIF process with a dedicated pneumatic supporting tool. The position between the master and slave tools was relatively rotated as shown in Figure 2.10. With the constant supporting force, the “reverse-bending” or “squeezing” effect can be produced in the local forming region according to the rotation angle. The error in both major and minor axes on the semi-ellipsoid cone part was measured and compared to demonstrate the restraining effort from different strategies to the springback effect. The numerical and experimental results showed an agreement that both the squeezing and reverse-bending strategies can reduce the offset due to springback effect, while the reverse-bending strategy can achieve more accurate geometry than the squeezing strategy. However, it should be noticed that depending on the desired shape, the improper reverse bending can result in “over-

bending" phenomenon which caused negative effect to formability and accuracy [91]. Thus further investigation needs to be made to clarify the optimal tool shift strategy can be applied to different geometries.

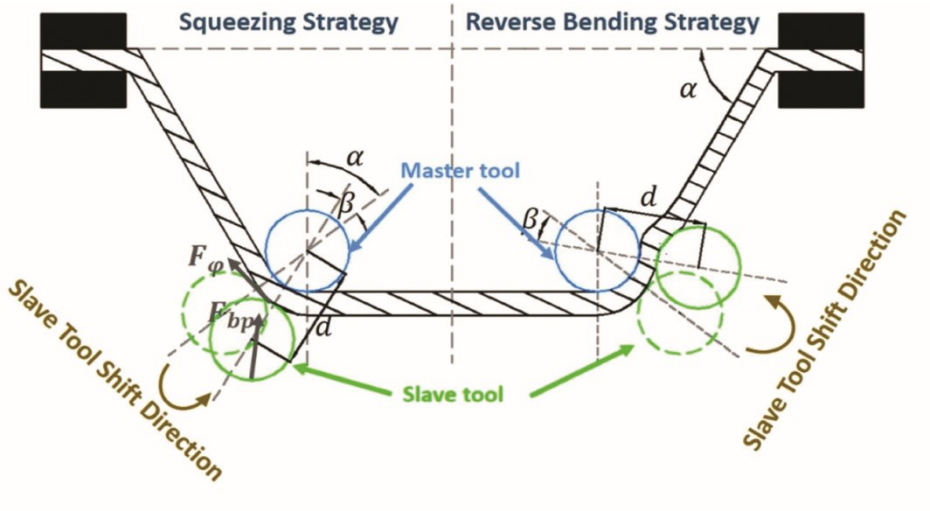


Figure. 2.10 Illustration of squeezing and reverse bending strategies for anti-spingback purpose *[58]*

Comparing with the compensation strategies conducted by Rakesh, et al. [44] and Meier, et al. [17] , the method considering the compensations of both sheet and tools shows advantages of higher accuracy and the capability of adaption for complex features. This may be attributed to the accurate force prediction (within 50N of deviation compared with the experimentally measured forming forces) and reasonable arrangement of toolpaths. The methods such as simplified algorithms with the consideration of tool machine stiffness [90], "squeezing" and "reverse-bending" strategies [58] can be implemented in DSIF processes for improved accuracy and the inhibition of springback effect with no requirement to the prediction of forming forces or deflections.

2.5.3. Feature-based toolpath strategy

The feature-based approach was initially proposed by Verbert et al. [92] for SPIF that was based on the local characteristics of profile and design specific toolpath with the aim of enhancing the accuracy. The strategy can be summarised into two main parts: (i) find the critical edges based on calculation of vertexes on curvature; (ii) recognition, segmentation and sequence for features and generating customized toolpath. Behera et

al. [93] proposed detailed principle of feature taxonomy and feature interaction with neighbouring features. The interactions leaded to the advanced compensation by generation of response surfaces [94]. Lu et al. [37] focused on the optimisation of toolpath generation for asymmetries features instead of classifications. A voltage field was calculated between critical edges and applied to derive the length and number of contours. Any two nearby edges were paired where between them the contour lines were generated from STL model through a specific voltage. The final toolpath utilised an interpolation technique from Malhotra et al [95].

This strategy was further developed to be adaptive to the DSIF process by Lingam et al [52] and Ndip-Agbor et al [96]. The additional support tool provides the suitability for forming features and sequences as the relative tool position controls local deformation and impacts the formed geometry and residual stresses. The initial step is the establishment of the component model and reading features from the desired surfaces to generate silhouettes. These silhouettes or saddle points are matched to the characteristics of features to recognize the geometrical features correctly. Then a proper forming sequence of features is selected in checking the corresponding effects between adjacent feature forming steps and the algorithm calculates the rectifying parameters. In the last, the DSIF toolpath was generated with helical trajectory combining declination optimisation [37, 44] and sheet deflection compensation [44]. Improvements in surface finish, geometric features and accuracy were confirmed by experiments. Maximum deviation to the ideal profile can be limited to 0.4 mm when the correct forming sequence and strategy were applied.

The further refinement of feature based DSIF was developed by Ndip- Agbor et al. [96]. Components with multiple features of convex and concave curvatures in Z-levels, which is normally difficult to produce by conventional ISF techniques, were made as the bottom tool acting as the forming tool when in need. The order of features forming was discussed and compared in a form of recursive algorithm extracted from feature relationship map.

Moser, et al. [97] developed another analogous method corresponding to the in-plane curvature effect. Figure 2.11a shows the region of loss of contact affected by the tool motion direction. The forming force on the support tool in the Z-direction also shows a drop after forming a turning point at the corner which indicates the occurrence of loss of contact (Figure 2.11a). The toolpath was divided into 4 parts according to the contour protrusion and tool moving direction (Figure 2.11b). Then the compensation was applied to the region with insufficient support. As a result, the uniformity of thickness distribution was improved and the possibility of failure was reduced.

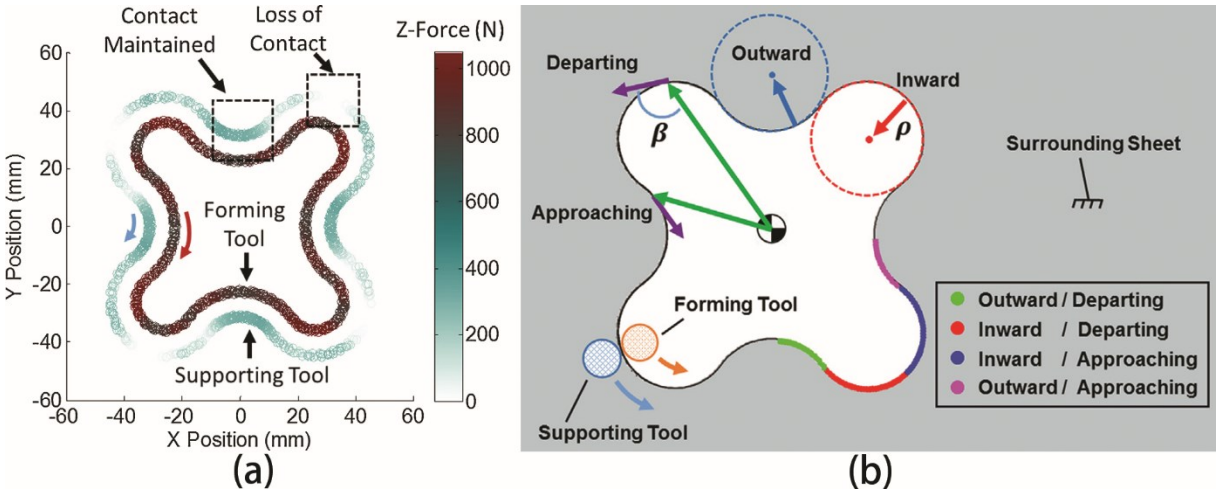


Figure. 2.11 (a) Contour plot of Z-forces predicted via FE simulation, and (b) Classification of tool movement based on tool movement and contour *[97]*

Zhang, et al. [77] proposed a mixed strategy which combined DSIF and ADSIF methods. ADSIF was used to form the main body of the part to avoid the loss of contact and to achieve a better geometry, whereas DSIF was used to form the finer details on the part in the next step. As a result, the mixed strategy can form the part with larger forming depth than that implemented by only using the conventional DSIF process, and achieve better details than that obtained from only the ADSIF method. Figure 2.12 presents an example of a part made by the mixed toolpath strategy [77]. However, it was also found that the fracture occurred during the DSIF process when forming parts of a large wall angle.The forming limits of both the DSIF and the ADSIF need to be investigated for further

development of combined forming strategies.

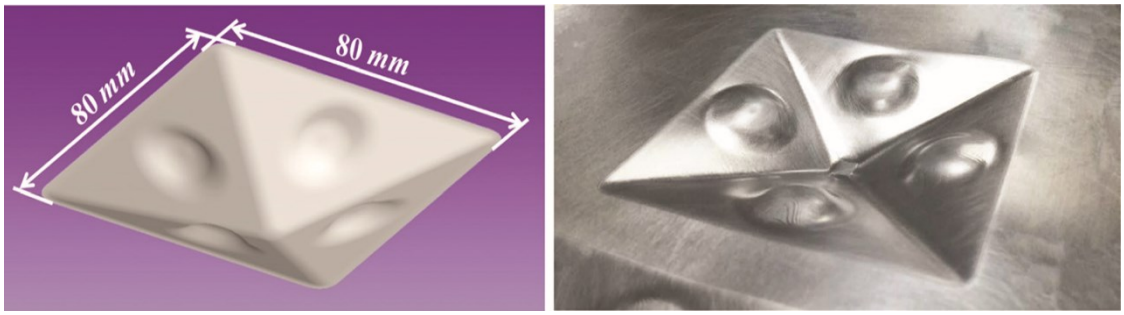


Figure. 2.12 The desired and final product fabricated via the mixed toolpath strategy *[77]*

In conclusion, the feature-based strategy is a useful method to optimise toolpath with different geometerical features. With suitable selection of strategy, the formability and production quality can be improved. Moreover, complex features as continuous concave- convex curvature in vertical direction or small localised change can be achieved that extend the boundary of ISF. Two essential issues to address are the separation of the contour model with proper arrangement of forming order and the implement of compensation. The feature-based strategy can be generalised in the form of detailed guidelines of toolpath design in the DSIF process, similar to the study presented in SPIF [34]. Two essential issues to be addressed are the separation of the contour model and the implementation of compensation. The feature-based and compensation-based strategies are compatible to each other and can be incorporated together for further enhancement of formability and accuracy, which is considered as a main research direction for the DSIF toolpath optimisation. There is a clear need for further study on the precision of feature recognition, the sequencing of forming features and corresponding optimisation methods.

2.6. Simulation of the DSIF process

There has been increasing demand for more accurate simulation of DSIF process for improved formability from SPIF to DSIF and better predictions of forming forces, sheet springback and fracture.

2.6.1. Constitutive models

The implementation of material constitutive models focusses on the material hardening behaviour under multi axial and cyclic load, coupling with the damage evolution. In SPIF simulation, kinematic hardening has the dominant effect in the individual loading cycle, when the isotropic hardening becomes significant and leads to increase of peak stresses after a large amount of loading [98]. Duflou et al. [30] proposed a phenomenological constitutive model that leads more accurate performance than the Gurson type models as reported in literatures. It was noticeable that the stress gradient through thickness may cause the inaccuracy because of uncorrelated material constitutive law and also insufficient mesh layers through-thickness.

In practice, there were always a gap between FE predicted geometry and forces as compared to experimental measurement. It is noteworthy that the forming forces prediction by current models are consistently higher than the practical data, which leads to a concern of material models for correct strain- stress response to Bauschinger effect, a material soften phenomenon occurs in cyclic loading and unload processes like ISF [30]. In DSIF simulation, Leem et al. [99] proposed an improved DSIF model covering machine deflections and Yoshida-Uemori hardening model to improve the prediction accuracy. The forces simulated with the Y-U model were closer to experiments when compared with conventional Voce model. This suggested the importance of material model to the accuracy in DSIF simulations. The simulation error may also be a consequence due to the lack of consideration to machine deflections. Moser et al. [9] incorporating the machine compliance in FE model using dashpot and spring element to simulate the tools mispositions during forming process. The novelty of FE tool configurations reduced the geometry deviations by 11.2% between the experimental and FE predicted profiles when compared to the conventional rigid tool model.

2.6.2. FE strategies with reduced CPU time

From simulation point of view, both SPIF and DSIF processes are quasi-static deformation that requires considerable number of elements and processing time.

However, the deformation area is relatively small comparing to the total size of sheet which requires high mesh density to capture the local strain evolution. Similar to SPIF processes, it is computationally demanding both in terms of computing time and size to simulate DSIF to acceptable accuracy. Moser et al. [100] examined the effect of element types and mass scaling to the computational efficiency and accuracy. The first-order continuum hexahedral elements are recommended with reduced- integration and hourglassing control to improve the nonlinearity in DSIF simulations.

Ndip- Agbor et al. [15] proposed a simplified model by implementing a narrow strip of blank material with two- end clamping. This model captured the effect of relative tool position to the final wall angles. With an acceptable prediction error, the simplified model substantially reduced the simulation time, which made it possible for parametric study and optimisation of the forming parameters [62]. For DSIF process, an efficient model constructed by integrated shell elements was able to give a reasonable estimation to stains and thickness within 72 hours on 24 CPUs computer, while almost double computing time using solid elements as reported by Moser et al. [19].

2.6.3. Applications of FE simulation in DSIF

The prediction to the forming forces and final geometry is another area of interest in FE simulation of DISF. Meier et al. [16] used FE simulation as a reference of geometry deviation to improve the accuracy of robot- forming DSIF. The simulative analysis is implemented as an effective tool to trace the local strain and thickness development for DSIF processes. The comparative study proposed by simulations supported the improvement for reducing strain concentration and forming errors [11, 45]. Smith et al. [8] implemented a FE model with 4-layer brick element in through- thickness direction. The strains varied from surfaces and their differences between ADSIF and SPIF processes indicated the significance of extra compression and through thickness shear to the improvement of formability. FE simulation can be a way to access information that is hard to be directly obtained from experiments. For instance, Subrahmanyam et al. [101] used X- ray and numerical tools to compare the residual stresses in SPIF and DSIF processes.

This study showed the lower magnitude of residual stress in DSIF when it distributed in similar patterns with SPIF. The tool diameter was another influential factor that the residual stress increased with tool diameter in outer surface in meridional direction. FE analysis revealed the formation of residual stresses, which was a result of bending and unbending in local deformation around forming tools.

In conclusion, the conventional FE models are sufficient to complete the simulation with reasonable accuracy in geometry and thickness distribution. The FE analysis provides a way to estimate the final shape and sheet springback with specific setting of forming parameters, and access to in-depth mechanism investigation based on strain and residual stress which are difficult to obtain in real- time experiment due to interferences by machine tools. Meanwhile, the simulation efficiency and accuracy are two major problems to solve. A detailed model could consume time up to 30 days [8] where a simplified model can reduce it to 23 hours or less [19, 62]. Besides the simplified model, the adaptive mesh technique [102, 103] was proved its adaptivity to the characteristics of ISF processes and can be used in DSIF process as well. The accuracy of prediction is heavily dependent on the simulation set-up and considering factors, i.e. machine compliances and material hardening model. Because of the direct impact to the relative tool positions, the machine deflections have more substantial effect in DSIF simulation than it in conventional ISF. Then the coexistence of tensile, shear and compression stresses in repeated loading and unloading cycles required an update of material hardening model for improvement of forming force prediction [99, 104]. There is a lack of works in fracture model in DSIF and ADSIF simulation which can be another focus in future studies.

2.7. Deformation mechanisms of DISF

The deformation modes and fracture mechanisms are important research topics in the ISF field. The deformation mechanisms in SPIF are generally the combinations of bending, stretching and shearing depending on the forming conditions [63]. An appreciable number of studies also focuses on the local deformation around the contact

point and concludes the significance of the plane strain stretching, bending-under-tension (BUT) and through-thickness shear to the improvement of material formability [22, 86, 105, 106]. In this area, FE simulation helps to gain the access to the in-depth investigation of the strain and stress development and the fracture mechanisms, as many damage models being developed and modified from classic fracture theories, including Gurson-Tvergaard-Needleman (GTN) model and Lemaitre continuum damage mechanics (CDM) model [23, 26, 107, 108]. Similar studies are making progress in the DSIF field based on FE modelling [8], parametric research [61, 62] or the stress analysis amended from the previous SPIF studies [14]. A clear understanding of the deformation mechanisms in various ISF processes helps to learn the reasons for the disparities and the ways for the further improvement of formability and geometry accuracy in SPIF, DSIF and ADSIF [14].

2.7.1. Tension under cyclic bending and compression

The local deformation around forming tool in ISF includes bending in circumferential and meridional directions. The complexity of local stress state prevents direct measurement of membrane forces and observation to influences of forming factor changes to local deformation. Continuous Bending under Tension (CBT) was proposed by Emmens and Boogaard [22] as a 2D representation of ISF. CBT tests can be conducted with a customised tensile testing machine, which provides a standard testing method to assess the material formability in a loading situation similar with ISF processes. The elongation to fracture also indicate the material resistance to failure in ISF according to “noodle theory” [26].

CBT studies produced several inspiring results for bending under tension mechanics [109, 110], continuous ductility and hardening [111, 112], microstructure evolution [111, 112] and simulation [104, 112]. For DSIF process, corresponding simplified testing method named tension under cyclic bending and compression (TCBC), shown in Figure 2.13, was developed by Ai et al. [20]. Two alloys AA5251- H22 and AA6082- T6 were parametrically tested with various set-up of bending, tool speed, tensile speed, compression forces and material thickness. Both materials processed by TCBC

achieved larger elongation than CBT. The compression force was showed as the most influential factor that can enhance the formability improvement by the bending effect. The elongation to fracture was increased more for material AA5251- H22 than AA6082- T6 that suggested AA5251- H22 was more sensible to the changes of forming parameters. Following this result, material- based optimisation for DSIF was recommended to maximise formability.

The simplified processes like CBT and TCBC show considerable potential for mechanism investigation of DSIF process. The formability improvement by TCBC is not only simply linear sum of effects of bending and compression, which works similarly in different materials, but an interaction between material property and combined stress state. The incorporation of TCBC optimisation and DSIF verification for its effectiveness can be conducted in the future. To the micro scale deformation behaviour, the evolution of strain components and microstructure in TCBC would be a direction of more in-depth investigation. This may be related to the reason as to why bending and compression performs differently on different materials, which can be revealed by comparative experiments with relatively low cost in TCBC process.

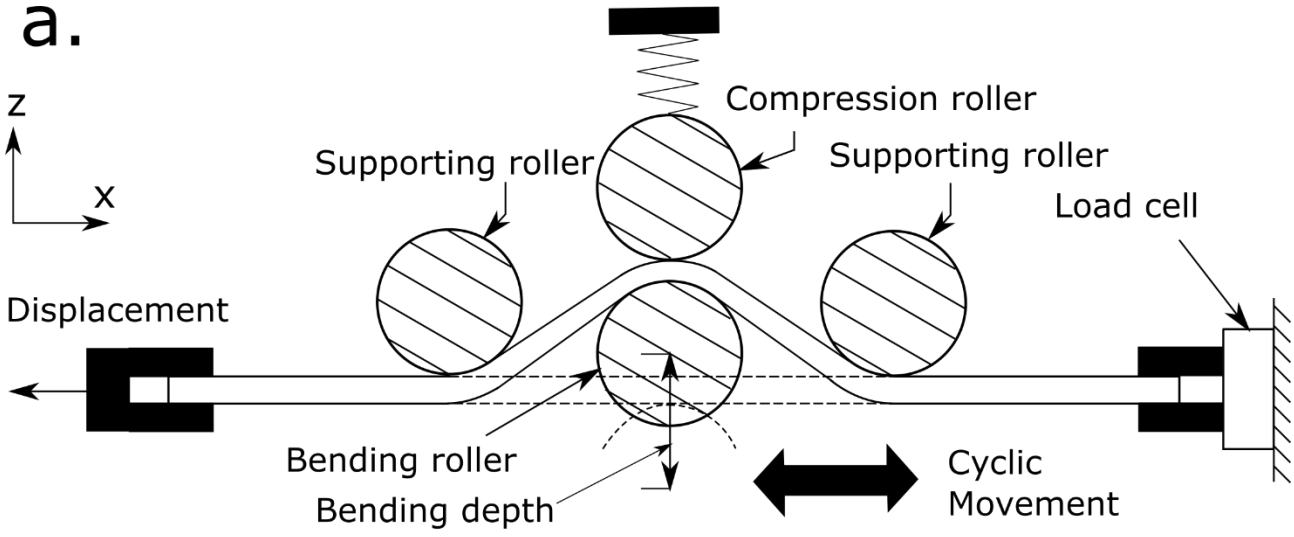


Figure. 2.13 Schematic of TCBC process

2.7.2. Deformation mechanisms in DSIF

The deformation mechanisms in DSIF have been discussed in early comparative

studies between SPIF and DSIF and toolpath research. A significant difference being revealed by FE method is that the maximum equivalent plastic strain in the DSIF process is less than that in SPIF and the failure caused by material over-thinning is more likely to occur in the wall region in DSIF, while it happens more in the corners in SPIF [11]. Malhotra, et al. [42] found that the squeezing effect of tools leads to the higher plastic strains concentrating in a small area around the contact point of the tools and workpiece. In experiments, this compressive effect results in high strain hardening of the formed part. This phenomenon was explained by a comprehensive investigation of mechanism in DSIF presented by Lu et al. [14]. Based on the similarity between the deformation mechanics in SPIF and DSIF, a membrane method was implemented in the stress analysis where the shear effect was only considered to occur in the tangential direction. The stress triaxiality was selected as an indicator of formability. As a result, the drop of stress triaxiality with the increase of equivalent strain in DSIF (Figure 2.14a) was found whereas in SPIF the stress triaxiality underwent a stationary development throughout the process (Figure 2.14b). It was concluded that the drop of stress triaxiality produced by the support tool in DSIF deferred the occurrence of failure and helped achieve a greater wall angle than in SPIF. Compared with the previous mechanism studies in SPIF, the additional squeezing and shear effects were the main differences. However, the distinct effects of compression and shear need to be further investigated.

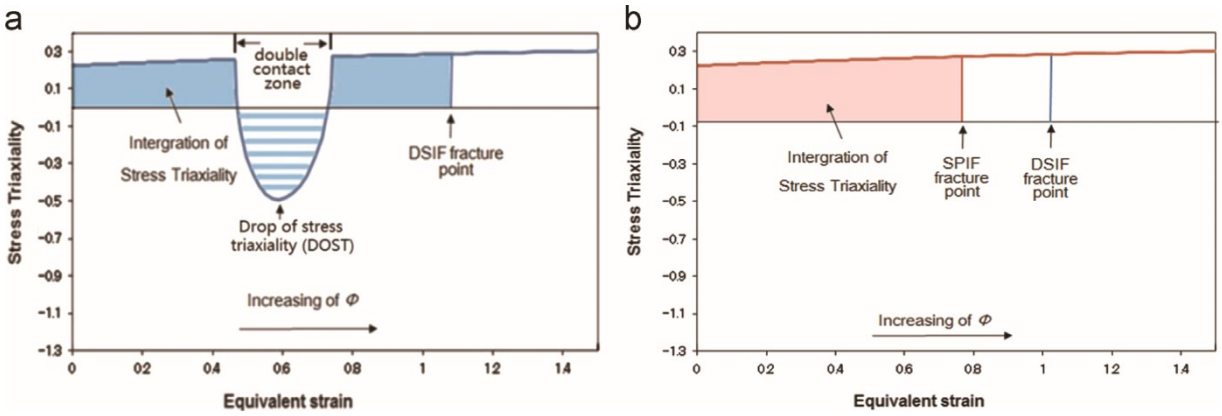


Figure. 2.14 Comparison plots of equivalent strain versus stress triaxiality in (a) DSIF , and (b) SPIF *[14]*

Valoppi et al. [113] investigated the fracture in the E-DSIF forming process with Ti-6Al-4V sheet. Three electric current intensities (50A, 87.5A and 100A) were applied on both the master and support tools to investigate the sheet fracture under different temperatures. The E-DSIF process was conducted until the sheet fracture occurred and the fracture surface was checked by a scanning electron microscopy (SEM). To investigate the material failure behaviour, the SEM results from the tested samples were compared with samples from uniaxial tensile and pure shear tests under corresponding temperature cases. The achievable forming depth was increased with the rise of current intensity. It was observed that the fracture began from the outer surface, then propagated along the tool movement direction and ended when the laceration formed. The fracture can be classified as Mode I, also named tearing by the SEM analysis. Combined with the analysis by Lu et al. [14], the fracture in E-DSIF is more likely to happen in the formed region during the progressive thinning of the sheet, instead of the compressive area contacted with both the forming tool and supporting tool. The reason can be that the material ductility in compressive area is increased due to local heating and the compressive pressure, which postpones the fracture because of the drop of stress triaxiality.

2.7.3. Deformation mechanisms in ADSIF

ADSIF, as a specific toolpath strategy of DSIF, exhibits a degree of peculiarity and different patterns of deformation mechanisms as initially revealed through FEM by Smith et al. [8]. Figure 2.15 shows the FE modelling for ADSIF process. An eight-layer model of linear brick elements with reduced integration is used for both SPIF and ADSIF analysis (Figure 2.15a). A radial mesh strategy was applied in order to capture the material behaviour in the directions parallel and perpendicular to the tool movement. Moreover, four sections along the forming depth were created (Figure 2.15b) to investigate the changes of strain components and hydrostatic pressure throughout the forming process. With the comparison of SPIF, a general view of the deformation of ADSIF can be analysed. In summary, the dominant deformation modes in ADSIF are local bending around the contact point between the tools and forming sheet, combined with a squeezing effect as

well as shear effect perpendicular and parallel to the tool moving direction. In contrast to SPIF, there are significant but consistent differences between the plastic strains as observed on the inner and outer surfaces in ADSIF, which may be attributed to bending and high through thickness shear effect. The support tool results in increased compressive pressure and shear. Compared to the DSIF process, ADSIF is characterised by high through thickness shear and the lack of downward pressure because the counteracting effect from material bunching reduce the stretching effect.

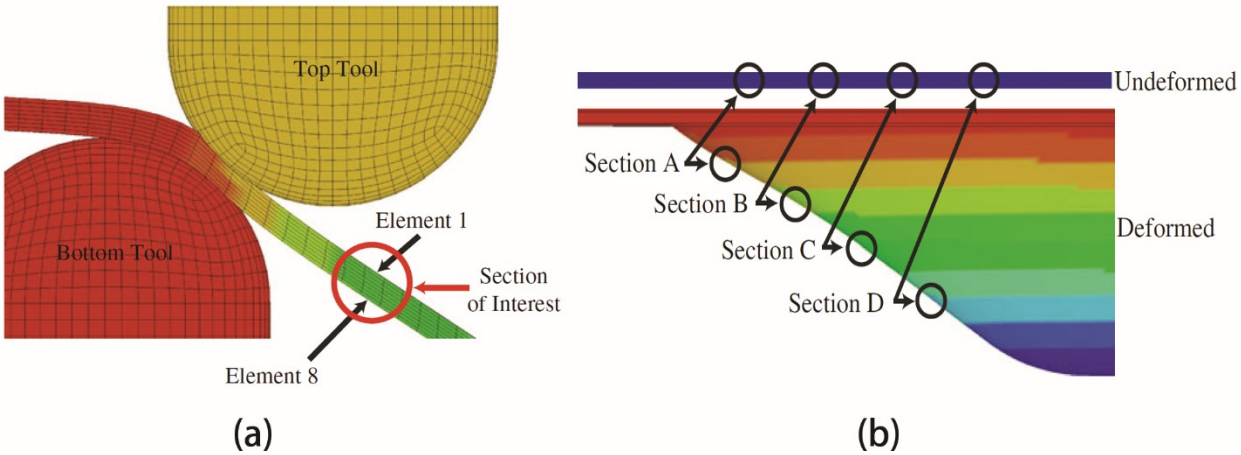


Figure. 2.15 (a) Element layers through thickness, and (b) sections separation by forming depth for different forming stages in FE model for both SPIF and ADSIF *[8]*

Ndip- Abgbor, et al. [62] presented a parametric study using a simplified FE model to improve the simulation efficiency without losing too much accuracy in wall angle prediction. Figure 2.16a demonstrate the simplified FE model. A clamped narrow strip model was implemented to simulate a part of ADSIF process, which consumed 10-15 minutes for simulation instead of 7-10 days with a full scale of ADSIF model. The relative tool position, described as the horizontal distance D and vertical distance S, are used as research variables (Figure 2.16b). To compensate for the accuracy loss due to the simplified model, Latin Hypercube Sampling method is applied to find the relationship between the values of D, S and the achievable wall angle. The prediction via the simplified model was very close to the experimental results in a certain range of angles and the deviation was controlled within 5°. The results show that the combination of the values of

D and *S* is not unique when forming a specific wall angle [62]. A similar parametric study was also reported by Ren, et al. [61] as the tool gap and tool position angle were chosen as parameters. The stable wall angle in the forming region was used as a representative indicator of the whole formed part. The entire ADSIF model with an advanced mesh density of 8-layers of solid elements was executed using LS- DYNA. Thus, the accuracy of FE prediction was significantly improved at the cost of long simulation time. The conclusion agrees with the deduction of Lu, et al. [14] that the excessive squeezing brings a negative effect on formability.

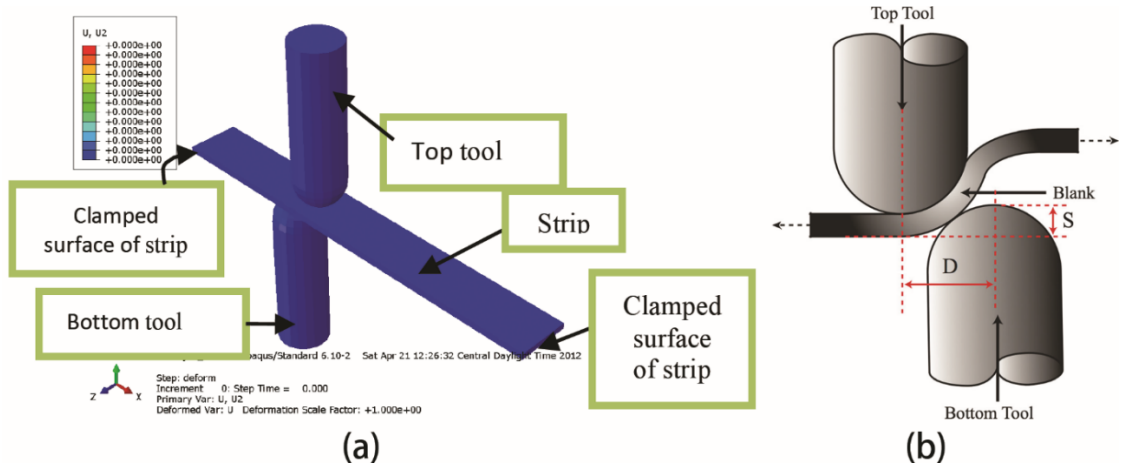


Figure. 2.16 Schematics of (a). simplified ADSIF model, and (b). variables D and S in ADSIF *[15, 62]*

2.8. Discussion and Conclusions

The DSIF process has been shown to achieve improved formability and geometric accuracy as compared to the SPIF process. The additional tool provides extra supporting force and increases the deformation stability whilst the benefit of high flexibility is kept and the low set-up cost feature is maintained as compared to the TPIF process. Most of the published research focuses on the development of the DSIF toolpath strategies or the evaluation of deformation mechanics. As a variant of DSIF, ADSIF shows distinctive characteristics in forming accuracy and deformation mechanics. This review presents an overview of the current state of the art and the most important areas of DSIF focused research as summarised in the following sections.

2.8.1. Formability

The DSIF process exhibits a better formability than the SPIF process. The additional supporting force stabilizes local deformation and homogenizes the thickness distribution of the formed part. In terms of stress analysis, the sudden drop of stress triaxiality indicates that the possibility of failure in DSIF is lower than that in SPIF when forming the same parts. The compression reduces the magnitudes of residual stress difference on the formed surfaces. As a result, the springback effect is mitigated in DSIF. However, the unpredicted material thinning could lead to the loss of contact of the support tool with the workpiece and degenerate DSIF into a SPIF process. Thus, the avoidance of losing contact is an important requirement to maintain the formability of DSIF.

The maximum achievable wall angle α_{max} can be used to describe the formability of the DISF process. Similar to other ISF processes, the thickness reduction results in failure and prevents the part from achieving larger wall angles. Other indicators such as stress triaxiality are introduced from previous ISF research in terms of stress analysis and fracture evaluation. In DSIF, the wall thickness is also controlled by the squeeze factor s which indicates the extent of the squeezing between the tools and workpiece. The squeezing effect controlled by the supporting force affects the shearing and compression and is a main affecting factor to the formability in both DSIF and ADSIF. The squeezing effect improves the formability although excessive contact pressure over deforms the workpiece and reduces the formability. The formability in DSIF is also studied by varying tool gaps and relative angles of the master and support tools. In general, the DSIF process formability is mainly dependent on the relative position between tools including the distance and angle. Alternatively, the interaction between tools can also be presented by the value of supporting force and relative position of tools.

The performance of DSIF in composite materials and high-performance alloys is investigated in preliminary stage. For polymers, the formability improvement of DISF is confirmed as effective. For hard-to-form materials such as titanium alloys, local heating can improve the formability of the material. In the DSIF process, electric currents can be

applied through the sheet and two forming tools, which provide an effective means for electrically assisted heating over SPIF processes.

2.8.2. Toolpath strategies in DSIF

The toolpath strategies of DSIF can be achieved via the ADSIF, close-loop iteration, compensation and geometrical feature-based methods. The ADSIF process is based on an in-to-out toolpath strategy that forms the workpiece from the inner annulus traveling outwards to the fringe and can maintain the contact between the tools and workpiece throughout the process. This leads to improved forming accuracy and formability. The drawbacks of ADSIF include limited forming wall angle, long forming time due to the small incremental depth and high compressive pressure throughout the process. Unlike the other toolpath strategies, reversing the forming direction also causes the change of the deformation mechanisms, which requires more in-depth investigation.

The compensation-based strategy can be divided into the prediction of tool or sheet deflections, which forms the basis for developing corresponding compensation strategies to toolpath generation. The performance of compensation-based toolpath is highly dependent on the accuracy of the prediction of forming forces and geometrical deviation as well as the algorithm of calculating the adjustment to the toolpath. The compensation-based strategy can significantly improve the forming accuracy. However, the prediction through FE simulation or experimental test is either a computing intensive process or requires iterative forming test and measurement steps for improved accuracy of these predictions. This rises an issue about the stiffness estimation to DSIF machine system and clamping frame. The precision of calculation to system deflection will subsequently determine the effect of compensation- based strategy.

Feature-based toolpath implements algorithm to recognise the geometric features and adjust the density of toolpath contours. The feature recognition can be also used to improve the quality and efficiency of deflection prediction in the compensation-based strategy. In this case, the correct feature partition and the order of the forming sequence

for features are of significance.

2.8.3. Simulations for DSIF

FE simulation is a powerful tool to obtain the evolution of strain, residual stress during local deformation, which is almost impossible to measure in experimental DSIF process. FE model produces simulated geometry and errors to support optimisation to toolpaths or reveal the difference in local strains development between SPIF, DSIF and ADSIF. However, the long simulation time is the biggest obstacle for FEM being frequently used. Using shell element or simplified model can significantly reduce computing time without lose much accuracy. The time-saving models makes it possible for parametric study and material- based comparison in DSIF. The deformation mechanism study driven by FEM would be one of its primary uses. The update of simulation techniques i.e. adaptive mesh strategy can further cut down the computing time. Meanwhile, the existing gap between FE predicted and experiment measured forming forces requests new material models, which can be used to correctly solve the stress – strain response under low stress triaxiality.

2.8.4. Deformation mechanisms in DSIF

The deformation mode of DSIF is generally a combination of stretching in the meridional direction, compression in the radial direction and slight through thickness shear in the tool movement direction. Compared with the SPIF process, the additional support tool provides an extra compressive effect which reduces through-thickness shear in the tool moving direction. The formability improvement is a result of both BUT and compression effects, where the different materials have different sensitivity to bending and squeezing.

The drop of stress triaxiality postpones the fracture in the double-contacted area in the DSIF process. Thus, the material failure is more likely to occur in the deformed region, starting from the outer side of the sheet and propagating in the circumferential direction due to material thinning and tool movement. In the E-DSIF process, the increase of material ductility by local heating in contact area is another factor to defer fracture.

The deformation mechanisms in ADSIF are mainly associated with local bending of the sheet around the contact point between the workpiece and the master tool, accompanied with a squeezing effect due to the support tool as well as shearing perpendicular and parallel to the tool moving direction. The history of equivalent strain shows that there is a constant strain discrepancy between the inner and outer surfaces in ADSIF instead of the artificial dynamic oscillations and uncontrolled nature of deformation in SPIF. In contrast to DSIF, ADSIF has high through-thickness shear and low downward pressure, as well as material bunching that counteracts the downward deformation of sheet.

2.9. Challenges of DSIF research

- The improvement of accuracy and formability is still a priority in DSIF research. There are still needs to develop alternative ways for keeping consistent local support such as closed-loop algorithm and the pneumatic support. Besides, the support tool with the controllable forces can provide precise control of local stress state. This means it is possible to design specific DSIF toolpath aiming for the further improved formability and geometrical accuracy.
- The relative tool position determines local bending direction and applies compression to material, which is a unique characteristic for DSIF specific toolpath design. It is evident from tests that modified tool shift suppressed the residual stress and springback in the formed component. Although the springback and residual stress has been proved to be lower in DSIF than SPIF, the related quantitative study has not been conducted yet. The relationship between the mechanisms of compression forces and residual stress can be an interesting topic. TCBC tests showed the material sensitivity to bending and compression parameters, which means further studies may not be limited in process itself but should take material property into account.
- FE simulation is still a powerful tool to investigate the deformation mechanics of

the DSIF process. The main challenges are the reduction of computing time such as applying adaptive mesh strategy and the prediction of damage in DSIF and ADSIF processes with sufficient accuracy. However, the development of damage prediction in FE should be based on detailed understanding of DSIF deformation mechanisms, including loading conditions, through-thickness effect, and selection of appropriate damage models. The machine compliance can potentially be a reason that causes the discrepancies between the FE results and experimental data. The numerical investigation with well-defined scopes, validation and discussion is expected to be a useful direction to continue in the following years and feedback to the practice such manufacture of complicated shapes.

- There is evidence for microstructure changes by DSIF in polymer material [70]. This leads to concerns about microstructure evolution and its related mechanisms and a need of updating material model used in simulations of DSIF. The capability and performance of using non-metal material i.e. polyether ether ketone (PEEK) material in heat-assisted DSIF process are waiting for detailed assessment.
- The excessive deflection of the master tool may not only cause the geometrical inaccuracy, but also the rotation of the relative position between the master and support tools, which could lead to the change of local deformation mode. The design of the DSIF machine in aspects of controllability and stiffness need to be investigated.

CHAPTER 3 DEFORMATION AND FRACTURE MECHANISMS OF TENSION UNDER CYCLIC BENDING (TCB) AND TENSION UNDER CYCLIC BENDING AND COMPRESSION (TCBC) TESTS

3.1. Introduction

The limitations of direct experimental observation and measurement impede deeper understanding of the deformation and fracture of both SPIF and DSIF processes. Such difficulties for detailed investigation have motivated researchers to find a comparable and measurable process for study. Tension under Cyclic Bending (TCB) and Tension under Cyclic Bending and Compression (TCBC) are considered as two representative test methods. Figure 3.1 illustrates the concepts of TCB, TCBC, SPIF and DSIF processes.

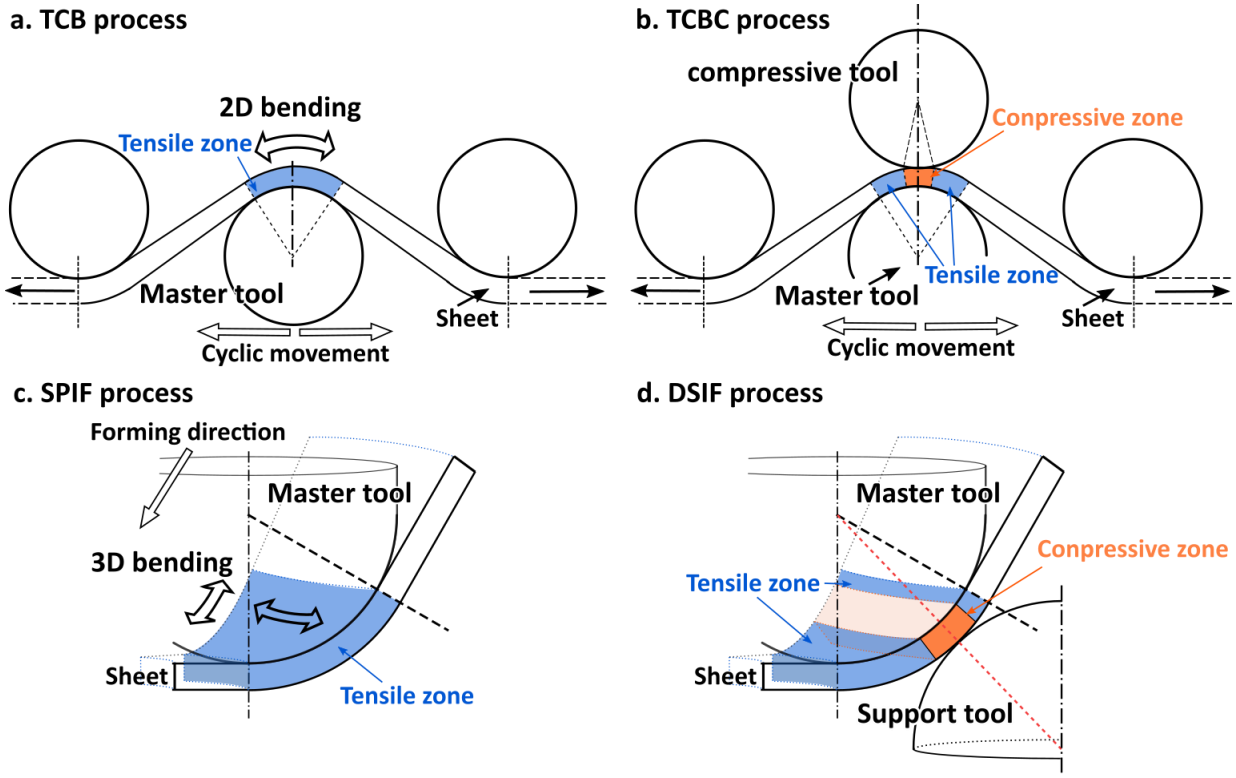


Figure 3.1 Schematics of (a) TCB (b) TCBC (c) SPIF and (b) DSIF processes.

When the local strain exceeds 100% in ISF and other sheet metal forming operations, the conventional tensile tests are inadequate to capture the deformation and

fracture behaviours [114]. Emmens and Boogaard [22] proposed TCB as another form of testing in sheet forming to achieve large deformation similar to the SPIF process. Under the TCB test condition, the samples can achieve larger maximum strain than common tensile test for both steel and aluminium sheet materials, in which the pulling speed and bending depth had dominant effects to the achieved elongation-to-fracture. TCB may be regarded as a reasonable representation of SPIF process that simplifies the complicated 3-dimension contact problem, including 3-dimensional bending in two directions (Figure 3.1c), to a solely 2-dimensional propagated local bending-under-tension condition (Figure 3.1a). It allows the easy control of process parameters, such as strain rate, and measurement of tensile forces and local strain development. Benedyk et al. [114] studied and compared in-plane strain behaviours in TCB and uniaxial tensile tests by Circle Grid Analysis (CGA) and confirmed that a larger elongation is achievable by TCB as reported in the earlier study by Emmens and Boogaard [22]. These strain results also indicated that the TCB process prolongs the stability of plastic deformation and homogenises the strain distribution in the tensile direction. An in-depth investigation of microstructural evolution supported the aforementioned conclusions by Zecevic et al. [111]. From Electron Back Scatter Diffraction (EBSD) and Scanning Electron Microscope (SEM) images, the microscopic texture of the samples and the void formation obtained from TCB showed similarity to the necking region in uniaxial tension. The uniformly scattered damage was assumed to enhance the neck limit which was considered as a reason of improved formability in TCB and ISF [1, 115]. Barrett et al. [104] noticed the material softening during cyclic loading and unloading and utilised a material model with calibrated elastic-plastic response by compression-tension test. The modified material model produced the forming force prediction in agreement with experimental measurement.

Tension under cyclic bending and compression (TCBC) was initially introduced and researched by Ai et al. [20, 116]. The additional compression by a compressive roller resulted in the superior formability than uniaxial tensile, TCB and tension under continuous compression (TCC) tests. The reduced tensile force was also observed in the

TCBC test which indicated the benefit of localised bending to avoid excessive tensile force and early fracture in both TCBC and DSIF processes. Based on FE simulations, the evolution of strain in TCB, TCBC, SPIF and DSIF showed similar patterns, which was increased by steps of tool forming cycles. This indicates that TCB and TCBC are comparable to SPIF and DSIF processes. Detailed investigation of both would help provide an insight into the deformation and fracture mechanisms of SPIF, DSIF and indeed ISF processes in general.

The objective of this chapter is to study the deformation and fracture mechanisms of TCB and TCBC processes and to analyse the ductile fracture behaviours for formability improvement. This chapter is divided into two parts including the discussion to TCB and TCBC deformation behaviour and validation of a newly proposed modified Gurson-Tvergaard-Needleman (GTN) model.

The first part presents a theoretical analysis to the deformation stages in terms of the stress and strain evolutions. This leads to an explanation of the reduced forming forces and stress distribution, as well as a comparative assessment of key parameters to the formability using damage function implemented by stress triaxiality and plastic strain rate. A modified Gurson-type model was proposed for improving damage prediction of ductile materials. A novel shear model based on fracture locus in the space of stress triaxiality, and Lode angle parameter was developed to enable phenomenal calibration to shear damage mechanism. A benchmark was conducted in a single element model for validation to show the improvement of the modified GTN model for accurate FE simulation of both TCB and TCBC. It is followed by the experimental investigation, using a dedicated TCBC test rig to produce samples with controlled parameters including bending depth, compression force and sheet thickness. The maximum elongation and thickness reduction on fracture were measured and compared to evaluate the formability. From FE simulations of TCB and TCBC, the stress distributions and strain evolutions were plotted and compared by sections in the longitudinal and through-thickness directions. The predictions to material failure were compared with practical tests. The in-process stress

states and damage evolution obtained in FE results were also evaluated to apprehend the roles of the localised bending and compression. Combining with experimental testing and FE investigation, the local deformation and fracture behaviours were depicted with an in-depth discussion.

3.2. Theoretical analysis of TCB and TCBC tests

Material deformation in TCB, TCBC and ISF are regarded as processes of highly localised deformation [22, 110-112, 114, 116], which are observed in experimental tests and strain results by FE simulation. Ai et al. [20] presented a brief derivation to reveal the relationship between the stresses in the tension and through-thickness directions. However, a more detailed theoretical analysis to capture local stress state is nearly absent in TCB and TCBC studies. In this section, the analysis focuses on the region under contact point and the adjacent regions in order to reveal the change of stresses nearing the contact point, which offers indications about the key differences between the deformation mechanisms in TCB and TCBC and its influences on fracture.

For simplicity, there are two basic assumptions to be made:

- The compressive stress σ_c in TCBC is controlled by compressive force F_c, as shown in Figure 3.2b. However, the explicit stress value may not be determined as the actual contact area is difficult to be measured. For convenience, the compressive stress σ_c is used in derivation and monotonically increases with the compressive force F_c.
- The material is assumed to be elastic till reaching the yield stress then being perfectly plastic.

3.2.1. General case of deformation

To investigate the stress state of localised deformation, the region around the contact point is extracted and divided into three regions: i) region before contact, ii) contact region, iii) post-contact region (Figure 3.2a). At an arbitrary moment during the process, the deformation in contact region can be made up with elastic part and plastic

part, which are separated by the surface at $y = m\frac{t}{2}$, where $m \in [-1,1]$ indicates the position of the boundary between elastic and plastic deformation regions in through-thickness direction. The material deformation is fully elastic when $m = 1$ or fully plastic when $m = -1$ (Figure 3.3). Assume the yield stress under this stress state is S, the strain at $y = m\frac{t}{2}$ can be written as:

$$\varepsilon_{y=\frac{mt}{2}} = \frac{S}{E\prime} \tag{3.1}$$

where E' is the modulus of elasticity in plane strain condition and can be calculated by young's modulus E and Poisson's ratio ν.

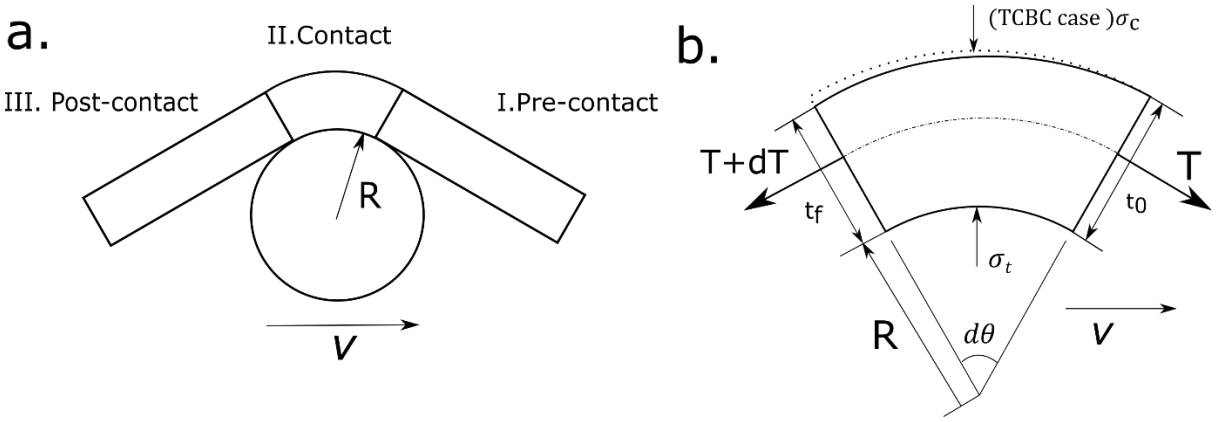


Figure 3.2 General local bending for TCB and TCBC: (a) deformation regions by contact condition, and (b)stress and tension equilibrium

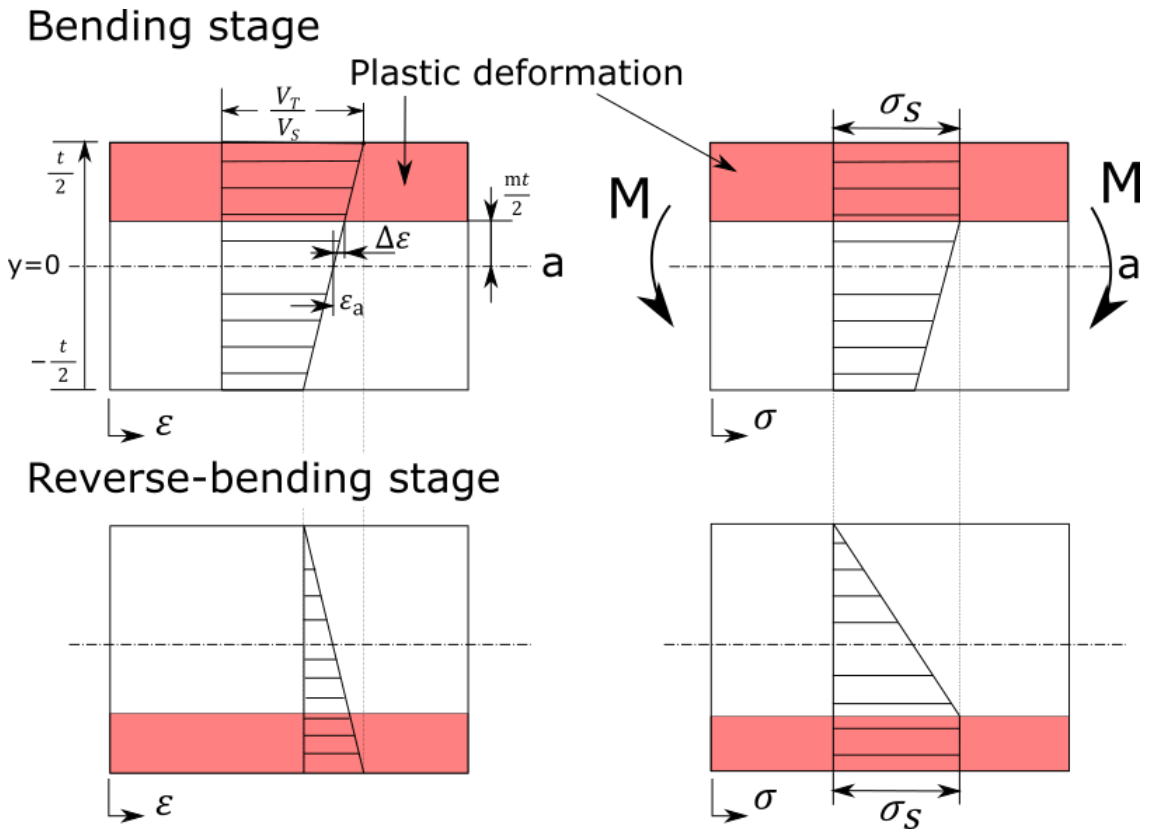


Figure 3.3 Strain diagram and stress diagram for typical bending and tension process, divided into bending and reverse-bending stages

$$E' = \frac{E}{1-\nu^2} \tag{3.2}$$

Based on material rigidity, the strain distribution through-thickness is proportional to bending curvature. The strain at central plane a is presented in the equation below:

$$\varepsilon_a = \varepsilon_{y=\frac{mt}{2}} - \Delta\varepsilon = \frac{S}{E'} - \frac{1}{\rho} \cdot \frac{mt}{2} \tag{3.3}$$

$$\rho = R + \frac{t}{2} \tag{3.4}$$

The through-thickness strain distribution can be presented as:

$$\varepsilon = \varepsilon_a + \Delta\varepsilon = \frac{S}{E'} - \frac{1}{\rho} \cdot \frac{mt}{2} + \frac{y}{\rho} \tag{3.5}$$

where ρ, R, t are the distances from tool centre to central surface, tool radius and sheet thickness, respectively. Equation (3.5) indicates a discrepancy among through-thickness

strains. This strain imbalance caused by bending deformation is lowered in the reverse bending stage where the bent material is stretched back to a straight strip (Figure 3.3). The tension distribution in radial direction can be given based on equation (3.5):

$$T = \int \sigma \cdot dt = \int_{-t/2}^{mt/2} E' \cdot \varepsilon dy + \int_{mt/2}^{t/2} S dy = St\left[1 - \frac{E't}{8}(m+1)^2\right] \tag{3.6}$$

3.2.1.1. TCB case

By force equilibrium in the thickness direction in the contact region (Figure 3.2b):

$$\sigma_t \cdot 1 \cdot Rd\theta = (T + dT) \cdot sin\frac{d\theta}{2} + T \cdot sin\frac{d\theta}{2} \tag{3.7}$$

where σ_t is the contact stress between the sample and the bending roller. Assume the higher-order terms is small enough, Equation (3.7) can be reduced to:

$$\sigma_t \cdot Rd\theta = (2T)\frac{d\theta}{2}$$

Thus, Equation (3.7) can be reduced to:

$$\sigma_t = \frac{T}{R} \tag{3.8}$$

Similarly, the equation about the current yield stress can be derived with the use of Tresca's yield criterion in the plastic deformation region:

$$\begin{cases} \sigma_y = S + \sigma_t^{y=mt/2} \\ T_y = S \cdot (\frac{t}{2} - \frac{mt}{2}) \\ T_y \cdot sin\frac{d\theta}{2} + \left(T_y + dT_y\right) \cdot sin\frac{d\theta}{2} = \sigma_t^{y=mt/2} \cdot \left(\rho + \frac{mt}{2}\right) d\theta \end{cases} \tag{3.9}$$

where σ_y is material yielding stress, m is the position of the dividing surface between the elastic and plastic regions through-thickness. S denotes the stress in the tensile direction in the yielding region $\frac{mt}{2} \le y \le \frac{t}{2}$, T_y is the tension per thickness of the yielding region. By ignoring the higher-order terms, Equation (3.9) is reduced to:

$$\sigma_t^{y=mt/2} = \frac{T_y}{\rho + mt/2}$$

$$S = \frac{\rho+mt/2}{\rho+t/2} \cdot \sigma_y \tag{3.10}$$

Combining Equations (3.6) and (3.10):

$$T = \sigma_y t \cdot \frac{\rho+mt/2}{\rho+t/2} \cdot \left[1 - \frac{E't}{8}(m+1)^2\right] \tag{3.11}$$

It is clear that there is no m in $[-1,1]$, which satisfies $T = \sigma_y t$ in Equation (3.11) (because $\left(\frac{\rho+mt/2}{\rho+t/2}\right) \leq 1$ and $\left[1 - \frac{E't}{8}(m+1)^2\right] \leq 1$, $\left(\frac{\rho+mt/2}{\rho+t/2}\right)_{max} = 1$ when $m = 1$ and $\left[1 - \frac{E't}{8}(m+1)^2\right]_{max} = 1$ when $m = -1$). This means in all cases in local bending deformation, the tensile force T is always smaller than the value $T < \sigma_y t$ to prompt the pure tension deformation which localised the plastic deformation in local bending region in TCB and TCBC processes. It is shown characteristically that the tension measured during the TCB and TCBC processes is smaller than that measured in the uniaxial tensile test.

3.2.2. TCBC case

By applying additional compressive stress σ_c, Equations (3.7) and (3.9) can be converted to TCBC case:

$$\sigma_t \cdot 1 \cdot Rd\theta = (T + dT) \cdot sin\frac{d\theta}{2} + T \cdot sin\frac{d\theta}{2} + \sigma_c \cdot 1 \cdot (R + t)d\theta \tag{3.12}$$

$$\begin{cases} \sigma_y = S + \sigma_t^{y=mt/2} \\ T_y = S \cdot (\frac{t}{2} - \frac{mt}{2}) \\ T_y \cdot sin\frac{d\theta}{2} + \left(T_y + dT_y\right) \cdot sin\frac{d\theta}{2} + \sigma_c \cdot 1 \cdot (R + t)d\theta = \sigma_t^{y=mt/2} \cdot \left(\rho + \frac{mt}{2}\right)d\theta \end{cases} \tag{3.13}$$

Following a similar procedure, these equations can also be reduced to:

$$\sigma_t = \frac{T}{R} + \sigma_c\left(1 + \frac{1}{R/t}\right) \tag{3.14}$$

$$S = \frac{\rho+mt/2}{\rho+t/2} \cdot \sigma_s - \sigma_c \tag{3.15}$$

3.2.3. Strain evolution in bending and unbending process

Assume the deformation is perfectly localised that only the material under bending is deformed. As the tensile speed V_T and stroke speed V_S keeping constant during a unit time dt in the process, the incremental elongation is the elongation $V_T dt$, where the length of material being deformed is the length of material being contacted which is equal to $V_S dt$. Thus, the strain increment of each tool passage ε_{incr} can be defined with V_T and V_S [22]:

$$\varepsilon_{incr} = \frac{V_T}{V_S} / 1s \tag{3.16}$$

For every part of the specimen, the material is deformed at each time of tool contact and experiences a bending and an unbending operation. The strain increment per contact is also uniform because of consistent tensile and stroke velocities. Combining Equations (3.5) and (3.16), the value of elastic limit m can be solved:

$$\frac{V_T}{V_S} = \frac{S}{E\prime} - \frac{1}{\rho} \cdot \frac{mt}{2} + \frac{t}{2\rho}$$

$$m = 1 + \frac{2\rho S}{E't} - \frac{2V_T\rho}{V_S t} \tag{3.17}$$

Due to the characteristic of local bending deformation in TCB and TCBC, the material elongations throughout thickness are unequal after the contact. This unbalance would be levelled in the following reverse-bending stage. Using Equations (3.13), (3.15) and (3.17), the yielding stress in the longitudinal direction can be calculated. Then the stress, tension and moment distribution in the thickness direction can be determined. Given a relative position of $y = \frac{pt}{2}, p \in [-1,1]$, the stress and strain at a distance to the central line can be presented based on the stress and strain distribution through-thickness (Figure 3.3):

Bending stage:

$$\begin{cases} \varepsilon^{y=pt/2} = \frac{V_T}{V_S} - \frac{(1-p)t}{2\rho} \\ \sigma_L = \begin{cases} E'\left(\frac{V_T}{V_S} - \frac{(1-p)t}{2\rho}\right), & -1 \le p < m; \\ S, & m \le p \le 1; \end{cases} \\ \sigma_t = \frac{\int_{pt/2}^{t/2} \sigma_L dt}{\rho + \frac{mt}{2}} + \kappa \cdot \sigma_c\left(1 + \frac{(1-p)t}{2\rho+pt}\right) \end{cases} \tag{3.18}$$

$$m_{rb} = 1 - \frac{2\rho\sigma_s}{E't} \begin{cases} \varepsilon^{y=pt/2} = (1-p)\frac{t}{2\rho} \\ \sigma_L = \begin{cases} (1-p)\frac{t}{2\rho} \cdot E', & m_{rb} < p \le 1; \\ \sigma_s, & -1 \le p \le m_{rb}; \end{cases} \\ \sigma_t = 0 \end{cases} \tag{3.19}$$

where σ_L is the longitudinal stress presented as a distribution function of position in thickness y; κ is an indicator for compression, i.e., $\kappa = 0$ is under TCB condition and $\kappa = 1$ is under TCBC condition.

The in-plane shear stress can be given by the shear force per unit area, which is subjected to the tension increase ΔT between sections B and C (Figure 3.4b). Assume the moment in a section is M and the tension at the face between contact and pre-contact regions is T, the total work can be presented as a sum of bending and tension work if the transfer loss is neglected:

$$M = \int Tydy$$

Figure 3.4 (a) Geometry of local bending area and (b) Schematic of force and moment equilibrium

dl is the length of material being deformed in a certain amount of time dt which

can be given by the moving speed of tool stroke V_S as $dl = V_S dt = \rho d\theta$, as well as the material being bent by incremental angle $d\theta$. Therefore, the work rate of bending and tension can be derived as:

$$\dot{W}_b = \frac{M d\theta}{dt} = M \cdot \frac{V_S}{\rho} \tag{3.20}$$

$$\dot{W}_t = \frac{T \cdot \varepsilon_a dl}{dt} = V_S T \cdot \varepsilon_a \tag{3.21}$$

Thus, the total power and the increase of tension can be determined as:

$$\dot{W}_{ext} = \dot{W}_b + \dot{W}_t = V_S \cdot \left(\frac{M}{\rho} + T \cdot \varepsilon_a\right) = V_S \cdot [(T + \Delta T) - T] \tag{3.22}$$

$$\Delta T = \left(\frac{M}{\rho} + T \cdot \varepsilon^{y=0}\right) \tag{3.23}$$

At bending stage:

$$M = \int_{-\frac{t}{2}}^{\frac{mt}{2}} E'\varepsilon y dy + \int_{\frac{mt}{2}}^{\frac{t}{2}} S y dy$$
$$= \int_{-\frac{t}{2}}^{\frac{mt}{2}} E'\left(\frac{V_T}{V_S} - \frac{(1-y^2)t}{2\rho}\right) y dy + \int_{\frac{mt}{2}}^{\frac{t}{2}} S y dy$$
$$= \frac{t^2}{8}(m^2-1)\left(E'\left(\frac{V_T}{V_S} - \frac{t}{2\rho}\right) - S\right) + \frac{E't^3}{24}(m^3+1) \quad (3.24)$$

$$T = \int_{-\frac{t}{2}}^{\frac{t}{2}} \sigma_L dt$$
$$= \int_{\frac{mt}{2}}^{\frac{t}{2}} S dt + \int_{-1}^{m} E'^{\left(\frac{V_T}{V_S} - \frac{(1-y)t}{2\rho}\right)} dy$$
$$= \frac{St(1-m)}{2} + \frac{E'V_T}{V_S}(m+1) - \frac{E't}{2\rho}\left(m - \frac{m^2}{2} + \frac{3}{2}\right) \quad (3.25)$$

At reverse-bending stage:

$$M = \int_{-\frac{t}{2}}^{\frac{mt}{2}} \sigma_y y dy + \int_{\frac{mt}{2}}^{\frac{t}{2}} E'\varepsilon \cdot y dy$$

$$= \frac{\sigma_y t^2(m^2-1)}{8} + \frac{E't}{2\rho} \cdot \left(\frac{t^2(1-m^2)}{8} - \frac{t^3}{24}(1-m^3)\right) \quad (3.26)$$

$$T = \int_{-\frac{t}{2}}^{\frac{mt}{2}} \sigma_y dt + \int_{m}^{1} \frac{(1-y)tE'}{2\rho} dy$$

$$= \frac{tE'}{2\rho}\left(\frac{1}{2} - m + \frac{1}{2}m^2\right) + \frac{\sigma_y t}{2}(m+1) \quad (3.27)$$

For specific depth in the thickness direction $y = pt/2$, The shear force F_{shear} is defined as differential force ΔT in the longitudinal direction of the section, which has centroid at $y = pt/2$. It can be assumed the tension distribution is proportional to stress. The shear force F_{shear} and shear stress τ are defined:

$$F_{shear} = \Delta T \cdot \frac{\int \sigma dA}{\int_0^t \sigma dt} = \begin{cases} \Delta T \cdot \dfrac{\int_{\left(p-\frac{1}{2}\right)t}^{\frac{t}{2}} \sigma dt}{\int_0^t \sigma dt}, & if\ p \geq 0; \\ \Delta T \cdot \dfrac{\int_{-\frac{t}{2}}^{\left(p+\frac{1}{2}\right)t} \sigma dt}{\int_0^t \sigma dt}, & if\ p < 0 \end{cases} \quad (3.28)$$

$$\tau = \frac{F_{shear}Q}{Ib} \tag{3.29}$$

where, Q and I are the first and second moments of area, respectively. For sheet material, these can be shown in the equations below:

$$Q = \int ydA = A\bar{y} = 1 \cdot \frac{t}{2}(1-p) \cdot \left[\frac{t}{2} - \frac{1}{2} \cdot \frac{t}{2}(1-p)\right] = \frac{t^2}{8}(1-p^2) \tag{3.30}$$

$$I = \int y^2 dA = \int_{-t/2}^{t/2} p^2 dp \cdot 1 = \frac{t^3}{12} \tag{3.31}$$

where, for plane stress condition, b is default for 1 as a unit width. Combining Equations (3.23) to (3.29), the shear stress τ can be derived as:

$$\tau = \frac{3F_{shear}(1-p^2)}{2t} \tag{3.32}$$

The sheet forming process can be recognised as a plane stress case where the stress in the width direction, $\sigma_w = 0$. The stress triaxiality can be calculated by Equations (3.18), (3.19) and (3.32):

$$\eta = \frac{\sigma_{kk}}{\sigma_e}$$

$$\sigma_{kk} = \frac{1}{3}Tr(\boldsymbol{\sigma}) = \frac{1}{3}(\sigma_L - \sigma_t)$$

$$\sigma_{eq} = \sqrt{\frac{3}{2}\boldsymbol{S}:\boldsymbol{S}} = \sqrt{\frac{3}{2}[(\sigma_L - \sigma_{kk})^2 + (\sigma_t - \sigma_{kk})^2 + 2\tau^2]} \tag{3.33}$$

where σ_{kk} is hydrostatic stress and σ_{eq} is von Mises stress.

Stress triaxiality can be applied for the prediction of material damage, suggested by Bai and Wierzbicki [27] in comparison with other ductile fracture models, which is defined as below:

$$D = \int_0^{\varepsilon} \eta d\varepsilon \tag{3.34}$$

Using Johnson-Cook hardening model $\sigma_y = A + B\varepsilon_{eq}^n$ and Equation (3.16), the

equivalent strain and yielding stress function by forming cycles can be established. For any position y through thickness, the longitudinal strain increment in bending and reverse bending stage can be obtained by Equations (3.18) and (3.19). Assume the thickness strain ε_t is in a constant ratio k of the longitude strain ε_L and ignore the shear strains, the effective strain ε_{eq} is calculated by definition:

$$\varepsilon_{eq} = \sqrt{\frac{2}{3}\boldsymbol{D}_{ij} \cdot \boldsymbol{D}_{ij}} = \sqrt{\frac{2}{3}\left[\varepsilon_L^2 + (k \cdot \varepsilon_L)^2 + \left(\varepsilon_L \cdot (-k-1)\right)^2\right]} \tag{3.35}$$

Thus, the incremental damage can be accumulated by the product of the stress triaxiality and effective strain increment in each deformation stage:

$$\dot{D}^{y=pt} = \left(\eta^{bending}\dot{\varepsilon}_{eq}^{bending} + \eta^{reverse-bending}\dot{\varepsilon}_{eq}^{reverse-bending}\right)^{y=yt} \tag{3.36}$$

Although quantitative evaluation of failure is less tangible, the relative development of damage can be obtained and correlated to reflect the effect of process parameters, i.e. initial sheet thickness, compression stress and bending depth. The distributions of shear stress, stress triaxiality and damage accumulation are plotted in Figure 3.5. From Figure 3.5a, the peak of shear stress is reached on the central surface where a smaller value is obtained in TCBC process. The overall stress triaxiality is suppressed by additional compression in TCBC as well. The values of stress triaxiality are monotonously increasing from the concave to the convex surface, which is away from the bending centre and suffered larger strain under stretching (Figure 3.5b). However, more damage is accumulated on the concave side for all stages including the reverse-bending (Figure 3.5c). This result suggests the crack is more likely to initiate from the convex surface of bending and the reverse-bending stage is worth more investigation in terms of its contribution to damage formation in ISF processes.

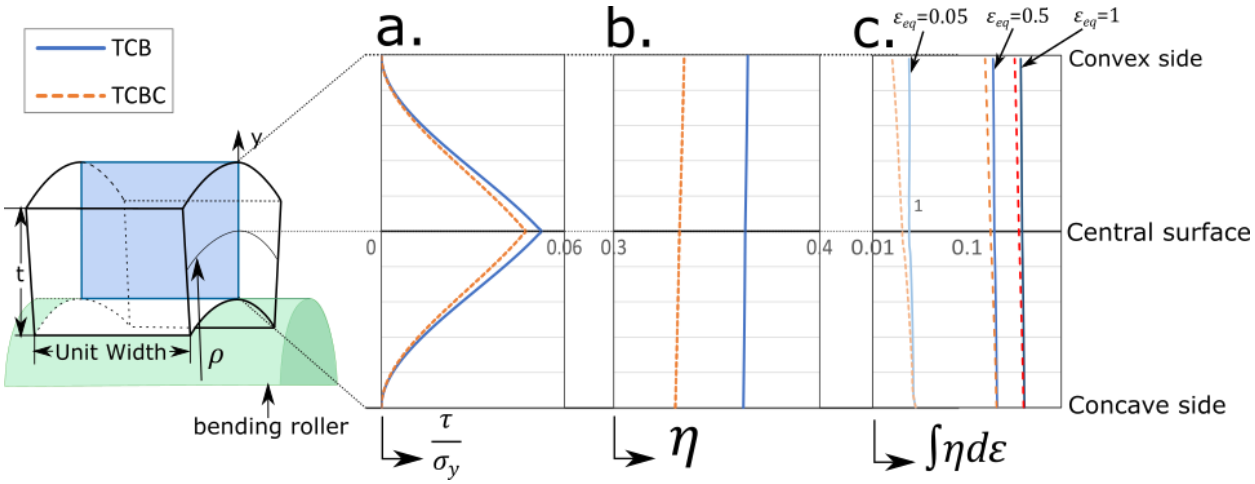


Figure 3.5 Through thickness distribution of (a) normalised shear stress, (b) stress triaxiality and (c) representative material damage during bending process in TCB and TCBC

3.2.4. The effect of bending depth

Increasing bending depth may generate two aspects of impact to both TCB and TCBC processes. As the geometry is shown in Figure 3.4a, firstly, increasing bending depth involves more material between two support rollers that is equivalent to more bending-under-tension deformation. The local bending around the contact point with bending roller is also affected. Due to the sheet stiffness, the bending radius cannot be simply equal to the radius of bending tool R as the material is hard to fully fit the tool surface (Figure 3.4b). Inspired by the analysis made by Emmens and Boogaard [109], the force equilibrium is written as:

$$M_B = T_C(\rho_C - Rcos\theta)$$

$$\rho_C = \frac{M_B}{T_C} + Rcos\theta \tag{3.37}$$

And the bending angle θ can be given by solving geometry relation in Figure 3.4a:

$$tan\theta = \frac{AC}{AB} = \frac{D_R - R_S cos\theta}{d + R/sin\theta - R - R_S + R_S sin\theta} \tag{3.38}$$

where R_S is the radius of the support roller. Equation (3.38) can be rearranged to a quadratic formula:

$$a\cos^2\theta + b\cos\theta + c = 0 \tag{3.39}$$

$$\begin{cases} a = D_R^2 + (d - R - R_S)^2 \\ b = -2D_R(R + R_S) \\ c = 2d(E + E_S) - d^2 \end{cases}$$

Then the value of θ can be obtained by solving Equation (3.39).

The moment at point B and the tension in C can be calculated by Equations (3.24) and (3.26). It shall be noticed that this bending radius ρ_C indicates a trend of the bending radius reduction by the position of bending roller instead of a quantitative solution. It is because the curvature of sheet is not a perfect arc with a constant radius.

The damage variable, defined in Equation (3.34) and (3.36), on convex side at equivalent strain $\varepsilon_{eq} = 1$ in TCB and TCBC against the forming parameters is plotted in Figure 3.6. Figure 3.6a, b and c present the damage evaluation by normalised compression stress and bending depth in TCB and TCBC drawn in various thickness values, respectively. All these graphs exhibit a tendency that more damage is accumulated in thicker sheets though larger thickness brings better resistance to total crack as well. The sheet thickness also affects damage evolution by the change of process parameters. The damage suppression effect by compression is enhanced with the increase of compressive stress and the reduction of thickness (Figure 3.6a). From Figures 3.6b and 3.6c, the damage of TCB is higher than that of the TCBC process when the sheet thickness is the same. The effect of bending depth is reviewed in the combination of compression and thickness. It can be observed that the impact of bending depth on damage evolution is secondary. One possible reason is that the increase of bending depth has minimal impact on bending angle θ, as well as the influence of deformation stress states. Figure 3.6d and 3.6e scaled the difference of damage since 0 bending depth. For the TCB process, the relevance between bending depth and damage is receded for thin workpieces (Figure 3.6d). For the TCBC process, the additional compression amplifies the bending effect for all thicknesses, especially for the thicker sheet with a high compression level (Figure 3.6e). Combining Figures 3.6c and e, the damage in high compression case is lower in overall amplitudes

but has the larger growth rate of damage in the chosen range of bending depth in contrast with the case of low compression. It can be expected that the formability improvement by compression is diminished with the increase of sheet thickness and the bending depth ratio. In conclusion, the damage accumulation in TCB can be effectively reduced by compression where the bending depth is less effectual. However, more damage is formed by increasing bending depth specifically for thicker material when the compression is high. This result suggests that the formability improvement achieved by increasing bending depth and compression is not monotonous which highlights the importance of forming parameter selection and optimisation.

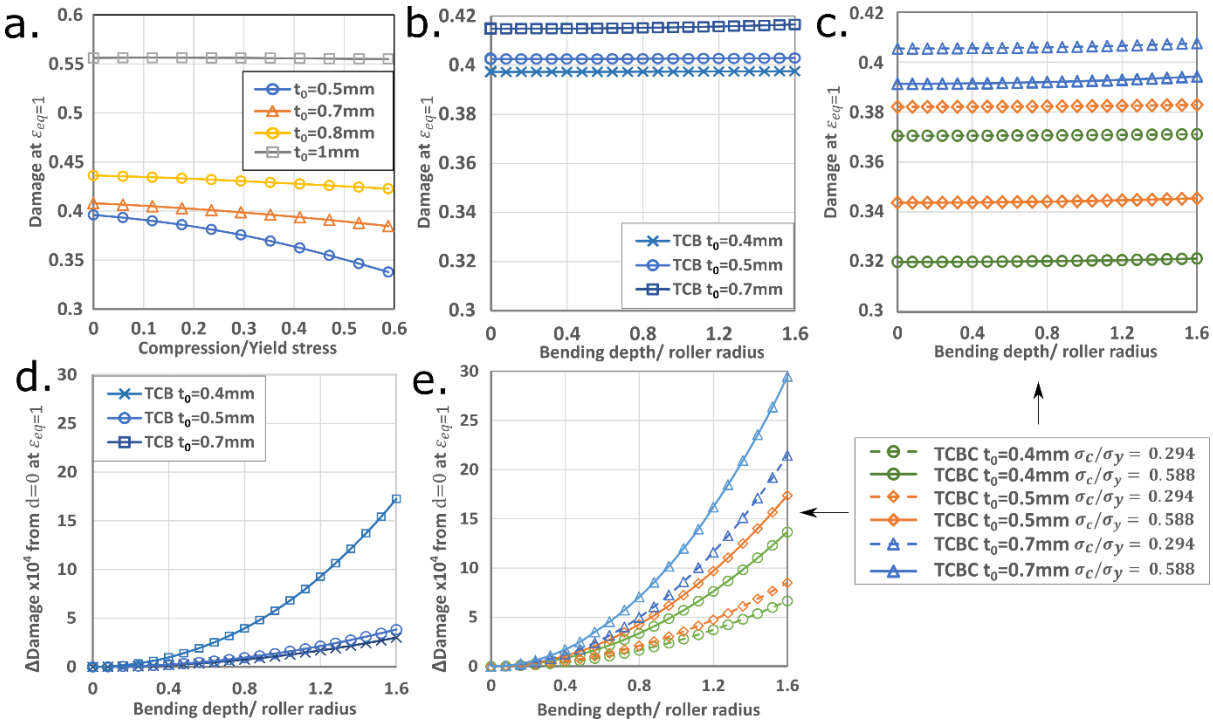


Figure 3.6 Material damage evaluation based on stress triaxiality when equivalent strain equal to 1, (a) normalised compression stress, (b) normalised bending depth in TCB, (c) normalised bending depth in TCBC, and damage increments as a function of the ratio of bending depth and roller radius (d) TCB, and (e) TCBC

3.3. Damage evolution under low stress triaxiality

Figure 3.7 summarises the basic model of void growth and interaction. The void

grows homogenously under hydrostatic stresses (Figure 3.7a). With the increase of void volume and under the shear stress condition, coalescence between voids occurs which leads to the reduction of load capability (Figure 3.7b and 3.7c). When the compressive force is applied, voids may be collapsed and closed (Figure 3.7d). These mechanisms of voids evolution, controlled by stress histories of material, lead to different void shapes and directions that significantly affects the material strength and failure.

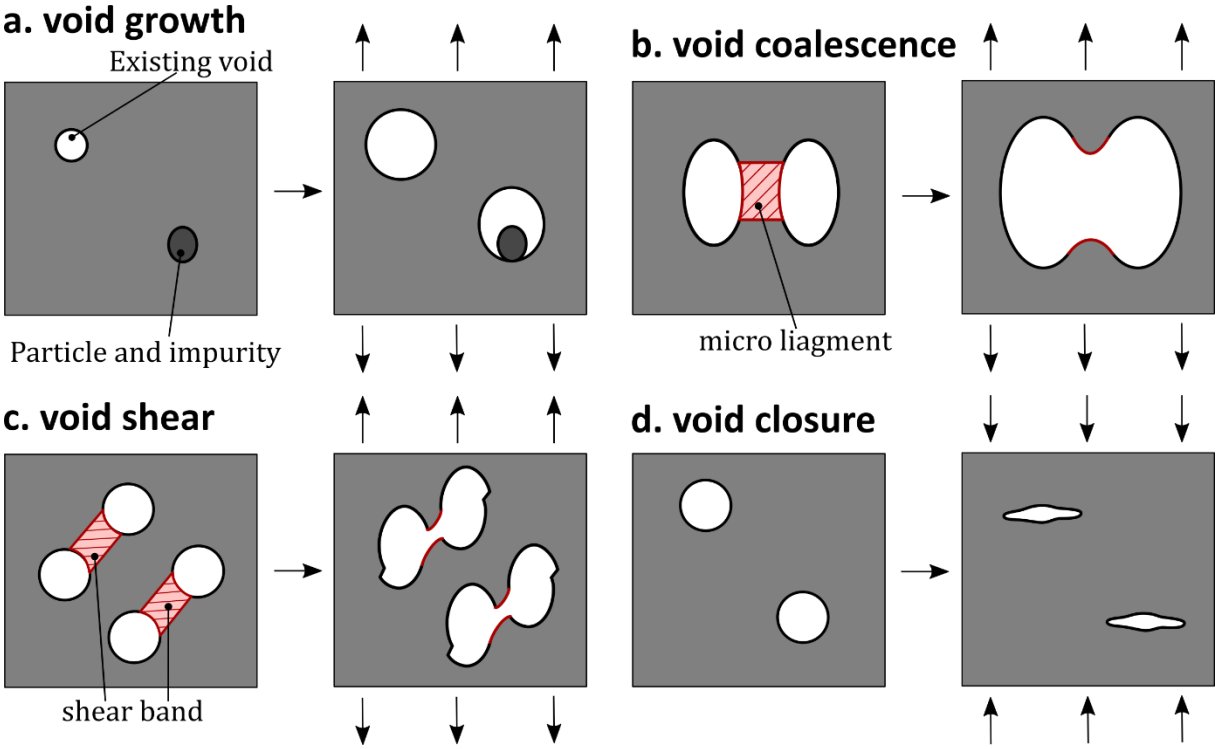


Figure 3.7 Void behaviours of (a) growth (b) coalescence (c) shear and (d) closure.

The studies of fracture criterion based on microstructure mechanism were initially studied by McClintock [117] and Rice and Tracey [118]. Associated with experimental observations [117], the ductile rupture of material was initialised by the growth and nucleation of existing voids or particulates. This was further developed by Gurson [119] and modified by Tvergaard [120] as a well-known constitutive model for the porous material. These models were established on the hypothesis that voids keep a spherical shape during their growth, which was identical to practical images of voids under pure hydrostatic stress states. However, the early porous fracture criterion failed to

give accurate predictions under shear load or compression. The limitation of the GTN model to problems under low stress triaxiality led to further modification for the more precise capture of the shear effect [121-124]. One approach is to simulate more accurately the void behaviours based on practical observations. It was found in experiments and numerical simulations that the evolution of voids was empowered by its primary shapes and orientations [125, 126]. This fact motivated the development of visco-plastic material models based on ellipsoidal microstructure basis and homogenised pore shapes and directions which gave more accurate predictions than the original GTN model [126-130]. However, the void rotation and interaction cause rising difficulty to predict the volume and shape transformations of a single ellipsoidal void in an element, which impedes the implementation of void shape-based models in complex stress evolution states.

The complexity of void behaviour under low stress triaxiality was not only due to the shear band formation in pure shear case (Figure 3.7c), but also because of the combined tension and compression that lead to void collapses of ellipsoidal shapes (Figure 3.7d). The presentation of stress states at different stress triaxialities was shown in a series of experimental results by Bai and Wierzvicki [27], which reveal the effect of the third stress invariant J_3 on ductile fracture. Lode parameter was introduced as another dimension about the deviatoric stresses as an indicator of shear effect to present the accurate mapping of stress states associated with stress triaxiality. Figure 3.8a shows a fracture locus, which correlates the fracture strain and stress triaxiality in 2D space. On the other hand, Figure 3.8b shows the fracture locus in a 3D space of the fracture strain, stress triaxiality and Lode angle parameter. The conventional 2D fracture loci on the plane of stress triaxiality and effective fracture strain [131-133] was a projection in specific cases which is incapable to show the shear effect to the material formability.

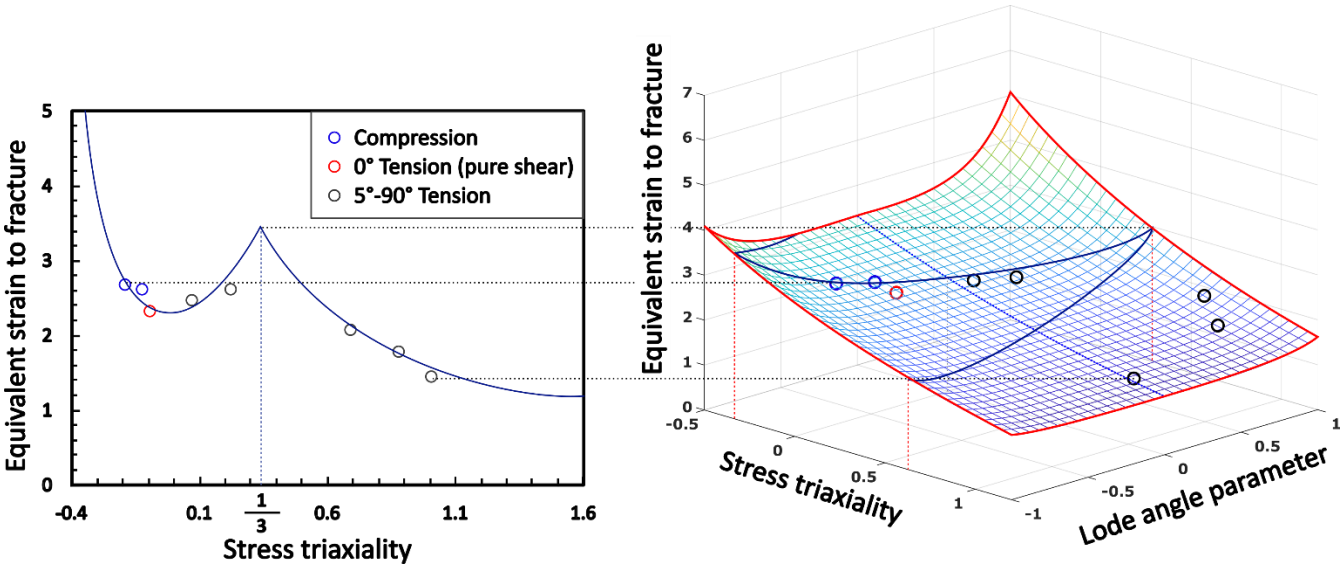


Figure 3.8 Approximation of fracture loci in the (a) 2D plane of equivalent fracture strain and stress triaxiality, and (b) 3D space of equivalent fracture strain, stress triaxiality and Lode parameters (reproduced by testing data of A710 steel from Wierzbicki et al. [134])

Therefore, the criteria of the onset of void coalescence or closure were proposed to distinguish void behaviours under different stress states. This enables the development of feasible models for shear load conditions with collapse mechanisms as a complementary method for improved accuracy of prediction over the original GTN model [135-137]. Xue [122] and Nahshon and Hutchinson [121] introduced void development mechanisms under shear based on theoretical analysis. The closure behaviours were further extended by using Representative Volume Element (RVE) models [138-141] or experimental observations [142]. Zhang and Cui [143, 144] studied void closure by volume fraction changes under variational Lode parameter and stress triaxiality. Srivastava and Needleman [145] revealed the influence of void aspect ratio and relative ligament width between crystals on the void growth and collapse. Liu et al. [135] studied the transition between void collapse and coalescence under changing Lode parameter and stress triaxiality. In conclusion, the porous damage evolution in low stress triaxiality was decided by void geometry, including shapes and relative orientation between voids volume fraction, micro coalescence and stress states and history. The stress state history plays a key role in the whole void evolution process as shown in Figure 3.9. Figure 3.9a

shows the reduction speed of void volume fraction, referring to void closure, which is relevant to the stress triaxiality values and inhomogeneous strain increase in RVE models. Figure 3.9b indicates that the evolution of void volume fraction is also influenced by the Lode angle parameter from -1 to 1 when the stress triaxiality at a low level equal to $1/\sqrt{3}$. This carried out challenges to previous damage models for predicting fracture in processes of combined stress status or complicated stress history [146].

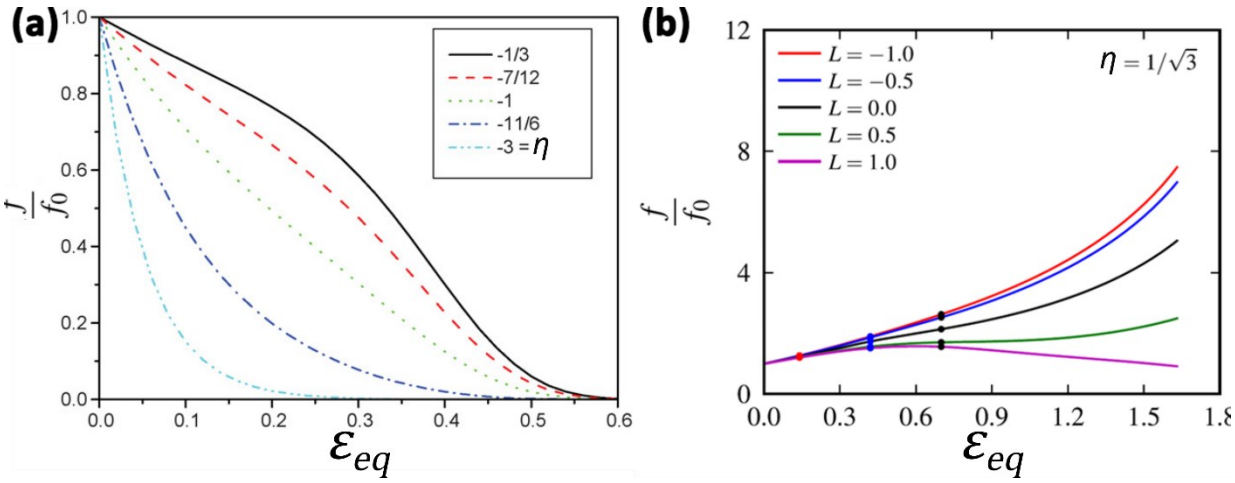


Figure 3.9 Typical void growth behaviours of various (a) stress triaxiality and (b) Lode angles in RVE model when stress triaxiality at $1/\sqrt{3}$ [143, 147]

3.4. Modified GTN model

In terms of ductile fracture model based on the void growth and nucleation of material defects, Gurson model was widely used in predicting material rapture under high stress triaxiality [119]. The recent extension complements void nucleation and shear mechanism to the damage under shear dominated stress state [121]. In the past decades, the essentiality of the Lode angle, especially for high Lode dependent metal and low stress triaxiality cases, was revealed by several researchers [27, 148-150]. The Lode angle effect in the characterisation of material yielding and fracture is a major cause of inaccurate prediction made by the existing GTN model. This section aims to present a modified GTN model based on the extension of Zhou et al. [123], which uses fracture strain surface in space of stress triaxiality and Lode angle parameter to calibrate the shear damage and its

influence to void evolution and material yielding. The Lode angle effect is focused on the use of weight function. A shear damage indicator was introduced as an adjunct variable to evaluate the material softening by shear damage.

3.4.1. Original GTN model

The core concept of the GTN model is to combine the plastic flow equation and the void growth. The yield function in its original form is:

$$\Phi = (\frac{\sigma_{eq}}{\sigma_M})^2 + 2q_1 f^* \cosh\left(\frac{q_2\sigma_{kk}}{2\sigma_Y}\right) - [1 + (q_1 f^*)^2]=0 \tag{3.40}$$

where , q_1, q_2 are parameters for adjustment, which were suggested to be $q_1 = 1.5, q_2 = 1$ by Tvergaard [120, 151]; f^* is equivalent void volume fraction; σ_{eq} is the von Mises stress and σ_Y is the current yield stress; σ_{kk} is hydrostatic stress. These can be defined by stress tensor $\boldsymbol{\sigma}$ and deviatoric stress tensor $\boldsymbol{S}$ as follows:

$$\boldsymbol{S} = \boldsymbol{\sigma} - \sigma_{kk} \cdot \boldsymbol{I} \tag{3.41}$$

$$\sigma_{kk} = \frac{1}{3} Tr(\boldsymbol{\sigma}) \tag{3.42}$$

$$\sigma_{eq} = \sqrt{\frac{3}{2}\boldsymbol{S}:\boldsymbol{S}} \tag{3.43}$$

Where $\boldsymbol{I}$ is the second order identity tensor.

The effective void volume fraction f^* is a function of porosity evolution and coalescence stages, which is characterised as in the following:

$$f^* = \begin{cases} f, & if\ f < f_c \\ f_c + \frac{\frac{1}{q_1} - f_c}{f_f - f_c}(f - f_c), & if\ f \geq f_c \end{cases} \tag{3.44}$$

f_c and f_f are, respectively, the critical and final void volume fractions, which can be determined by in-situ test. The void volume fraction f is mainly consisted of two parts: void growth f_g and nucleation f_n. f_g is the void volume evolution due to material incompressibility during plastic deformation. f_n presents the micro void nucleation. The commonly used increment laws by Gurson [119] and Tvergaard and Needleman [152] are:

$$\dot{f} = \dot{f}_g + \dot{f}_n \tag{3.45}$$

$$\dot{f}_g = (1 - f)\dot{\varepsilon}_{kk}^p \tag{3.46}$$

$$\dot{f}_n = \frac{f_N}{s_N\sqrt{2\pi}} exp\left[-\frac{1}{2}\left(\frac{\bar{\varepsilon}^p - \varepsilon_N}{s_N}\right)^2\right]\dot{\bar{\varepsilon}}_M^p \tag{3.47}$$

where the $\dot{\varepsilon}_{kk}^p$ is the trace of the plastic strain rate tensor; f_N is the void volume fraction of nucleation; ε_N and S_N are the average value and standard deviation in the normal distribution of the nucleation strain; $\dot{\bar{\varepsilon}}_M^p$ is the rate of equivalent plastic strain.

3.4.2. Shear mechanism

The modification to inherent limitations of the GTN model under low stress triaxiality was proposed by several researchers in the form of shear modifications [121, 122, 153, 154]. The effectiveness of these shear mechanisms was validated under simple shear conditions. The key question is to incorporate the shear effect from low to high stress triaxialities and to achieve the accurate assessment of damage evolution under combined stress states, such as tension and shear or tension under compression [153].

3.4.2.1. Xue's shear mechanism

Xue [122] developed a modified void shearing mechanism based on numerical analysis of unified cells with inherent voids. The model approximated the coalescence of shear bands due to geometry changes under pure shear condition. The incremental void shear damage can be presented as below:

$$\dot{D}_{shear} = g_\theta q_3 f^{q_4}\varepsilon_{eq}\dot{\varepsilon}_{eq} \tag{3.48}$$

where q_3 and q_4 are parameters introduced to address the effects of idealised volumetric interactions and void volume fraction to shear band coalescence. In 2D case, $q_3 = 1.69$ and $q_4 = 1/2$; In 3D case, $q_3 = 1.86$ and $q_4 = 1/3$. $g(\theta_L)$ is the function of Lode angle dependence defined as the following equations of the Lode angle θ_L:

$$\theta_L = tan^{-1}\left\{\frac{1}{\sqrt{3}}\left[2\left(\frac{S_2-S_1}{S_1-S_3}\right)-1\right]\right\} \tag{3.49}$$

$$g(\theta_L) = 1 - \frac{6|\theta_L|}{\pi} \tag{3.50}$$

where θ_L is Lode angle and S_1, S_2 and S_3 are the principal deviatoric stress tensors.

3.4.2.2. Nahshon-Hutchinson's shear mechanism

Nahshon and Hutchinson [121] established the relationship between the logarithmic strain ε_L^P and shear stress τ through flow stresses of matrix material. The shear damage was integrated to void volume fraction f in GTN model. The equivalent increment of void rate by shear is:

$$\dot{f}_{shear} = k_w f g_0 \cdot \boldsymbol{S_{ij}} : \dot{\boldsymbol{\varepsilon}}_{\boldsymbol{ij}} / \sigma_{eq} \tag{3.51}$$

k_w is a parameter to modify the shear damage growth rate. $g(\theta)$ is the weight function of Lode dependence, which is defined by the third invariant of the Lode parameter ξ and the deviatoric stress tensor $J_3 = \det(\boldsymbol{S})$:

$$\xi = \frac{27 J_3}{2\sigma_{eq}^3} \tag{3.52}$$

$$g(\theta_L) = 1 - \xi^2 \tag{3.53}$$

3.4.2.3. Zhou's shear mechanism

It is difficult to use the original Gurson model and integrate shear damage in the form of void volume fraction increment to simulate the shear effect in material yielding and its subsequent evolution of voids as well. For instance, the porosity evolution in the ductile fracture and shear fracture processes are different even at the same stress triaxiality. In the microscopic view, the shrink and elimination of void linkage are understood as void coalescence. The coalescence is highly localised and usually begins in the direction normal to the loading, which appears as necking of intervoid ligament, or in

the void shear direction [122]. However, the coalescences by hydrostatic stress (Figure 3.7b) or shear stress (Figure 3.7c) influence the void behaviours in distinct ways. This difference can be observed in 3D fracture strain loci and recognised as the Lode dependency of specific material [155].

Zhou et al. [123] refined the yield function, focusing on the shear effect and implemented the damage variable in void growth mechanics. The shear damage was separated from the void evolution mechanisms as an independent variable and presented in a phenomenal form of damage evolution based on fracture strain loci in experimental tests. This modification allowed the experimental calibration to shear damage, which improves the response of the original GTN model to various stress states.

The plastic flow potential equation is incorporated with shear damage into the following form below:

$$\Phi = (\frac{\sigma_{eq}}{\sigma_M})^2 + 2q_1 f^* \cosh\left(\frac{q_2\sigma_{kk}}{2\sigma_M}\right) - [1 + (q_1 f^* + D_s)^2 - 2D_s]=0 \tag{3.54}$$

D_s is the shear damage variable. When $D_s = 0$, the function becomes the same as the original Gurson model. Assume the plastic strain for shear fracture is denoted as ε_f^s, D_s can be presented as a ratio of the equivalent plastic strain $\bar{\varepsilon}^p$ and shear fracture strain ε_f^s, which can be written as:

$$D_s = \left(\frac{\bar{\varepsilon}_M^p}{\varepsilon_f^s}\right)^n \tag{3.55}$$

where n is a power constant greater than one. The differentiation of Equation (3.55) gives:

$$\dot{D}_s = n \cdot \left(\frac{\bar{\varepsilon}_M^p}{\varepsilon_f^s}\right)^{n-1} \frac{\dot{\bar{\varepsilon}}^p}{\varepsilon_f^s} \tag{3.56}$$

Applying a weight function $\psi(\theta_L, \eta)$:

$$\dot{D}_s = \psi(\theta_L, \eta) \cdot n \cdot \left(\frac{\bar{\varepsilon}_M^p}{\varepsilon_f^s}\right)^{n-1} \frac{\dot{\bar{\varepsilon}}_M^p}{\varepsilon_f^s} \tag{3.57}$$

where the weight function $\psi(\theta, \eta)$ was defined as:

$$\psi(\theta,\eta) = \begin{cases} g(\theta), & \eta > 0 \\ g(\theta)(1-k)+k, & \eta \leq 0 \end{cases} \tag{3.58}$$

In the above equation, $g(\theta)$ can be presented by any Lode dependency function and k is a weight factor to negative stress triaxiality.

Then, the total damage can be given as an entity involving both void and shear damage:

$$D = q_1 f^* + D_s \tag{3.59}$$

3.4.3. Lode angle effect

The Lode angle effect is focused on material fracture mechanisms research in recent decades. The fracture strains of material showed a dependency to the third deviatoric stress invariant $J3$, referred to the deviatoric angle θ_d in stress plane and its developed variants [27, 131, 134, 156, 157]. As these Lode variables were used in the past studies, Figure 3.10 illustrates the deviatoric angle θ_d, the Lode angle θ_L, and the normalised Lode angle $\bar{\theta}$ by Lode angle parameter ξ, which helps to clarify the mathematical relationships among these variants.

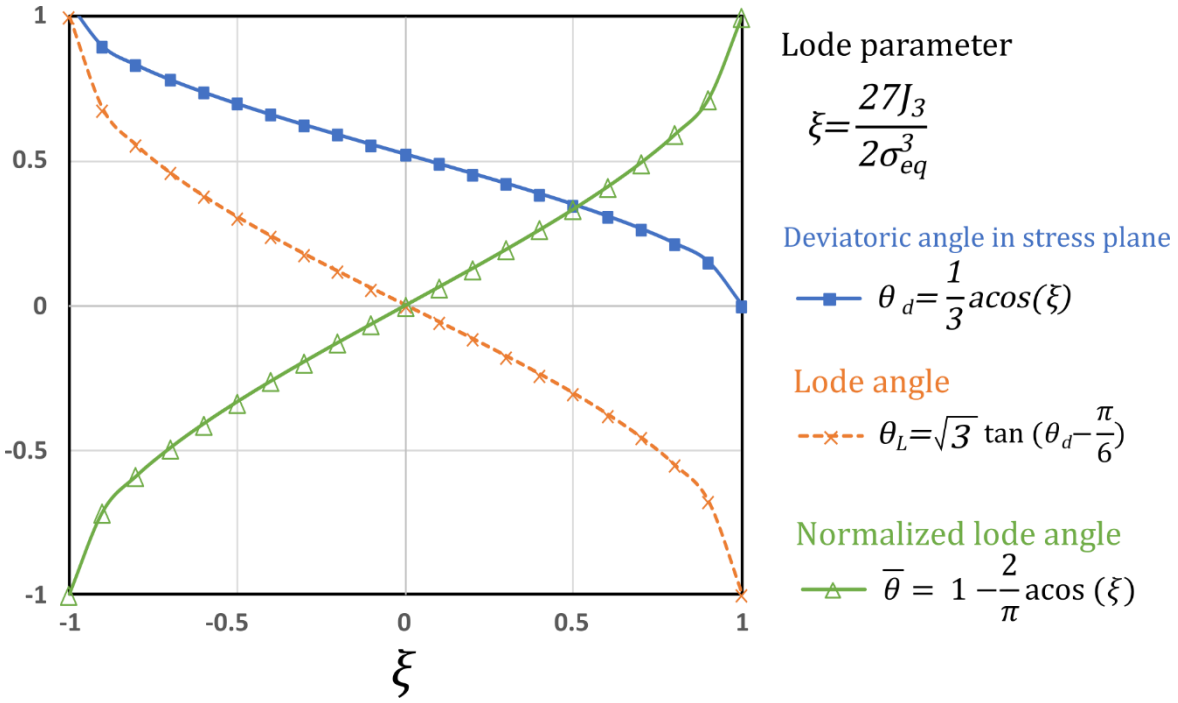


Figure 3.10 Illustration of generally used Lode angle and parameters as a function of the third invariant of deviatoric stress ξ.

The equivalent strain to ductile fracture was presented in many experimental works and exhibited a trend of monotonic reduction with the increase of stress triaxiality [158]. Figure 3.11 plotted the fracture strain surface of two typical materials based on the test data by Bai et al. [27, 134], A710 steel with Lode dependency and 1045 steel without Lode dependency, in the space of stress triaxiality η and the third invariant of deviatoric stress ξ. Figure 3.11a shows the Lode dependent material has reduced formability when the Lode angle parameter approaching 0. This trend is strengthened under low stress triaxiality which is also a reason of difficulties for the fracture prediction using the original GTN model under shear or compression conditions.

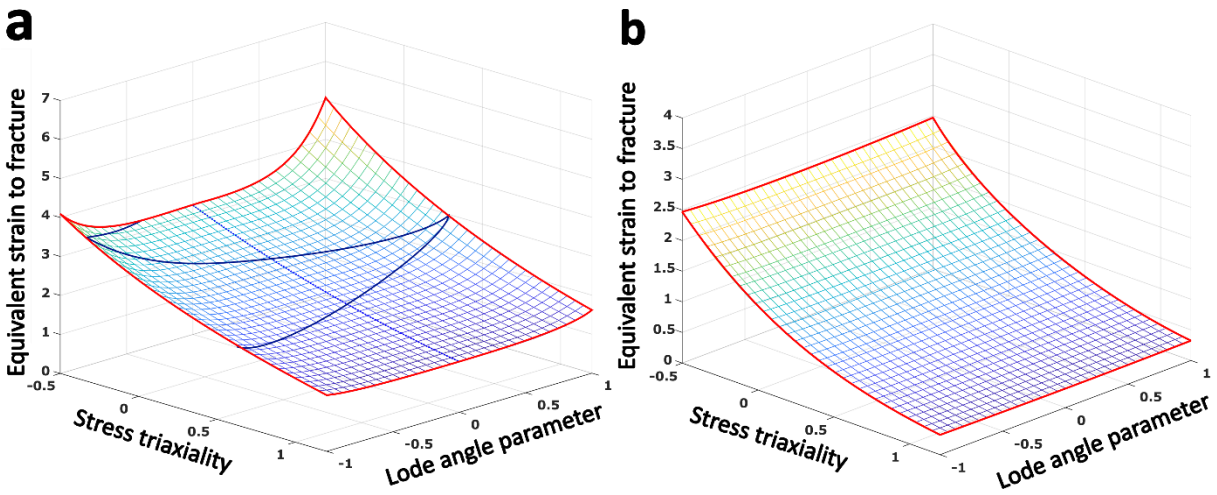


Figure 3.11 Equivalent fracture strain loci in a space of stress triaxiality and Lode angle parameter in (a) material with Lode dependence i.e. A710 steel, and (b) material with weak dependence i.e. 1045 steel (reproduced with test data from [27, 134])

Lode angle θ_L and stress triaxiality η play a key role in classifying the stress state in weight function $\psi(\eta, \theta_L)$ (presented as Lode function $g(\theta_L)$ in Xue's and Nahshon-Hutchinson's models) of shear mechanisms. In taking into account the effect of the shear mechanism, the weight function reaches a unit value in pure shear condition ($\eta = 0, \xi = 0$) and drops to 0 in hydrostatic tension condition ($\eta > 1/3, \xi = 1$). Thus, the shear damage would only increase in the shear dominant deformation without over-prediction the damage in tension dominant region [153]. However, the transit region of mixed

tension, shear and compression could be challenging and is significantly influenced by the weight function $\psi(\eta, \theta_L)$. If a model has been validated in both pure tensile and shear conditions, its damage prediction in combined stress states highly relies on the weight function in space of stress triaxiality and Lode angle parameters.

Figure 3.12 presented the weight function surfaces by shear mechanisms in various GTN based models (Xue [122], Nahshon-Hutchinson [121], Zhou's modified Nahshon-Hutchinson [123], Malcher modified Nahshon-Hutchinson [153] and Dæhli's modification using RVE [147]). This shows their preferences for damage evaluation in stress spaces. From Figure 3.12a and b, the Lode functions from Xue's and Nahshon-Hutchinson's models only show the dependency to the Lode parameter. The remaining models have various customisation for stress triaxiality changes which may lead to more accurate prediction in mixed stress states.

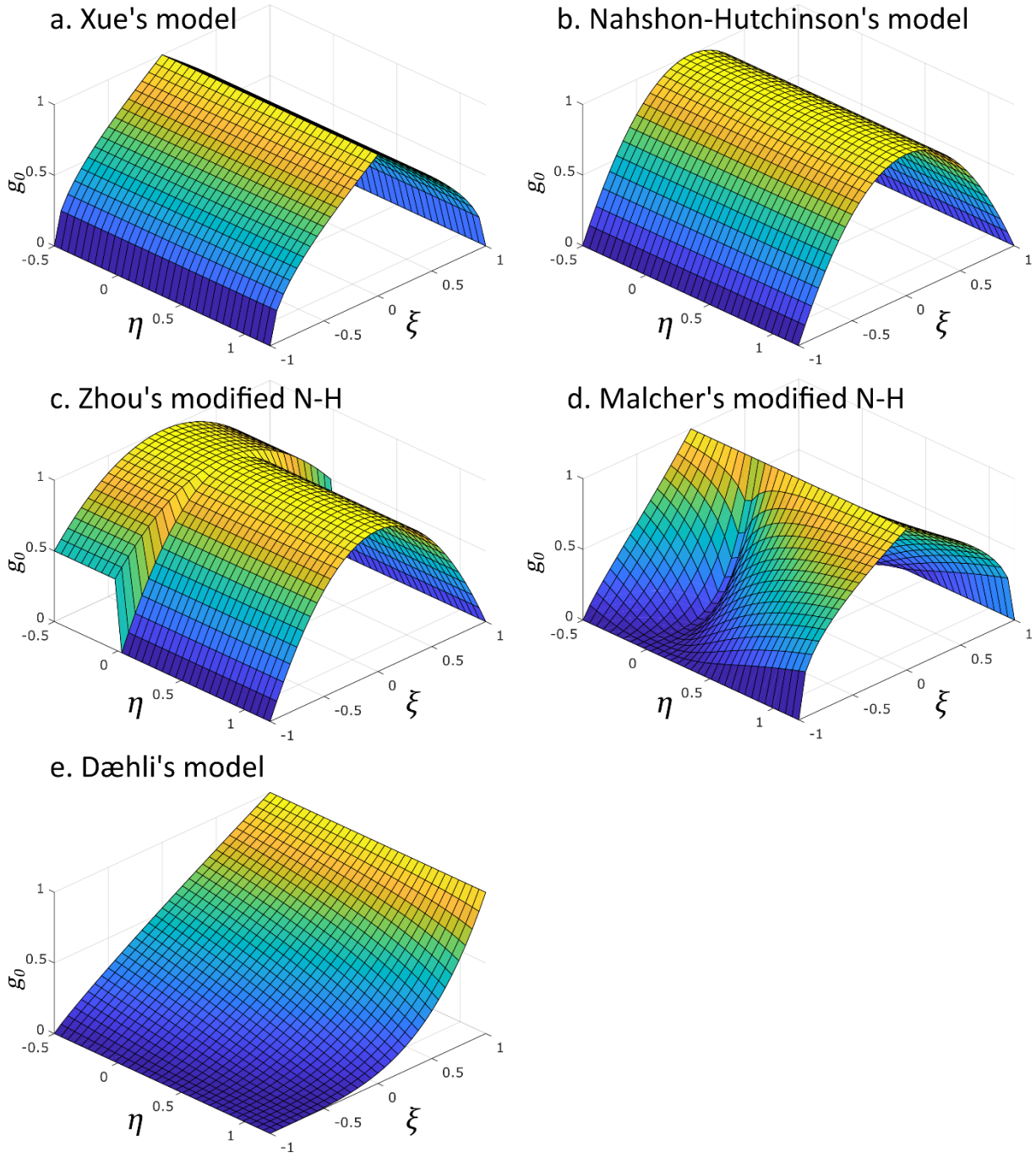


Figure 3.12 Shear mechanisms weight functions in space of stress triaxiality and Lode parameter from (a) Xue [122], (b) Nahshon-Hutchinson [121], (c) Zhou's modified Nahshon-Hutchinson [123], (d) Malcher modified Nahshon-Hutchinson [153], and (e) Dæhli's modification using RVE [147] .

3.4.4. Modified void evolution function

The existing nucleation mechanism in the original GTN model gave an averaged distribution of all potential second phase for nucleation only considering the void

interactions without shear effects, as presented in Equation (3.47). Considering shear condition on nucleation process, Malcher et al. [153] introduced a Lode function into the existing function. Equation (3.47) in the combination of Nahshon-Hutchinson's shear mechanism [121] is re-defined to be in the following form:

$$\dot{f}_n = (\xi^2) \cdot \frac{f_N}{s_N\sqrt{2\pi}} exp\left[-\frac{1}{2}\left(\frac{\bar{\varepsilon}^p - \varepsilon_N}{s_N}\right)^2\right] \dot{\bar{\varepsilon}}^p \tag{3.60}$$

3.4.5. Modified shear mechanisms

The Lode dependency is a main reason for the inaccurate prediction by the original GTN model in low stress triaxiality. The current modified shear damage model is based on the study of Zhou et al. [123]. The Lode dependency incorporates the derivation by Malcher et al. [153] and the void interactions calibration by Xue [122]. The modification focuses on two aspects: the update to the yield function and the evolution law of shear damage. Malcher et al. [153] proposed an extended GTN model for ductile fracture under high and low stress triaxiality, which introduced another distinct damage variable into the plastic flow equation. In this study, the Lode angle function $g(\theta)$ is reconstructed based on Malcher et al. [153]:

$$g(\theta) = \frac{1}{2} \cdot [1 + \cos(3\theta)] = \frac{1}{2} \cdot (1 + \xi) \tag{3.61}$$

$$\psi(\theta, \eta) = \begin{cases} f^{q4} \cdot (1 - g(\theta)^2)^{\frac{1}{|\eta|+k}}, \ \eta_{lim}^{(-)} \leq \eta \leq \eta_{lim}^{(+)} \\ 0, \eta > \eta_{lim}^{(+)} \ or \ \eta < \eta_{lim}^{(-)} \end{cases} \tag{3.62}$$

In the weight function, the void volume fraction exponent is for idealised cell structure where $q4 = 1/2$ for 2D and $q4 = 1/3$ for 3D problems [122]. k is a weight factor to adjust the Lode angle effect with offset of stress triaxiality. As shown in Figure 3.13, Liu et al. [135] used a RVE model to investigate the boundaries of void coalescence and collapse in the plane of stress triaxiality and Lode angle. Two cut-off values of stress triaxiality $\eta_{lim}^{(+)}$ and $\eta_{lim}^{(-)}$ are set in the weight function to calibrate the void closure and coalescence and to improve computing efficiency.

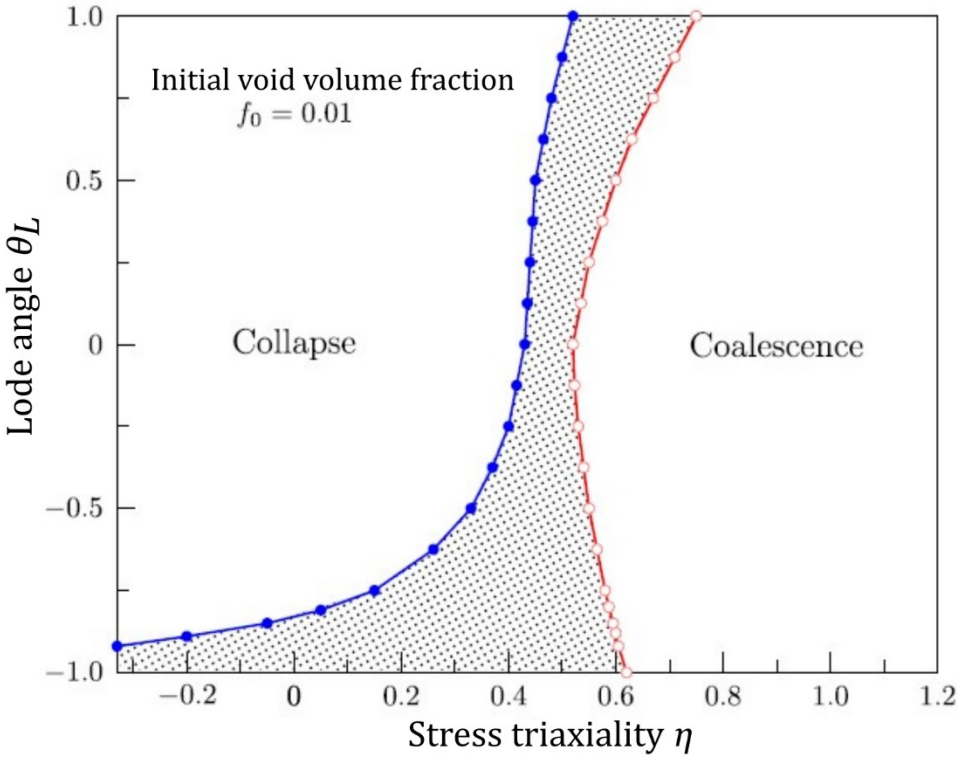


Figure 3.13 Effective regions of void collapse and coalescence of dependent lode angle and stress triaxiality when the initial void volume fraction $f_0 = 0.01$ [135].

3.4.6. Equivalent fracture strain locus function

To present a 3D model of experimental fracture strains, Bai and Wierzbicki [27] designed and conducted several tests under various stress states to obtain fracture locus in the space of stress triaxiality η and the third stress invariant ξ. Lou et al. [159] proposed a changeable cut-off value for stress triaxiality to present the Lode effect.

Bai and Wierzbicki fracture strain locus function:

$$\varepsilon_f = \left[\frac{1}{2}\left(\hat{\varepsilon}_f^{(+)} + \hat{\varepsilon}_f^{(-)}\right) - \hat{\varepsilon}_f^{(0)}\right]\bar{\theta}^2 + \frac{1}{2}\left(\hat{\varepsilon}_f^{(+)} - \hat{\varepsilon}_f^{(-)}\right)\bar{\theta} + \hat{\varepsilon}_f^{(0)}$$

$$= \left[\frac{1}{2}(D_1 e^{-D_2\eta} + D_5 e^{-D_6\eta}) - D_3 e^{(-D_4\eta)}\right]\bar{\theta}^2 + \frac{1}{2}(D_1 e^{-D_2\eta} - D_5 e^{-D_6\eta})\bar{\theta} + D_3 e^{-D_4\eta}$$

Lou's fracture locus function:

$$\varepsilon_f = C_3 / \left[\left(\frac{2}{\sqrt{\theta_L^2 + 3}}\right)^{C_1}\left(\frac{1}{1+C}\left(\eta + \frac{3 - \theta_L}{3\sqrt{\theta_L^2 + 3}} + C\right)\right)^{C_2}\right]$$

where $D_1 \sim D_6$ and $C, C_1 \sim C_3$ are material constants, which can be calibrated by

experimental tests of fracture strain.

Though the above models were effective and proved to be able to depict the fracture strain surface, the effectiveness of stress triaxiality and Lode angle parameter was not intuitively shown in the function. According to the asymmetric surface of 3D fracture strain loci, ε_s^f is reconstructed in a function as below:

$$\varepsilon_s^f = \begin{cases} +\infty, \eta \le \eta_{lim}^{(-)} \\ \varepsilon_0 \cdot \exp\left[\left(q_5(\eta - \eta_{lim}^{(+)}\right)^{n_s}\right] + \left(k_s \cdot \frac{(|\xi + q_6|^2)^{n_s}}{\exp\left(\eta - \eta_{lim}^{(-)}\right)}\right)^2, \eta_{lim}^{(-)} < \eta < \eta_{lim}^{(+)} \\ \varepsilon_0, \eta \ge \eta_{lim}^{(+)} \end{cases} \quad (3.63)$$

where ε_0 is the fundamental fracture strain under high stress triaxiality; k_s is a scaling parameter to control the Lode effect; q_5 and q_6 are constants related to stress triaxiality and Lode effect to be calibrated in material tests; $\eta_{lim}^{(-)}$ and $\eta_{lim}^{(+)}$ are two cut-off values for computational efficiency. The parameters in Equation (3.63) can be calibrated by the fracture strains obtained from material testing. For pure Ti grade 1 with testing data from Zhai et al. [160] and Gatea [98], ε_0, q_5, q_6 can be determined to be 0.52, 2 and 0.7. Then, the reconstructed fracture strain surface can be shown geometrically as Figure 3.14.

Table 3.1 Types of classical tests and corresponding stress triaxiality and Lode angle parameters for fracture strain surface calibration of pure Ti grade 1 (extracted and processed from [27, 98, 160])

Test	Stress triaxiality η	Lode angle parameter ξ	Fracture strain
Smooth round bar	0.33	1	0.6
Notched round bar	1.13	1	0.46
Torsion tension	0	0	0.57
Flat grooved plate	0.72	0	0.44
Uniaxial tensile test	0.33	1	0.61
Nakajima test 1 (width=20mm)	0.4	-1	0.59
Nakajima test 2 (width=60mm)	0.45	-1	0.46

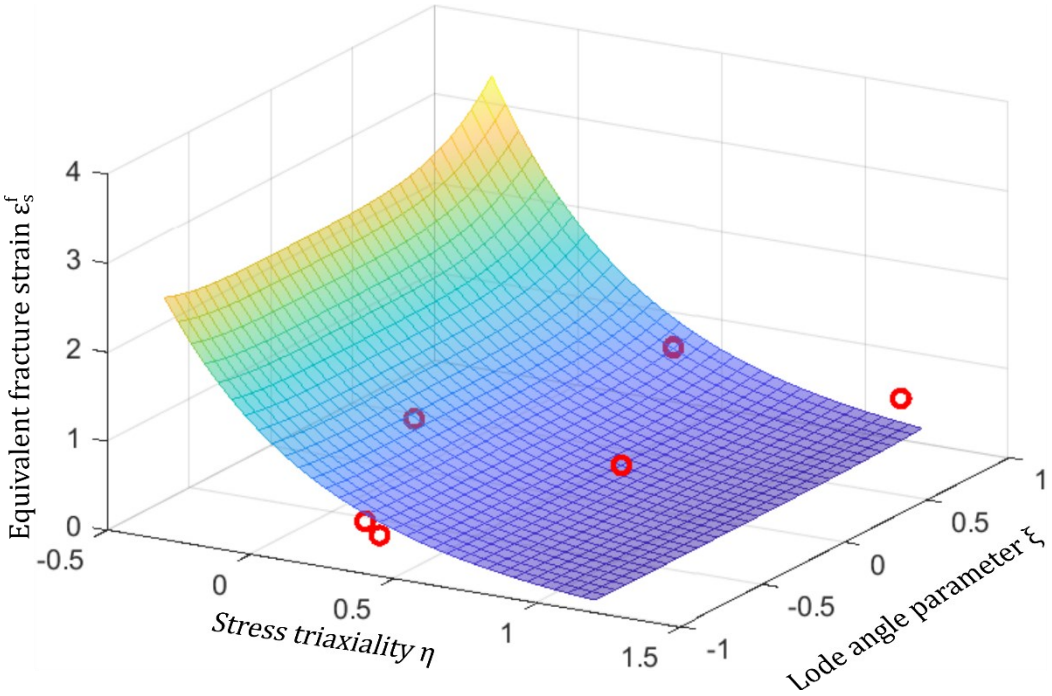


Figure 3.14 A new normalised fracture strain locus for Pure Ti Grade 1.

3.4.7. Implementation of the new modified GTN model

The modified GTN model is implemented in ABAQUS with explicit package analysis through ABAQUS user subroutine VUMAT. The functionality of VUMAT starts with trial stresses calculation and plastic admissibility evaluation via yield function. If the current state is checked as plastic, the stress is updated, and the plastic strain can be determined. Finally, the increments of damage and void evaluation should be calculated and accumulated in solution dependent variables (SDVs). Once the damage and void volume friction values reach the critical value, the element will be deleted through the element deletion function which is built-in ABAQUS.

The basic framework of the GTN model via ABAQUS VUMAT user subroutine used is referred from the study of Gatea et al. [23, 98], which was proven to be suitable for incremental sheet forming. The plastic strain computation is calculated by returning mapping algorithm from Ortiz and Simo [161] and Engelmann and Whirley [162]. Based on the basic frame of the GTN model, the adaption is made for the modification of damage variables [123] and the shear damage modification that calibrated by the newly defined equivalent fracture strain surface.

The trial stress is obtained by Hook's law while the element is assumed to be purely elastic at the beginning of VUMAT computation. Giving shear modulus $\mu = \frac{E}{2(1+\upsilon)}$ and first Lamé parameter $\lambda = \frac{E\upsilon}{(1+\upsilon)(1-2\upsilon)}$, the Cauchy stress tensor $\boldsymbol{\sigma}_{t+\Delta t}^{trial}$ should be calculated with the increment of elastic strain $\Delta\boldsymbol{\varepsilon}_{ij}^{el}$:

$$\boldsymbol{\sigma}_{t+\Delta t}^{trial} = \boldsymbol{\sigma_t} + 2\mu\Delta\boldsymbol{\varepsilon}_{ij}^{el} + \lambda\boldsymbol{\varepsilon}_{ij}^{el}\delta_{ij} \tag{3.64}$$

where ε_{ij}^{el} is the trace of the elastic strain tensor; δ_{ij} is a Kronecker delta that $\delta_{ij} = 1$ when $i = j$, or $\delta_{ij} = 0$ if $i \neq j$; $\boldsymbol{\sigma_t}$ is the Cauchy stress tensor in the previous step. Then the deviatoric stress components S_{ij} is:

$$S_{ij}^{trial} = \sigma_{ij}^{trial} + p^{trial} \tag{3.65}$$

$$p^{trial} = -\frac{\sigma_{ii}^{trial}\delta_{ij}}{3} \tag{3.66}$$

p^{trial} is hydrostatic stress. The equivalent stress σ_q^{trial} can be calculated as:

$$\sigma_q^{trial} = \sqrt{\frac{3}{2}S_{ij}^{trial}S_{ij}^{trial}} \tag{3.67}$$

Applying the obtained hydrostatic and equivalent stresses in the modified yield function (Equation (3.54)), if $\Phi > 0$ then the plastic deformation happens. The plastic strain increment $\dot{\varepsilon}_{ij}^{p}$ is determined as below:

$$\dot{\varepsilon}_{ij}^{p} = \dot{\lambda}\frac{\partial\Phi}{\partial\sigma_{ij}} \tag{3.68}$$

The $\dot{\lambda}$ is the plastic multiplier and defined as:

$$\dot{\lambda} = \frac{\Phi}{V_{ij}D_{ik}V_{ik} - \xi_1 h_1 - \xi_2 h_2} \tag{3.69}$$

The parameters of ξ_1, ξ_2 and V_{ik} are defined by the following set of equations:

$$\begin{cases} \xi_1 = \frac{\partial \Phi}{\partial \bar{\varepsilon}^p} = -\frac{2H}{\sigma_M^3}\left[\frac{3}{2}\sigma_{ij}\sigma_{ij} - \frac{1}{2}\sigma_{ii}^2\right] - \frac{Hf^* q_1 \sigma_{ii}}{\sigma_M^2} sinh\left(\frac{q_2\sigma_{ii}}{2\sigma_M}\right)\delta_{ij} \\ \xi_2 = \frac{\partial \Phi}{\partial f} = 2q_1 cosh\left(\frac{q_2\sigma_{ii}}{2\sigma_M}\right) - 2q_3 f^* \\ V_{ik} = \frac{\partial \Phi}{\partial \sigma_{ik}} = \frac{1}{\sigma_M^2}(3\sigma_{ik} - \sigma_{ii}\delta_{ik}) + \frac{f^* q_1 q_2}{\sigma_M} sinh\left(\frac{q_2\sigma_{ii}}{2\sigma_M}\right)\delta_{ik} \end{cases} \quad (3.70)$$

The h value can be found as:

$$h_1 = \sqrt{\frac{2}{3}V_{ij}V_{ij}} \quad (3.71)$$

$$h_2 = (1 - f^*)V_{ii} \quad (3.72)$$

The elastic constant matrix is:

$$D_{ik} = \begin{bmatrix} 2\mu+\lambda & \lambda & \lambda & 0 & 0 & 0 \\ \lambda & 2\mu+\lambda & \lambda & 0 & 0 & 0 \\ \lambda & \lambda & 2\mu+\lambda & 0 & 0 & 0 \\ 0 & 0 & 0 & \mu & 0 & 0 \\ 0 & 0 & 0 & 0 & \mu & 0 \\ 0 & 0 & 0 & 0 & 0 & \mu \end{bmatrix} \quad (3.73)$$

As the shear damage is independently counted, the equivalent plastic strain is updated as:

$$\dot{\bar{\varepsilon}}_M^p = \frac{\boldsymbol{\sigma}:\dot{\boldsymbol{\varepsilon}}_{ij}^p}{(1-D/q_1)\sigma_M} \quad (3.74)$$

The plastic volume change associated with damage and material incompressibility can be obtained along with the flow rule [123]:

$$\dot{\varepsilon}_{kk}^p = \dot{\lambda} \cdot \frac{3Dq_2}{\sigma_M} sinh\left(\frac{q_2\sigma_{kk}}{2\sigma_M}\right) \quad (3.75)$$

3.5. Experimental testing

To investigate the influential factors to formability improvement, uniaxial tensile tests, TCB and TCBC were conducted with pure Ti grade 1 specimens. Tensile tests were carried out on an Instron 5969 universal testing machine with 2 mm/min tensile speed, calibrated via Digital Image Correlation (DIC) measurement to obtain the stress-strain curve and the maximum elongation as shown in Figure 3.15a. As shown in Figure 3.15b, a

dedicated TCBC machine was used to conduct the TCB or TCBC testing of the test samples. The speeds for tensile elongation and cyclic tool motion were fixed at 2 mm/min and 2 mm/s, respectively. The bending depth and compression force were chosen as variables which were defined as shown in Figure 3.16a.

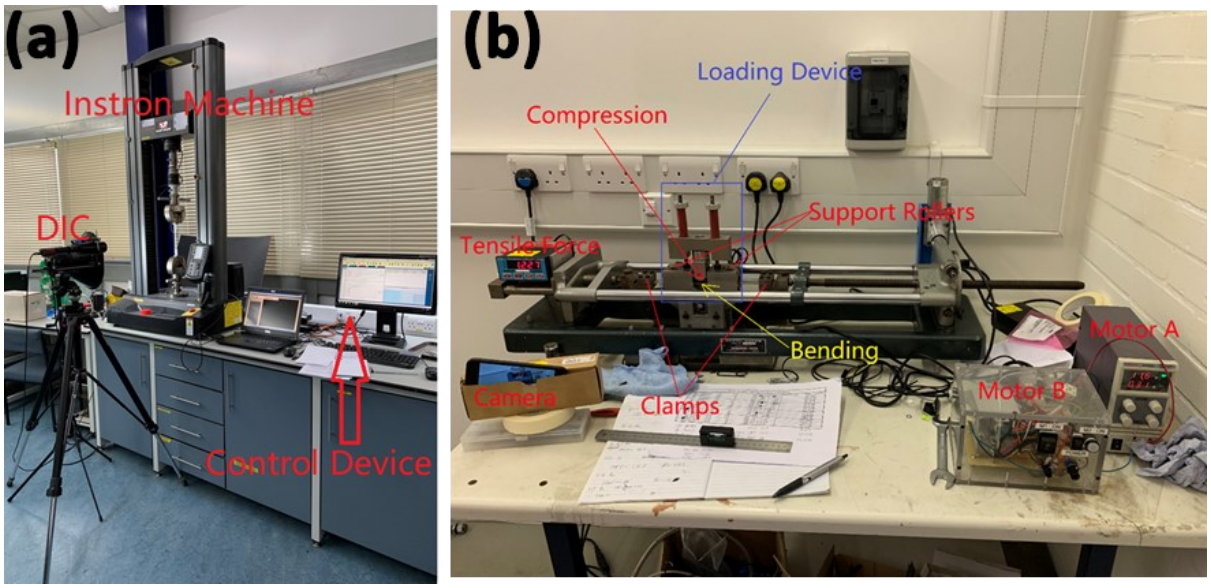


Figure 3.15 (a) Tensile test equipment with instron machine and DIC system (b) TCBC testing rig.

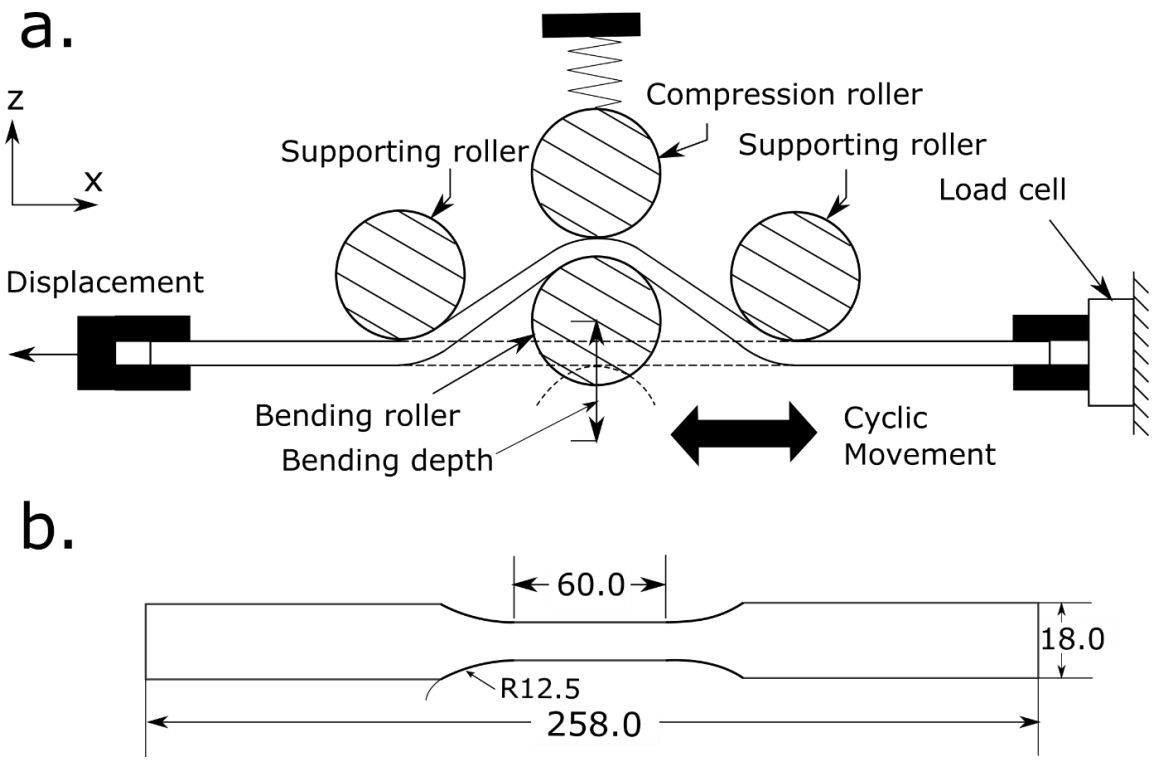


Figure 3.16 (a) TCBC test set-up and parameters (compression, bending depth) during process and (b) dimension of specimen design

The dimensions of a specimen to ASTM-E8 standard are given in Figure 3.16b. Two thicknesses, i.e., 0.5 mm and 0.7 mm were implemented in the tests to compare how the sheet thickness influenced the effect of bending and compression extent. Table 3.2 presents a summary of the values of thickness of test specimen, bending depth and compression force used in both the TCB and TCBC tests. In the case of TCB test, no compression force was applied.

Table 3.2 Experimental designs and maximum elongation results for Pure Ti grade 1

Exp No.	Thickness (mm)	Bending depth (mm)	Compression force (N)
1	0.5	4.5	0
2	0.5	4.5	400
3	0.5	4.5	900
4	0.5	7	400
5	0.5	7	900
6	0.5	9	400
7	0.5	9	600
8	0.5	9	900
9	0.7	4.5	0
10	0.7	4.5	400
11	0.7	4.5	900
12	0.7	9	400
13	0.7	9	900

For TCBC test, it was necessary to keep a constant initial bending and position on the workpiece. In the beginning, the specimen was inserted into the clamping fixture and tightened at the fixed end of force transducer. The bending and compression roller was put in place to apply local deformation and squeezing around the middle of the test sample. With one end (right side in Figure 3.16a) of the sample to be clamped, tension was applied by a motor at the other end (left side in Figure 3.16a) of the sample at a constant speed of 2 mm/min. The cyclic bending and compression were affected by generating an oscillating horizontal motion of the roller subassembly to apply only bending in the case of TCB and bending and compression in the case of TCBC test conditions. The displacement of the pulling head at fracture was measured as the maximum elongation in TCB and TCBC tests.

3.6. Validation of the new modified GTN model

3.6.1. Benchmark test of a single element

Three single element models were implemented via ABAQUS/Explicit package. The shear modifications to the GTN model were defined in VUMAT user subroutine, including the GTN model with Xue's shear mechanism and the modified Zhou's model for validation. A single 8-node hexahedral element with reduced integration (C3D8R) was defined with

pure Ti grade 1 material properties. The same GTN parameters were used for all models for comparison. The uniaxial tension, pure shear and tension under compression tests were conducted to compare the predictions for material softening and damage under different stress states as shown in Figure 3.17.

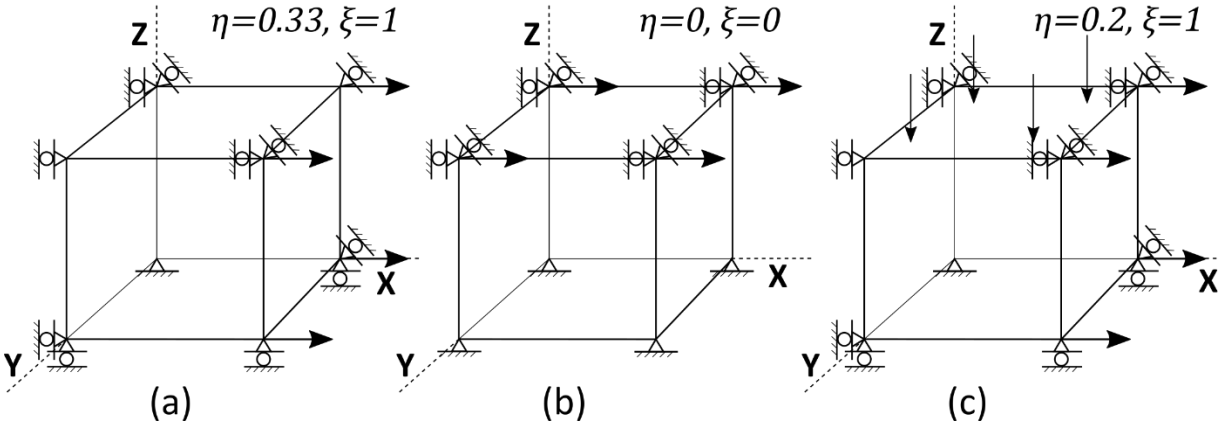


Figure 3.17 Boundary conditions for: (a) uniaxial tension, (b) Pure shear and (c) tension under compression

According to the assessment proposed by Malcher et al. [155], as shown in Figure 3.18, the original GTN model gave a close matching in high stress triaxiality, where the predictions were accurate as compared to Xue's modification under pure shear and combined tension and shear conditions. In the single element testing, the normalised von Mises stress, void volume fraction and damage evolution were compared between the modified GTN models and Xue's, Nahshon-Hutchinson and the modified Zhou's shear mechanisms. Particularly, the shear damage evaluations by Xue's and the modified Zhou's shear mechanisms were compared instead of void volume fraction in the pure shear case. The total damage in Xue's model was defined in the same formula with Zhou's total damage evaluation as presented in equation (3.59).

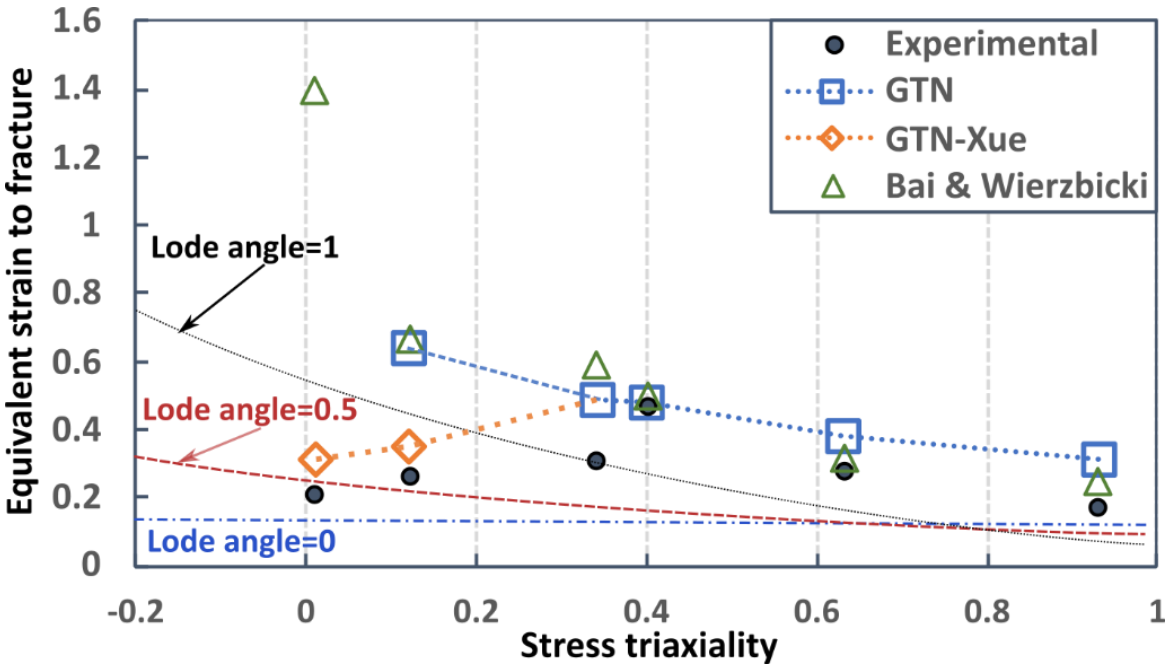


Figure 3.18 Fracture loci illustrated in the plane of Equivalent strain to fracture and stress triaxiality for aluminium alloy 2024-T351 (Reproduced based on experimental data from Bao and Wierzbicki [131] and Bai and Wierzbicki [27], and numerical model assessment from Malcher et al. [155])

3.6.1.1. Uniaxial tension

Figure 3.19 showed the comparison of equivalent stress and void volume fraction evolution versus the equivalent strain. The predictions of equivalent stress and void from the GTN models with Nahshon-Hutchinson's shear mechanism and the modified Zhou's mechanism closely matched in the early stage of deformation ($\varepsilon_{eq} < 0.6$). However, Zhou's modification exhibited a trend of overestimation for material softening at large strain. This may be an inherent defect of a phenomenon-based model, in which the designed weight function cannot find the exact cut-off stress triaxiality to minimise the shear damage effect in the pure tension case. In the modified constitutive function, the predicted shear damage variable would directly result in the reduction of yield stress. Though the shear damage development decreases with the increasing stress triaxiality under the control of weight function, it is hardly avoidable for over-predicted softening when the strain was extremely large. For overall damage evolution, the modified Zhou's model shows a perfect match

with Xue's shear damage mechanism (Figure 3.19c), which means the new model is still precise in holistic damage evaluation.

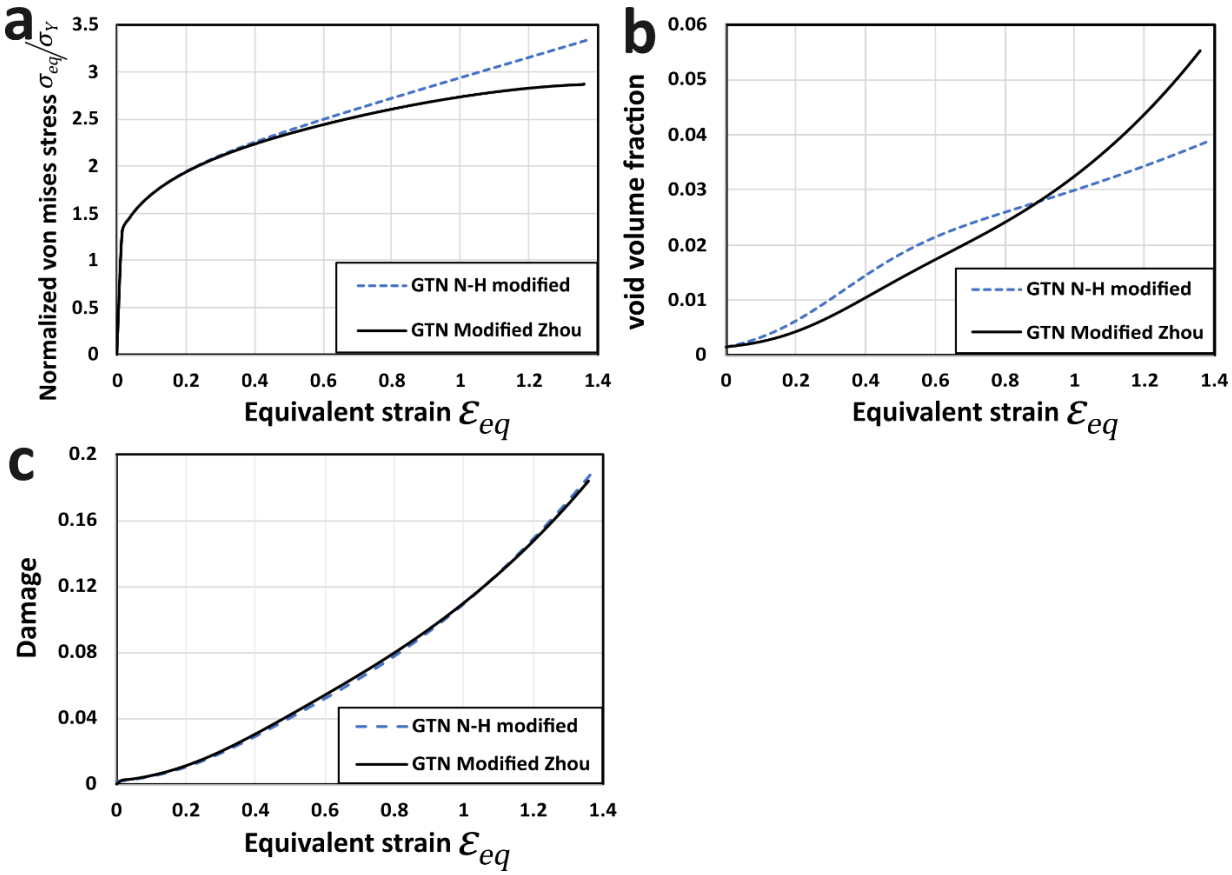


Figure 3.19 (a) Ratio of equivalent stress and yielding stress, (b) void volume fraction and (c) damage evolution by equivalent strain from GTN model with the modification of Nahshon-Hutchinson's and Zhou's shear mechanisms by single element simulation under uniaxial tension.

3.6.1.2. Pure shear

The results of equivalent stress and shear damage predictions by GTN models with Xue's and the modified Zhou's shear mechanisms were illustrated in Figure 3.20. All results show a close agreement that means the modified Zhou's model can give accurate damage evaluation for pure shear stress state.

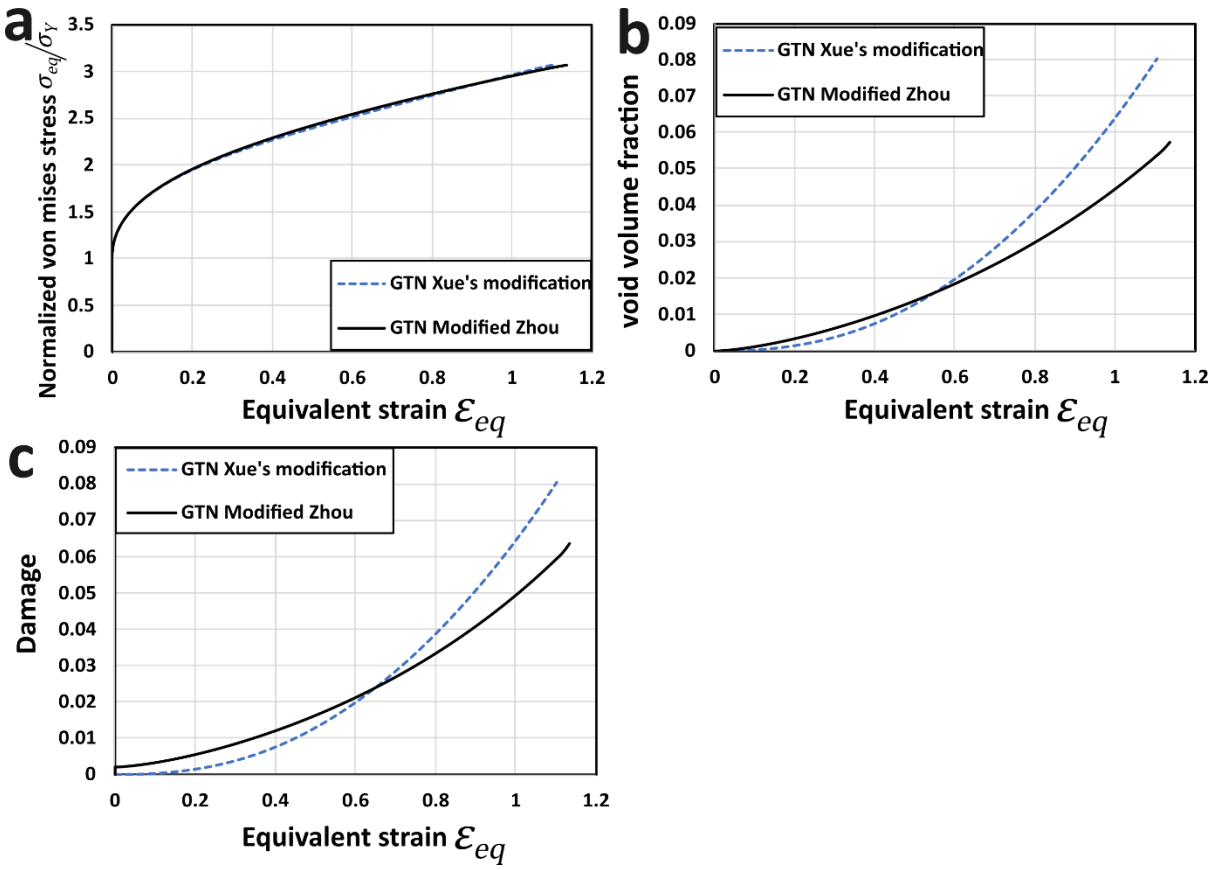


Figure 3.20 (a) Ratio of equivalent stress and yielding stress, (b) shear damage and (c) total damage evolution by equivalent strain from GTN model with Xue's and the modified Zhou's shear mechanisms by single element simulation under pure shear states.

3.6.1.3. Tension under compression

The tension under compression case was expected to have the compressed void evolution as compared to the pure tension case. Figure 3.21 illustrated the equivalent stresses, void volume fraction and damage evolutions as a function of equivalent strain. The original GTN model with Nahshon-Hutchinson's modification failed to distinguish uniaxial tension and tension under compression cases which made almost identical predictions in void volume fraction (Figure 3.21b). In contrast, the modified Zhou's model correctly delayed the void volume fraction growth in tension under compression case. The GTN model with Xue's shear mechanism gave a comparable damage evolution to the prediction of the modified Zhou's model, where the modified Zhou's mechanism presented the higher estimation when $\varepsilon_{eq} > 1.2$. However, the fracture criterion in Xue's

modification is a critical value for void volume fraction. Thus, the model with Xue's modification is likely to give an earlier or close fracture prediction to the original GTN model because the core yielding function and void growth mechanism are not directly correlated to the shear damage. In conclusion, the modified Zhou's shear mechanism is capable to distinguish pure shear and tension combining with compression under low stress triaxiality and it gives reasonable predictions to both void volume fraction and shear damage development.

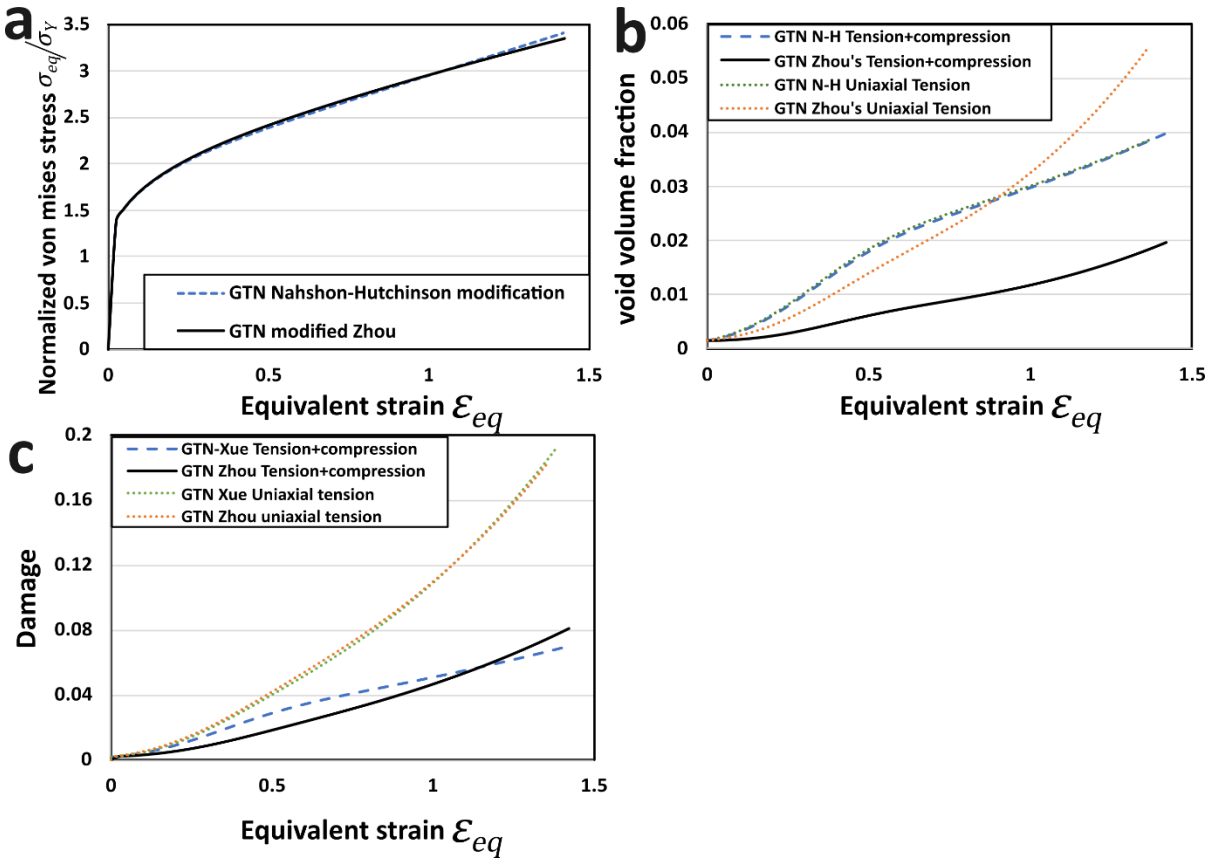


Figure 3.21 (a) Ratio of equivalent stress and yielding stress, (b) void volume fraction and (c) damage evolutions by equivalent strain from GTN model with the modification of Nahshon-Hutchinson's, Xue's and Zhou's shear mechanisms by single element simulation under uniaxial tension and tension combined compression conditions.

3.6.2. FE simulation of uniaxial tensile test

A symmetric half model was implemented for the tensile test to validate the modified GTN model and calibrate the fracture loci. A 4-layer 0.7 mm thick sheet of C4D8R

elements was established in accordance with the uniaxial tensile experiment. The tensile speed was set 1 mm/min. Mass scaling was applied with a minimum incremental size of $2 \times 10^{-5}\ s$. The predicted elongation-to-fracture and the force-displacement curve were used to assess the reliability of the new model in comparison with the experimental measurement.

3.6.3. FE models for TCB and TCBC

Two FE models were separately established for the 0.7 mm thick pure Ti grade 1 sample. A 4.5 mm bending depth was used for both TCB and TCBC tests with a 400 N compression force applied in the case of TCBC. C3D8R brick elements were used to generate the mesh with 4 layers through the thickness and improved mesh density from element length of 0.5 mm in the area under TCB and TCBC loading of oscillating roller motion and 1.5 mm in the remaining area of the test specimen. All rollers including the support, bending and compression rollers were built as analytical rigid shell parts. For the TCBC tests, connector elements (slot + align) were used to connect the compression roller to apply the defined force. The bending depth was applied in step 1 to build up tension in the specimen and this was followed by the application of extension of the specimen in the lateral direction in step 2. To improve the computational efficiency, mass scaling was applied with a minimum increment time of $1 \times 10^{-5}\ s$. The localised deformation and damage propagation on the specimens were closely monitored to reveal the deformation mechanisms in both TCB and TCBC test conditions. The whole model was defined to be frictionless. Figure 3.22 shows the assembly of the FE model.

In this study, the material properties for pure Ti grade 1 were used from uniaxial tensile tests and study by Gatea et al. [23]. All material and damage model parameters are listed in Table 3.3. These parameters were verified by uniaxial tensile test in terms of force-displacement relationship and elongation until fracture. $q1, q2, q3$ are GTN model constants and ε_N, S_N and f_n are void nucleation coefficients of material that determined by in-situ test by Gatea [98]. $\varepsilon_0, q4, q5, q6, n_s, k_s, k_w$ are the material fracture strain parameters calibrated using fracture strains by various experimental tests by Gatea [98]

and Zhai et al. [160]. $\eta_{lim}^{(-)}$ and $\eta_{lim}^{(+)}$ are stress triaxiality limits to define the boundary of fracture strain surface and improve the calculation efficiency. Besides, E, ν are the Young's modulus and Poisson's ratio, respectively. A, B and n are parameters for Johnson Cook's constitutive model, which is calibrated by uniaxial tensile test shown in Section 3.5.

Table 3.3 Material and GTN model parameters for grade 1 pure Ti used in FE simulations [23]

E	ν	A	B	ε_0	n	q_1	q_2
105000	0.34	170	356	0.52	0.53	1.5	1
q_3	f_f	f_c	ε_N	S_N	f_n	q_4	q_5
2.25	0.3025	0.2593	0.3	0.2	0.017	1/3	2
q_6	k_w	k_s	n_s	$\eta_{lim}^{(-)}$	$\eta_{lim}^{(+)}$		
0.7	1.4	1	1.2	-1	1		

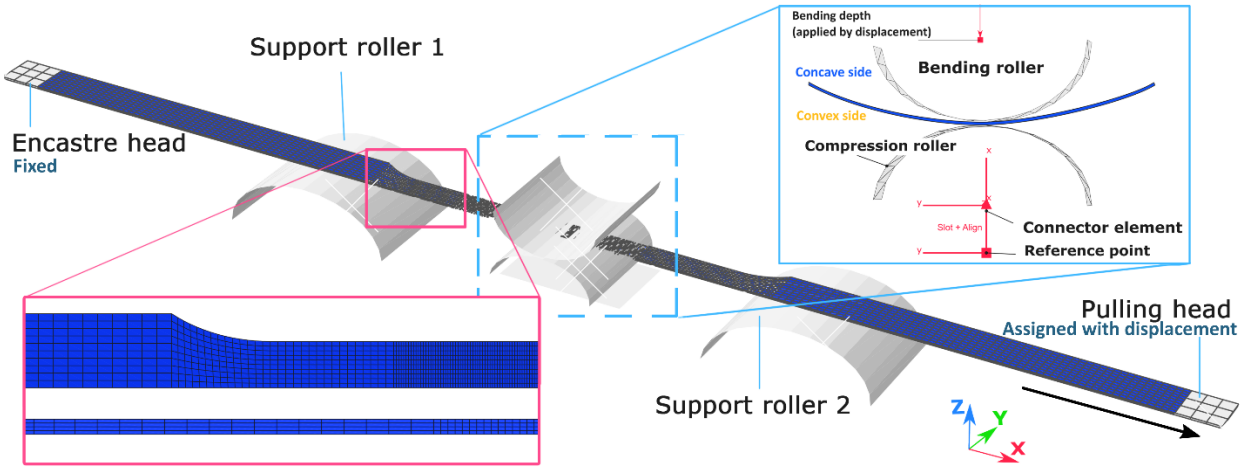


Figure 3.22 Finite element model of TCBC with mesh and rollers set configuration.

3.7. Results and discussion

3.7.1. Experimental results

3.7.1.1. Uniaxial tensile test

The maximum elongation obtained from the uniaxial tensile test was used as a benchmark for material ductility under simple tension condition. As shown in Figure 3.23, the true stress-strain curve was obtained at various strain rates for 0.7 mm thickness pure Ti grade 1 specimens. These curves are used to calibrate the Johnson-cook parameters (A, B, n) used in the modified GTN model.

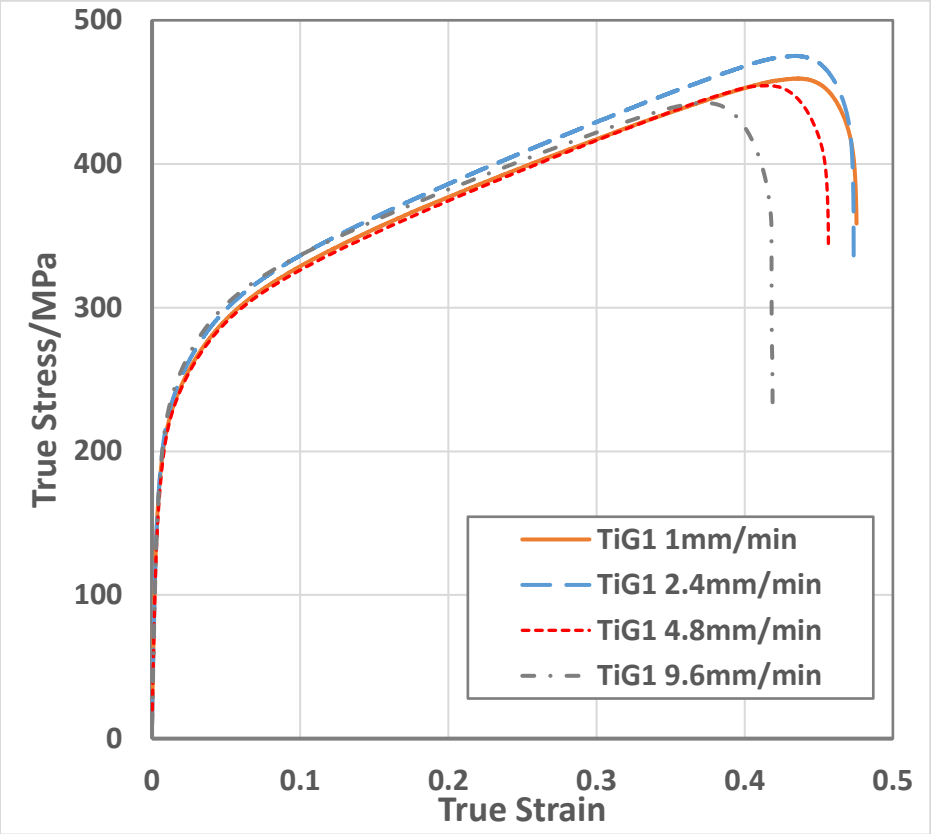


Figure 3.23 True stress-strain curves for material pure Ti grade 1 at various strain rates.

3.7.1.2. TCB and TCBC tests

The fractured samples by uniaxial tensile, TCB and TCBC tests were shown in Figure 3.24. The fracture behaviour was first investigated on the exterior. Of all samples, the crack behaviours were similar to simple uniaxial tension rapture, in which the section of failure was at an angle to the tensile direction. In both TCB and TCBC, the fracture positions were close to the fixed end. The reduction of sample width was uniformly distributed throughout the deformation region. On surface appearance, there was smooth trace of roller contact and compression in both TCB and TCBC samples. However, there were no apparent micro-cracks caused by cyclic bending from the pure Ti grade 1 samples, as also observed on the AA5251-H22 sheets reported by Ai et al. [20].

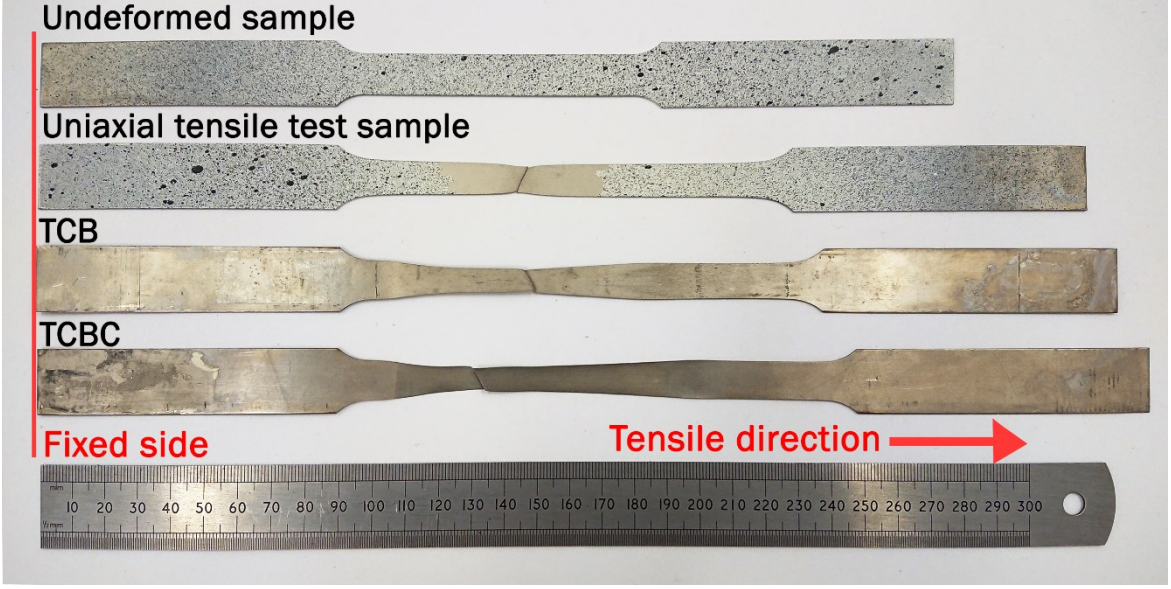


Figure 3.24 Completed samples for comparison in uniaxial tensile, TCB and TCBC tests.

The maximum elongation results from TCB and TCBC were plotted in Figure 3.25 at different test conditions. The results from two thicknesses were collected for evaluation of the thickness sensitivity to elongation. Generally, both TCB and TCBC processes have achieved above 40% larger elongation than that obtained from uniaxial tensile testing, which was 44 mm. The elongation was further improved with the increase of the bending depth and compression force. However, the 0.5 mm thick specimens exhibited extra sensitivity to the change of parameters, especially to the compression forces as predicted in the analytical model (Figure 3.6). Another trend was that the elongation benefitted from the thicker specimen was diminished under high compression. For instance, the achieved elongations by both the 0.5 mm and 0.7 mm thick samples under 900 N pressure were the closest in all figures. When the test samples formed with a bending depth of 9 mm and compression force of 900 N, the 0.5 mm thick sheet achieved 73 mm elongation till fracture in comparison to 70.5 mm from the 0.7 mm thick specimen. These results indicate a negative impact by excessive bending on thicker specimens, strengthened by the larger amount of compression force as predicted by the developed analytical model (Figure 3.6a). The reduced bending depth and thickness lessen the bending effect and the discrepancy of strain in through-thickness direction. As a result, the post-contact deformation on the

side contacting with the master tool is fallen in the reverse-bending stage, where the stress state is close to pure uniaxial tension with the higher stress triaxiality. This shift of deformation mode may play a key role in the highly localised deformation in TCB and TCBC processes and determine how much formability improvement can be achieved.

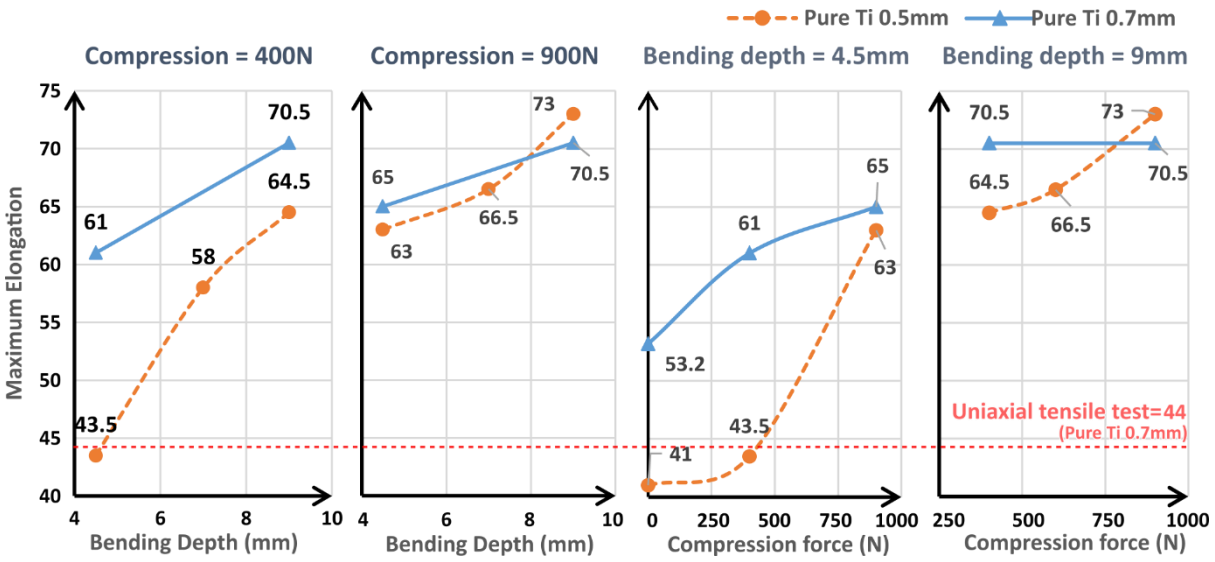


Figure 3.25 Maximum elongations obtained under various bending depths and compression forces in TCB and TCBC (note: zero compression force refers to TCB test condition)

3.7.1.3. Forming forces

The forming forces recorded in the uniaxial tensile test, TCB and TCBC processes of 4.5 mm bending depth and 400 N compression force vs displacement is plotted in Figure 3.26. It was observed that the tensile force was reduced in both TCB and TCBC processes. However, further reduction of forming forces in TCBC was insignificant, which was somewhat different to the cases with AA5251 [20]. Besides, for each cycle of stroke movement in TCBC, the difference between the peak and valley values were larger than that of TCB.

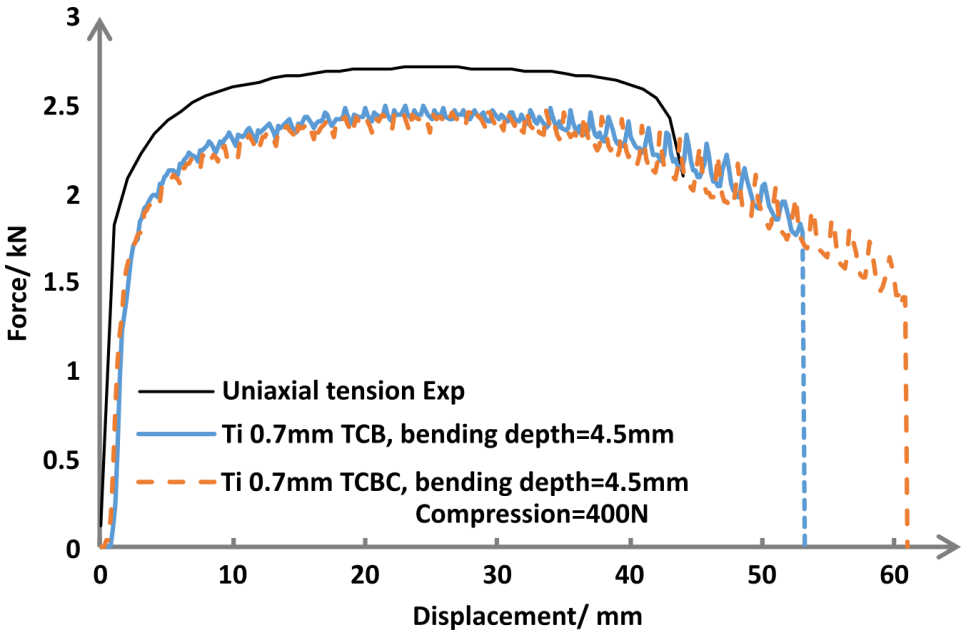


Figure 3.26 Tensile forces comparison from uniaxial tensile, TCB and TCBC tests for Pure Ti 0.7mm

3.7.2. FE results

3.7.2.1. Validation of FE model under uniaxial tensile condition

To validate the modified GTN model, FE simulation was carried out in the case of uniaxial tensile condition. The predicted force-displacement curve by FE was compared with experimental data as shown in Figure 3.27. The FE results provided an accurate prediction of elongation-to-fracture. The softening behaviours from experimental testing and FE simulation were also in broad agreement. It demonstrates that the modified GTN model with shear can capture the material softening and failure.

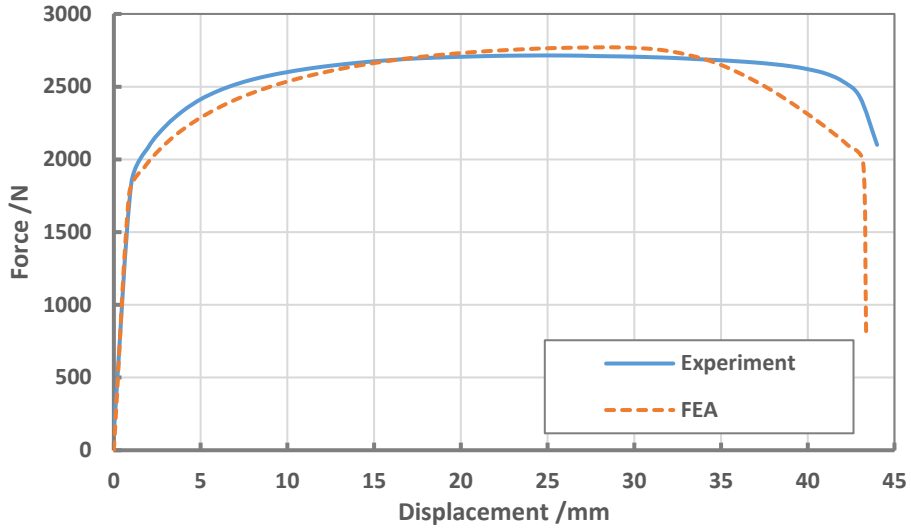


Figure 3.27 Load-displacement curve comparison by experimental data and FE prediction

3.7.2.2. Strain and damage distribution in TCB and TCBC

The data of the equivalent plastic strain and damage variable obtained from FE simulation via ABAQUS user subroutine were extracted as filed outputs, and showed in Figures 3.27 and 3.28, respectively. The length in the tensile direction (x-axis in Figure 3.28) was scaled by a factor of 0.5 for better presentation. The equivalent plastic strain suggested that a uniformed distribution of plastic deformation occurred in TCB and TCBC in the tensile or longitudinal direction. This material behaviour is in agreement with previously reported experimental strain results in TCB of other materials such as aluminium alloys [110, 111, 114]. As the larger amount of elongation-to-fracture was achieved in TCBC, the plastic strain was decentralised in a wider range and reached a higher value in the region around fracture location as compared to the case of TCB.

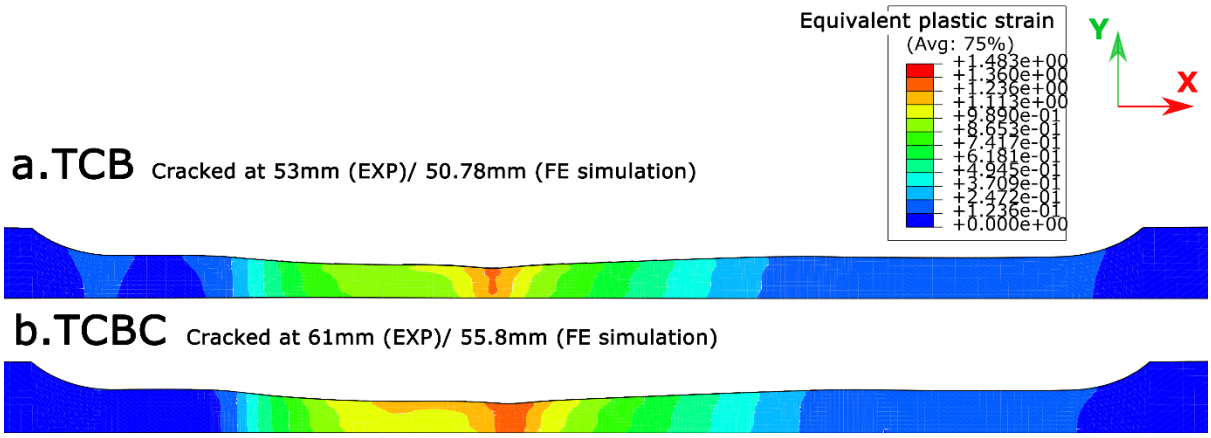


Figure 3.28 Plastic strain distribution in (a) TCB and (b)TCBC

The damage variable embedded void volume fraction and the modified shear damage (Equation (3.59)) gave predictions of elongation-to-fracture and an indication of the initial location of failure. The predictions of fracture were 50.78 mm for TCB as compared to 53 mm from the experiment, and 55.8 mm for TCBC as compared to 61 mm from the experiment. Due to the local deformation produced and propagated by the cyclic motion of the support, bending and compression rollers, the damage distributions in TCB and TCBC were exhibited in a similar pattern to the equivalent plastic strain distribution. However, the discrepancy in the through-thickness direction was exhibited allowing for the different deformation modes between the concave side in contact with the bending roller, and the convex side with or without the compression force applied by the compression roller in TCBC testing. It was observed that the fracture initiated on the concave side, captured from the cross-section view at the moment before the fracture extends to the whole section in TCBC as shown in Figure 3.29. As the strain distribution in the through-thickness direction was similar, the damage evolution is highly dependent on the local stress state, which is controlled by bending and compression roller contact.

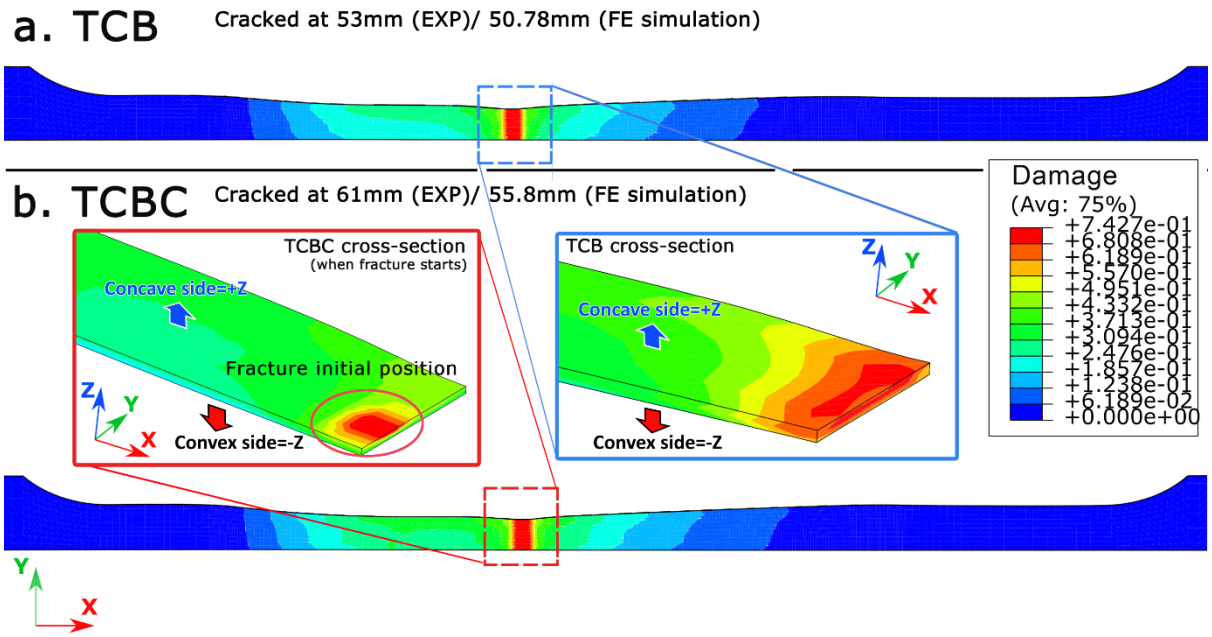


Figure 3.29 Distribution of damage variable in (a)TCB and (b)TCBC

3.7.2.3. Localised stress during deformation

To reveal the mechanisms of how the deformation was evolved and developed, the stress state at contact location was investigated. The material yielding can be determined by the level of von Mises stress. Based on stress distribution, three deformation stages, i.e. post-contact, contact and pre-contact stages or regions, could be classified by the relative position of material to the bending rollers contact, as shown in Figure 3.30. The deformation initiated before the roller contact and high tension was generated on the convex side. In this pre-contact stage, the stress state was similar to the typical bending deformation, where the stress and strain were dependent on the bending radius and sheet thickness. The stress profiles changed under roller contact where the material is transformed to curvature with largely cross-sectioned tension. During this process, there was a considerable amount of shear stress variations due to the contact force of the moving roller in the through-thickness direction. In the post-contact region, the concave side of the material undertook an amount of reverse bending as the bending roller moved away from its current position. The high-stress area was on the concave side in this stage. In conclusion, the stress distribution clearly indicated the different stress states in the

three stages of deformation. To investigate the deformation and fracture mechanics of the whole process, the reverse-bending stage needs to be considered as well.

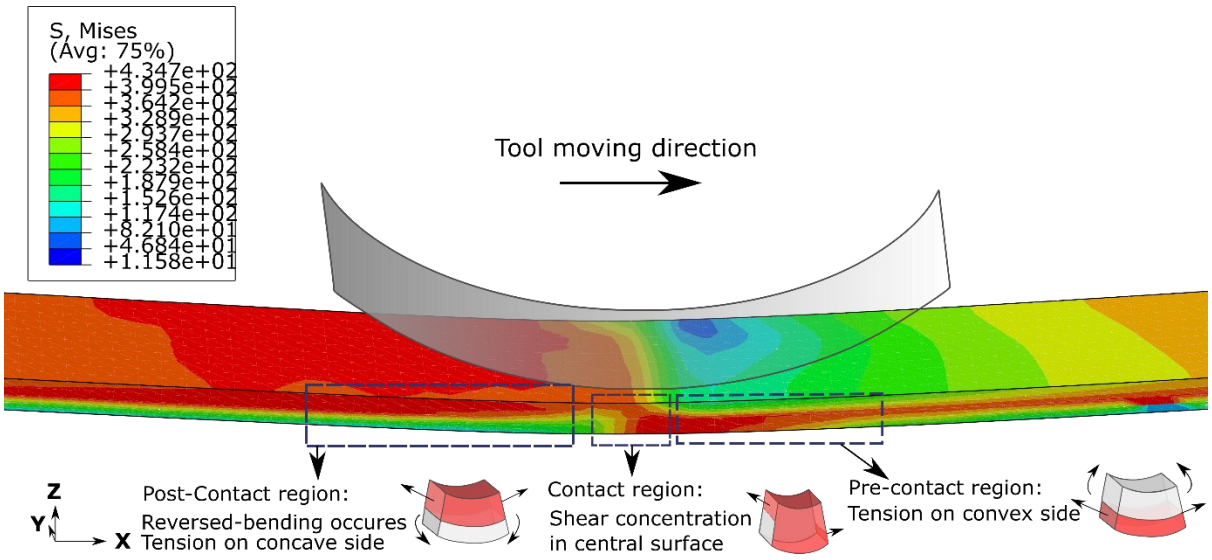


Figure 3.30 Von mises stress (MPa) distribution and stages classification in the local deformation region for TCB and TCBC process

3.7.2.4. Localised strain evolution associated with stress state parameters

Localised deformation may vary because of the locations and through-thickness effect. With continuous elongation of material, the deformation area on the specimen changes according to the rollers' stroke range and position. The deformation zones could be divided by the number of contacts with the bending roller. The maximum principal logarithmic strain in the TCBC specimen was plotted on the undeformed sample with the number of bending roller oscillation cycles as shown in Figure 3.31. Due to the longitudinal elongation of the sample, the stroke range for the bending and support rollers would result in a smaller area of deformation under both TCB and TCBC conditions. The contour plot suggests that the maximum principal strain reached a higher level in section 2 with the increased forming cycles of 40. This conclusion could be confirmed by the equivalent plastic strain history of different sections on the sample as shown in Figure 3.31. The material in sections 3 and 4 exited the range of cyclic tool stroke after a certain amount of elongation, which showed the plastic strain levelled after this section moved

out of the contact region of the roller frame by certain displacement. The strain development by sections verified the characteristic of localised deformation in TCB and TCBC processes as presented in Equations (3.9) and (3.11), where the bending effect reduced the required stress to yield and limited the plastic deformation only occurring in the contact region. The reduced yield stress, observed as the reduction of tensile force, prevented the strain concentration and homogenised damage in both TCB and TCBC samples. which led to larger elongation-to-fracture than that from the simple tensile test.

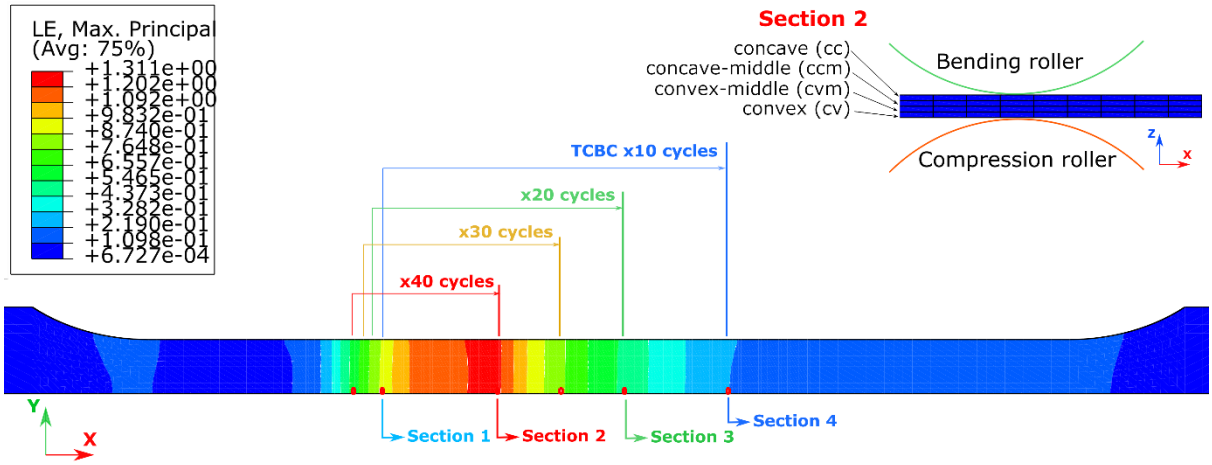


Figure 3.31 Maximum principle logarithmic strain distribution in TCBC numerical result, with location selection in longitudinal and through-thickness directions.

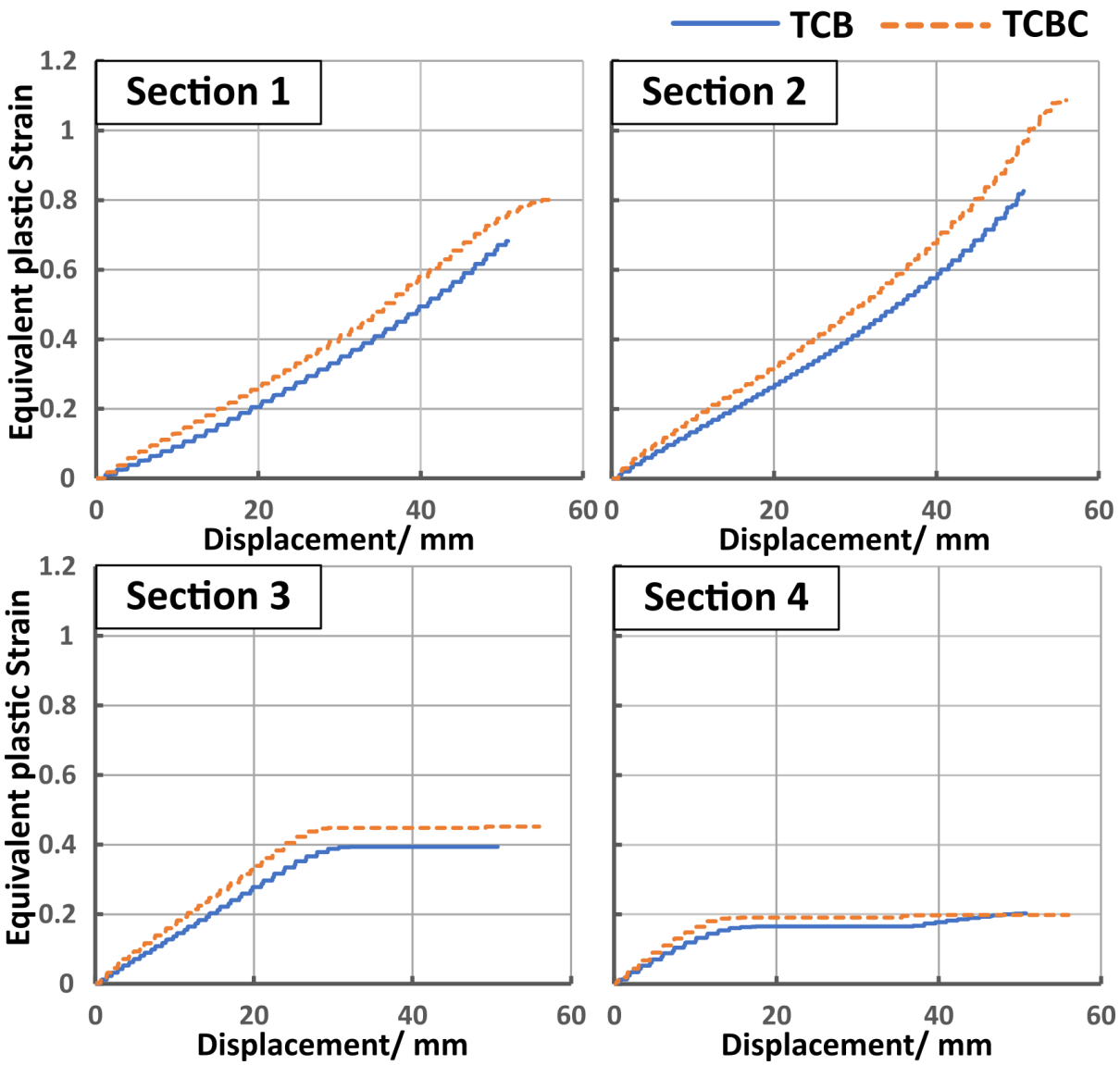


Figure 3.32 Comparisons of FE plastic strain development in longitude direction between TCB and TCBC processes at (a) section 1, (b) section 2, (c) section 3, and (d) section 4.

The through-thickness effect was investigated based on four layers of elements in the thickness direction in section 2. Figure 3.33 shows the relative increases of the equivalent plastic strain and damage values before, during and after contact in these elements. The x-axis was relative "time" when the contact start at x=0. The whole contact duration was indicated with the shadow area. The variables were magnified and presented in a form of accumulation, starting from 0 at a given time window. In both TCB and TCBC processes, the equivalent plastic strain growths were induced by roller contact

where the plastic strain increase in a contact period was larger in TCBC than that in TCB (Figures 3.33a and b). It is also observed in Figures 3.33a and b that there was a delay of strain increase on the side (concave) contacting to bending roller, which was the rebalance of through-thickness strain discrepancy in the reverse bending after the contact period. In contrast, the damage evolution on the concave side was higher than the other in a single bending cycle as suggested by Figures 3.33c and d. Therefore, it can be concluded that the reverse-bending resulted in more damage accumulation which is the reason for fracture initiation in the concave layer. It was also observed that TCBC suppressed the damage evolution in contrast to TCB process. In the original GTN model, the material damage accumulation including the void growth and nucleation (as presented in equations (3.46) and (3.47)), was proportional to plastic strain increment. However, this trend was reversed in TCB and TCBC, where a larger amount of deformation hence higher level of plastic strain led to less damage, which suggests the shear mechanism introduced in the new modified GTN model responded correctly to the different stress states in TCB and TCBC for improved formability.

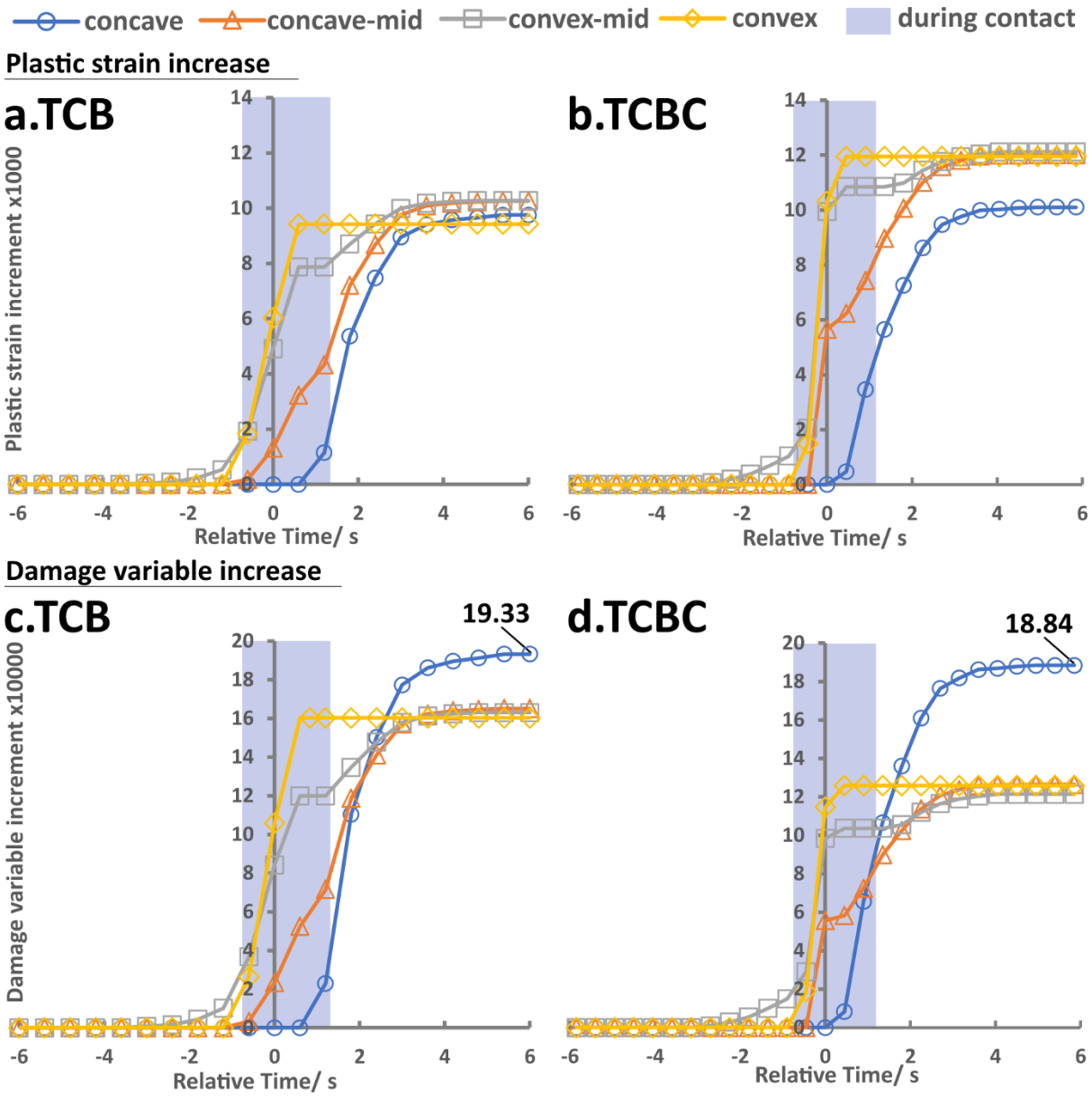


Figure 3.33 Increases of plastic stain (a) TCB and (b) TCBC, and damage (c) TCB and (d) TCBC during a single contact period

The stress state parameters such as stress triaxiality η and Lode angle parameter, related to the third deviatoric stress invariant ξ, during the same local deformation period are described in Figure 3.34. The contact and bending effect generally induced stress fluctuation at the surface layers while the deformation in the intermediate layers remained largely constant. In the case of TCB (Figures 3.34a and c), a drop of stress triaxiality and Lode angle parameter occurred in the layer directly in contact with the bending roller. While on the opposite side, the stress triaxiality and Lode angle parameter

increased due to the bending effect. In the case of TCBC (Figures 3.34b and d), the additional compression brought in a reduction of stress triaxiality and Lode angle parameter in all layers.

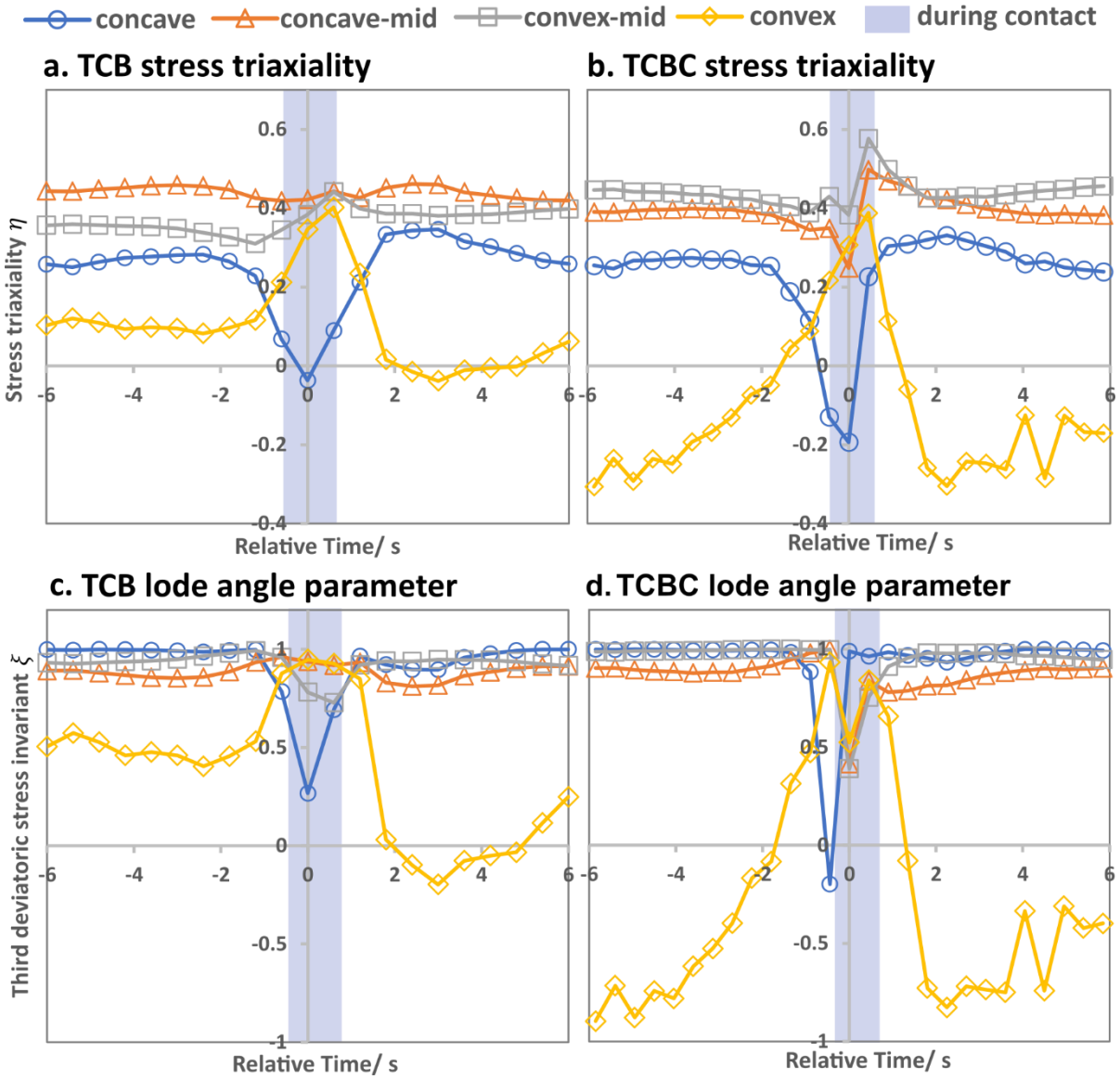


Figure 3.34 Comparison of stress indicators development during a single contact period: Stress triaxiality in (a) TCB and (b) TCBC, and Lode angle parameters in (c)TCB and (d)TCBC

The paths of deformation stress state could be mapped on the conceptual representation plane of stress triaxiality and normalised Lode parameter proposed by Bai and Wierzbicki [27] as shown in Figure 3.35. The stress paths pointed out the key differences of deformation mode in the through-thickness direction between TCB and

TCBC. It was suggested that the intermediate layers were under pure tension while the concave layers followed the line of plane stress condition. In TCBC, a trend of a shift beyond shear state towards axial symmetric compression was shown throughout the local deformation period. This is accompanied by a decrease of stress triaxiality. The comparison between the stress paths of TCB and TCBC process clearly shows the reduced shear effect and increased compression that benefits the delay of fracture, especially for the concave layer where the crack is initiated.

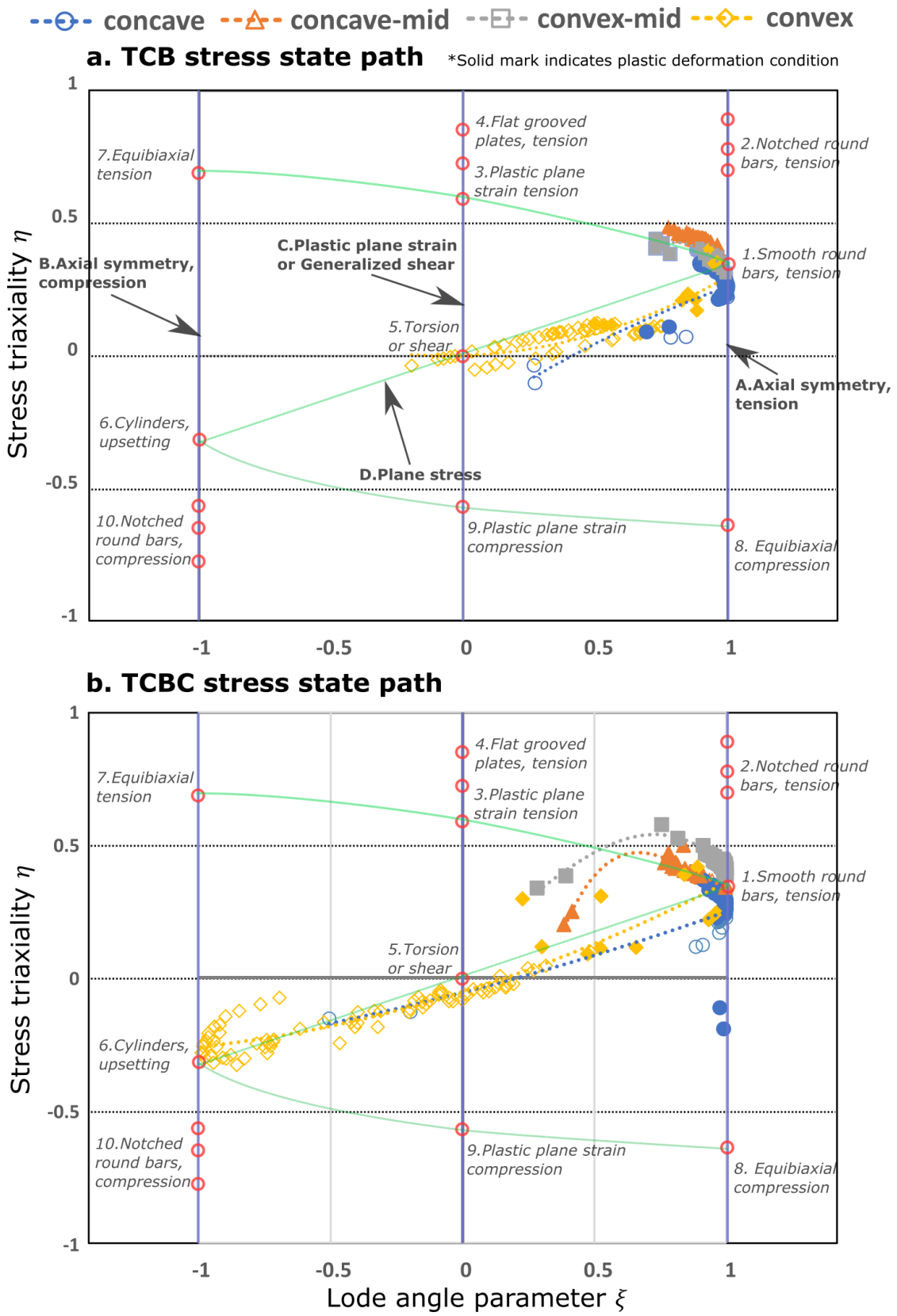


Figure 3.35 Stress state path plotted on the conceptual plane constructed by stress triaxiality and Lode angle parameter (a)TCB and (b)TCBC

3.8. Discussion

From experimental results, the improvement of formability from uniaxial tensile to TCB and TCBC was evident. The material formability was further enhanced by increasing bending depth and compression force in TCBC. In the comparison of elongation-to-fracture, the samples with smaller thickness achieved better formability with a higher level of bending depth and compression. This specific case was indicated in the analytical model as compression accelerates the damage accumulation in the case of the larger amount of bending depth, which may lead to the smaller bending radius. The reduced bending radius intensifies the inhomogeneous strain distribution of material through-thickness during the bending stage, which also means the larger amount of strain recovery in the following reverse-bending stage. It suggested the importance of the bending and reverse-bending effect that the material in different layers through-thickness is being deformed under different stress states.

The developed FE model using shear modified GTN fracture mechanism provided an insight into material deformation and fracture mechanisms under TCB and TCBC conditions. The numerical results confirmed the localised deformation bringing in harmonised strain and damage distribution throughout the region of deformation in the longitudinal direction. However, the stress states were diverse due to bending and contact with rollers on the surface layers. As a result, there were differences between the deformation modes according to the location relative to the contact point and into the depth of the sample cross-section. Therefore, the plastic strain evolution and damage accumulation in the through-thickness direction was observed to be stress triaxiality and Lode angle dependent. The stress state path could be a representative expression of the discrepancy in the elongation and formability under TCB and TCBC conditions. Such an effect may have a role to play in the differentiation of SPIF and DSIF as well as multi-pass SPIF forming processes.

3.8.1. The effect of localised bending

The deformation mode of TCB and TCBC was a combination of two aspects: the highly localised deformation including bending and reverse-bending and its propagation. The localised deformation was proven in the theoretical analysis and confirmed by FE simulation (Figure 3.31). The longitudinal strain contour plot exhibited a clear pattern where the local strain was highly proportional to the number of tool contact with the specimen under both TCB and TCBC test conditions. The material bending due to oscillated roller motion homogenised the strain to delay concentrated deformation and necking, which led to a considerable increase of elongation-to-fracture if the tool contacted zone was extended.

The deformation that the material went through could be divided into three stages relative to the contact with the bending roller. This single direction bending causes different stress distribution of the layers in the through-thickness direction. The local stress state determines the damage evolution during the plastic deformation process. Figure 3.33 shows this difference that the side in contact with bending roller accumulated more damage than the other layers. Associated with Figure 3.34, the additional compression only reduced the Lode angle parameter and stress triaxiality at the instant of contact. However, the increase of damage variable was considerably restrained in TCBC. As compared to compression, the increase of the bending depth helps to bring more material into the deformation region and to increase the contact surface instead of changing the stress state. Meanwhile, the increased bending depth brought a smaller bending radius that increased the strain imbalance between the stretching in the convex side and the compression in the concave side. When this strain gap is released in the reverse-bending stage, where the tension accumulated relatively more damage as compared to bending-under-tension or bending-under-tension and compression. This can be a reason that the formability improvement achieved by increasing bending depth shows the limited effect on the sample with increased thickness.

3.8.2. The effect of compression

The compression promotes the extent of localised deformation and reduces the stress triaxiality during the tool contact stage. By utilising Tresca yield criterion, it was found that the material was easier to achieve the yielding condition with the existence of bending and compression. The FE result suggested the change of local stress state where the low stress triaxiality was empirically beneficial to formability [27]. However, as reported from previous work on TCBC and DSIF process, there was a limit for formability improvement by increased compression as excessive compression had an adverse effect [14, 20]. The local deformation around the contact point prevents the stress increase in through-thickness direction by increasing the compression force [163]. On the other hand, the undue squeezing may cause large friction force and result in tear damage to the material. The local deformation, including the contact surface deformation and friction, is not considered in the analytical model. Besides, it is hard to estimate the influence of local deformation with the changes of bending depth and compression by FE simulation without using extremely fine mesh.

Figure 3.36 shows the strain paths reminding the resemblance of material deformation in TCBC to the sheet rolling process. There is more material thinning at the same strain in longitude direction in TCBC than that in TCB process, which means the larger equivalent plastic strain is obtained in TCBC to reach the same elongation. It can be concluded that TCBC has better resistance to fracture. The possibility of material hardening and microstructure reorientations by compression cannot be ignored. The elongation achieved in TCBC is accompanied by thickness reduction. This phenomenon generally results in the grain refinement under tension combined compression conditions similar to rolling [164, 165], or equal channel angular pressing (ECAP), which is associated with bending as well [166, 167]. Meanwhile, the material softening by cyclic loading and unloading of bending or compression is also a factor worth to be considered [168, 169]. Barrett et al. [104] proposed a modified flow stress model to involve the Bauschinger effect, calibrated by compression-tension test, which improved the forming

force prediction in TCB process. The material hardening by cyclic tension and compression after TCBC process would be a significant aspect to understand the microscopic effect of compression and the formability improvement of DSIF.

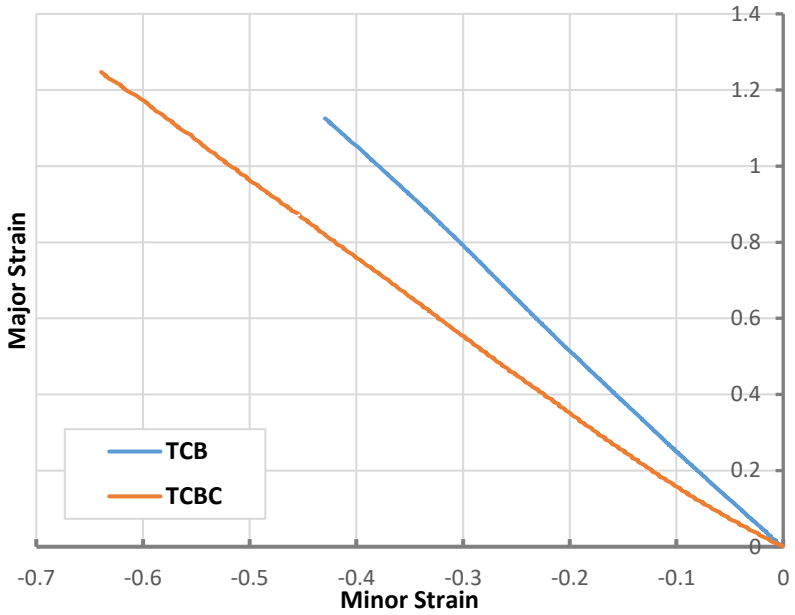


Figure 3.36 Strain paths of TCB and TCBC based on elements in section 2

3.8.3. The through-thickness effect

The bending and local deformation on the sheet surface induced by roller contact affect stress discrepancy in the through-thickness direction. From Figure 3.34b, the stress triaxiality reduction in intermediate layers was not remarkable as compared with the top layers. The strain evolution is also affected by thickness value. Despite the incomplete elastic recovery, the plastic strain should be constant in different layers through thickness as the bending sample turns back to the straight strip. After localised bending, the strain difference would be flattened by reverse-bending. However, the material deformed in the pre-contact stage undergoes nearly pure tension which tends to accumulate more damage. Thus, if the material is equally and fully deformed before the reverse-bending (or post-contact) stage, the damage accumulation will be reduced accordingly. Figure 3.37 presented the von Mises stress distribution in TCB and TCBC at two moments of thickness reduction of 20% and 50%. An overall trend of homogenised stress distribution through

thickness was observed with the reduction of thickness. Therefore, the effect of compression is enhanced when the thickness is reduced. It may explain the thickness sensitivity to compression as well.

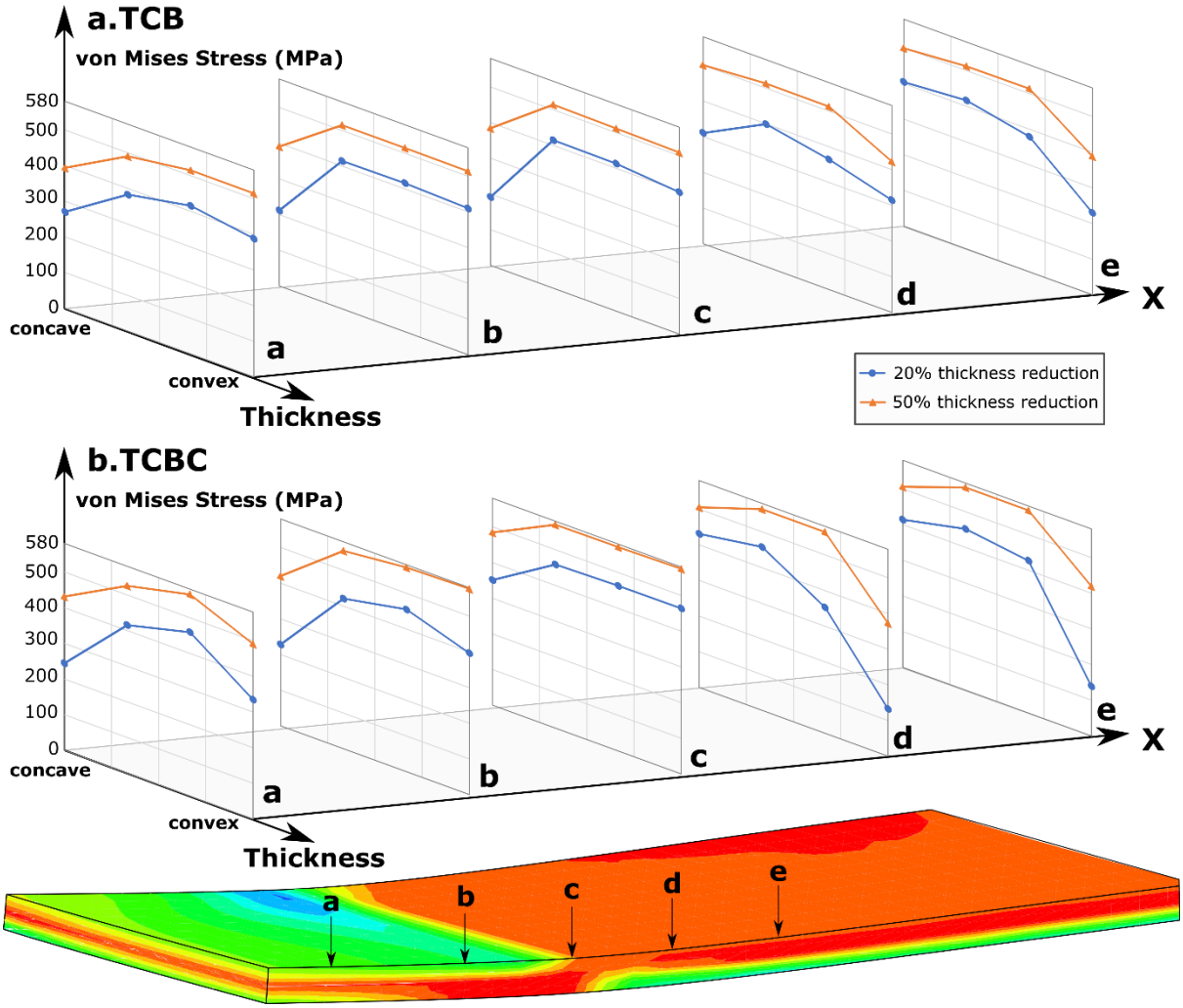


Figure 3.37 Von Mises stress distribution through thickness under 20% and 50% thickness reduction cases in (a) TCB and (b) TCBC

3.8.4. Limitations of the new modified shear GTN model

The GTN model with the new modified shear mechanism has successfully predicted the elongation-to-fracture with an error of 4.1% in the case of TCB and 8.5% in the case of TCBC. The differences of damage evolution in the thickness direction were revealed with a notice to the reverse bending process to the fracture initiation position. The advantage of this model is the implementation of fracture locus in the plane of stress

triaxiality and Lode angle parameter. This new modified shear mechanism establishes a clear correlation between the estimation of damage and the experimental determination of material formability under different stress conditions. The constructed function (Equation 3.63) presenting the 3D fracture strain loci provides an intuitive way to calibrate the material dependence to stress triaxiality and Lode parameter accordingly. The modified shear mechanism helps to simulate the damage response under complex stress histories, and at the same time, import source of error as the practical tests cannot keep the stress state constant and at a precise value. Otherwise, the determined fracture loci still show the influence of stress history to void growth and nucleation, which may be released in the damage integral process.

There are two aspects for future work to further improve the accuracy of numerical prediction. Firstly, the elastic-plastic behaviour can be refined in the constitutive model as early yielding occurs in the reverse deformation process and permanent softening starts after the transient period of repeated loading and unloading [170]. The effectiveness of the combined isotropic-kinematic hardening model has been confirmed in the TCB investigation [104]. In terms of enhancement of damage model, the void shape alteration and closure are considered to be sensitive to the Lode angle under low stress triaxiality conditions in many studies using representative volume element model [141, 144, 148, 150]. The void dimension ratio essentially determined the void evolution corresponding to the stress direction. Thus, there is a scope for improvement in void evolution law according to the stress history.

3.8.5. The link between TCB/TCBC and ISF processes

The TCB and TCBC processes show many similar characteristics to ISF processes, such as reduced forming forces (compare to deep drawing) and cyclic-localised deformation. In TCB and SPIF processes, there are many comparable factors, such as wall angle to the bending depth or feed rate combined step size to the speed of oscillated roller frame movement. There is clearly a resemblance of TCBC to DSIF as well. The strain and damage evolutions in TCB and TCBC studies highlighted the importance of bending and

reverse-bending effect causing differences in stress state in through-thickness direction. The relating parameters, such as bending radius or the additional compression tool, may affect the formability through the change of strain growths through-thickness or the modification of stress states in specific layers. Such conclusions can be linked to SPIF and DSIF cases that the stress states and tool radius effect are different from TCB and TCBC cases when transferred from 2D bending to 3D bending. As a result, the discrepancies in formability, location of fracture initiation and deformation modes between TCB/TCBC and SPIF/DSIF can be expected. However, the additional tool in DSIF process makes a similar effect with the compression roller in TCBC process, which indicates possible similarities in formability enhancement between these processes.

Thus, conclusions drawn from TCB and TCBC may be used to explain the formability improvement in SPIF and DSIF as well as other variants of ISF processes such as multi-pass SPIF as well. For instance, the additional compression in DSIF to SPIF may suppress the void growth and shear to delay the damage. However, every unit area of material in ISF may be just contacted with tools at a specific location on the tool path. This is different from the TCB test, where some area is visited throughout the whole process. Generally, reducing step size and increasing tool feed rate is beneficial to forming depth to fracture [171].

Another concern is for the final thickness distribution of ISF parts. Assume the material deformation is proportional to contact times and the contact time is determined by the desired geometry, tool radius and step size, the thickness reduction in the wall region should be perfectly homogenous if a conical shape of constant wall angle is made by the ISF process with constant step depth. This derivation agrees with the sine law but the concentration of equivalent strain is observed in many previous studies [8, 11, 23]. A possible explanation can be the number of times of material deformation is not equal on the workpiece because of the material flow, which is similar to the shift of the contacted region on TCB and TCBC samples as shown in Figure 3.31. The inhomogeneous tool contacts lead to inhomogeneous strain and thickness distribution. However, it also means

a possibility of formability improvement by using the material tracing technique [172], for the sake of more uniform distribution of the formed thickness, through toolpath optimisation such as varying step size versus predicted strain. This is similar to the concept presented as a feature-based toolpath strategy [37] that makes full use of material deformation potential.

3.9. Conclusions

In this study, 0.5 mm and 0.7 mm thickness of pure titanium grade 1 sheet had been used to tension under cyclic bending (TCB) and tension under cyclic bending and compression (TCBC) tests at different test conditions. The results showed significant formability improvement from the uniaxial tensile test to TCB and TCBC processes. An analytical model was established to evaluate the effect of process parameters, which agreed with experimental results. Using FE simulation, a new shear modified GTN damage model was developed to enable accurate prediction of the elongation-to-fracture in TCB and TCBC processes. The deformation and fracture mechanisms in TCB and TCBC are discussed based on stress and strain histories extracted from FE simulation. From these results, the following conclusions can be drawn:

1. For grade 1 pure titanium sheet, the increased bending depth equally enhances the maximum elongation for both samples of thickness in TCB and TCBC. The increased compression improved the formability as well, which is more effective in samples with smaller thickness in TCBC process.
2. In both TCB and TCBC, the deformation is highly localised due to the bending effect and propagated by cyclic tool movement, which leads to a proportional relation between local strain and the number of contacts with tools.
3. The localised bending can be divided into three stages related to the material relative position to the bending roller. The material on the convex side is stretched when local bending starts, followed by tension combined

compression during the roller contact period. The convex side is elongated in a nearly pure tension state in the reverse-bending process (post-contact stage).

4. The theoretical conclusions made by the proposed analytical model, such as the formability improvement by bending depth and compression and the negative effect of the larger thickness, are validated by the experimental results. However, the predictions of this analytical model are limited to the complexity of surface contact, and the influence of different thicknesses on elongation-to-fracture. Thus, the analytical model can only indicate the possible effect resulted by forming parameters instead of presenting a quantitative estimation of elongation-to-fracture.
5. The additional compression reduces the stress triaxiality during the tool contact stage that improves the formability. Meanwhile, the bending effect generates the strain imbalance through-thickness. This effect is more prominent when a thicker specimen is used with a larger amount of compression force applied. For example, when bending depth is 9 mm, compression force is 900 N, the elongation-to-fracture of 0.7 mm sample is smaller than that of the 0.5 mm sample.
6. The compression reduces stress triaxiality but the effect fades from sheet surface to intermediate layer. The smaller thickness helps create a homogenised stress distribution through thickness with reduced strain variations. Thus, the compression is more effective for thinner sheet samples.
7. The new modified shear mechanism utilised the fracture loci in space of stress triaxiality and Lode angle parameter. A function is established to describe the fracture surface. From the result presented, the modified GTN model successfully predicts the fracture in TCB and TCBC processes with reasonable accuracy.

8. The fracture starts from the concave side, the surface in contact with the bending roller, because of the reverse-bending process accumulated more damage, as suggested by the FE model.

CHAPTER 4 MACHINE TOOL STIFFNESS AND ITS IMPACT ON DSIF PROCESS

4.1. Introduction

The loss of contact in Double-Side Incremental Forming (DSIF) leads to detrimental effect to process formability and hence highlights a need for accurate estimation to practical tool positions and its effect on the formability. In the conventional DSIF process using either robotic systems or a dedicated DSIF machine, the tool positions are fully defined by the tool path. When the formed geometry diverges from the desired shape due to material thinning and machine deflection, the loss of contact happens and degenerates the DSIF process to Single Point Incremental Forming (SPIF). The force-based compensation strategy, using active support tool to compensate for the deflections by closed-loop control [16], algorithm [90] or use of a pneumatic cylinder [14], is studied as compared to the positional compensation in toolpath strategy [18, 42, 54, 173]. However, using the force-based approach for the support tool [14], there is a risk of the support tool acting as a forming tool which causes unexpected local deformation of the workpiece. For example, Figure 4.1 showed the observation by Lu et al. [14] in which the relative tool shifting produced different geometries and reduced achievable forming depth (Figure 4.1b) in using a pneumatically supported DSIF process. This “over-forming” case, opposite to the case of loss of contact, can also affect the geometric accuracy and reduce formability. Thus the machine tool errors during forming process need to be considered in toolpath planning and result analysis.

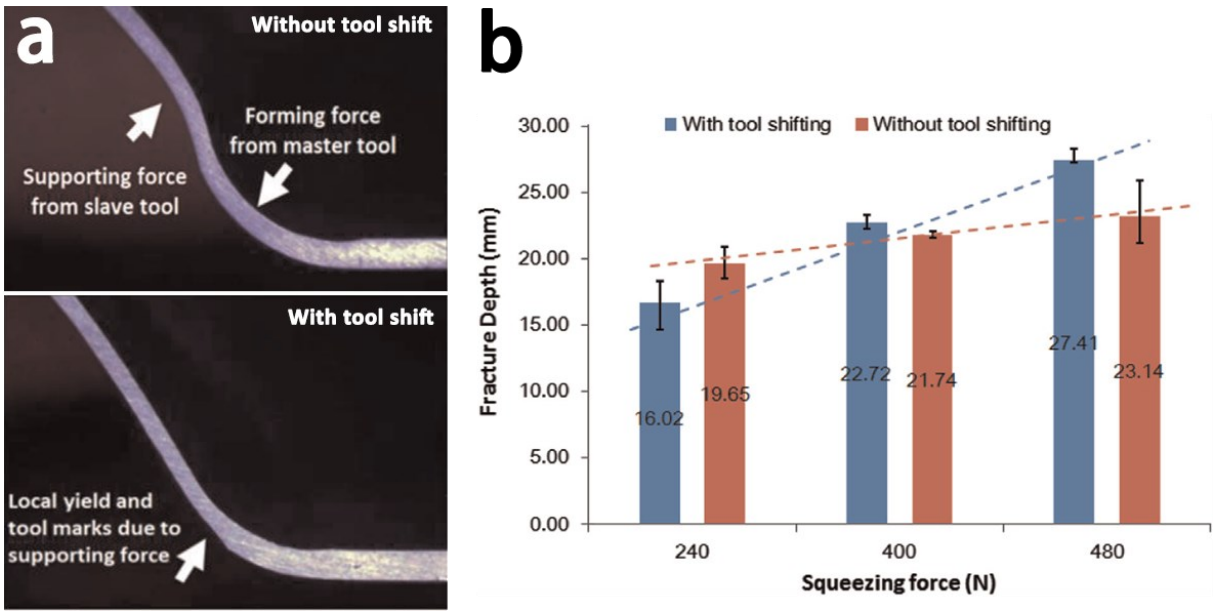


Figure 4.1 Influence of slave tool shifting in DSIF processes (a) geometries, and (b) formability in space of fracture depth and compressive force [14].

The machine stiffness or compliance in FE simulations of current DSIF studies is not often considered as a toolpath of the rigid tool is implemented in most studies reported. The discrepancies between the formed profiles of numerical and experimental results were commonly observed [19]. Moser et al. [9] developed a FE model using a spring and damping element system to simulate the machine stiffness and improved the accuracy of forming forces and geometry predictions. Besides, the force interaction between the rigid tool and deformable parts represents a more kinetic nature than a kinematic condition of the contact behaviour in practical forming conditions, especially when the machine stiffness is not enough. Combining with insufficient understanding to material constitutive behaviour under continuous bending and unbending processes [99, 104], this leads to considerable differences between the predicted and experimental measured results of forming accuracy [19].

This chapter presents a general approach that can be used to quantify machine stiffness in an analytical model to implement the machine stiffness in FE simulations of the DSIF process. In the following sections, the general approach of machine compliance is firstly introduced using a simplified beam model and coordinate transformation matrix

for machine stiffness quantification. Secondly, the possible effect of the tool deflections in pneumatically supported DSIF is discussed, which helps reveal a phenomenon of over-forming without the loss of contact based on experimental observation. This is followed by a case study of applying the machine stiffness estimation method on a DSIF machine, to improve the prediction to the component geometry in FE simulation as compared to the measured profiles obtained by DISF processing. Detailed discussions for improvement help to draw several conclusions.

4.2. A general approach of machine stiffness quantification

Although the importance of machine and tool stiffness for forming accuracy has been recognised, there is a lack of sufficient attention to quantifying the stiffness of a bespoke ISF machine tool or a robotic system. Most bespoke ISF machines have similar structural configurations to Cartesian CNC machines [30, 174]. The component deformation and joint errors are non-negligible for many bespoke ISF machines as they are often constructed by fabrication instead of a single piece of structure by casting as commonly used in conventional milling machines shown in Figure 4.2. This means the commonly used error modelling methods for multi-axis machine tools are applicable to most ISF machines. Therefore, a Homogeneous Transformation Matrix (HTM) based approach may be used to describe the system's positioning errors generated by volumetric deformation of components, across axis transformation and determination of the end-effector position. Finally, a simplified FE model is established to calibrate the parameters of the machine stiffness matrix in a case study of a dedicated DSIF machine.

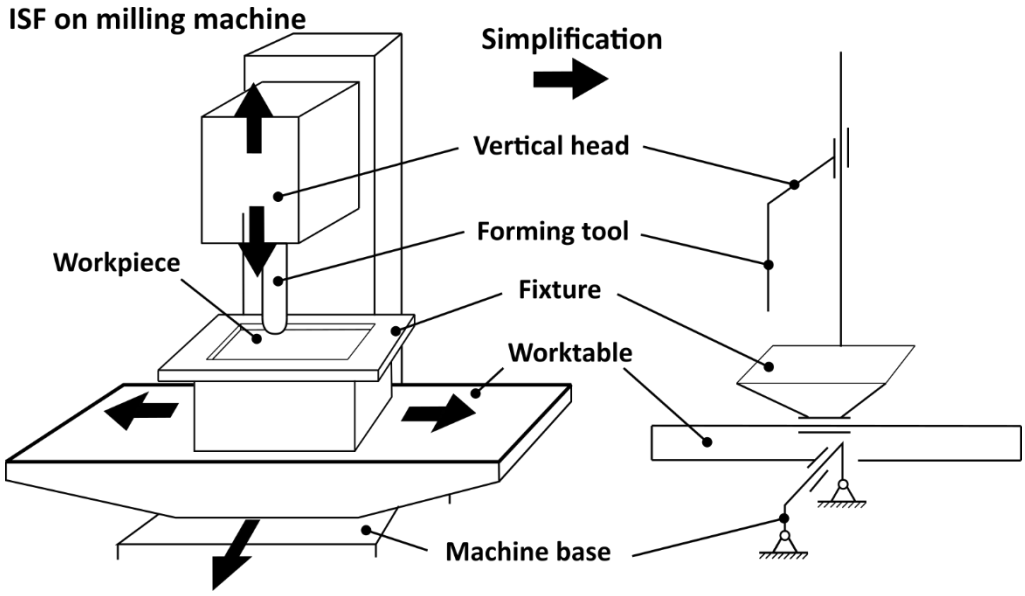


Figure 4.2 Schematic of three orthogonal axes milling machine structure and simplification in incremental sheet forming.

4.2.1. Transformation matrix of coordinates

HTM is commonly used in robotic and CNC systems as a method to derive and represent the aggregate component deformation in a multi-degree of freedom system [175]. Compared with the conventional stiffness method, the effect of components and tool movement on overall machine stiffness is involved. A coordinate transformation matrix $[C_T]$ is constructed by the rotation matrix $[A]$ and relative positions $[p]$ between the coordinate systems of adjacent machine components. In the Cartesian space, $[C_T]$ of order 4x4 can be presented as two parts:

$$[C_T] = \begin{bmatrix} \boldsymbol{A} & \boldsymbol{p} \\ 0 & 1 \end{bmatrix} = \begin{bmatrix} a_{11} & a_{12} & a_{13} & \vdots & a_{14} \\ a_{21} & a_{22} & a_{23} & \vdots & a_{24} \\ a_{31} & a_{32} & a_{33} & \vdots & a_{34} \\ \cdots & \cdots & \cdots & \vdots & \cdots \\ 0 & 0 & 0 & \vdots & 1 \end{bmatrix} \tag{4.1}$$

The relative rotation and position of neighbouring coordinate systems are represented through rotation matrix $[A]$ and position vector $[p]$, respectively. For example, Figure 4.3 illustrated a simplified machine component or tool as a cantilever beam. Two coordinate systems S_{i-1}, S_i are established, whose origins are the connection joints at both ends of the beam. The rotation matrix $[A]$ represents the angular deflection $[\Delta\theta] =$

$[\theta_X \quad \theta_Y \quad \theta_Z]^T$ in deformation and can be calculated as follows:

$$[A] = \begin{bmatrix} a_{11} & a_{12} & a_{13} \\ a_{21} & a_{22} & a_{23} \\ a_{31} & a_{32} & a_{33} \end{bmatrix} = [A_z][A_Y][A_X]$$

$$= \begin{bmatrix} cos\theta_Z & -sin\theta_Z & 0 \\ sin\theta_Z & cos\theta_Z & 0 \\ 0 & 0 & 1 \end{bmatrix} \begin{bmatrix} cos\theta_Y & 0 & sin\theta_Y \\ 0 & 1 & 0 \\ -sin\theta_Y & 0 & cos\theta_Y \end{bmatrix} \begin{bmatrix} 1 & 0 & 0 \\ 0 & cos\theta_X & -sin\theta_X \\ 0 & sin\theta_X & cos\theta_X \end{bmatrix}$$

$$= \begin{bmatrix} C\theta_Z C\theta_Y & -S\theta_Z C\theta_X + S\theta_X C\theta_Z S\theta_Y & S\theta_Z S\theta_X + C\theta_Z S\theta_Y C\theta_X \\ S\theta_Z C\theta_Y & C\theta_Z C\theta_X + S\theta_Z S\theta_Y S\theta_X & -C\theta_Z S\theta_X + S\theta_Z S\theta_Y C\theta_X \\ -S\theta_Y & C\theta_Y S\theta_X & C\theta_Y C\theta_X \end{bmatrix} \tag{4.2}$$

where $C\theta_j$ and $S\theta_j$ are the abbreviations of $cos\theta_j$ and $sin\theta_j$ $(j = X, Y, Z)$, respectively. In most conditions, the angular deflection is close to 0 that allows the approximation $\theta_j \to 0, sin\theta_j \to \theta_j, cos\theta_j \to 1$. Therefore, the simplification of $[A]$ is:

$$[A] = \begin{bmatrix} 1 & -\theta_Z & \theta_Y \\ \theta_Z & 1 & -\theta_X \\ -\theta_Y & \theta_X & 1 \end{bmatrix} \tag{4.3}$$

The positional vector $[p]$ indicates the relative position between the connected frames, which is the coordinate of origin O of the new system S_i in previous space S_{i-1}. This contains the length of components, the active movement of relative components, and the linear deflection $[\Delta\delta] = [\delta_X \quad \delta_Y \quad \delta_Z]^T$. In the example shown in Figure 4.3, the positional vector $[p]$ can be written as a sum of beam length vector $[L]$ and the linear deformation $[\Delta\delta]$:

$$[p] = (-1) \cdot [L] + (-1) \cdot [\Delta\delta] = \begin{bmatrix} 0 \\ 0 \\ -L \end{bmatrix} + \begin{bmatrix} -\delta_x \\ -\delta_y \\ -\delta_z \end{bmatrix} = \begin{bmatrix} -\delta_x \\ -\delta_y \\ -L - \delta_z \end{bmatrix} \tag{4.4}$$

Thus, the location presented by coordinate $\boldsymbol{r_i} = [x_i, y_i, z_i]^{\boldsymbol{T}}$ in coordinate system S_i can be displaced to S_{i-1} through the constructed transformation matrix $[C_T]$:

$$\begin{bmatrix} \boldsymbol{r_{i-1}} \\ 1 \end{bmatrix} = [C_T] \cdot \begin{bmatrix} \boldsymbol{r_i} \\ 1 \end{bmatrix} = \begin{bmatrix} 1 & -\theta_Z & \theta_Y & -\delta_x \\ \theta_Z & 1 & -\theta_X & -\delta_y \\ -\theta_Y & \theta_X & 1 & -L - \delta_z \\ 0 & 0 & 0 & 1 \end{bmatrix} \cdot \begin{bmatrix} x_i \\ y_i \\ z_i \\ 1 \end{bmatrix} \tag{4.5}$$

If there is a vector in coordinate form, it can be represented as:

$$\vec{\boldsymbol{v}} = [x \quad y \quad z \quad 0]^T \tag{4.6}$$

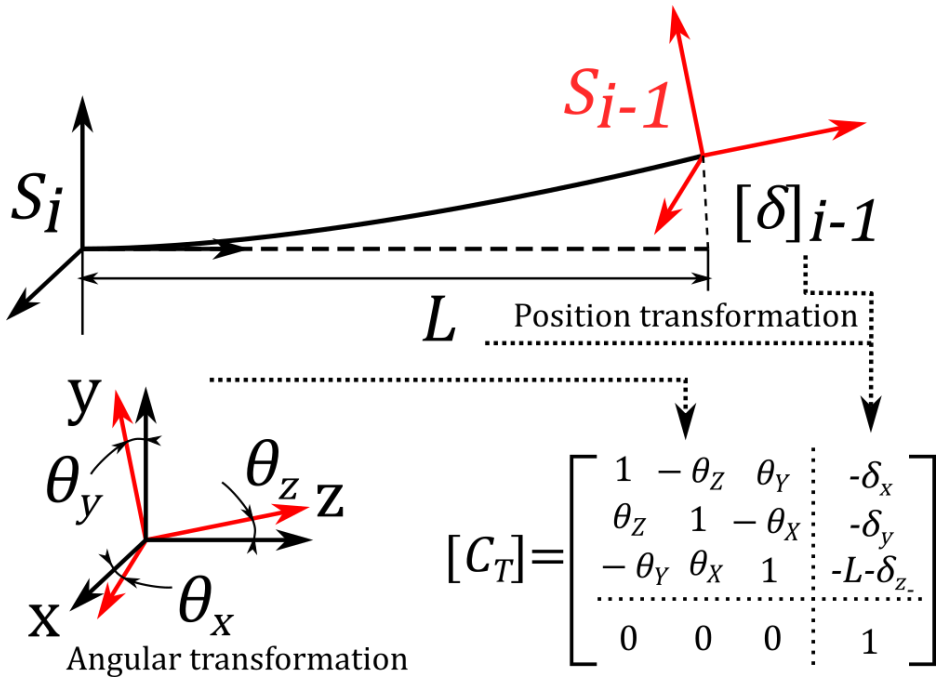


Figure 4.3 An example of the coordinate system transformation matrix

We define following the connection chain that the global coordinate system S_0 is on the base of machine and S_i is on the end-effector. Thus, the actual position of the tool centre $\boldsymbol{r_0}$ after the aggregated component deformations can be obtained through the chains of coordinate transformation matrices $[C_T]$ between components to the global space S_0:

$$\begin{bmatrix} \boldsymbol{r_0} \\ 1 \end{bmatrix} = \prod_{i=0}^{i} [C_T]_i \cdot \begin{bmatrix} \boldsymbol{r}_i \\ 1 \end{bmatrix} \tag{4.7}$$

In the global space S_0, the coordinate of the tool centre $\boldsymbol{r_0}$ is equal to the sum of the coordinate in S_0 at zero point and the displacement of the tool $\boldsymbol{r_i}$, when the machine compliance is not considered. The coordinate in S_0 at zero point is the distance from the initial tool position to the origin of S_0 which can be determined by the machine structure and lengths of components $[L_0] = [L_x \quad L_y \quad L_z]^T$. This relationship between $\boldsymbol{r_i}$ and $\boldsymbol{r_0}$ may be stated including overall deflections $\Delta^i\delta_0$ from S_i to S_0:

$$\boldsymbol{r_0} = [L_0] + \boldsymbol{r_i} + \Delta^i\delta_0 \tag{4.8}$$

Thus, the overall machine deflection $\Delta^i\delta_0$ can be obtained by comparing the reference coordinate $\boldsymbol{r_i}$ in tool space S_i and the actual coordinate $\boldsymbol{r_0}$ in the global frame, minus the differences by machine structure $[L_0]$ and tool movement $[x \quad y \quad z]^T$:

$$\Delta^i\delta_0 = \boldsymbol{r_0} - [L_0] - \boldsymbol{r_i} \tag{4.9}$$

4.2.2. Transformation matrix of forces and moments

The linear and angular deflection $\begin{bmatrix}\Delta\delta\\ \Delta\theta\end{bmatrix}$ in coordinate system S_i of an independent component is calculated by local force and moment $\begin{bmatrix}f_i\\ m_i\end{bmatrix}$ and estimated component flexibility matrix $[F_i]$, which is the inverse of the stiffness matrix $[K_i]$:

$$\begin{bmatrix}\Delta\delta_i\\ \Delta\theta_i\end{bmatrix} = [K_i]^{-1}\begin{bmatrix}f_i\\ m_i\end{bmatrix} = [F_i]\begin{bmatrix}f_i\\ m_i\end{bmatrix} \tag{4.10}$$

Figure 4.4 shows the transfer of force and moment components through a simplified machine component. The force and moment transformation matrix $[{}^{i-1}T_i]$ is established to transfer the forming force and moment $\begin{bmatrix}f_{i-1}\\ m_{i-1}\end{bmatrix}$ acting at one connection joint, the origin of the coordinate system S_{i-1}, to the other joint, which is the origin of the coordinate system S_i. Similar to the HTM used for the coordinate transformation, the force and moment transformation matrix $[{}^{i-1}T_i]$ can be written according to the relative position matrix $\left[{}^{i-1}P_i\right]$ between force acting positions, and the rotational matrix $\left[{}^{i-1}A_i\right]$ as presented in Equation (4.7). The force and moment transformation from the coordinate system S_{i-1} to S_i can be described as:

$$[f_i] = \left[{}^{i-1}A_i\right] \cdot [f_{i-1}]$$

$$[m_i] = \left[{}^{i-1}A_i\right] \cdot [m_{i-1}] + \left[{}^{i-1}P_i\right] \cdot [f_{i-1}]$$

$$\left[{}^{i-1}P_i\right] = \begin{bmatrix} 0 & \left(L + \delta_z^i\right) & -\delta_y^i \\ -\left(L + \delta_z^i\right) & 0 & \delta_x^i \\ \delta_y^i & -\delta_x^i & 0 \end{bmatrix} \tag{4.11}$$

Integrating these equations in the form of matrix, the force and moment transformation matrix $\left[{}^{i-1}T_i\right]$ can be written:

$$\left[{}^{i-1}T_i\right] = \begin{bmatrix} {}^{i-1}A_i & \mathbf{0} \\ {}^{i-1}P_i & {}^{i-1}A_i \end{bmatrix}$$

Therefore, the force and moment in the coordinate system S_i transferred from S_{i-1} can be calculated.

$$\begin{bmatrix} f_i \\ m_i \end{bmatrix} = \left[{}^{i-1}T_i\right] \cdot \begin{bmatrix} f_{i-1} \\ m_{i-1} \end{bmatrix} = \begin{bmatrix} {}^{i-1}A_i & \mathbf{0} \\ {}^{i-1}P_i & {}^{i-1}A_i \end{bmatrix} \cdot \begin{bmatrix} f_{i-1} \\ m_{i-1} \end{bmatrix} \tag{4.12}$$

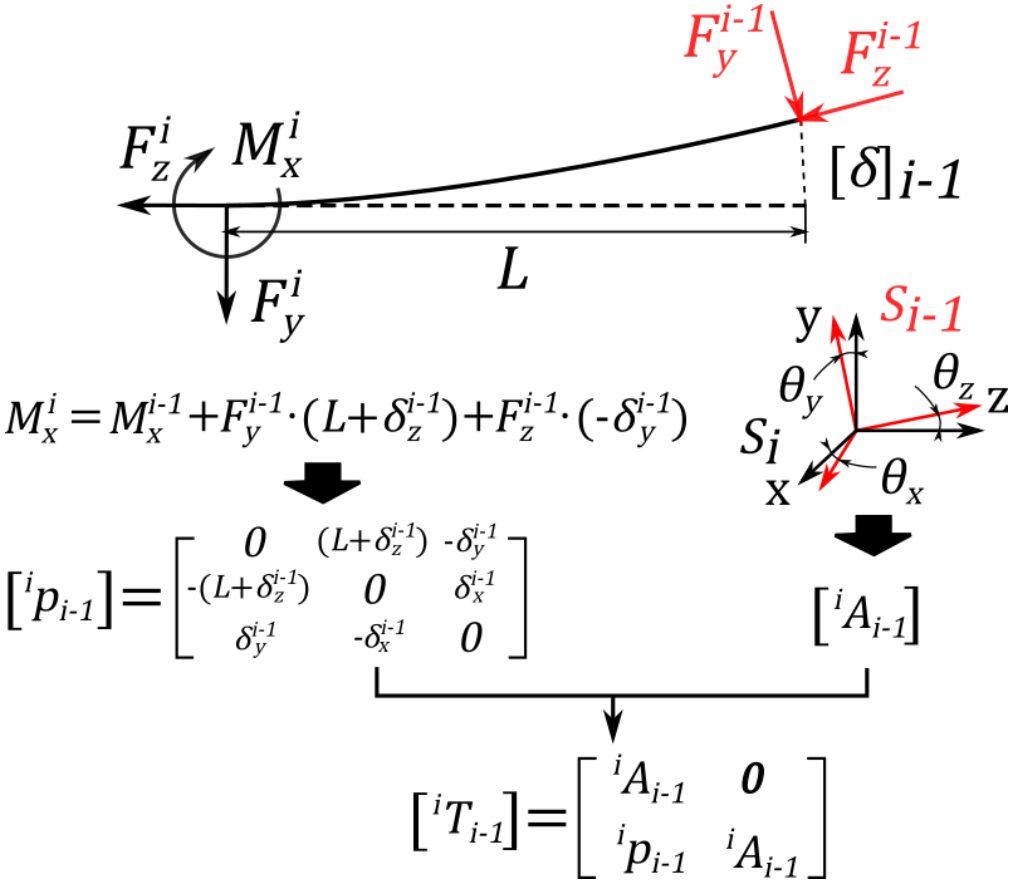


Figure 4.4 An example of force and moment transformation matrix

4.2.3. Simplified beam models of ISF machine stiffness

Because of the machine complexity, the exact deflection due to forming forces for each axis is difficult to precisely quantify. Therefore, it is reasonable to assume that the connection between components of an ISF machine system is sufficiently rigid with only linear and angular clearances to be considered. However, it is possible to use a generic

beam model to describe its major deformation and transformation. According to the constructions of the ISF machines considered, parts and sub-assemblies can be categorised into a cantilever beam type as shown in Figure 4.5, or a simply supported beam model as shown in Figure 4.6. In the case of the cantilever beam type machine component, for example, with the ISF tool placed in the z axis as shown in Figures 4.3 and 4.5, the stiffness matrix of tool K_{Tool} can be calculated as:

$$K_{Tool} = \begin{bmatrix} K_{Tool}^{xx} & 0 & 0 & 0 & K_{Tool}^{y'x} & 0 \\ 0 & K_{Tool}^{yy} & 0 & K_{Tool}^{x'y} & 0 & 0 \\ 0 & 0 & K_{Tool}^{zz} & 0 & 0 & 0 \\ 0 & K_{Tool}^{yx'} & 0 & K_{Tool}^{x'x'} & 0 & 0 \\ K_{Tool}^{xy'} & 0 & 0 & 0 & K_{Tool}^{y'y'} & 0 \\ 0 & 0 & 0 & 0 & 0 & K_{Tool}^{z'z'} \end{bmatrix} \tag{4.13}$$

where the stiffness components in the stiffness matrix may be given as

$$K_{Tool}^{xx} = K_{Tool}^{yy} = \frac{3EI}{L^3}$$

$$K_{Tool}^{x'y} = K_{Tool}^{y'x} = K_{Tool}^{xy'} = K_{Tool}^{yx'} = -\frac{2EI}{L^2}$$

$$K_{Tool}^{zz} = \frac{E \cdot A}{L}$$

$$K_{Tool}^{x'x'} = K_{Tool}^{y'y'} = -\frac{EI}{L}$$

$$K_{Tool}^{z'z'} = GI$$

where E and G are the Young's modulus and shear modulus, respectively, I is the second moment of inertia, L is the length of cantilever beam and A is the cross-section area.

In a general beam model, the values of E, G, A and I are not only an inherent property of the material but also are influenced by the part or machine structure. The components of stiffness matrix can be calibrated through modulus E, G and the second moment of inertia I. The tool movement and machine structure determine the position of

the connection joints and affect the effective length of components, L . Thus this simplified beam model reflects the stiffness changes with the current tool position and gives an accurate representation to machine and tool deflections in the practical situation.

The calibration process can be conducted by measuring the force-deflection response at multiple locations of tool travelling in the workspace. Alternatively, a simplified FE model based on the structure of a dedicated DSIF machine is established to complete the calibration process.

If the beam direction is in y-axis or x-axis, a transformation matrix $[R]$ can be multiplied to transform the location of stiffness components.

$$[K_{Tool}^{new}] = [R] \cdot \left[K_{Tool}^{beam\ in\ z}\right] \cdot [R] \tag{4.14}$$

If the beam is in x-axis:

$$[R] = \begin{bmatrix} 0 & 0 & 1 & 0 & 0 & 0 \\ 0 & 1 & 0 & 0 & 0 & 0 \\ 1 & 0 & 0 & 0 & 0 & 0 \\ 0 & 0 & 0 & 0 & 0 & 1 \\ 0 & 0 & 0 & 0 & 1 & 0 \\ 0 & 0 & 0 & 1 & 0 & 0 \end{bmatrix} \tag{4.15}$$

If the beam is in y-axis:

$$[R] = \begin{bmatrix} 1 & 0 & 0 & 0 & 0 & 0 \\ 0 & 0 & 1 & 0 & 0 & 0 \\ 0 & 1 & 0 & 0 & 0 & 0 \\ 0 & 0 & 0 & 1 & 0 & 0 \\ 0 & 0 & 0 & 0 & 0 & 1 \\ 0 & 0 & 0 & 0 & 1 & 0 \end{bmatrix} \tag{4.16}$$

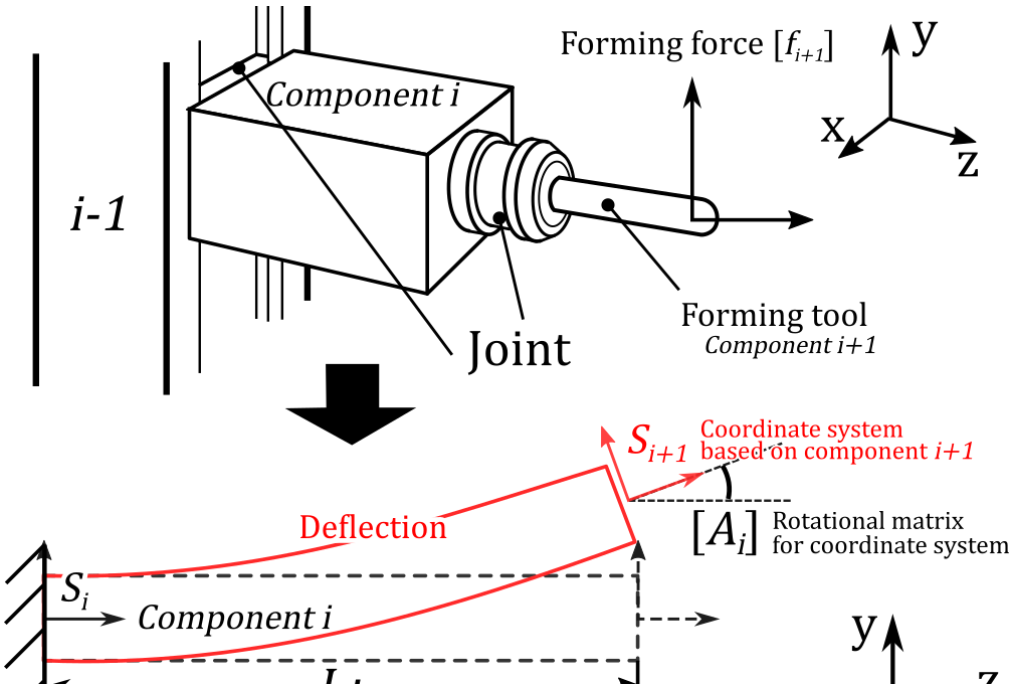


Figure 4.5 Cantilever beam model for simplified one-end connection component.

If the ISF machine is based on a gantry construction and the ISF tool is at the middle of a simply supported beam as shown in Figures 4.6 and 4.7, the stiffness of this gantry structure can be calculated as a function of the current force bearing position on the beam:

$$K_{Gantry} = \begin{bmatrix} K_{Gantry}^{xx} & 0 & 0 & 0 & K_{Gantry}^{y'x} & 0 \\ 0 & K_{Gantry}^{yy} & 0 & K_{Gantry}^{x'y} & 0 & 0 \\ 0 & 0 & K_{Gantry}^{zz} & 0 & 0 & 0 \\ 0 & K_{Gantry}^{yx'} & 0 & K_{Gantry}^{x'x'} & 0 & 0 \\ K_{Gantry}^{xy'} & 0 & 0 & 0 & K_{Gantry}^{y'y'} & 0 \\ 0 & 0 & 0 & 0 & 0 & K_{Gantry}^{z'z'} \end{bmatrix} \tag{4.17}$$

The stiffness components in Equation (4.17) may be given in the following:

$$K_{Gantry}^{xx} = K_{Gantry}^{yy} = \frac{3EI \cdot L}{x^2 \cdot (L^2 - x^2)}$$

$$K_{Gantry}^{x'y} = K_{Gantry}^{y'x} = -\frac{3EI \cdot L}{x(L^2 - 3xL + 2x^2)}$$

$$K_{Gantry}^{xy'} = K_{Gantry}^{yx'} = \frac{3EI}{2x \cdot (L - x)}$$

$$K_{Gantry}^{zz} = \frac{E \cdot A}{L}$$

$$K_{Gantry}^{x'x'} = K_{Gantry}^{y'y'} = -\frac{3EI \cdot L}{L^{2} - 3xL + 3x^{2}}$$

$$K_{Gantry}^{z'z'} = GI$$

where x denotes the position of the applied load in the middle of the supported cantilever beam. Similar to the case of the cantilever beam type of the ISF machine construction, $L, I, E, G\ and\ A$ are the length, second moment of inertia, Young's modulus, shear modulus, the cross-section area of the forming tool, respectively.

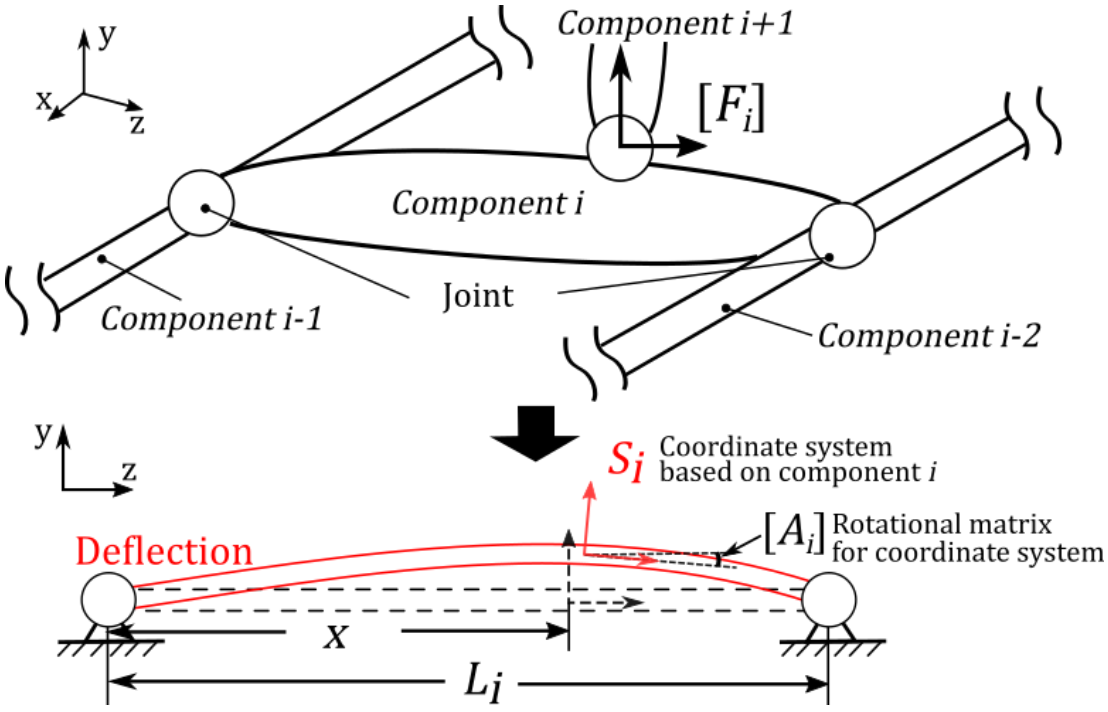


Figure 4.6 Simplified gantry-type beam model.

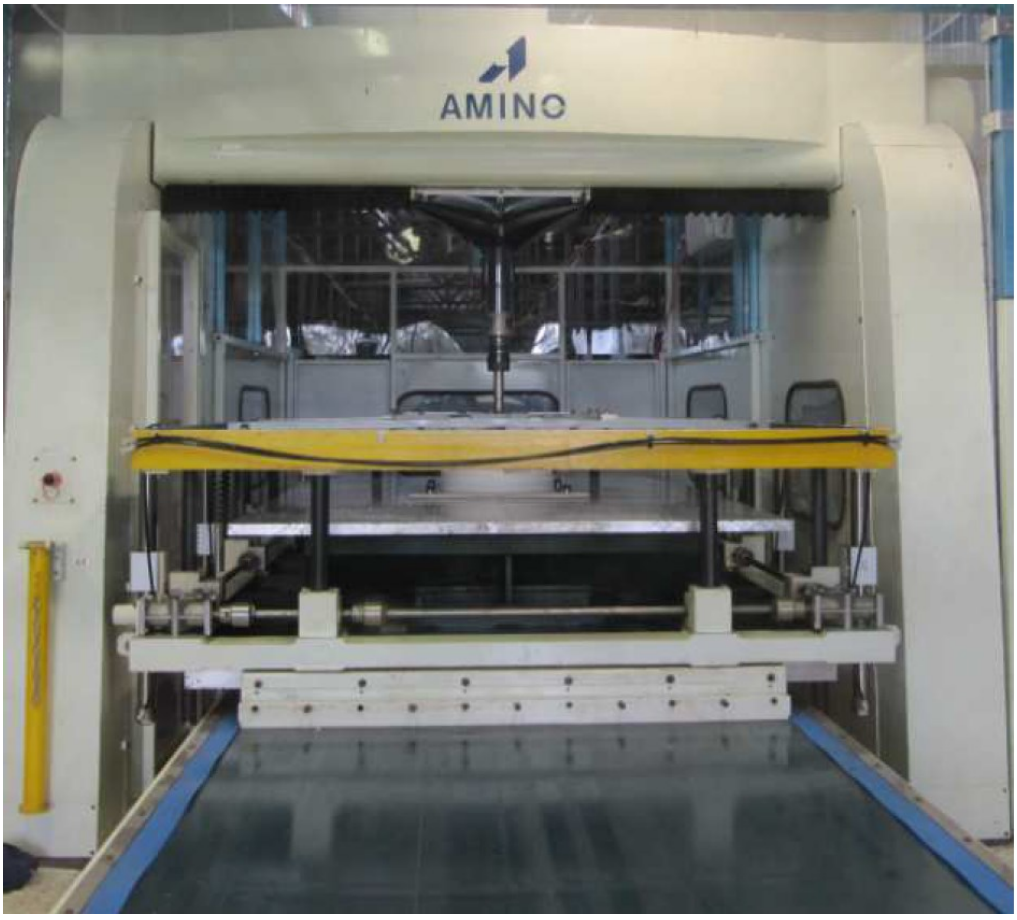


Figure 4.7 Gantry-type incremental sheet forming machine (AMINO DLNC-PC ISF machine, 2014 [176])

4.2.4. Quantification of the overall deflection of an ISF machine system

Figure 4.8 presents the flow chart for the calculation of the overall deflection of an ISF machine system. Firstly, the local coordinate systems $S_0, \dots, S_i$ are established following the chain of connection joints, from the machine base table to the forming tool, based on each independent machine component. By ignoring the effect of deflections on each independent component stiffness, the stiffness matrix $[K_i]$ are established according to effective beam lengths $[L_i]$ and the current tool coordinates $\boldsymbol{r}_i$, which captures the stiffness variations of the ISF machine as a function of forming tool travelling. Then the flexibility matrix of the ISF machine $[F_i]$ is obtained by the inverse of the stiffness matrix $[K_i]$ and it is used to calculate the deflection $\begin{bmatrix}\Delta\delta_i \\ \Delta\theta_i\end{bmatrix}$ in the local coordinate system S_i (Equation (4.10)). The deflection $\begin{bmatrix}\Delta\delta_i \\ \Delta\theta_i\end{bmatrix}$ is implemented to form the rotation matrix $[A_i]$

and positional vector $[p_i]$ and matrix $[P_i]$. Finally, the coordinate transformation matrix $[C_i]$ and the force transformation matrix $[T_i]$ are formed using Equations (4.5) and (4.9). The forces and moments $\begin{bmatrix} f_i \\ m_i \end{bmatrix}$ in local coordinate system S_i can be transferred to the adjacent component in S_{i-1} until the reference frame of machine base S_0. Finally, the overall deflections of the ISF $\Delta^i\delta_0$ can be calculated by using Equation (4.9).

The reason of the deflection being considered in the force transformation matrix $[T_i]$ rather than stiffness matrix $[K_i]$ is that the deflections have significant effect on force and moment transfer rather than the stiffness of component. Compared to the overall size of most components, the changes of component structure and position by machine deflection is negligible. However, the large axial force during forming process generates considerable moments even though the error in the radial direction is small. The neglect of parts deformation will result in significant inaccuracy in the chain of transmitting forces and moments. In contrast to conventional direct stiffness estimation method, the transformation matrices considered the effect of tool movement as well as the accumulative effect of deflections through the whole machine frames. This stiffness estimation method also has the potential to be used in different machine structures.

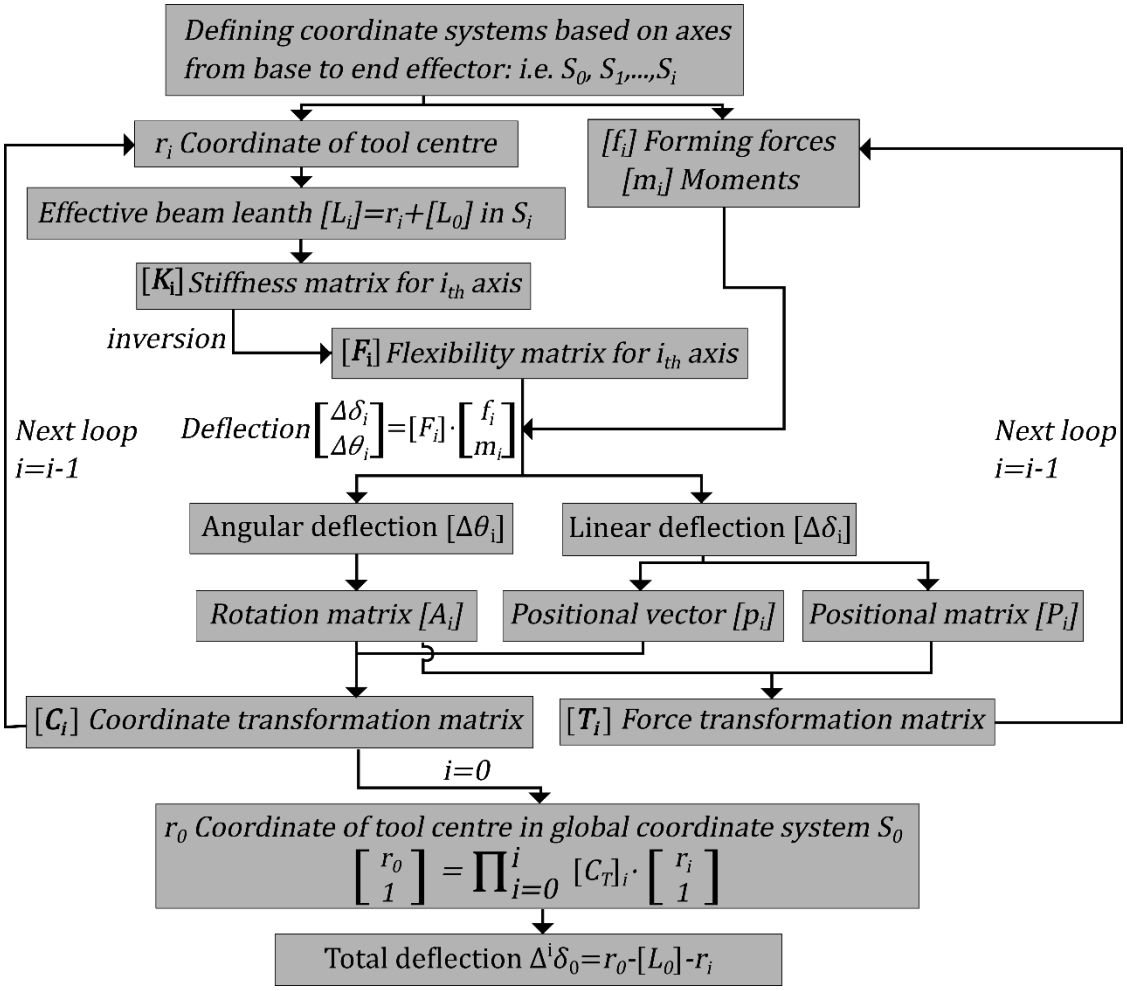


Figure 4.8 Flow chart to establish a machine structure-based deflection prediction model.

4.3. Theoretical analysis of the effect of machine deflection in DSIF

The enhancement of formability in the DSIF process is generally considered to be a direct result of the stabilisation effect brought by the additional support. However, there are limited investigations about the negative effect due to the disposition of the support tool. In the pneumatic-assisted DSIF process, the excessive bending, also referred to as the "over-bending" phenomenon, could happen due to the forming error including the clearances and deflection of machine and tools. In this study, the deflection of the support tool is neglected because the supporting force in compression with the sheet material is relatively small as compared with the forming force [90]. Figure 4.9 shows the generation and evolution of the "over-bending" phenomenon. Due to sheet thinning ($\Delta\delta_s$) and tools

deformation ($[\Delta\delta_t]$), the distance between the master and support tools should increase during the forming process as the forming forces increase. Thus, the support tool moves upward and generates a bending effect (Figure 4.9b). Consequently, the support tool no longer provides the intended squeeze to the workpiece. Instead, it works as a secondary forming tool that creates another bending region. However, the relatively rigid fixture in the horizontal direction forces the support tool to continuously bend the formed region when it travels towards the cone centre along the pre-defined tool path. As a result, the "over-bending" due to the misposition of the master and support tools during the DSIF process leads to an increased vertical wall angle in the formed parts.

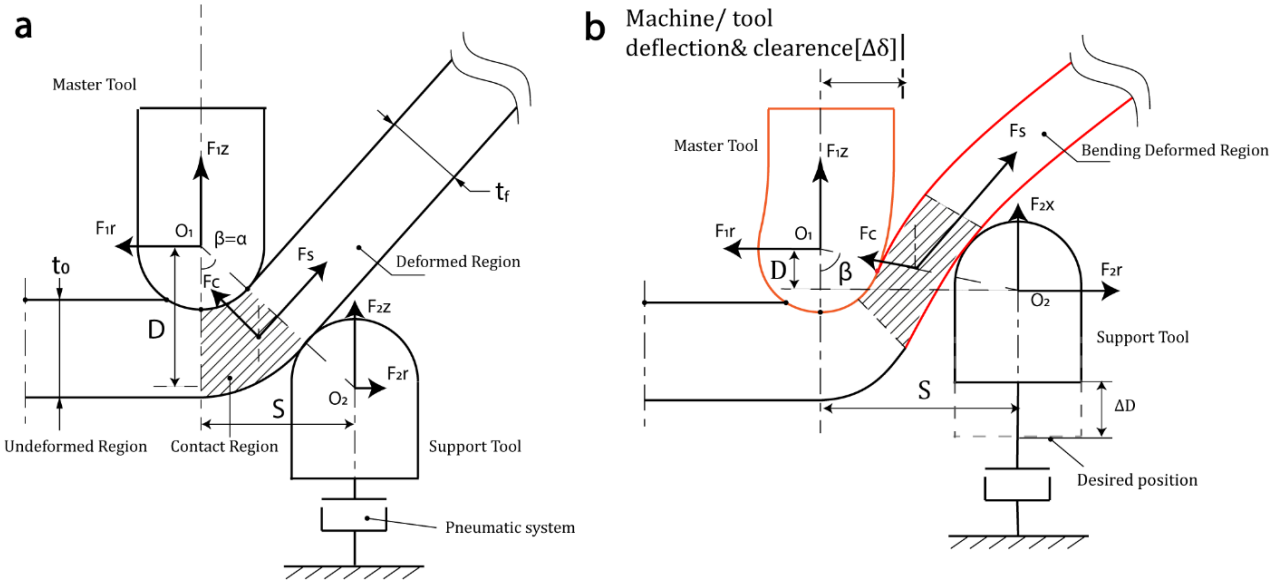


Figure 4.9 Forces and tools' relative positions in local deformation area in DSIF: (a). Ideal condition, and (b). "Over-bending"

The pneumatic supporting system provides automatic compensation for any misplacement of the master and support tools. This characteristic may also enlarge the relative position between the master and support tools. According to the sine law, the relative position of the two tools in DSIF process can be defined in the equations below:

$$t_f = t_0 \cdot cos\beta \tag{4.18}$$

$$D = (2r + t_f) \cdot cos\beta \tag{4.19}$$

$$S = (2r + t_f) \cdot sin\beta \tag{4.20}$$

$$\beta = arctan\left(\frac{S}{D}\right) \tag{4.21}$$

where t_f represents the thickness of the formed wall and r is the tool radius, β is the angle between the connecting line O_1O_2 and the vertical direction, D and S are the distances between the master and support tools in the vertical and horizontal directions, respectively. The force F_{2z} applied by the support tool and the reaction force due to compression F_c as given in Equation (4.22):

$$F_c = F_{2z} \cdot cos\beta \tag{4.22}$$

In an ideal condition, β is equal to the pre-defined wall angle α and O_1O_2 is normal to the sheet surface during the forming process. The support force generates a compression to the workpiece and leads to formability improvement. However, the tool distance in horizontal direction S increases and decreases in vertical direction D due to the automatic compensation for the support tool's position (Figure 4.9b). According to Equations (4.21) and (4.22), β rises and F_c reduces, which means a reduced compressive effect. In addition, the support tool causes a moment with the master tool in the local deformation area because O_1O_2 is no longer perpendicular to the sheet plane. The horizontal rigidity of the support tool generates increasing reaction force F_{2r} when tools move towards the centre of the cone shape workpiece. Therefore, the formability is decreased because of the misposition of the master and support tools and unintended bending occurs in the region between the master and support tools. It can also be inferred that the "over-bending" is more likely to happen when forming parts with the higher wall angle due to the larger deflections of the ISF machine and tools caused by the increased forming force. A steeper wall angle generates a greater effect of positional errors to the auto-compensation of the support tool, where the displacement for compensation equals

to the support tool displacement increment in the vertical direction ΔD and can be calculated by the horizontal deflection $\Delta\delta$:

$$\Delta D = D - (\Delta\delta + S)/\tan(\beta) \tag{4.23}$$

ΔD rises as β increase. The minimum value of β equals to the desired wall angle α, which indicates that the steeper the formed shape is, the easier the "over-bending" would occur during the DISF process. In conclusion, the adjustment to avoid the reduction of formability by the "over-bending" effect needs to be configured in the DSIF process using flexible support. A possible solution is to increase the machine and tool stiffness to reduce the defection ($\Delta\delta$) of the master tool. Alternatively, a compensation enabled toolpath to be generated based on the quantification of ISF machine stiffness and clearances, obtained either by FE simulation or experimental characterisation. This compensation enabled positional correction is expected to be effective to avoid the detrimental effect of the support tool on the process formability in DSIF processing.

4.4. Experimental testing

4.4.1. ISF tests for Al5052 of truncated cone shape

DSIF tests using a pneumatically actuated support tool were conducted by using a dedicated machine at Shanghai JiaoTong University. The working space was limited to a fixture size of 158 mm x 158 mm. Semi-spherical tools of R10 mm were used for both the master and support tools. The support force of 300 N was provided by a pneumatic cylinder. Aluminium 5052-O was chosen as the material for trail tests. The sheet size was 180 mm x 180 mm with a thickness of 1.0 mm. A truncated cone of 100 mm upper diameter was the designed shape to be formed. The lower diameter and forming depth were determined by the wall angle. Two sets of tests (45° wall angle for 32.5 mm depth and 60° wall angle for 35.5 mm depth) were selected. For each wall angle, there were two samples to be made separately with and without the support tool for the purpose of comparison. Helical tool paths were generated by using a MATLAB code with the step

depth of 0.5 mm and the feed speed was fixed at 800 mm/min. Rocol Rtd cutting compound was used as lubricant during the forming process.

4.4.2. ISF tests for grade 1pure Ti of hyperbolic cone shape

Two samples of grade 1 pure Ti with a hyperbolic shape were made by both the SPIF and conventional DSIF processes using the dedicated DSIF machine without pneumatic support. The sheet size was 140 mm x 140 mm, and the thickness was 0.7 mm. Due to the high strength of grade 1 pure Ti, the process parameters were modified to reduce the forming forces to comply with the capability of machine tool and force transducer. The radius of the semi-spherical tool was R5 mm. The step size was reduced to 0.25 mm. The wall angle of the chosen hyperbolic shape started from 22° and ended at 80° with a cone opening radius of 45 mm. The desired forming depth was 40 mm to achieve the maximum wall angle. The test was terminated till fracture and the reached depth was recorded to assess the material formability. The toolpaths were produced by using a MATLAB code and the feed rate was 800 mm/min. Rocol Rtd cutting compound was applied on both sides of the workpiece for lubrication. The detailed testing conditions and parameters were summarised in Table 4.1.

Table 4.1 Experimental testing parameters (PS=Pneumatical support)

No.	Material	Shape	ISF type	Diameter (mm)	Desired depth (mm)	wall angle (deg)	sheet size (mm)	sheet thickness (mm)	Tool radius (mm)	Step depth (mm)
1	Al 5052-O	Truncated cone	DSIF	100	32.5	45°	180 x 180	1	10	0.5
2			DSIF PS			45°				
3			DSIF		35.5	60°				
4			DSIF PS			60°				
5	Pure Ti G1	Hyperbolic cone	SPIF	90	40	22°-80°	140 x 140	0.7	5	0.25
6			DSIF			22°-80°				

4.5. Finite element simulation

4.5.1. FE modelling of DISF processes with and without a support tool

As the metal sheet was fully fixed, a 156 mm x 156 mm x 1 mm sheet model was

created with encastre boundary condition in the fringe area (Figure 4.10a). Both the master and support tools were defined to be rigid with 10 mm radius semi-spherical shape. A connector element was connected to the support tool, defined by non-linear elasticity to offer a constant upward force of 300 N in the vertical direction with other directions constrained. The density of the Al 5052-O material was defined to be 2.68 g/cc, while young's modulus was set at 70.3 GPa and Poisson's ratio at 0.33. The plasticity definition followed swift's strain hardening law for $\sigma = k(\varepsilon_0 + \varepsilon)^n$, where $\varepsilon_0 = 0.0416, k = 315$ and $n = 0.173$ [11]. The interaction between the tools and workpiece was created as frictionless contact to reduce the simulation time.

To verify the effect of tool displacement, FE simulations were conducted with the consideration of possible tool offset and deformation under DSIF processing conditions. A specific toolpath was defined and applied to the master tool to simulate the machine deflection (Figure 4.10). This toolpath was extracted based on the geometry of the 60° cone part made without the support force (test 3). There are two reasons for choosing the part geometry formed by the conventional DSIF process without support force as a reference of tool deflection. First, the additional bending changed the geometry of the part formed in DSIF with the support tool (Tests 2 and 4), which could no longer reflect the travelling toolpath of the master tool during the process. Then, the geometric results from the conventional DSIF without pneumatic support is representative to reflect the actual tool trajectory including the machine deflection. In this test, the machine deflection is mainly caused by the forming force to the master tool [90]. Though the conventional DSIF process includes both double-contact and single-contact periods, the additional displacement caused by the supporting force could be negligible in the simulation comparing to the major forming forces. The tool deflection is close to the DSIF process with the pneumatic support as the forming load is similar.

4-layer solid brick elements (C3D8R) with enhanced hourglassing control was used to define the workpiece (Figure 4.11). The whole model was separated into the forming and clamped region and meshed using a sweeping strategy with different mesh densities

to improve the simulation efficiency. The whole model contains 46,320 nodes and 36,764 elements. Mass scaling was also used with a minimum increment time was limited to $2 \times 10^{-5}\ s$. The simulation was conducted by using ABAQUS/Explicit. The forming process control was made by the modification of toolpaths.

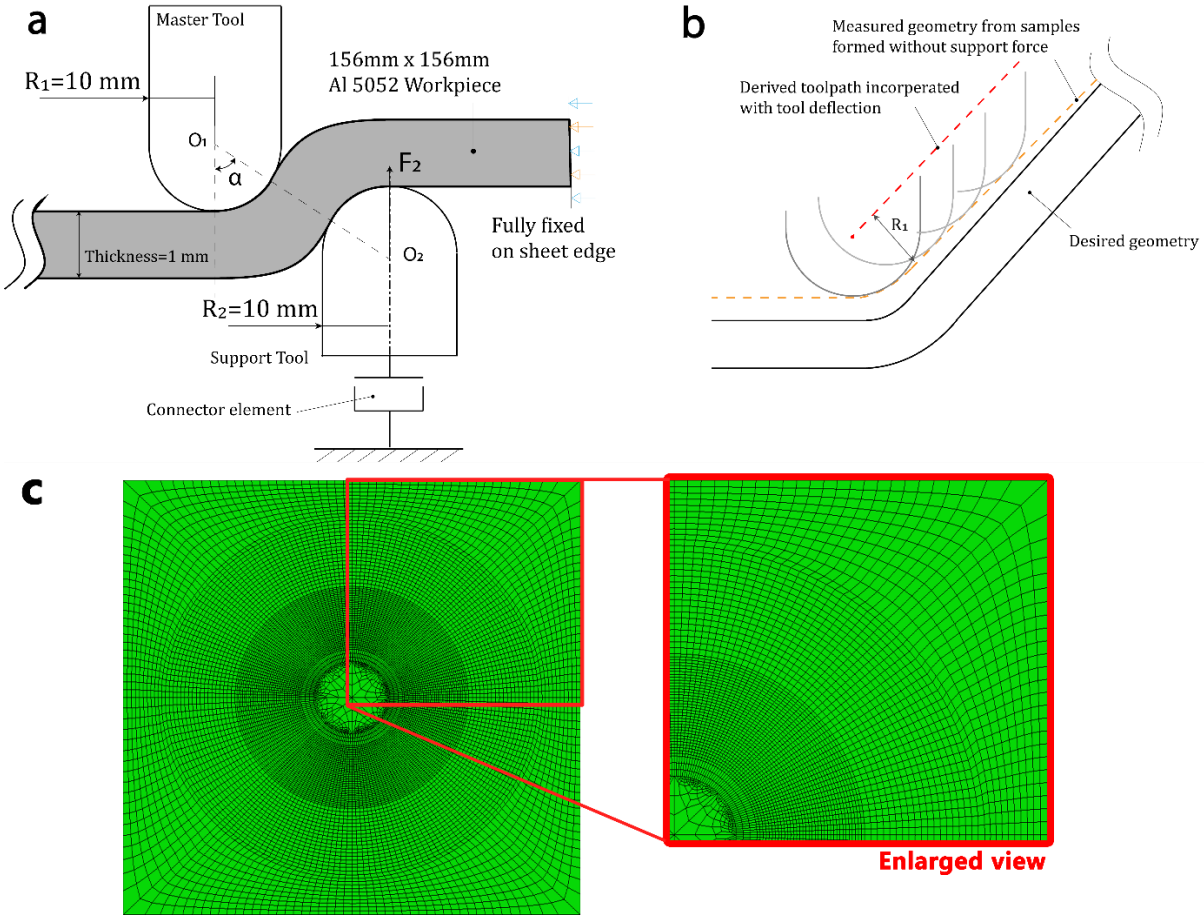


Figure 4.10 FE model schematics for DSIF processes with pneumatic support: (a) Assembly, (b) Modification of toolpath, and (c) FE mesh strategy.

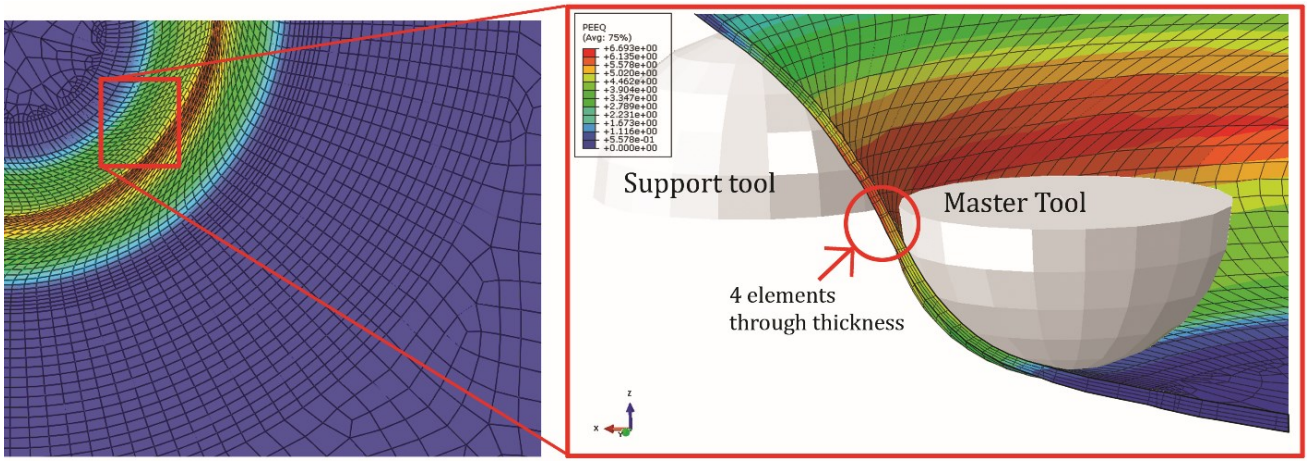


Figure 4.11 Equivalent strain distribution in FE modelling for DSIF Al5052-O sample with pneumatic support

4.5.2. Calibration of DSIF machine stiffness using FE simulation

A static finite element model was established to calibrate and validate the stiffness characteristics of the dedicated DSIF machine and the clamping frame. As illustrated in Figures 4.12 and 4.13, the machine frame, platform, and tool were modelled and connected through simplified screw nuts and lead screws. When the forming force was applied to the forming tool, the forces and moments were transmitted through the lead screw and guide rails that generated linear and rotational deflections over components. The positions of assemblies representing Y and Z axes were adjusted according to tool coordinates. The displacement of the centre of semi-spherical tool was calculated based on the relationships between the machine deflections, applied forces and current tool positions. X-axis was assumed to be rigid as the machine frame was installed on the machine base. Thus, the machine frame was fully fixed on the bottom surface.

The clamping frame of the workpiece was modelled as an entity where the load was applied at the forming tool centre. ABAQUS was used to simulate the force-displacement responses of the machine system to applied forming forces at specific tool positions.

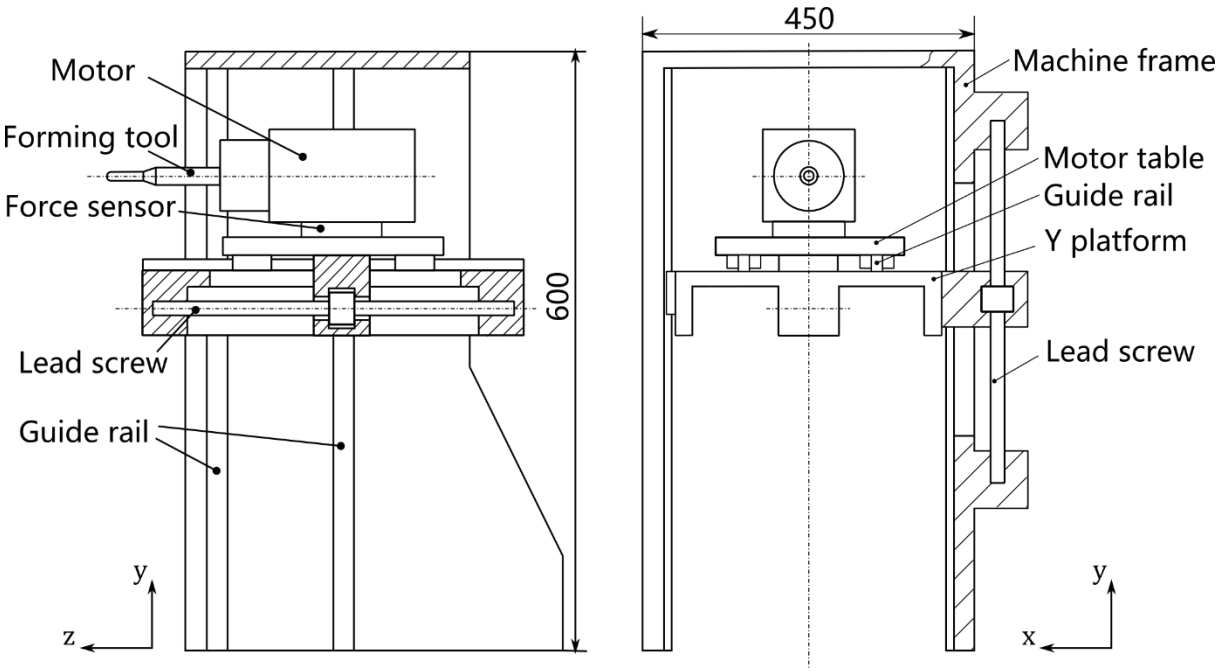


Figure 4.12 Schematic and coordinate system of DSIF machine

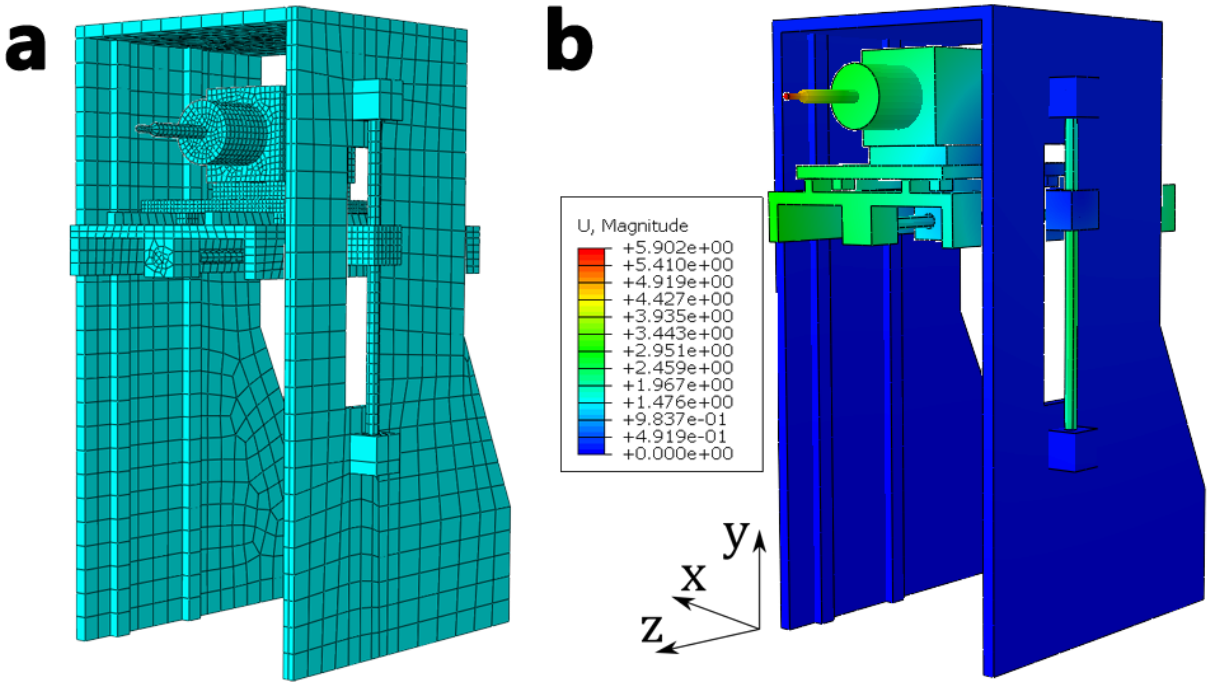


Figure 4.13 (a) FE mesh and (b) machine deflections under loading of DSIF machine.

As shown in Figure 4.14, the frame fixture was also modelled to determine the dependency of deflection to force loading position. A rigid semi-sphere tool head was placed at various positions on a rigid sheet. The steel material properties of the frame fixture are defined with a density of 8 g/cc, Young's modulus of 200 GPa and Poisson's

ratio of 0.25, respectively. As the fixture frame is set on the machine base independently, its stiffness and deflections are influential to workpiece offset during the forming process, which is not included in the transformation of DSIF machine system. Thus, the stiffness of the fixture frame was described by a fitting equation and calibrated by force-displacement curves of various tool loading positions from FE simulation.

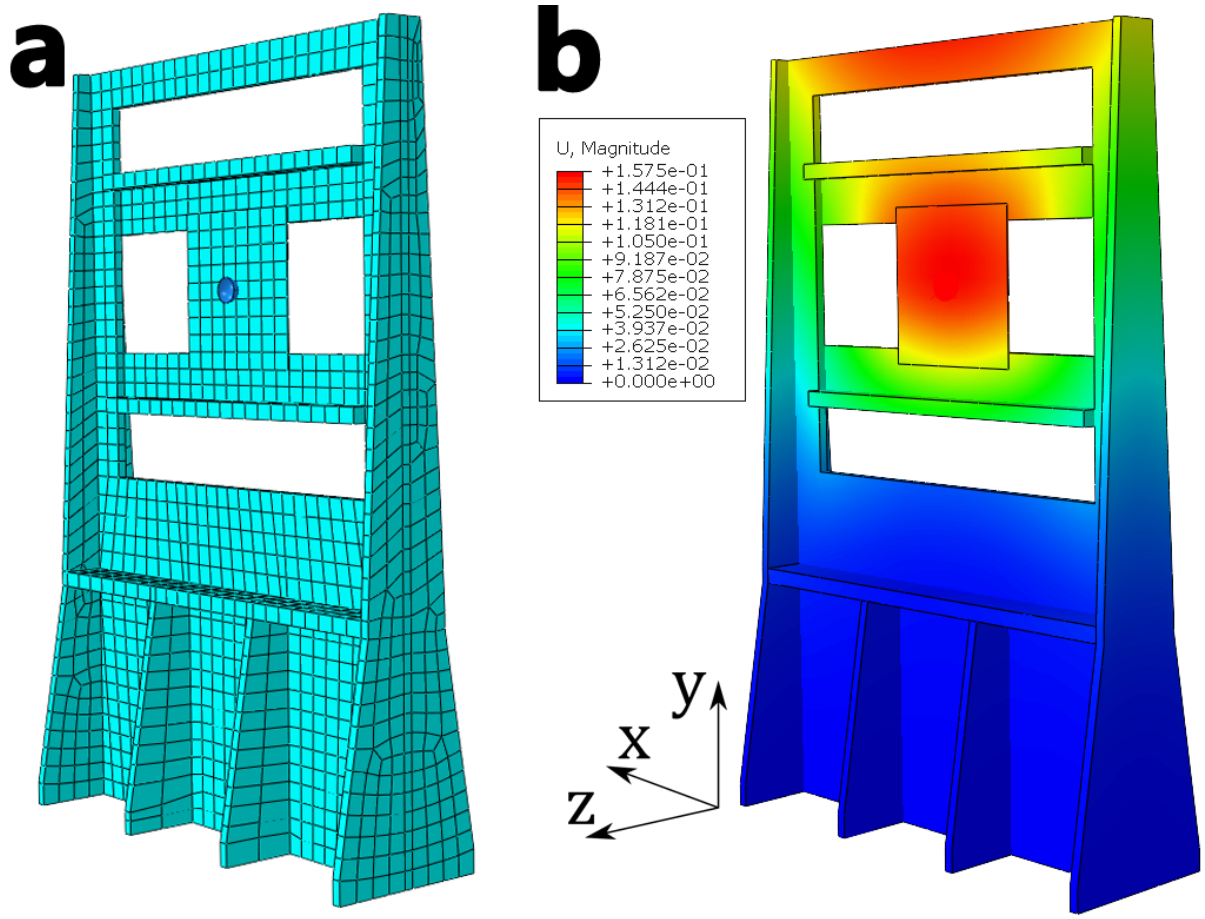


Figure 4.14 (a) FE Mesh and (b) machine deflections under loading of frame fixture.

4.5.3. FE simulation of DSIF with machine tool stiffness

Figure 4.15 shows the tool configurations and mesh of the FE model for a grade 1 pure titanium hyperbolic cone under conventional DSIF processing conditions with the inclusion of the machine stiffness. The connector elements available in ABAQUS were applied to both the master and support tools to attach the force-deflection matrix from the previous stiffness model. The sheet size was adapted to a clamping size of 120 mm x 120 mm x 0.7 mm. The sheet material was fully fixed at the flange region. The material

data for grade 1 pure titanium sheet was obtained from the uniaxial tensile test (see Chapter 3.8.1), where the density was defined to be 4,510 kg/m^3, Young's modulus was 105 GPa and Poisson's ratio at 0.33. The flow stress is obtained from uniaxial tensile testing (Figure 3.32). The contact property was defined by surface-to-surface contact with a coefficient of friction of 0.05.

The blank sheet was divided into 4 parts and applied with element sizes of 4 mm, 1.25 mm, 0.75 mm and 2.5 mm from edge to centre. 4 layers of C3D8R elements were created through the sheet thickness with a total of 30,816 elements and 38,885 nodes. The minimum incremental length was limited by a mass scaling of $3.2 \times 10^{-5} s$. The model was conducted using ABAQUS/Explicit package. The springback process was simulated in ABAQUS/Standard where the previous boundary conditions and interactions were removed with only rigid body motion at the centre of the undeformed region constrained at the springback stage.

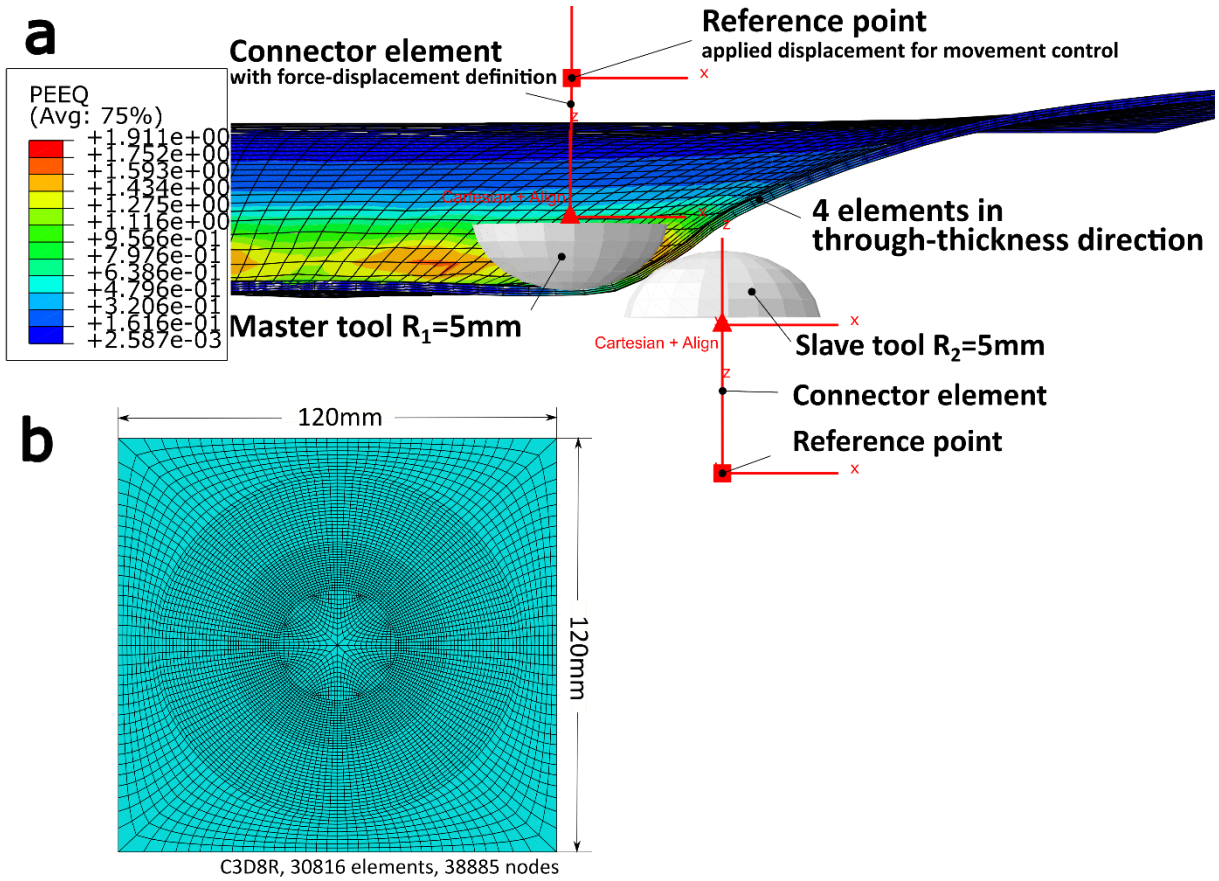


Figure 4.15 (a) Schematic of implementing stiffness matrix by connector element in DSIF simulation, and (b) Mesh strategy for DSIF simulations.

4.6. Results and discussion

4.6.1. "Over-bending" in DSIF with pneumatic support

4.6.1.1. Experimental results

Figure 4.16 shows all samples were formed by DSIF without fracture happening. The outer surface finish indicates the contact condition during DSIF processing. It can be seen that the contact ends near the upper flange of the parts were made without supporting force, which means that the support tool has lost contact with the workpiece in the early stage of the process. Figure 4.17 presents the comparison between part profiles and the designed shape. 45° cone parts are closer to the desired geometry than parts of 60° cone angle. For the part of 45° cone angle, the transfer from unformed to formed region is more apparent on the samples made with flexible support (Figure 4.17a).

However, a sudden change of curvature is noticeable in the wall area on the part of 60° wall angle, formed with supporting force, a clear indication of the "over-bending" phenomenon. The "over-bending" from DSIF is barely reported in the literature. The investigation to the causes of this phenomenon is beneficial to improve the forming accuracy of the DSIF process with flexible support.

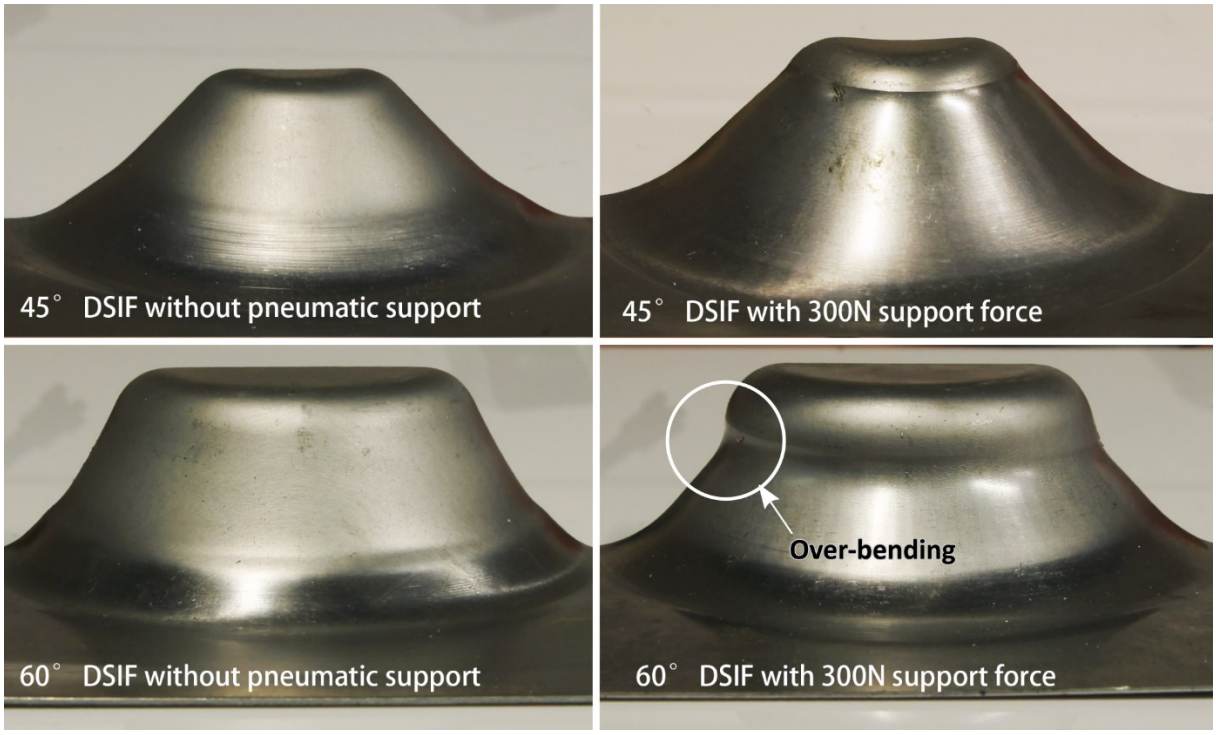


Figure 4.16 Parts formed with or without the supporting force.

The excessive thinning of the workpiece and the master tool deflection during the forming process are the main reasons for geometric errors and the loss of contact. The sheet thinning during DSIF processing leaves the space for the support tool to travel upward under the actuation force of the pneumatic system. This additional upward motion of the support tool causes the "over-bending" of the part with a steeper wall angle. The thickness distribution along radius for parts of 60° is plotted in Figure 4.17b. The "over-bending" phenomenon results in a sudden jump in thickness reduction in the formed region of a steeper wall angle. However, the peak values of the thickness in both parts are close to 0.4 mm and only 0.1 mm difference from the sine law predicted value of 0.5 mm. Such a difference is not sufficient to result in the amount of geometric error. It is

evident that the master tool deflection plays a more important role in the occurrence of the "over-bending" phenomenon.

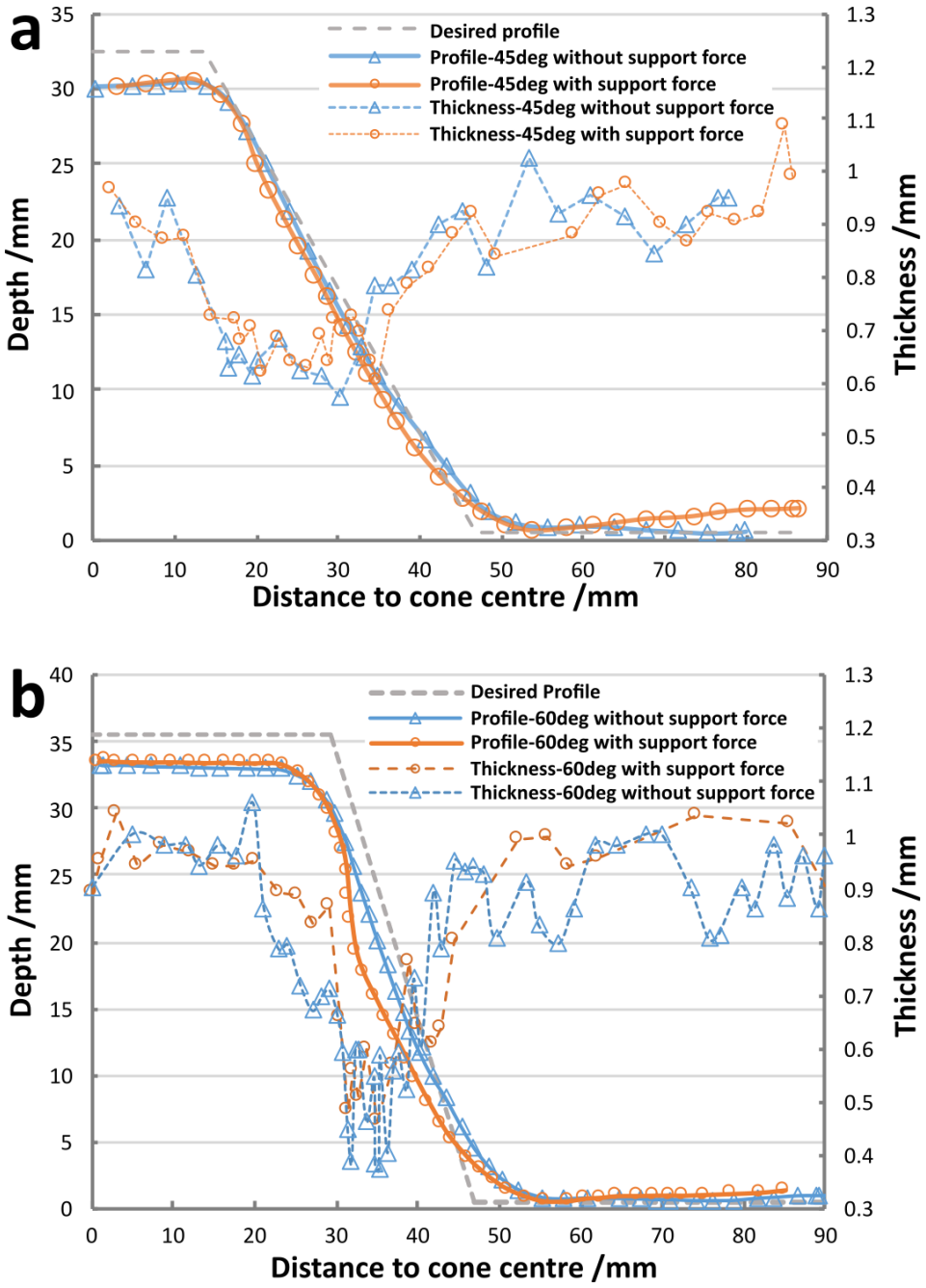


Figure 4.17 Overall geometry profiles and thickness distribution along with the radius direction (a) 45 deg cones, and (b) 60 deg cones

4.6.1.2. Replication of "Over-bending" in FE simulation for DSIF process with pneumatic support

The geometry and thickness results from the FE simulation, in which the toolpath of the master tool is modified by the anticipated machine offset measured from experimental parts, is plotted and compared with the 60° sample appearing "over-bending" phenomenon as shown in Figure 4.18. The FE and the experimental results agree well on the thickness distribution and the position of the over-bending although there are still some differences especially in the regions of the cone top and bottom. There are also some discrepancies in the thickness prediction from the FE simulations. These errors may be resulted from the reduction of system stiffness and stability due to the artificially increased feed rate, coarse mesh or the material property definition. However, this comparison can be considered as evidence of the aforementioned assumption that the "over-bending" phenomenon is caused by the deflection of the master tool. The predicted bending location also gives a hint that the completed geometry is only determined by the trajectory and the supporting force of the support tool since "over-bending" has started. This confirms that FE can be used to predict the occurrence and its location of "over-bending" when the machine deflections can be estimated and incorporated with the tool movement in FE simulation of the DSIF process.

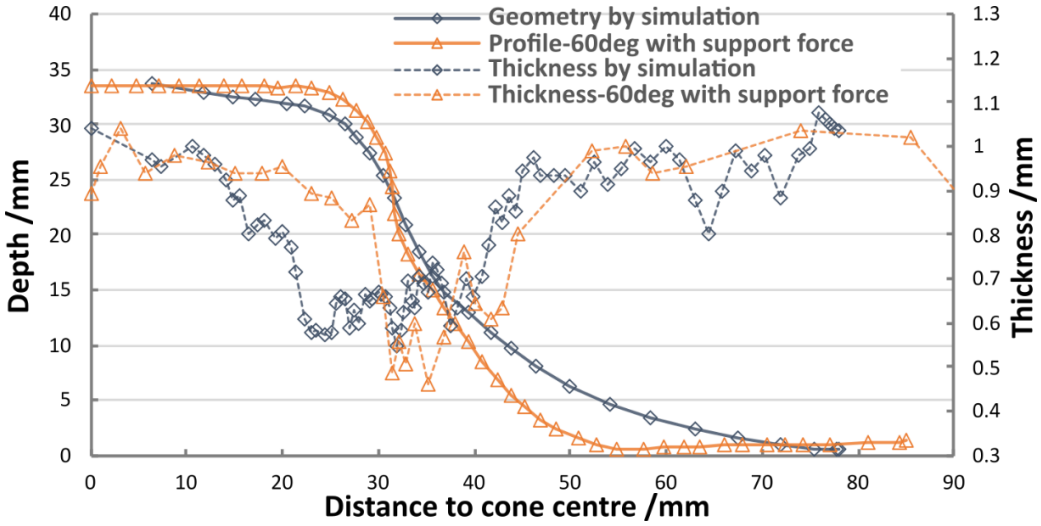


Figure 4.18 Comparison of geometry and thickness result from FEA and experiments

4.6.2. Stiffness model and implementation in ISF simulation

4.6.2.1. Case study: a DSIF machine

The experimental SPIF and DSIF processes were conducted by using a dedicated machine at Shanghai Jiao Tong University (Figure 2.5e). A stiffness model was established to estimate the machine and tool deflection following the procedure proposed in this study. Table 4.2 gives the parameters used in the derived stiffness model based on the machine structure. As shown in Figure 4.19, the machine was divided into three parts as the forming tool, Y-platform and Y-frame. The local coordinate systems were created with a principle that sets the connection joint between component i and $i-1$ as the origin of the coordinate system S_i. Y-frame shared the global reference coordinate system S_0. The orientations of the local coordinate system are aligned to S_0. The movement of x-axis is on the rails under Y-frame which is recognised as fully rigid in this case study.

Table 4.2 The dedicated DSIF machine divisions and calibrated parameters for stiffness estimation

Components	Forming tool	Y-platform	Y-frame
Coordinate system	S_2	S_1	S_0
Beam direction	z-axis	z-axis	y-axis
Effective length L (mm)	150	$300 - z$	$680 + y$
Effective Young's modulus E (MPa)	10^5	5×10^4	8×10^4
Poisson's ratio υ	0.33	0.33	0.33
Area (mm^2)	2.01×10^2	1.5×10^4	8.775×10^3
Second moment of inertia I (mm^4)	3.217×10^3	2.8125×10^7	1.2521×10^8

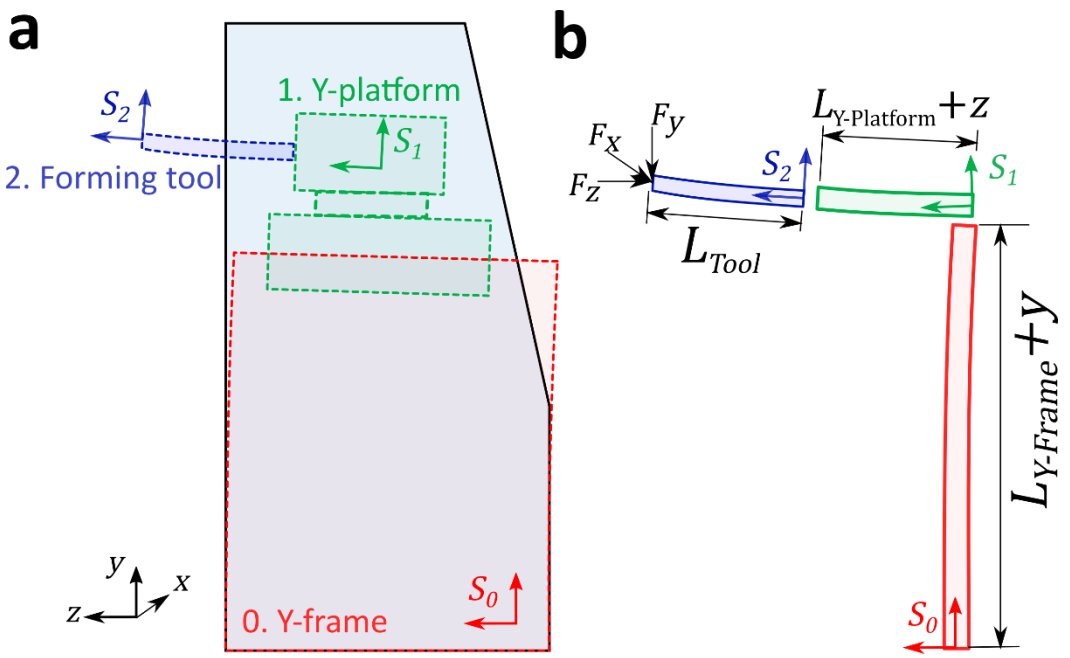


Figure 4.19 (a) Machine structure and main components division (b) simplified model for dedicated DSIF machine.

4.6.2.2. Validation of DSIF machine stiffness model in FE analysis

The force-displacement curves at different tool positions are plotted in Figure 4.20. Four coordinates were tested by changing the position of the tool-motor assembly along *y* and *z* axes to examine the machine stiffness variations versus tool movement. Overall, the derived stiffness model results using the proposed machine stiffness estimation method agree well with the DSIF machine model in FE simulation. The gradients of force-displacement curves show various stiffness dependencies to the current tool positions. The tool errors on *x* and *z* axes are not significantly affected by the current tool position with all differences below 0.02 mm under 1500 N load (Figure 4.20a, c). The stiffness in the *y* axis direction is varied by current tool position on *z* axis, where the maximum discrepancy is 0.2458 mm at 1500 N load in the workspace (Figure 4.20b). Due to the tool movement on *z* axis, the length of the lever arm is changed which induces the disparity of moment on the connection joint between the horizontal platform and vertical machine frame. As a result, the deflection on the *y* axis is amplified by the enlarged bending of the platform and frame.

The force, position and tool error data were generated by the stiffness model derived by the proposed general machine stiffness estimation method and imported in FE simulation in the next step through the connector elements from ABAQUS.

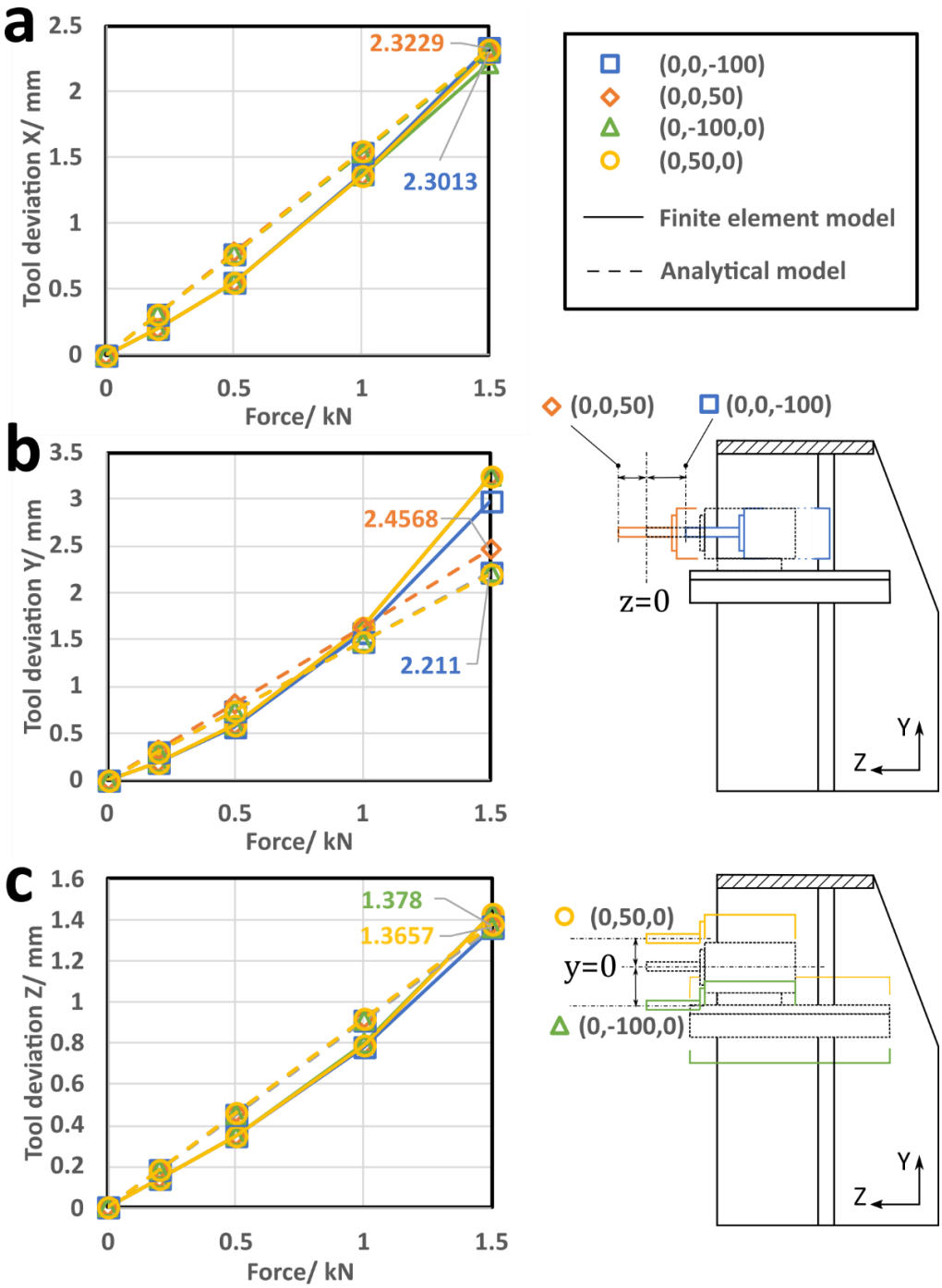


Figure 4.20 Change of tool displacements in (a) x-axis, (b) y-axis and (c) z-axis with applied load at 4 tool positions.

4.6.2.3. Calibration of the stiffness of the DSIF machine frame fixture

The displacement in z axis combined the frame fixture error was determined in Figure 4.21. The tool deviations of the frame fixture exhibit non-negligible differences with coordinates of the applied load. The fixture stiffness $K_{fixture}$ is given by a fitting equation with positional calibration factors as below:

$$K_{fixture} = K_0 + C_x|x| + C_y \cdot y \tag{4.24}$$

where $K_0 = 3536.4\ N/mm$ and $C_x = -1.56, C_y = -9.277$. This is integrated to the stiffness model attached to the ABAQUS connector elements for flexible tools validations in ISF simulations.

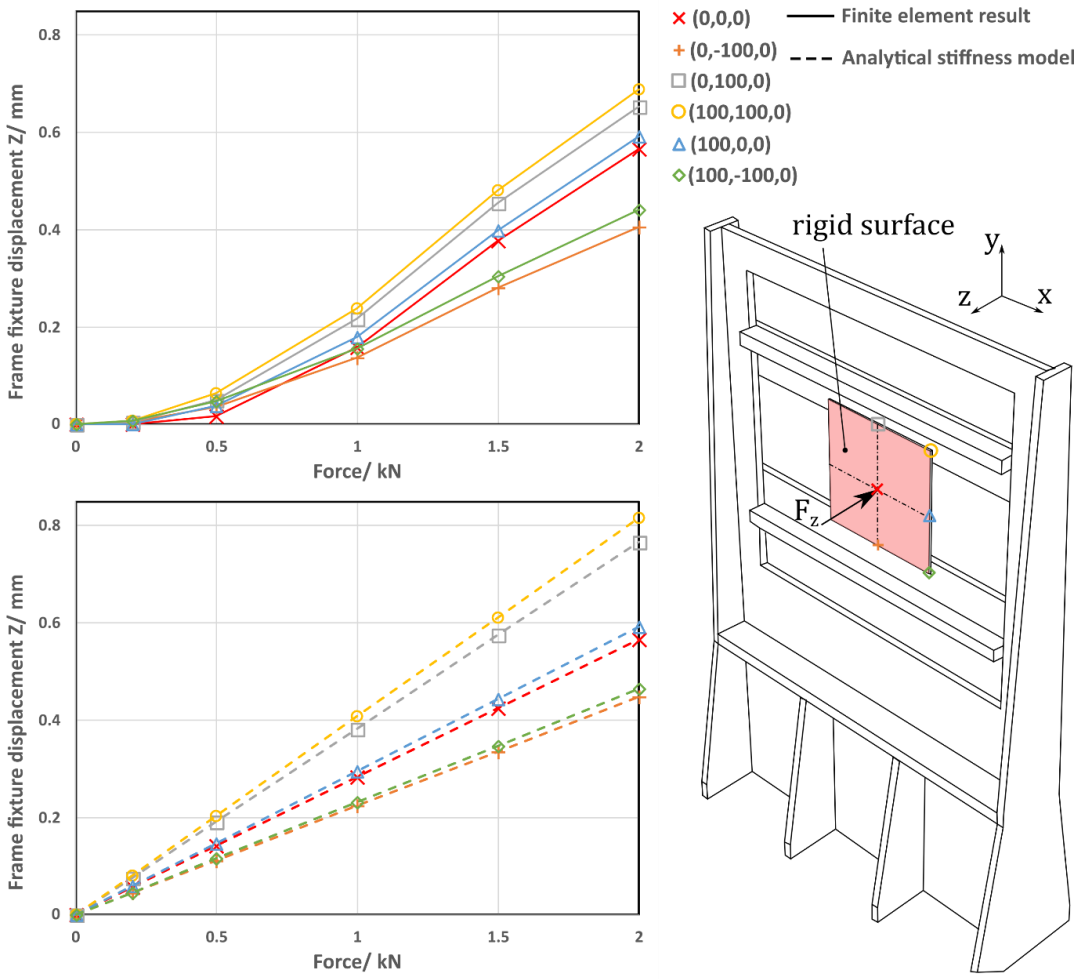


Figure 4.21 Illustrations of force-displacement curves in 6 different loading positions on frame fixture used in ISF testing.

4.6.3. Experimental results and FE stiffness validations for SPIF and DSIF processes

4.6.3.1. Experimental results

Two grade 1 pure Ti samples were formed by SPIF and DSIF till fracture as shown in Figure 4.22. It was clear that DSIF processes achieved a deeper fracture depth than SPIF.

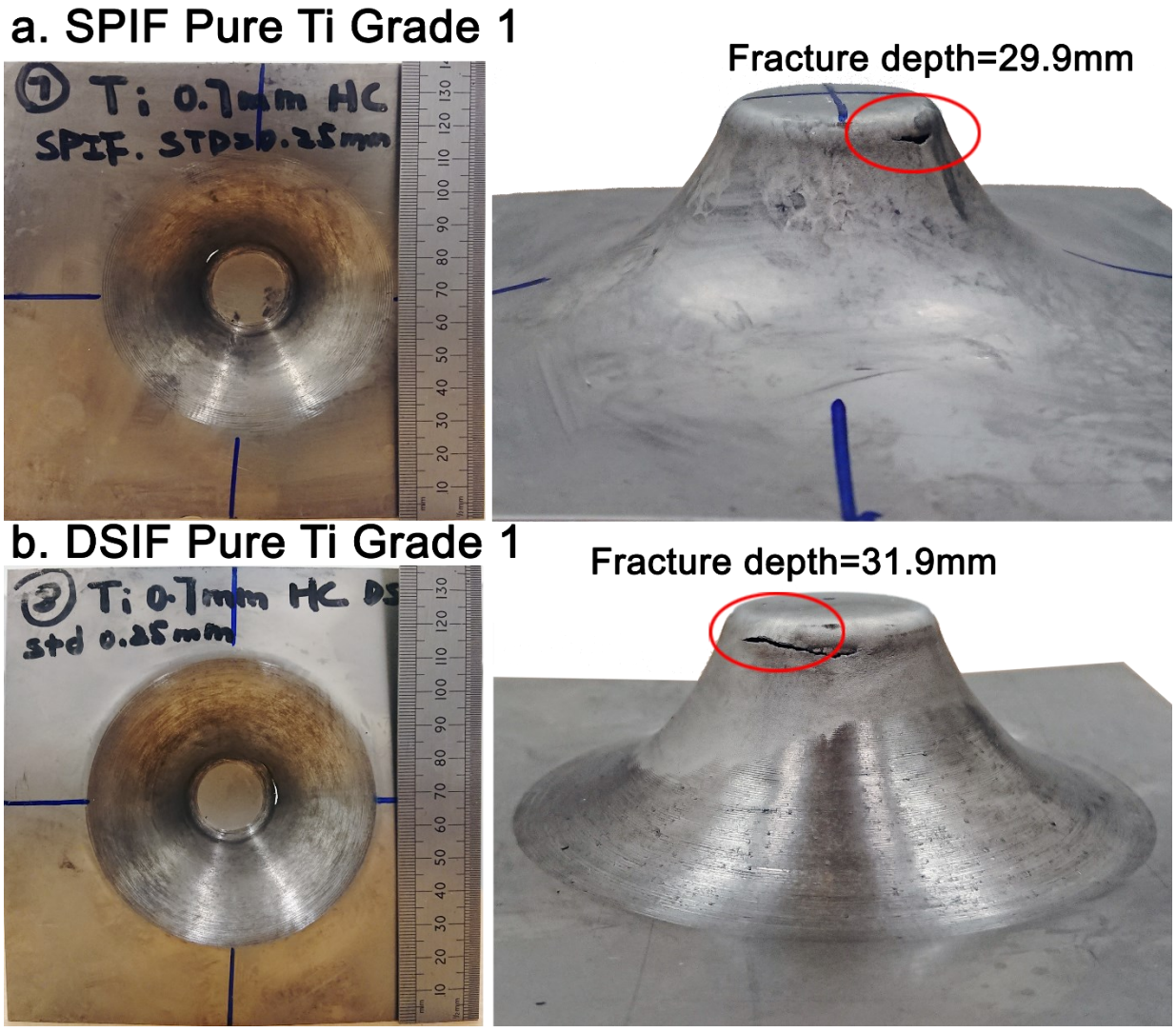


Figure 4.22 Pure Ti grade 1 samples of hyperbolic shape produced by (a)SPIF and (b)DSIF processes

4.6.3.2. Validation of the stiffness model in SPIF simulation

To demonstrate the improvement brought by the general stiffness model, the profiles from experimental testing, FE simulations with the rigid tool and stiffness-modified tool were shown in Figure 4.23a. Figure 4.23b shows that the gap between experimental measurement and FE prediction is significantly reduced that the geometry

deviation between experimental and FE results was reduced from 1.65 mm to less than 1 mm in the wall region after the machine tool stiffness was included in FE simulation. This also indicated the simplified beam model was sufficient to give a reasonable force-deflection representation to quantify the effect of tool positions under SPIF processing conditions.

Figure 4.24 illustrates the equivalent strain contour plots in the simulations using conventional rigid tool definition and tool with machine stiffness model. It can be observed that the changes of tool stiffness to strain distribution results are negligible in SPIF simulation. However, there are two peaks of equivalent strain concentration in the model with applied machine stiffness matrix due to element distortion during simulation.

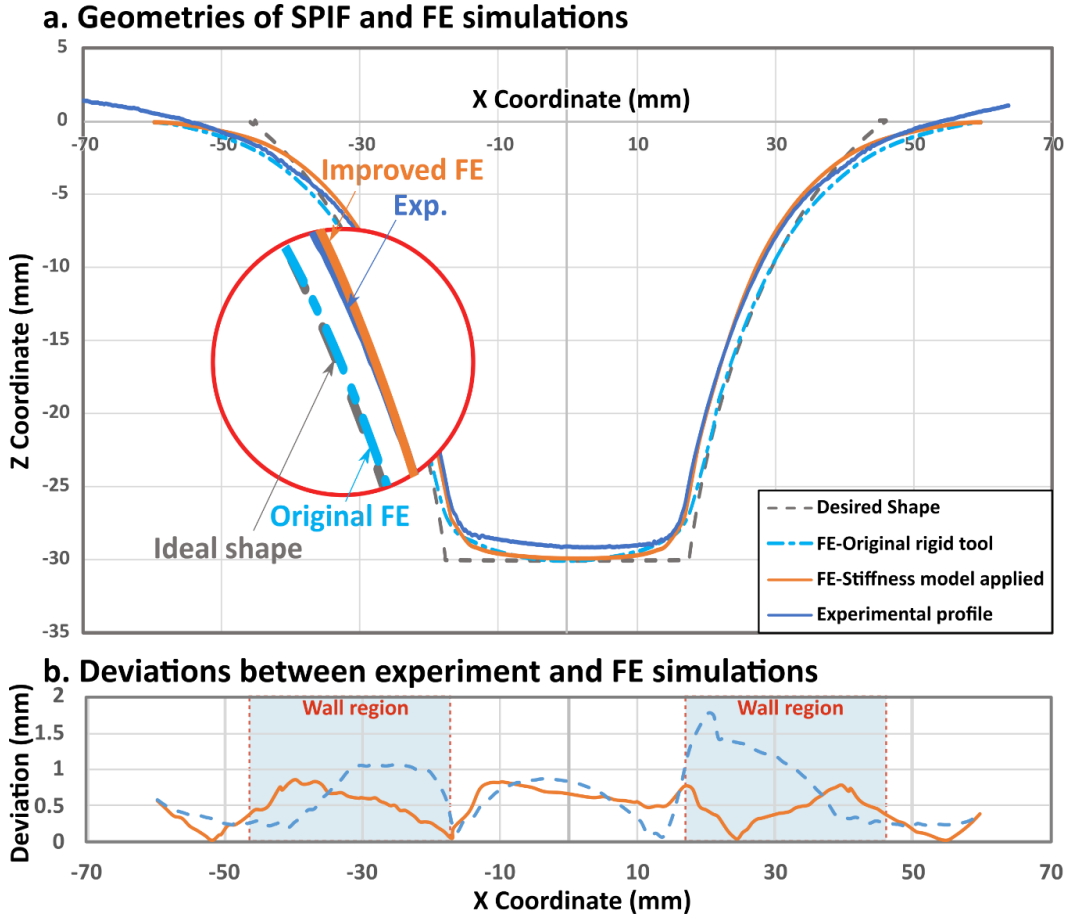


Figure 4.23 Comparison of profiles from desired shape, experimental testing, FE with rigid tool and FE with stiffness model in SPIF process (a) geometry profiles, and (b) deviations between experiment, and FE models with and without machine stiffness configuration.

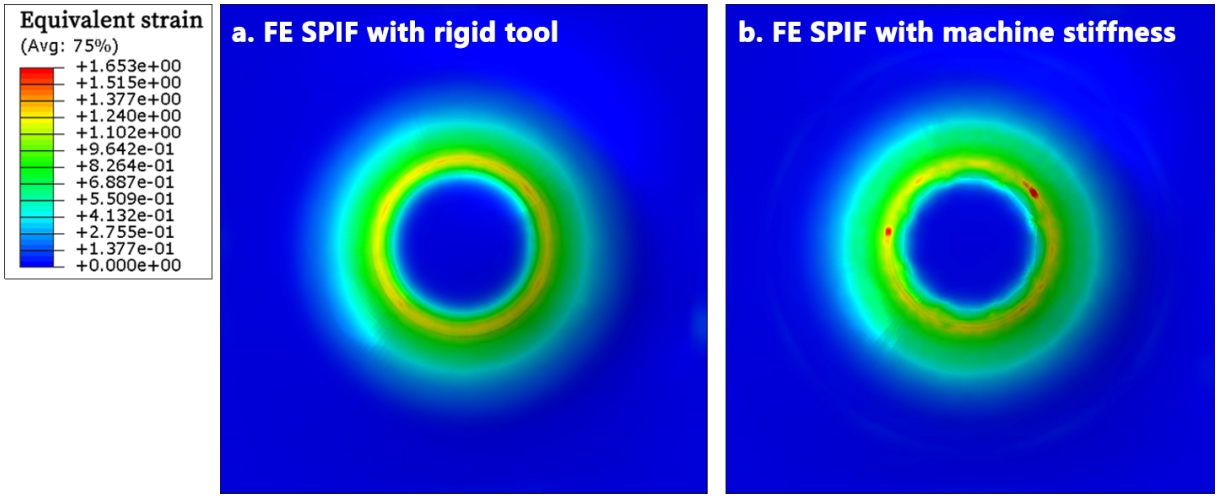


Figure 4.24 Equivalent strain contour plots for (a) FE model using rigid tool definition, and (b) FE model applied stiffness matrix in SPIF process.

4.6.3.3. Validation of the stiffness model in DSIF simulation

Figure 4.25a shows the comparison of geometry profiles from experimental test and FE simulation with and without tool and machine stiffness in DSIF processes. Similar to the SPIF results (Figures 4.23a and b), the profile obtained from FE simulation with the stiffness model is closer to the shape obtained from experimental testing. Figure 4.25b shows the prediction errors from FE simulations of both DSIF processes compared to experimental results that clearly indicate the improvement in forming geometry estimations with the implementation of the stiffness model.

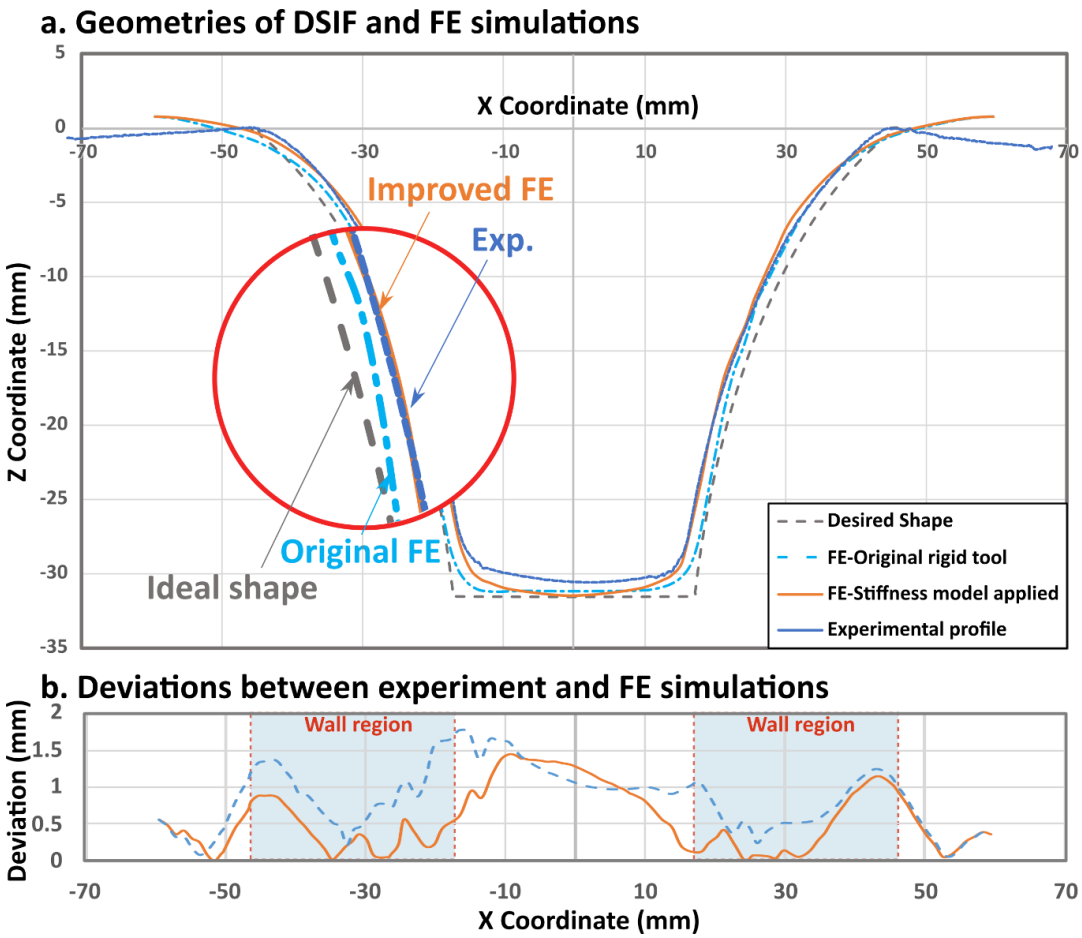


Figure 4.25 Comparison of profiles from the desired shape, experimental testing, FE with rigid tool and FE with stiffness model in DSIF process (a) geometry profiles, and (b) deviations between experiment, FE models with and without machine stiffness configuration.

By placing the geometric error between the desired shape and completed part profile by experiment and the tool deflections simulated in FE model into Figure 4.26, it is clear that the machine deflection is the major reason for geometry inaccuracy in DSIF practice. The tool deflections predicted in FE simulation precisely matched the peak values and positions of the geometric errors measured from the experiment. The maximum machine-tool deflection was calculated to be 1.4 mm at the horizontal position of $\pm$20 mm from cone centre in the radius direction along the *x*-axis, a position where the tool reached the fracture depth in testing and afforded the maximum forming forces. This is identical to two peaks of experimental geometric errors in values and locations as well. In the positive *x* direction, the peak value of the geometric error of the workpiece was 1.4

mm which is identical to the FE prediction of the machine-tool deflection under forming forces. In the negative *x* direction, the maximum geometric error achieved 1.8 mm, which was larger than the FE result. This comparison strongly suggests that the tool deflections are the main source of forming inaccuracy. The geometrical error in testing also showed a shifting in horizontal direction which may indicated the effect of tool axis offset or concentricity issue of the machine tool.

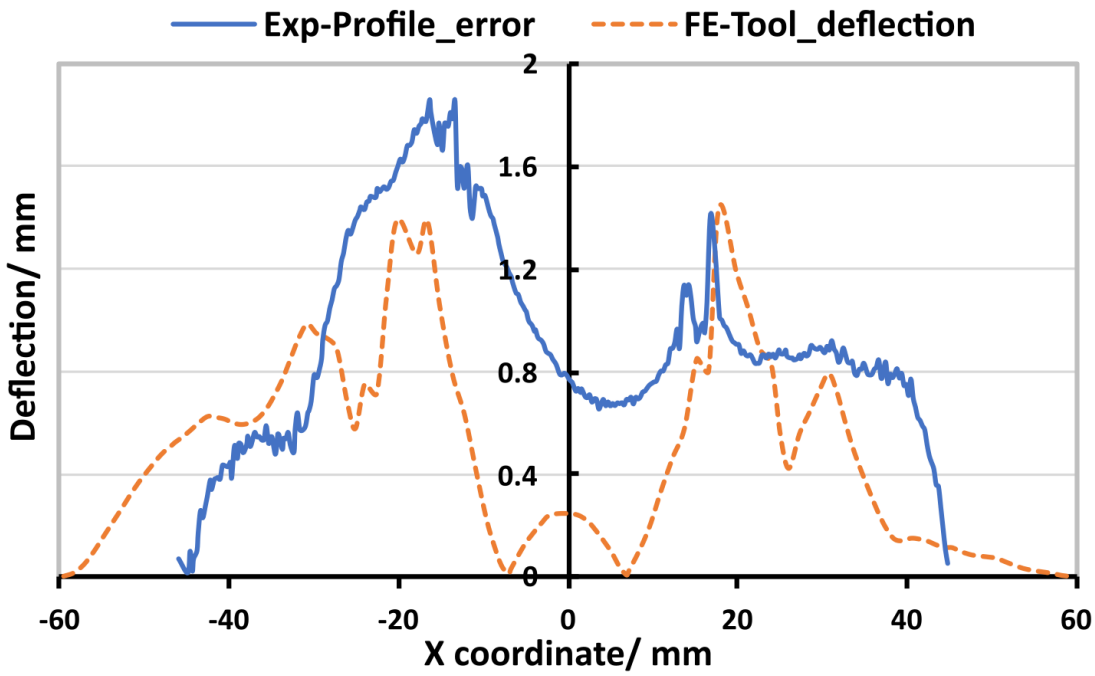


Figure 4.26 Comparison of profile errors from DSIF testing and detected tool deflection in FE simulation in DSIF

The implementation of stiffness matrix on forming tools reduced the strain concentration and the maximum equivalent strain in DSIF simulation. In the original FE model with rigid tool definition, the peak strain value reached 7.55 in a diagonal direction as shown in Figure 4.27a, whilst in the model with machine-tool stiffness included, the maximum equivalent strain reduced to 3.73 with a more even distribution as shown in Figure 4.27b. This significant difference in strains can be attributed to the essential difference of tool path specifications. The rigid tool path follows the specification to form the workpiece to the desired shape, which is essentially a kinematic loading condition.

When the machine-tool stiffness matrix is applied, the interaction between the machine-tool and the workpiece allows less plastic deformation and hence lower level of strain. The balance achieved by limited reaction forces and material deformation prevents excessive element elongation and compression. Thus, the strain distribution and values are expected to be closer to experimental samples in the FE simulation with the inclusion of machine-tool stiffness.

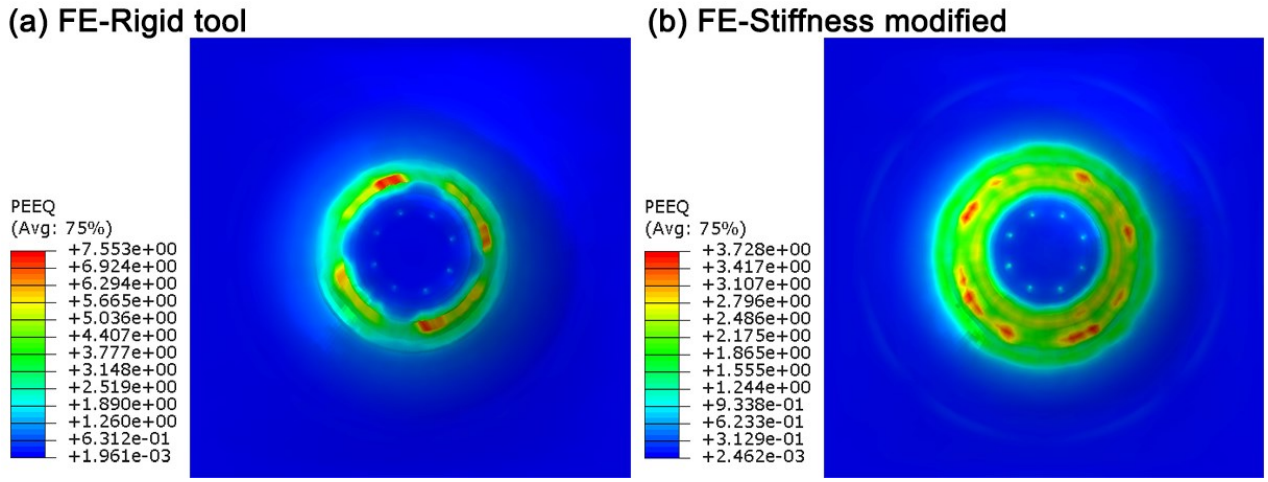


Figure 4.27 Equivalent strain contour plots for (a) FE model using rigid tool definition, and (b) FE model applied stiffness matrix in DSIF process.

4.7. Conclusions

1. In general, the DSIF process could achieve improved formability over the conventional SPIF process in experimental tests.
2. The pneumatically actuated support tool in DSIF is feasible to prevent the loss of contact to maintain the formability advantage. However, due to the master tool deflection, "over-bending" may occur in DSIF using the pneumatically actuated support tool when forming parts of a large wall angle.
3. By repeating the tool trajectory in FE model, the "over-bending" appeared at the same position of 60° cone profile. The FE simulation was able to predict the effect of machine-tool deflections on parts geometry and the occurrence of "over-bending".

4. The “over-bending” raised a need of machine stiffness estimation. In this study, a general approach to estimate the stiffness of ISF machine is proposed. The machine stiffness is estimated by a series of beams with effective lengths and structure related parameters based on rigid joint connection. The simplified beam model includes the positional effect of tool travel to machine structure. The calibration process can be conducted on a static FE model to obtain the force-displacement relationship.
5. The stiffness model of a dedicated DSIF machine, derived by the proposed machine stiffness estimation method, was proved to be effective to give an accurate evaluation of machine deflection during the forming process. The predicted profiles were significantly closer to the experimental result in both SPIF and DSIF FE simulations applied the machine-tool stiffness model as compared to the models without the machine-tool deflections.
6. The peak strains in FE predictions using models applied machine stiffness on forming tools were significantly reduced as compared with the conventional rigid tool configuration. This may be attributed to the change of the force interaction between the tool and deformable sheet in simulation because of the additional flexibility to tools. As a result, the peak strain value is reduced, and the strain distribution is more homogeneous.

CHAPTER 5 MODELLING OF DEFORMATION AND DUCTILE FRACTURE IN SPIF AND DSIF

5.1. Introduction

The fracture mechanism in Double-Sided Incremental Forming (DSIF) is a key question relating to the reasons of the enhanced Incremental Sheet Forming (ISF) formability. The studies of local deformation features in Tension under Cyclic Bending (TCB) and Tension under Cyclic Bending and Compression (TCBC) provided new insight into localised forming cycles of material deformation and their impact on the formability. However, the connection between forming mechanisms of the TCB, TCBC and ISF processes were barely explained [20, 22]. There is still a lack of understanding of the mechanisms for improved formability by additional compression and effective models to predict ductile damage in DSIF, even though there were considerable studies to achieve a good level of prediction in fracture of SPIF processes [23-26, 105, 177-180].

The objective of this chapter is to explain the deformation mechanisms of SPIF and DSIF in comparison with the SPIF/DSIF and TCB/TCBC processes. Based on the theoretical derivation of the TCBC as detailed in Chapter 3, an analytical model was developed for DSIF process in consideration of 3D bending deformation and stresses. The effect of compression and process parameters in the DSIF process was assessed in terms of fracture strain. FE models were developed to predict ductile fracture in SPIF and DSIF processes with considerations of machine stiffness. A shear modified Gurson-Tvergaard-Needleman (GTN) model was implemented by VUMAT user subroutine in ABAQUS/Explicit package to better capture the material damage evolution with Lode angle dependency at low stress triaxiality from the original GTN model. This enables the ductile and shear damage evolution in both SPIF and DSIF to be accurately estimated with a unified damage model. The results from FE simulation were validated by experimental tests of SPIF and DSIF processes of a truncated hyperbolic cone shape. Finally, the

mechanisms of deformation and formability enhancement in DSIF were discussed to draw a number of conclusions.

5.2. Theoretical analysis of deformation in SPIF and DSIF processes

The ISF deformation mechanics is defined by local contact between the workpiece and the forming tools. Concerning the consistency of local stresses during the contact period, there were several analytical models proposed for SPIF processes [106, 172, 181]. Fang et al. [35] expanded the stress analysis to the formed region and Ai et al. [182] considered strain evolutions and additional bending effect. In the DSIF research field, work in using an analytical method [14] was limited to local stress analysis for single and double contact situations. This section developed a model for DSIF fracture strain prediction based on stress analysis in both contact and the post-contact region. The stresses corresponding to strain development in each forming stage is given by differences between SPIF and DSIF processes. Finally, an assessment to process parameters is given with the shear modified GTN model damage criterion in terms of damage and fracture strain.

The analytical model is based on the following hypothesis:

1. The deformation is strictly localised in the contact and neighbouring regions after contact.
2. The horizontal displacement of material during deformation is ignored.
3. The circumferential strain ε_θ is negligible, which indicates a plane strain condition.

5.2.1. Local deformation and contact parameters in the i_{th} contact period

Figure 5.1 shows the material deformation process in both SPIF and DSIF processes at different forming stages and contact conditions. The current forming angle β is used as a progression indicator. For every new contact period, the material is fed vertically by single step size d to necessitate bending and elongation. Thus, the local bending stage can be divided into n_c load cycles by step size d in vertical axis, formed by each pass of tool

contact. The total number of contact times n_c can be defined by the step size d, the master tool radius r_1 and the desired forming angle ϕ:

$$n_c = \frac{r_1}{d}(1 - cos\phi) \tag{5.1}$$

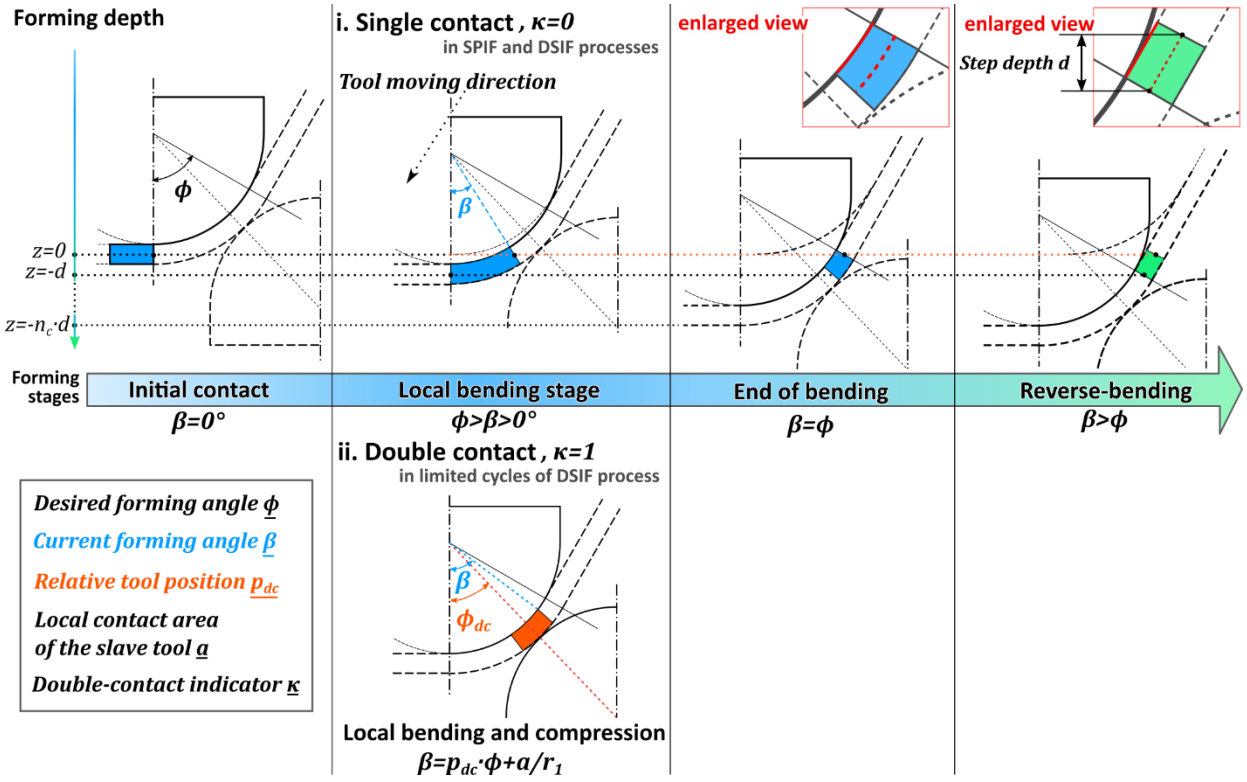


Figure 5.1 Schematics of the whole deformation processes of materials in SPIF and DSIF process.

The current forming angle β indicates the relative angular position of a unit of material to the initial contact. β is incrementally increased by each contact pass forming a new bottom for $\Delta z = -d$. Figure 5.2 presents the geometric relationship of the forming angles β_i at i_{th} pass and step size d, where the local forming angle β_i at the i_{th} pass can be obtained ($0 \le \beta_i \le \phi, i = 1, \dots, n_c, \beta_1 = 0$):

$$\left(r_1 + \frac{t_0}{2}\right) - \left(r_1 + \frac{t_0 cos\beta_i}{2}\right) cos\beta_i = (i-1)d$$

$$\frac{t_0}{2}\cos^2\beta_i + r_1 cos\beta_i + (i-1)d - \left(r_1 + \frac{t_0}{2}\right) = 0$$

$$cos\beta_i = \frac{-r_1+\sqrt{r_1^2-4\cdot\frac{t_0}{2}\cdot\left[(i-1)d-\left(r_1+\frac{t_0}{2}\right)\right]}}{2\cdot\frac{t_0}{2}}$$

$$\beta_i = \arccos\left(\frac{-r_1+\sqrt{r_1^2-2t_0\cdot\left[(i-1)d-\left(r_1+\frac{t_0}{2}\right)\right]}}{t_0}\right) \tag{5.2}$$

The material is under compression for certain load cycles by the support tool when the current forming angle β reaches at the relative tool angle ϕ_{dc} in the DSIF process. This compression effect is limited in the contact area between the sheet and the support tool. Using a ratio coefficient $p_{dc} \in [0,1]$ to represent the relative tool position, the double contact region can be determined as an interval of forming angle (Figure 5.2):

$$\Delta\phi_{dc} = \frac{a}{r_1+t_0\cos(p_{dc}\phi)} \tag{5. 3}$$

$$\phi_{dc} = p_{dc}\cdot\phi \tag{5. 4}$$

$$\kappa = \begin{cases} 1, p_{dc}\phi - \Delta\phi_{dc} < \beta < p_{dc}\phi + \Delta\phi_{dc} \\ 0, 0 \le \beta \le p_{dc}\phi - \Delta\phi_{dc}\ or\ p_{dc}\phi + \Delta\phi_{dc} \le \beta \end{cases} \tag{5. 5}$$

where a is the radius of contact area with the support tool. $\Delta\phi_{dc}$ is the angle of the arc region contacting both the master tool and the support tool. κ is the double-contact state indicator. As shown in Figure 5.2, $p_{dc} = 0$ is defined when the tool centres are in a vertical line. $p_{dc} = 1$ is the position where the angle of the vertical axis and connection line between tool centres is equal to the desired wall angle ϕ.

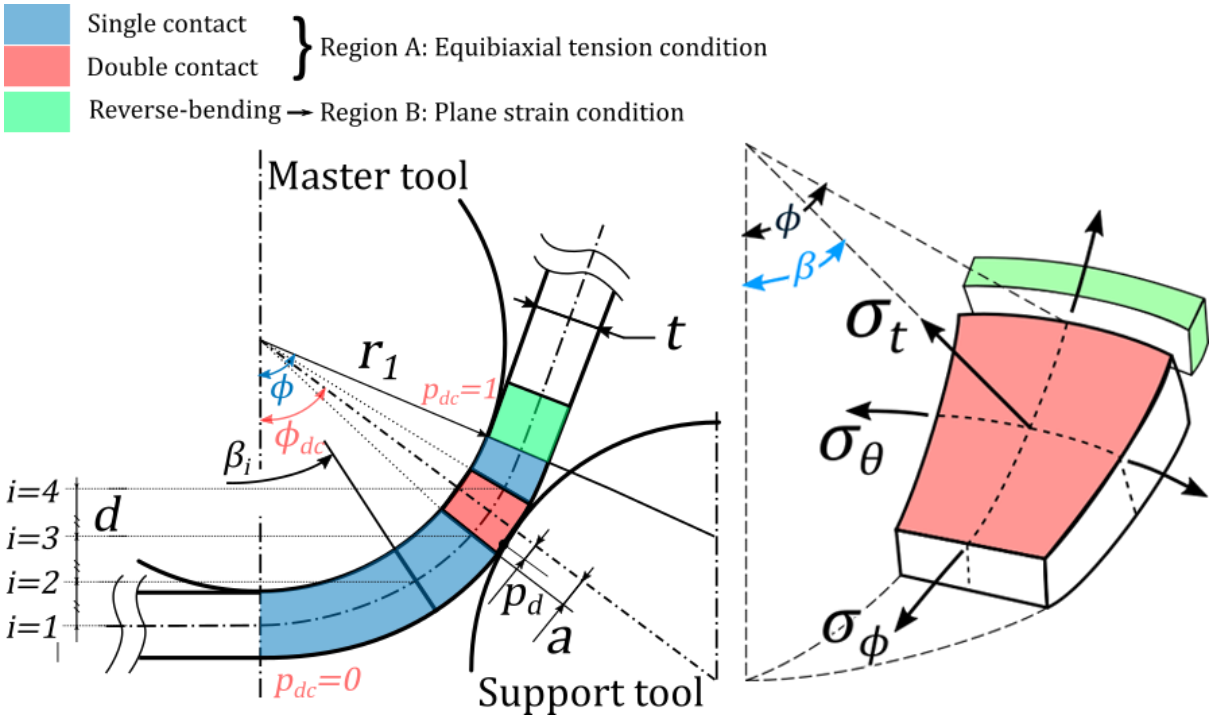


Figure 5.2 Schematic of analytical model: local deformation regions divided by forming passes in DSIF process.

5.2.2. Local strain development in ISF process

The local deformation in ISF can be divided into two parts: contacting region A and reverse bending region B (Figure 5.2). In region A, the material is supposed to closely wrap on the master tool surface. The relatively smaller tool radius compared to the bending radius defined by the desired shape creates a local stress state of equi-biaxial tension condition in region A. The additional compression in DSIF process is superimposed to this equi-biaxial tension stress condition. The deformation in the meridional direction is the strain increased by step sizes d and current wall angle β. The incremental strain can be written in equations:

$$\varepsilon_\beta^{engineering} = \frac{l-l_0}{l_0} = \frac{l-l\cos\beta}{l\cos\beta} = \frac{1}{\cos\beta} - 1 \tag{5.6}$$

$$\varepsilon_\beta^{true} = ln\left(\varepsilon_\beta^{engineering} + 1\right) = ln\left(\frac{1}{\cos\beta}\right) \tag{5.7}$$

$$\Delta\varepsilon_{\beta_i}^{true} = \varepsilon_{\beta_{i+1}}^{true} - \varepsilon_{\beta_i}^{true} = ln\left(\frac{cos\beta_i}{\cos\beta_{i+1}}\right) \tag{5.8}$$

where l_0 and l is the length of the raw material and its arc length after deformation for the wall angle β.

The geometric relationship between consecutive forming passes satisfies the following equation:

$$\left(r_1 + \frac{t_0}{2}cos\beta_i\right)(cos\beta_i - \cos\beta_{i+1}) = d$$

$$\frac{cos\beta_i}{cos\beta_{i+1}} = \frac{1}{1-\frac{d}{cos\beta_i\left(r_1+\frac{t_0}{2}cos\beta_i\right)}} \tag{5.9}$$

Combining Equations (5.8) and (5.9), the meridional strain increment in region A $\Delta\varepsilon_{\phi}^{A}$ can be given as:

$$\Delta\varepsilon_{\phi}^{A} = \Delta\varepsilon_{\beta}^{true} = ln\left(\frac{1}{1-\frac{d}{cos\beta\left(r_1+\frac{t_0}{2}cos\beta\right)}}\right) = -ln\left(1-\frac{d}{cos\beta\left(r_1+\frac{t_0}{2}cos\beta\right)}\right) \tag{5.10}$$

Ignore the plastic deformation in the circumferential direction, the thickness strain increment $\Delta\varepsilon_{t}^{A}$ is presented as:

$$\Delta\varepsilon_{t}^{A} = -\Delta\varepsilon_{\phi}^{A} = In\left(1-\frac{d}{cos\beta\left(r_1+\frac{t_0}{2}cos\beta\right)}\right) \tag{5.11}$$

The equivalent strain increment $\Delta\bar{\varepsilon}$ is calculated by given strain components from Equations (5.10) and (5.11). The total equivalent strain $\bar{\varepsilon}$ is the accumulation of its increment at step i:

$$\Delta\bar{\varepsilon} = \sqrt{\frac{2}{3}\left(\Delta\varepsilon_{\phi}^{A^2} + \Delta\varepsilon_{t}^{A^2}\right)} = \frac{2}{\sqrt{3}}\left|In\left(1-\frac{d}{cos\beta\left(r_1+\frac{t_0}{2}cos\beta\right)}\right)\right| \tag{5.12}$$

$$\bar{\varepsilon} = \sum_{i=n}^{i}\Delta\bar{\varepsilon}_i = \frac{2}{\sqrt{3}}\sum_{i=n}^{i}\left|In\left(1-\frac{d}{cos\beta_i\left(r_1+\frac{t_0}{2}cos\beta_i\right)}\right)\right| \tag{5.13}$$

5.2.3. Local stresses in ISF processes

Lu et al. [14] presented the stresses in the local bending region of the DSIF process:

$$\sigma_t^{\mathrm{A}} = \frac{\sigma_Y}{(\mu sin\beta\cdot\theta-1)\frac{r_1}{t}-1} + \kappa\frac{(1+\mu sin\beta\cdot\theta)\left(\frac{r_1}{t}+1\right)}{(\mu sin\beta\cdot\theta-1)\frac{r_1}{t}-1}P_{\mathrm{s}} \tag{5.14}$$

$$\sigma_\phi^{\mathrm{A}} = (\mu sin\beta\cdot\theta-1)\frac{r_1}{t}\sigma_t^{\mathrm{A}} - \kappa(1+\mu sin\beta\cdot\theta)\left(\frac{r_1+t}{t}\right)P_s \tag{5.15}$$

where σ_Y is the yielding stress calculated by strain-stress relationship presented by Johnson-cook equation:

$$\sigma_Y = A + B\cdot\bar{\varepsilon}^n \tag{5.16}$$

P_s is the local contact stress by Hertz contact theory given as:

$$P_s = \frac{3F_c}{2\pi a^2}\sqrt{1-\frac{p_d^2}{a^2}} \tag{5.17}$$

where a and p_d are the contact radius and the relative position to the contact centre, respectively. F_c is the compression force applied by the support tool.

In the derivation by Lu et al. [14], the circumferential stress was integrated from the boundary of the contact area. Ai et al. [182] assumed the contact stress state was an intermediate condition between the equi-biaxial tension and plane strain condition without consideration of shear and frictions. In this study, the circumferential stress σ_θ^A was based on the stress states considering the differences between the shear and friction generated by local bending in SPIF and double contacts in DSIF. In region A, the circumferential stress σ_θ^A is calculated by:

Equi-biaxial tension condition: $\sigma_\theta^A = \sigma_\phi^{\mathrm{A}} + \frac{\mu sin\beta\cdot\theta}{t}(r_1\sigma_t - \kappa(r_1+t)P_s)$ (5.18)

Only the shear stress in the plane of meridional and thickness directions is considered. Converting shear stress Equation. (3.32) from TCB to ISF cases, the maximum shear stress τ_ϕ in the middle plane ($y=0$) is given as:

$$\tau_\phi = \frac{3F_{shear}}{2t} = \frac{3\Delta T_\phi}{2t}/r_1 d\theta \tag{5.19}$$

where $d\theta$ is the angle of contact area in the circumferential direction. ΔT_ϕ is the tension increase in the meridional direction, which is converted from Equations (3.23), (3.24) and

(3.25):

$$\Delta T_{\phi} = \frac{M}{\rho} + T \cdot \varepsilon^{y=0} = \frac{M_{\phi}}{r_1 + \frac{t}{2}} + T_{\phi}^{\mathrm{A}} \left(\Delta\varepsilon - \frac{t}{2r_1} \right) \tag{5.20}$$

$$\begin{aligned} T_{\phi}^{A} &= r_1 d\theta \cdot \int_{-\frac{t}{2}}^{\frac{t}{2}} \sigma_{\phi}^{A} dt \\ &= r_1 d\theta \cdot \left(\int_{-\frac{t}{2}}^{\frac{mt}{2}} E' \left(\Delta\varepsilon - \frac{(1-y^2)t}{2\rho} \right) y dy + \int_{\frac{mt}{2}}^{\frac{t}{2}} \sigma_{\phi}^{A} dy \right) \\ &= r_1 d\theta \cdot \frac{E't}{4} \left[2\Delta\varepsilon(m_b + 1) - \frac{t}{r_1} \left(m_b - \frac{m_b^2}{2} + \frac{3}{2} \right) + \frac{2(1-m_b)\sigma_{\phi}}{E'} \right] \end{aligned} \tag{5.21}$$

$$\begin{aligned} M_{\phi} &= r_1 d\theta \cdot \left(\int_{-\frac{t}{2}}^{\frac{mt}{2}} E' \varepsilon_{\phi}^{A} y dy + \int_{\frac{mt}{2}}^{\frac{t}{2}} \sigma_{\phi}^{A} y dy \right) \\ &= r_1 d\theta \cdot \left(\int_{-1}^{m_b} \left(\frac{E'\Delta\varepsilon t^2 m}{4} - \frac{E't}{2r_1}(1-m)\frac{t^2}{4} m\, dm + \sigma_{\phi} \cdot \frac{t^2}{4} \cdot \int_{m_b}^{1} m dm \right) \right) \\ &= r_1 d\theta \cdot \left[\frac{E't^2}{16} m_b^2 \left(2\Delta\varepsilon - \frac{t}{r_1} - \frac{2\sigma_{\phi}}{E'} \right) + \frac{E't^3}{24r_1} m_b^3 - \frac{E't^2}{16} \left(2\Delta\varepsilon - \frac{5t}{3r_1} - \frac{2\sigma_{\phi}}{E'} \right) \right] \end{aligned} \tag{5.22}$$

$$m_b = 1 + \frac{2\left(r_1 + \frac{t}{2}\right)}{E't} \cdot \sigma_{\phi}^{A} - 2\left(r_1 + \frac{t}{2}\right) \cdot \Delta\varepsilon_{\phi}^{A} \tag{5.23}$$

$$m_b = \begin{cases} 0, m_b \le 0 \\ m_b, 0 < m_b < 1 \\ 1, m_b \ge 1 \end{cases} \tag{5.24}$$

In region B, the material is no longer in contact with the tools and is recovered from the bending status to the formed straight wall. Thus the reverse-bending occurs and the through-thickness stress σ_t^B is negligible. The meridional strain increment $\Delta\varepsilon_{\phi}^{B}$ can be determined by the strain difference through-thickness in the local bending area:

$$\Delta\varepsilon_{\phi}^{B} = In\left(\frac{l^{A}_{y=-\frac{t}{2}} - l^{A}_{y=\frac{t}{2}}}{l_0} + 1 \right) = In\left(\frac{(r_1+t)\phi - r_1\phi}{d/tan\phi} + 1 \right) = In\left(\frac{t\phi}{d/tan\phi} + 1 \right) \tag{5.25}$$

$$\Delta\bar{\varepsilon}^{B} = \frac{2}{\sqrt{3}} \Delta\varepsilon_{\phi}^{B} \tag{5.26}$$

$$\sigma_t^B = 0$$

Then the meridional stress in region B σ_{ϕ}^{B} can be given:

Plane strain condition: $$\sigma_\theta^B = \frac{1}{2}\left(\sigma_\phi^{\mathrm{A}} + \sigma_t^{\mathrm{A}}\right) = \frac{1}{2}\sigma_\phi^B \tag{5.27}$$

$$\sigma_Y = A + B\bar{\varepsilon}^n = \sqrt{\left(\sigma_\phi^B - \sigma_\theta^B\right)^2 + \left(\sigma_\phi^B - \sigma_t^B\right)^2 + \left(\sigma_t^B - \sigma_\theta^B\right)^2} = \frac{\sqrt{3}}{2}\sigma_\phi^B$$

$$\sigma_\phi^B = \sigma_Y \cdot \frac{2}{\sqrt{3}} \tag{5.28}$$

The shear stress in region B is not considered. Using Equations (5.14), (5.15) and (5.25)-(5.28), the stress indicators such as stress triaxiality η and Lode angle parameter ξ can be obtained by using Equations (3.33) and (3.52). Thus the stress states and local plastic deformation are quantitatively described for the deformation stages in a single contact loading cycle.

5.2.4. Damage evolution by a simplified GTN model

The modified GTN model is used to set a fracture criterion. The void growth function is reconstructed by mathematical equality [157] and the damage model with details given in Chapter 3 can be summarised as:

$$\dot{f}_{growth} = (1-f)\cdot 3D\cdot\Delta\bar{\varepsilon}\cdot\left(\frac{q2}{2}\right)\cdot\sinh\left(q2\cdot\frac{\sigma_{kk}}{2\sigma_Y}\right) \tag{5.29}$$

$$\dot{f}_{nucleation} = \frac{f_N}{s_N\sqrt{2\pi}} exp\left[-\frac{1}{2}\left(\frac{\bar{\varepsilon}^p-\varepsilon_N}{s_N}\right)^2\right]\dot{\bar{\varepsilon}}_M^p \tag{5.30}$$

$$\dot{f} = \dot{f}_g + \dot{f}_n \tag{5.31}$$

$$f^* = \begin{cases} f, & if\ f < f_c \\ f_c + \frac{\frac{1}{q_1}-f_c}{f_f-f_c}(f-f_c), & if\ f \geq f_c \end{cases} \tag{5.32}$$

$$\dot{D}_{shear} = \psi(\theta_L,\eta)\cdot n_s\cdot\left(\frac{\bar{\varepsilon}}{\varepsilon_s^f}\right)^{n-1}\frac{\Delta\bar{\varepsilon}}{\varepsilon_s^f} \tag{5.33}$$

$$\varepsilon_s^f = \begin{cases} +\infty, \eta \leq \eta_{lim}^{(-)} \\ \varepsilon_0\cdot\exp\left[\left(q_5(\eta-\eta_{lim}^{(+)}\right)^{n_s}\right] + \left(k_s\cdot\frac{(|\xi+q_6|^2)^{n_s}}{\exp\left(\eta-\eta_{lim}^{(-)}\right)}\right)^2, \eta_{lim}^{(-)} < \eta < \eta_{lim}^{(+)} \\ \varepsilon_0, \eta \geq \eta_{lim}^{(+)} \end{cases} \tag{5.34}$$

$$\psi(\theta_L,\eta)=\left(\frac{\eta_{lim}^{(+)}-\eta}{\eta_{lim}^{(+)}-\eta_{lim}^{(-)}}\right)^2\cdot f^{q_4}\cdot(1-g_0^2)^{\frac{1}{|\eta|+k}} \tag{5.35}$$

$$D=q1\cdot f+D_{shear} \tag{5.36}$$

where $\dot{f}$ is the void volume fraction increment. $\dot{f}_g$ and $\dot{f}_n$ represent the void volume fraction rates by hydrostatic stress and nucleation between voids, respectively. The overall damage variable D combines the normalised void volume fraction and shear damage D_{shear}. The shear mechanism is calibrated by the stress state related to function $\psi(\theta_L,\eta)$, which is defined by stress triaxiality η and Lode angle parameter ξ. $q1, q2, q3$ are GTN model constants. ε_N, S_N and f_N are void nucleation coefficients of material. $\varepsilon_0, q4, q5, q6, n_s, k_s, k_w$ are the material fracture strain surface parameters. $\eta_{lim}^{(-)}$ and $\eta_{lim}^{(+)}$ are stress triaxiality limits to define the boundary of fracture strain surface and improve the calculation efficiency. Besides, E, ν are respectively Young's modulus and Poisson's ratio. A, B and n are parameters for Johnson Cook's constitutive model. These parameters for grade 1 pure Ti are listed in table 5.1 with the detailed discussion given in Chapter 3.3.

Table 5.1 Material and GTN model parameters being used for grade 1 pure Ti.

E (MPa)	ν	*A (MPa)*	*B (MPa)*	ε_0	n	q_1	q_2
105000	0.34	170	356	0.46	0.53	1.5	1
q_3	f_f	f_c	ε_N	S_N	f_N	q_4	q_5
2.25	0.3025	0.2593	0.3	0.2	0.017	1/3	2
q_6	k_w	k_s	n_s	$\eta_{lim}^{(-)}$	$\eta_{lim}^{(+)}$		
0.3	1	1	1.2	-1	1		

The whole damage evolution progression can be summarised in the flow chart shown in Figure 5.3. The analytical model is structured and processed on MATLAB code.

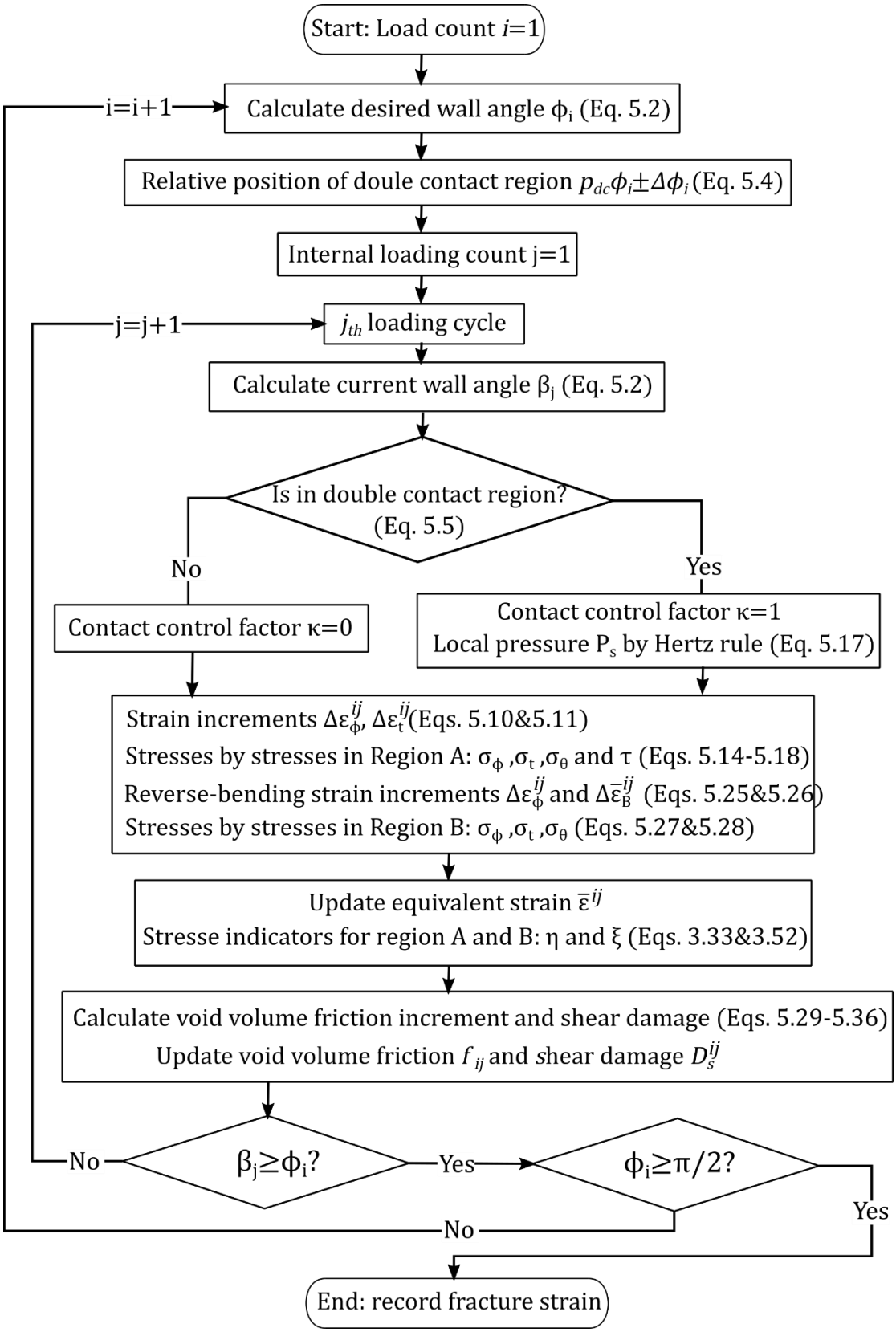


Figure 5.3 Flowchart for the analytical model for SPIF and DSIF associated with shear modified GTN model.

5.2.5. Effects of process parameters in SPIF and DSIF

The representative damage evolution by equivalent strain is calculated to benchmark formability. It should be emphasised that the equivalent strain means the equivalent strain obtained after the desired wall angle is achieved ($\beta_j \geq \phi_i$,) at the end of the full forming process with the completion of both bending and reverse-bending deformation processes. Thus the equivalent fracture strain is a discrete result of incremental loading representing whether the fracture occurrence is at a certain forming pass.

The process parameters are consistent with the experimental set-up as summarised in Table 5.2.

Table 5.2 Process parameters applied in ISF analytical model.

Parameters	Values
Master tool radius, r_1	5 mm
Step size, d	0.25 mm
Initial sheet thickness, t_0	0.7 mm
Friction coefficient, μ	0.05
Compression force, F_c	240 N
Slave tool contact radius, a	0.5 mm
Tangential contact angle, θ	10°
Relative tool position coefficient, p_{dc}	0.9

Figure 5.4 shows the stress triaxiality variation with the equivalent strain increase using the derived analytical model for the SPIF and DSIF processes. The stress triaxiality curve of DSIF has a sudden drop of strains between 1.46 and 2.14, which is in the range of the last 5 tool contact passes. This exactly matches the pre-set relative tool position coefficient $p_{dc} = 0.9$, which shows the effectiveness of this analytical model to correctly simulate the occurrence of double-contact in the DSIF process. The drop of stress triaxiality due to compression agrees with the work by Lu et al. [14]. It can be concluded that the presented analytical model is feasible to calculate the stresses and strain in the SPIF and DSIF deformation regions as expected.

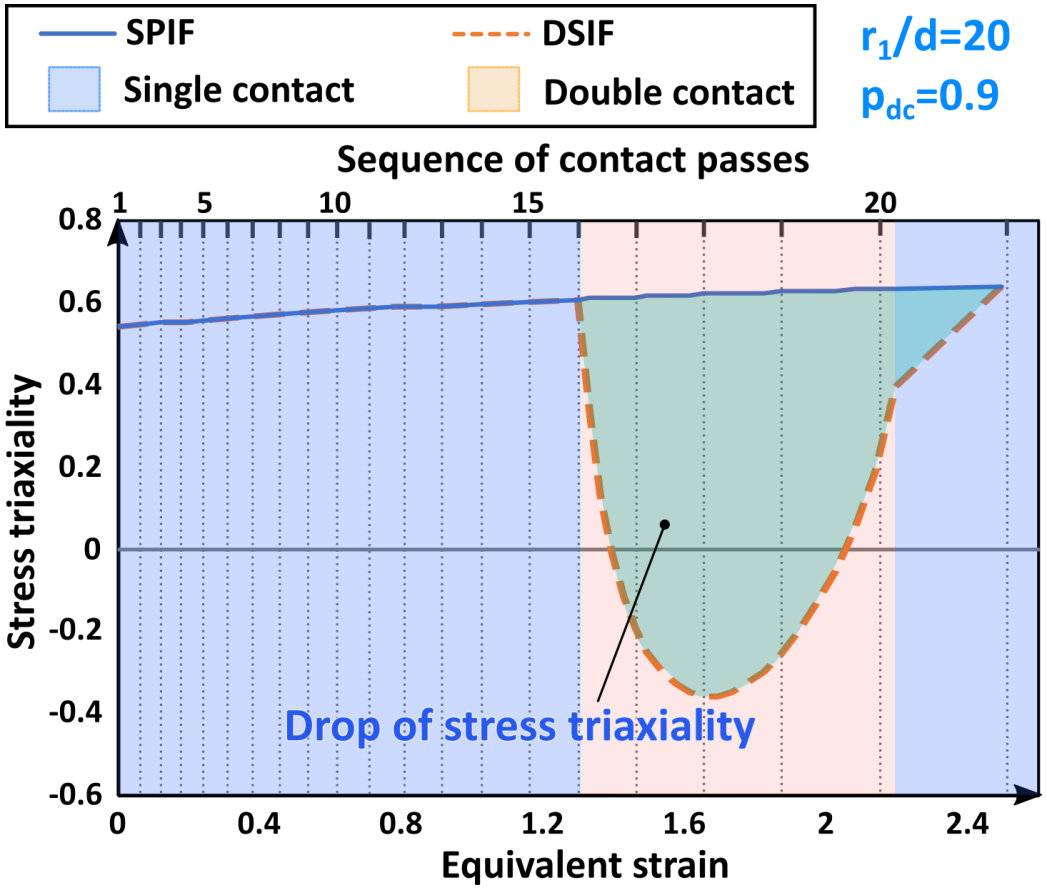


Figure 5.4 Stress triaxiality by equivalent strain curve from the analytical model of SPIF and DSIF processes.

The evolution of representative damages as a function of equivalent strain for both the SPIF and DSIF processes are plotted in Figure 5.5. The forming angle versus equivalent strain curve is plotted to link the experiment results with the fracture depths converted to the fracture angles. The consideration of the reverse-bending effect suggests significantly earlier fracture in both SPIF and DSIF processes. The prediction of equivalent fracture strain for SPIF agrees reasonably with the experimental result, where the estimated fracture strain occurred in between 1.5 and 1.87 and the experimental result is about 1.6. On the other hand, the predicted fracture strain from DSIF is in the range of 1.6-1.87 as compared to the experimental result of 2.14. Although there is a scope for improvement particularly in the case of DSIF, these results indicate the feasibility of the presented analytical model for a reasonable prediction to the final fracture in ISF

processes and the possible effect of process parameters.

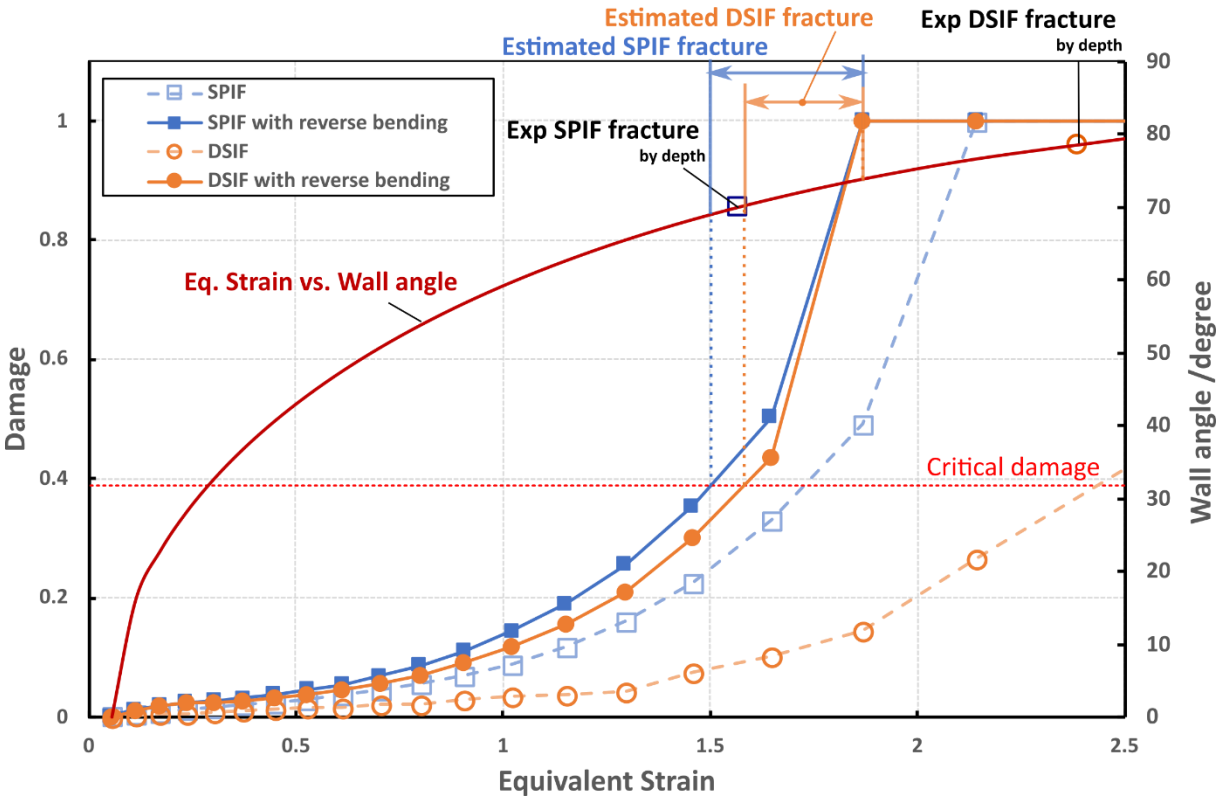


Figure 5.5 Damage evolution by the development of the equivalent strain

The effect of the step size, master tool radius and the ratio between them are predicted by the presented analytical model as shown in Figure 5.6. The fracture criteria are determined by the critical void fraction ($f = f_c = 0.2593, D = 0.3889$, initiation of fracture), the final void fraction of fracture ($f = f_f = 0.3025, D = q_1 f = 0.4537$, the baseline of fracture) and the complete fracture ($D = 1$) based on microstructure observation from grade 1 pure titanium [98]. The fracture strains are presented with a base value of strain at the final void fraction of fracture plus an error bar including strain values from initiation to the completion of fracture. The results suggest that the DSIF process can effectively improve the formability of the SPIF process. When the tool radius is fixed, the equivalent fracture strain shows a downward trend with the increase of the step size as shown in Figure 5.6a. The fracture strain difference between the SPIF and DSIF processes is reduced when the step size increases from 0.2 to 0.4 mm. However, this difference dramatically enlarges at $d = 0.5\ mm$ which is considered to be the inaccuracy

caused by increased strain increment because of the large step size. Figures 5.6b and 5.6c show that a larger tool radius has a negative effect on the formability of both the SPIF and DSIF processes. This reduction in formability by increasing the tool radius cannot be explained by the change of the ratio of step size and tool radius as shown in Figure 5.6c. Compared to the step size and tool radius, the effect of relative positions of the tools is negligible. Moving the support tool from the bottom ($p_{dc} = 0$ in Figure 5.2) to the corresponding position ($p_{dc} = 1$ in Figure 5.2) has a slight improvement to the final fracture strain as shown in Figure 5.6d. This conclusion is conflicted to the previous experimental result [14], which showed the tool shift reduces the achievable forming depth under 240N compression as reproduced in Figure 5.7. The formability improvement by tool shifting was more effective when the squeezing force reached $400N$ and above. The estimation of formability of DSIF process under high compression may beyond the capability of this analytical model and GTN model because of the lack of considerations to changes of the contact area and through-thickness effect.

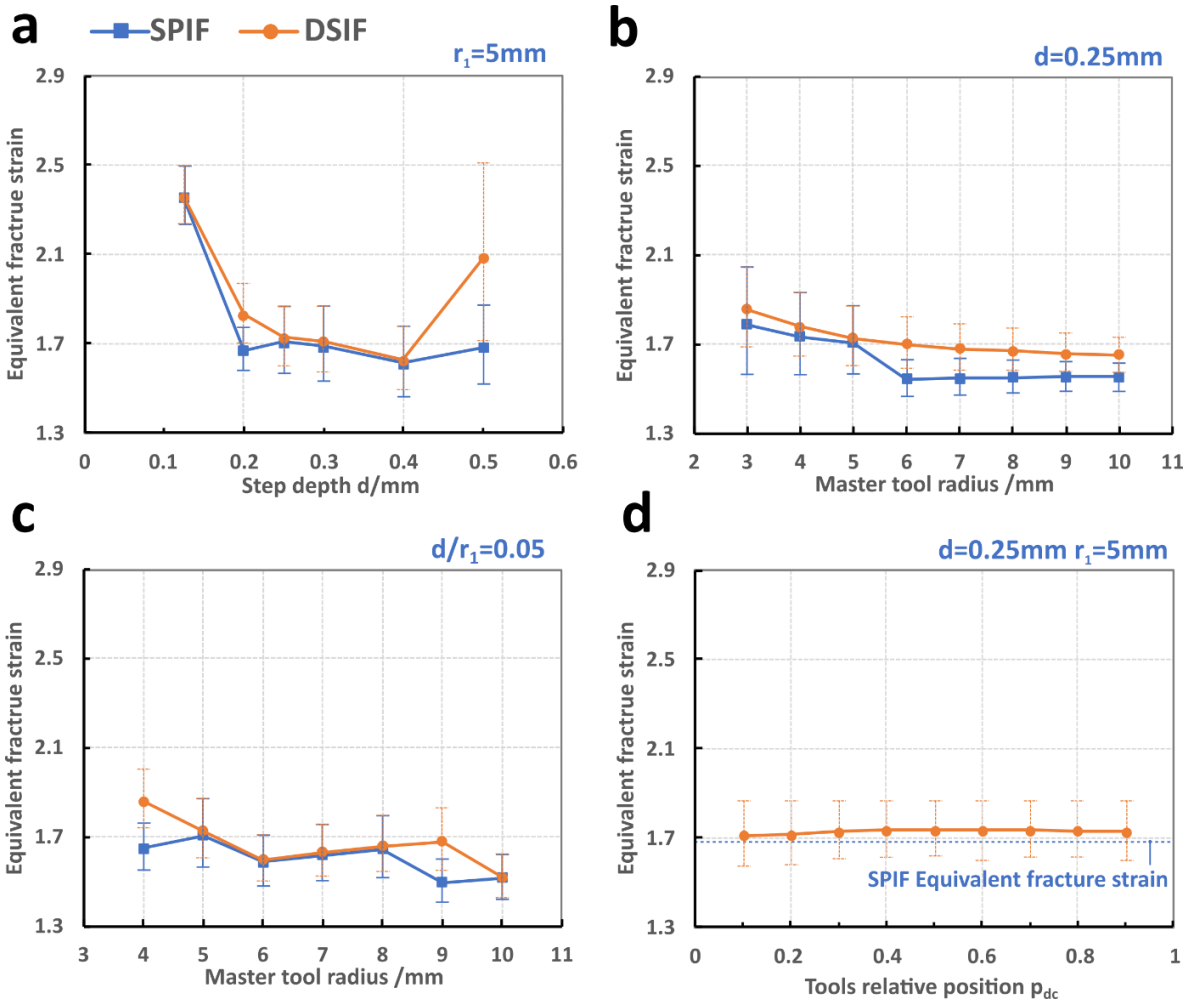


Figure 5.6 The equivalent fracture strain development by (a) step size, (b) master tool radius, (c) master tool radius under fixed ratio d/r_1 and (d) the relative position of tools in DSIF process.

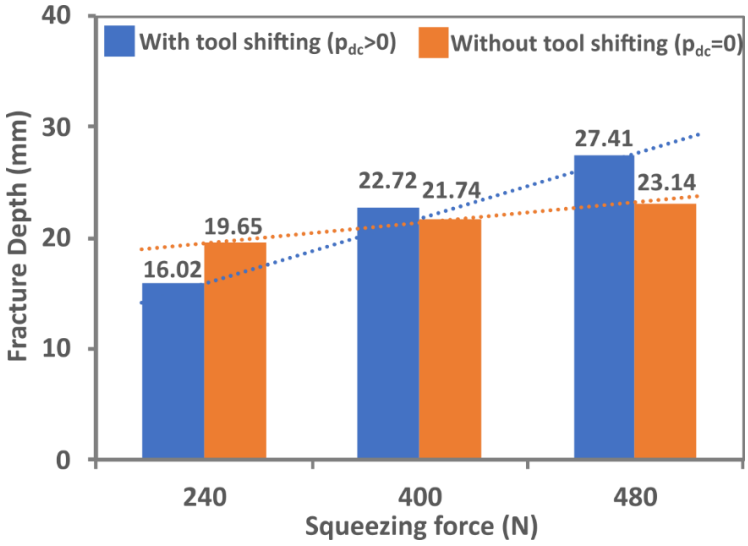


Figure 5.7 Influence of relative tool position to process formability in DSIF (reproduced from [14])

In conclusion, the analytical model involved the reverse-bending effect is effective to predict the fracture strain for both SPIF and DSIF processes. This model captures well the essential difference between constant local contact in SPIF and limited cycles of double contact in DSIF as shown in Figure 5.4. The postponement of damage development in DSIF can be predicted. The relationship between the formability changes and process parameters were produced. For any set of step size and tool radius, a larger fracture strain can be achieved by the DSIF process than that of the SPIF. It is also shown that the increased step size and tool radius have a negative effect on formability in both SPIF and DSIF. The model also shows insignificant effect on formability by relative tool positions in DSIF. Although this conclusion matched with previous experimental evidence, the effect of relative tool position was insufficient to reach a verdict with limitation of contact area estimation and GTN model under low stress triaxiality. Further experimental investigation is preferable to reveal the impact of compressive forces and relative tool positions on the fracture in the DSIF process.

5.3. Finite element simulation

5.3.1. Tool path modification for machine compliance

In chapter 4, the implementation of the stiffness of ISF machine and tools in FE modelling was verified to be an effective means to obtain a closer geometry to experimental results in both SPIF (Figure 4.24) and DSIF processes (Figure 4.26). Considering the fact that the geometrical difference and ISF machine tool configurations may lead to discrepancies in damage evaluation, the FE simulations are tested and compared using three strategies as shown in Figure 5.8. In Case A, a rigid tool is assigned with the original toolpath used in the experimental test (Figure 5.8a). In Case B, a flexible tool is attached to a connector element defined by machine stiffness to introduce the real-time response of machine deflection (Figure 5.8b). In Case C, the same rigid tool is used as in Case A. The toolpath is modified by the machine and tool deflections which is calculated through the experimental measured forces and the analytical stiffness model

(Figure 5.8c). The predictions to fracture depth were given by three different tool settings and compared with experimental results.

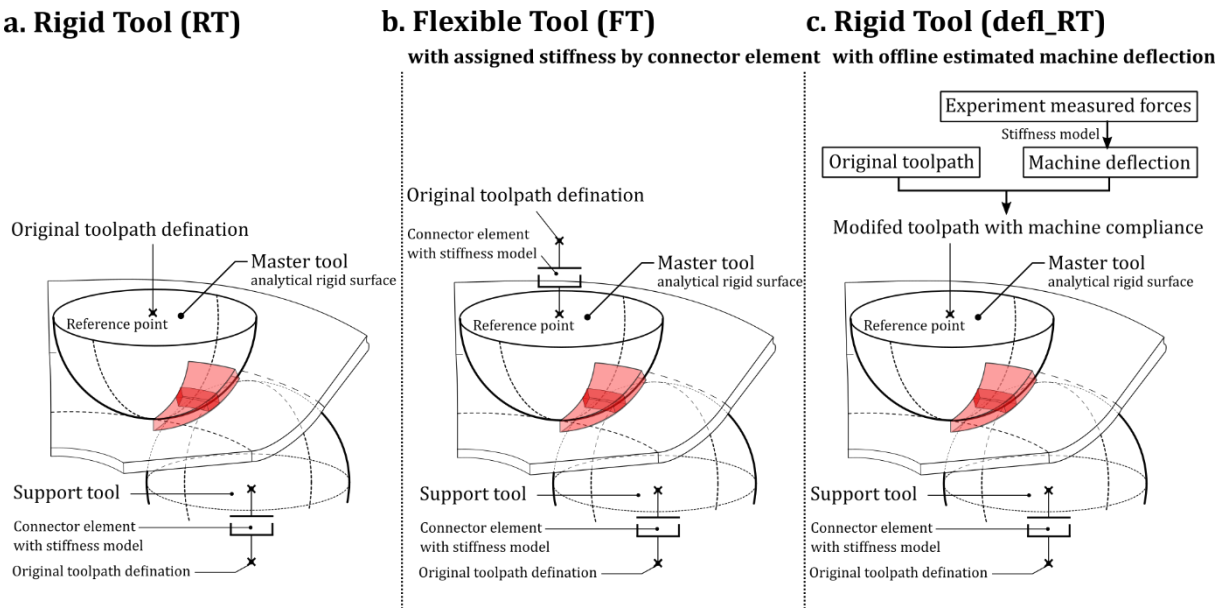


Figure 5.8 Tool modelling with and without implementation of machine stiffness tested in FE simulation.

5.3.2. Finite element models

The workpiece was modelled with 156 mm × 15 6 mm × 0.7 mm size and fully constrained in the flange area as detailed in Chapter 4.6.3 (Figure 4.17). The reduced integration brick elements (C3D8R) were used with an element size of 1 mm × 0.7 mm × 0.175 mm to achieve sufficient accuracy. The feed rate of the tool is fixed at 800 mm/min throughout the process.

The material property and damage criteria are employed using the shear modified GTN damage model validated in the TCB and TCBC studies, which is presented in Chapter 3. The new shear modified GTN model is able to include the Lode angle effect and to improve the prediction under low stress triaxiality conditions. Equations (5.30) – (5.35) calculate the void volume fraction and damage evolution. A brief outline of the constitutive model and the void volume growth f_g function working in FE simulations are listed below.

Summary to the shear modified GTN model (Constitutive part):

$$\Phi = (\frac{\sigma_{eq}}{\sigma_M})^2 + 2q_1 f^* \cosh\left(\frac{q_2\sigma_{kk}}{2\sigma_M}\right) - [1 + (q_1 f^* + D_s)^2 - 2D_s]=0 \tag{5.37}$$

$$\dot{\bar{\varepsilon}}_M^p = \frac{\boldsymbol{\sigma}:\dot{\varepsilon}_{ij}^p}{(1-D/q_1)\sigma_M} \tag{5.38}$$

$$\dot{\lambda} = \frac{\Phi}{V_{ij}D_{ik}V_{ik} - \xi_1 h_1 - \xi_2 h_2} \tag{5.39}$$

$$\begin{cases} \xi_1 = \frac{\partial\Phi}{\partial\bar{\varepsilon}^p} = -\frac{2H}{\sigma_M^3}\left[\frac{3}{2}\sigma_{ij}\sigma_{ij} - \frac{1}{2}\sigma_{ii}^2\right] - \frac{Hf^*q_1\sigma_{ii}}{\sigma_M^2} sinh\left(\frac{q_2\sigma_{ii}}{2\sigma_M}\right)\delta_{ij} \\ \xi_2 = \frac{\partial\Phi}{\partial f} = 2q_1 cosh\left(\frac{q_2\sigma_{ii}}{2\sigma_M}\right) - 2q_3 f^* \\ V_{ik} = \frac{\partial\Phi}{\partial\sigma_{ik}} = \frac{1}{\sigma_M^2}(3\sigma_{ik} - \sigma_{ii}\delta_{ik}) + \frac{f^*q_1q_2}{\sigma_M} sinh\left(\frac{q_2\sigma_{ii}}{2\sigma_M}\right)\delta_{ik} \\ h_1 = \sqrt{\frac{2}{3}V_{ij}V_{ij}} \\ h_2 = (1-f^*)V_{ii} \end{cases} \tag{5.40}$$

$$\lambda = \frac{E\upsilon}{(1+\upsilon)(1-2\upsilon)} \tag{5.41}$$

$$\dot{\varepsilon}_{kk}^p = \dot{\lambda}\cdot\frac{3Dq_2}{\sigma_M} sinh\left(\frac{q_2\sigma_{kk}}{2\sigma_M}\right) \tag{5.42}$$

$$\dot{f}_{growth} = (1-f)\cdot\dot{\varepsilon}_{kk}^p \tag{5.43}$$

There are two parts of FE simulations to serve the purposes of tool configuration validations and the detailed investigations of local deformation and mechanics. For each part, the same FE model is employed that only differs in mesh density, contact detection frequency and the minimum increment length in mass scaling. For the tool configuration validation, 36,000 elements are created with a contact detection frequency of per 100 increments, and the minimum increment at $3.2\times10^{-5}\,s$. For the detailed fracture predictions, 45,280 elements are used in the model. The contact detection frequency and minimum increment are reduced to per 40 increments and $2.4\times10^{-5}s$. Each set of FE simulation is conducted for both SPIF and DSIF processes. Table 5.3 provides the detailed parameters used in the FE simulations.

Table 5.3 FE simulations parameters for both SPIF and DSIF

Material property	Shear modified GTN model via VUMAT			
Sheet size	$156\ mm \times 156\ mm \times 0.7\ mm$			
Element type	C3D8R			
Feed rate	800 mm/min			
Support tool	Rigid tool with stiffness matrix assigned by connector element			
Tool configuration	a. Rigid tool	b. Flexible tool	c. Rigid tool with deflected toolpath	
Tool stiffness	None	Connector element	Offline calculated tool deflection from the forming force	
Element number	36,000		36,000	45,280
Contact detection frequency	Per 100 increments		Per 100 incr.	Per 40 incr.
Mass scaling min. increment	$3.2 \times 10^{-5}\ s$		$3.2 \times 10^{-5}\ s$	$2.4 \times 10^{-5}\ s$

5.4. Results

5.4.1. Fracture depths and geometries

The fracture depth predicted by different FE simulations are plotted in Figure 5.9. Figure 5.10 shows the comparisons of the formed shape and profile by FE prediction and experimental testing. Overall, the strategy using rigid tool and deflected toolpath (Case C) gives the most accurate prediction. This model correctly presented the fracture occurrence with an 11.78% discrepancy from the experimental result in DSIF, which was reduced to 6.96% by increasing the mesh density, and 8.75% in SPIF process. The profile predictions from Case C were the closest to the test results as well, where the original model and the model of a denser mesh gave almost identical geometries as plotted. In the contrast, the model with rigid tool applied with original toolpath (Case A) and with flexible tool combining machine stiffness (Case B) predicted the earlier fractures than the experimental results, especially in the case of DSIF. It is worth noting that the result from flexible tool (Case B) produced even larger error in fracture depth than that of conventional tool set-up, although the predicted geometries were closer to the profiles from experimental measurement (Figure 5.10).

In conclusion, the predictions based on the rigid tool and deflected toolpath (Case C) are the most accurate by FE modelling. The following stress and strain analysis are obtained from the model of the denser mesh using rigid tool and the deflected toolpath (Case C) except for any additional references.

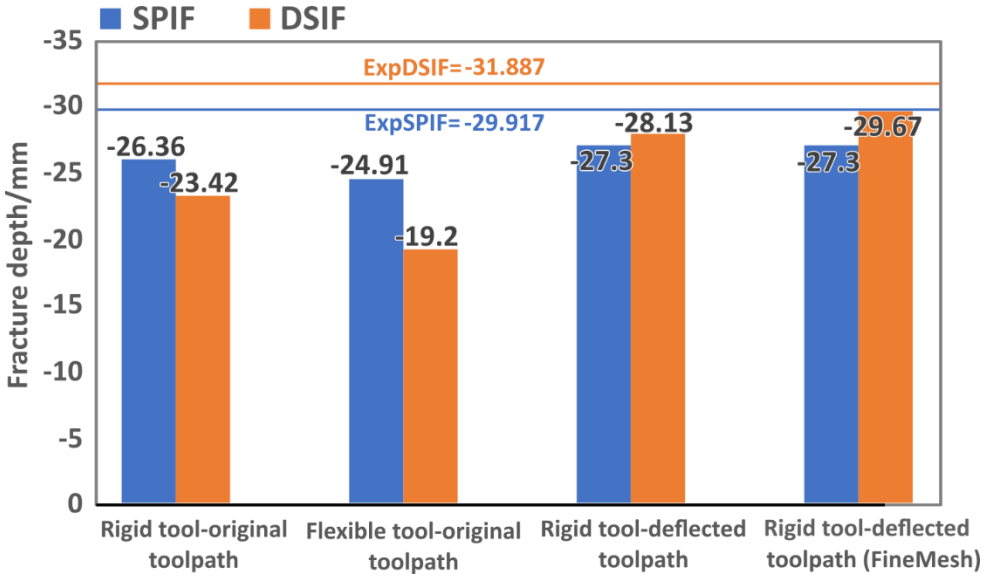


Figure 5.9 Predictions to maximum forming depth by different tool modification strategies with the modified GTN model

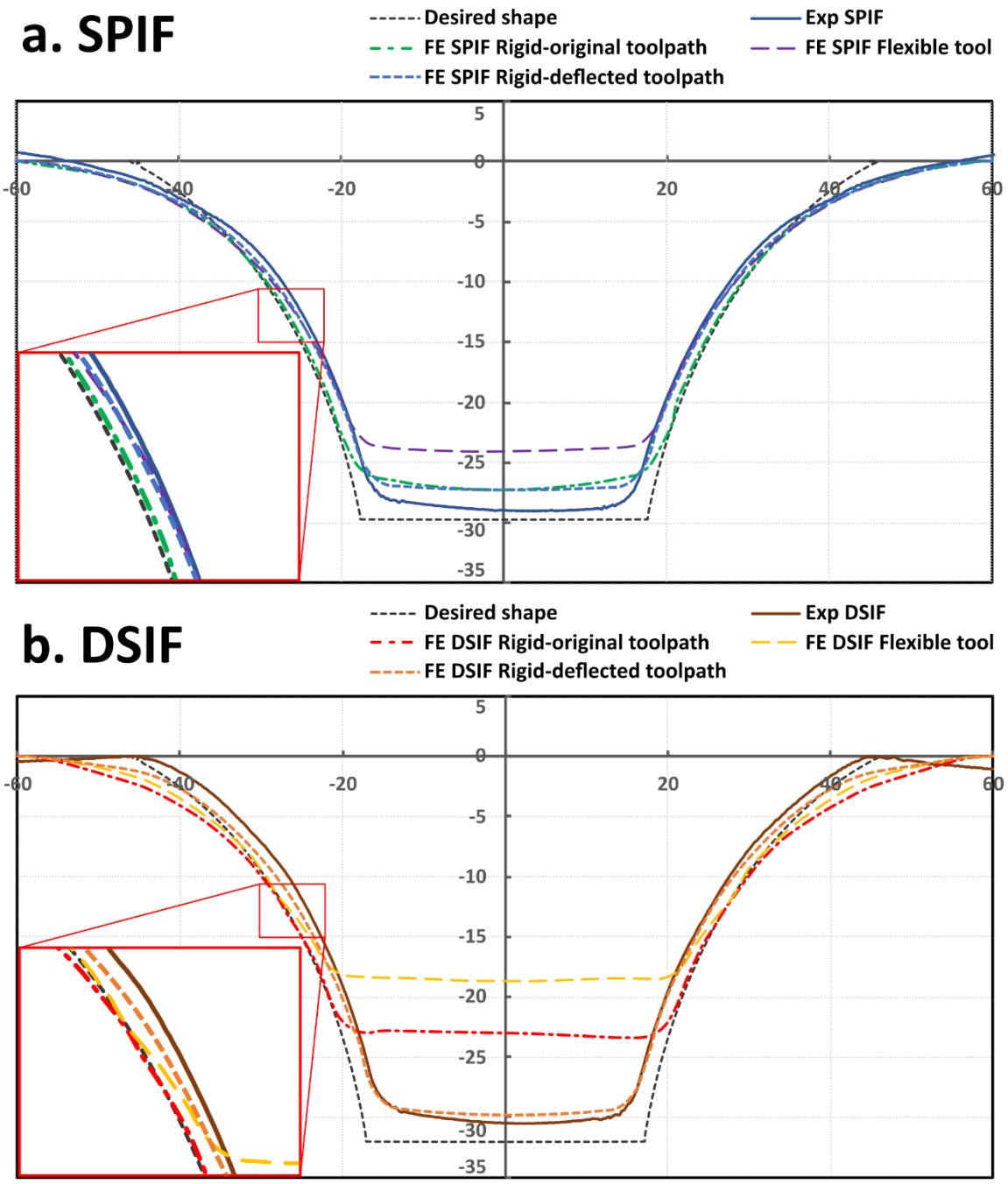


Figure 5.10 Comparisons of predicted profiles by FE simulations with different tool strategies (a). SPIF, and (b). DSIF

5.4.2. Equivalent strain and damage distributions

The geometries and fracture depth predicted by the modified GTN model with deflected toolpath strategy (Case C) are shown in Figure 5.12. In the case of SPIF, the experimental results indicate the occurrence of fracture in the diagonal direction. On the

other hand, the FE predicted a fracture location is near the edge of the sample. Meanwhile, the fracture location prediction in DSIF process is identical to the experiment which is propagated from the position perpendicular to the diagonal. In the thickness direction, the fracture initiates on the surface opposite to the master tool contact (convex side) in both SPIF and DSIF processes. Similar to the accurate prediction of fracture in the cases of TCB and TCBC, the FE simulation results from this Chapter show that the shear modified GTN model can also give good predictions of ductile fracture in SPIF and DSIF processes.

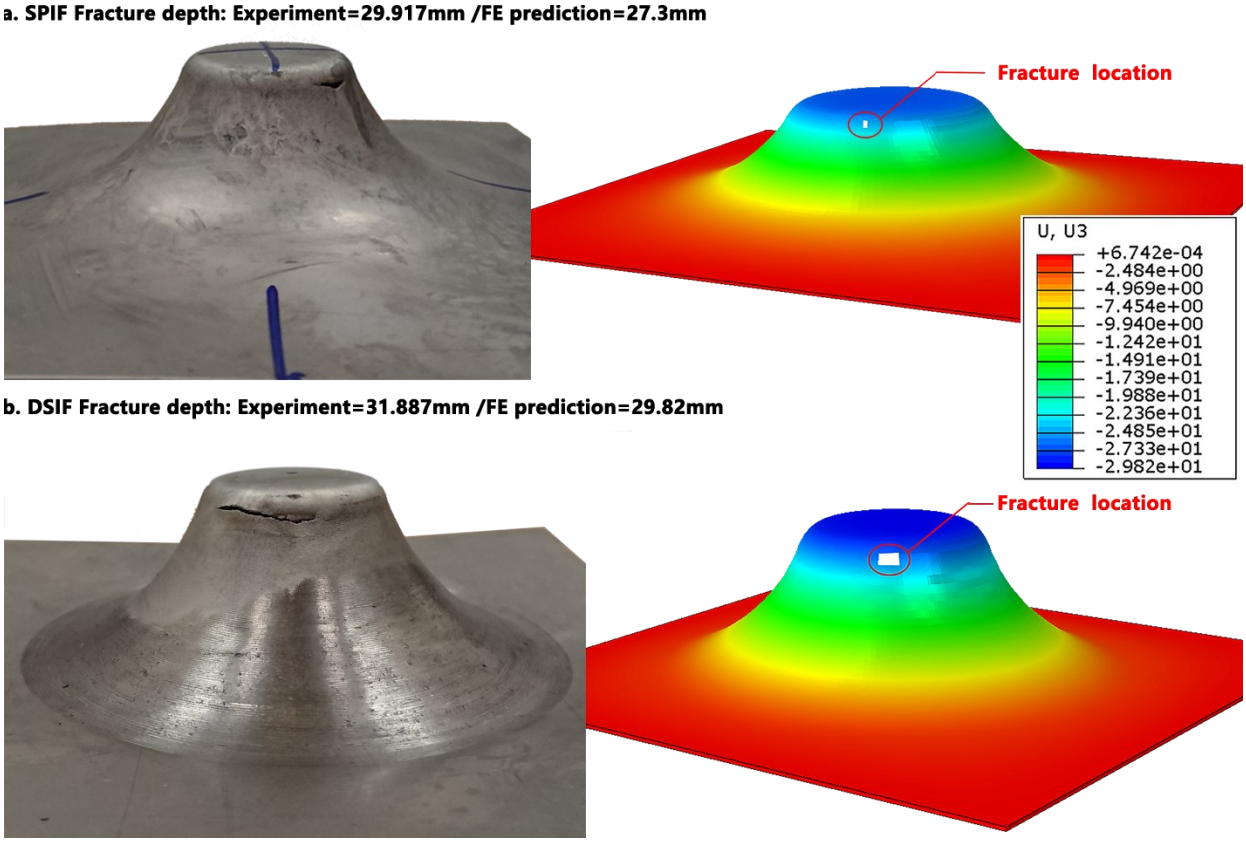


Figure 5.11 Experimental and FE simulated results with fracture depth comparison from the modified GTN model for (a) SPIF, and (b)DSIF

Figure 5.12 shows the distribution of equivalent strain at fracture in both the SPIF and DSIF processes. The fracture strains are 1.65 in SPIF and 1.77 in DSIF, which are in general agreement with the analytical model prediction from 1.5-1.87 for SPIF and 1.6-1.87 for DSIF (Figure 5.4). The equivalent strain is evenly distributed, and the peak is achieved in the close proximity to the region of material deformation and tool contact

above the bottom cap (Figure 5.13c). The local distribution of equivalent strain supports to the previous whole process analysis that the maximum strain and fracture are obtained at the boundary between the contact region and the region of deformation, where the reverse-bending occurs (Figure 5.13c). This predicted initial fracture position is in agreement with the previous experimental and analytical study by Fang et al. [35].

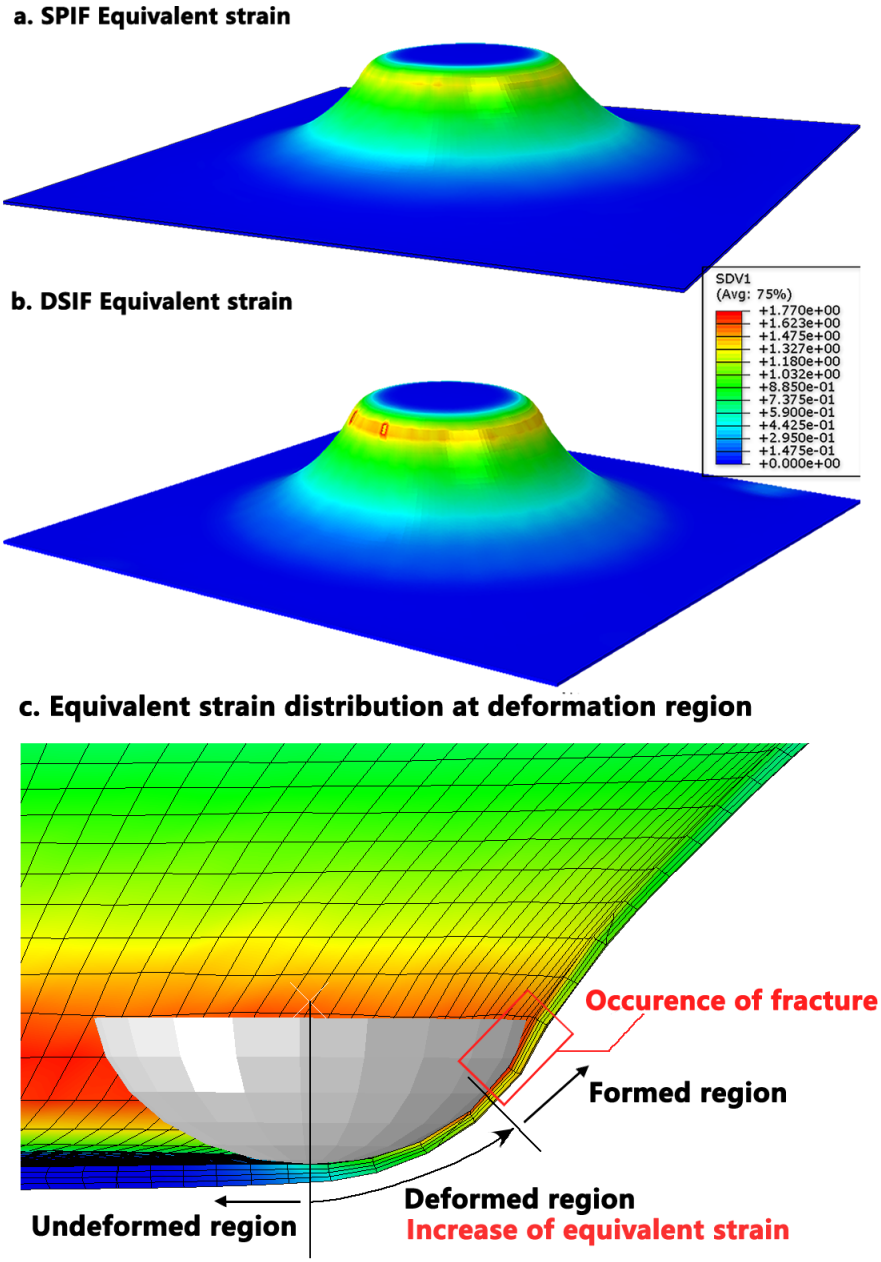


Figure 5.12 Contour plot of equivalent plastic strain at fracture in (a) SPIF (b) DSIF processes, and (c) strain at contact region

5.4.3. The effect of different tool settings

There has been little attention paid to the impact of contact algorithms and tool configurations in FE simulation of ISF processes in the past. The default assumption including rigid tool and sufficient machine stiffness served as the basis to use a rigid tool surface with time-displacement boundary conditions to define the tool path. However, the displacement of tool was re-calculated by the convergence achieved from the interaction between the tool surface and the elements in the contact region of the workpiece. This means the actual tool location was not kinematically identical to the initial time-displacement definition. This rigid tool definition guarantees stable rigid-to-deformable contact. The flexibility of tool allows real-time machine deflection to the pre-defined trajectory. However, this may also give the possibility of erroneous results due to such as excessive mesh distortion. This is due to the introduction of machine stiffness attached to the rigid tool creating multiple kinematic contact pairs between the deformable workpiece nodes and rigid tool surface.

A significant evidence of contact instability in FE simulations of ISF processes is the reaction acceleration of the ISF tool. Figure 5.13 shows the comparison of the average and maximum accelerations of the ISF tool during FE simulations. The average and maximum accelerations from flexible tools applied with machine stiffness (Case B) were significantly larger than the conventional rigid tool setting (Case A) and rigid tool with deflected toolpath (Case C) in both SPIF and DSIF simulations. This result suggests that although the flexible tool with machine stiffness could appropriately simulate the effect of machine compliance and obtain a close prediction in parts profile, the contact instability from actual FE simulation results in exaggeratedly interaction stress calculations hence the prediction of fracture damage. The reaction acceleration in DSIF with flexible tool is 3 times larger than that in the SPIF process. The large tool acceleration indicates it is harder to achieve a converged solution and, at the same time, more likely to result in inaccuracy in simulation.

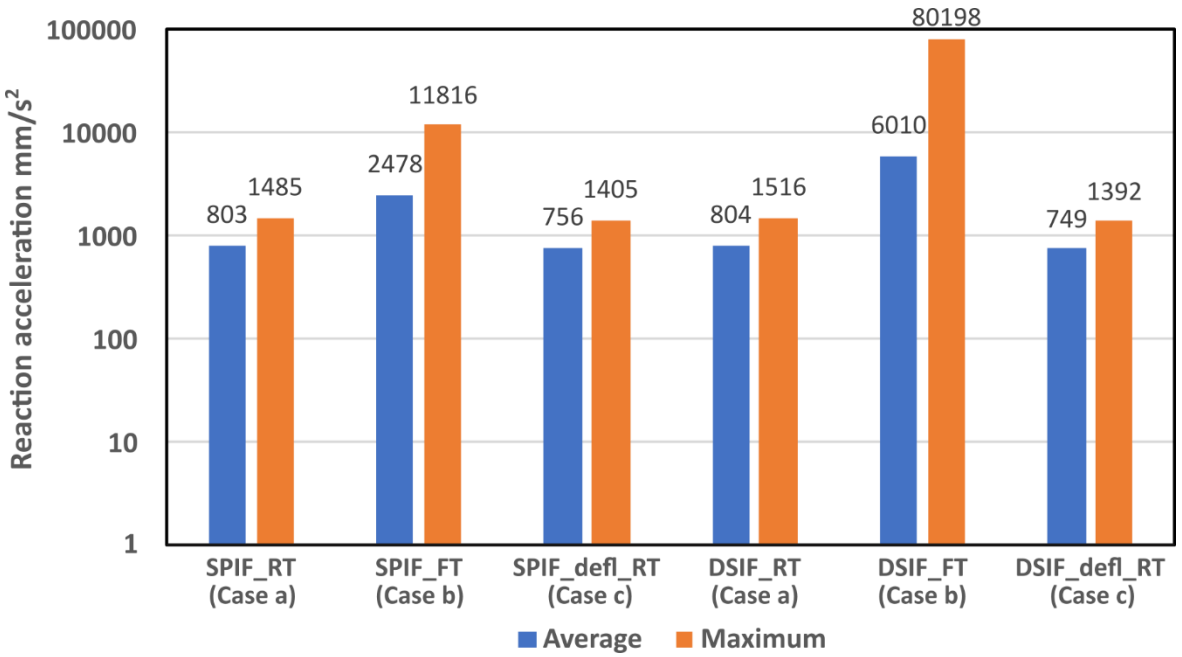


Figure 5.13 Comparison of average and maximum reaction acceleration during FE simulation among different tool strategies

The equivalent strain and damage evolutions by forming depth between the tools attached with machine flexibility and with deflected toolpath are compared in Figure 5.14. It is observed in SPIF and DSIF processes that the damage grows at a comparatively low rate when using flexible tool with machine stiffness. However, rapid acceleration of damage occurs at the end of forming stage and leads to material failure (Figure 5.14c, d). The equivalent strain rises rapidly as the elements lose load capability leading to a high damage value (Figure 5.14c, d). Thus the predicted fracture in simulations with flexible tools is significantly prior to the experimental results.

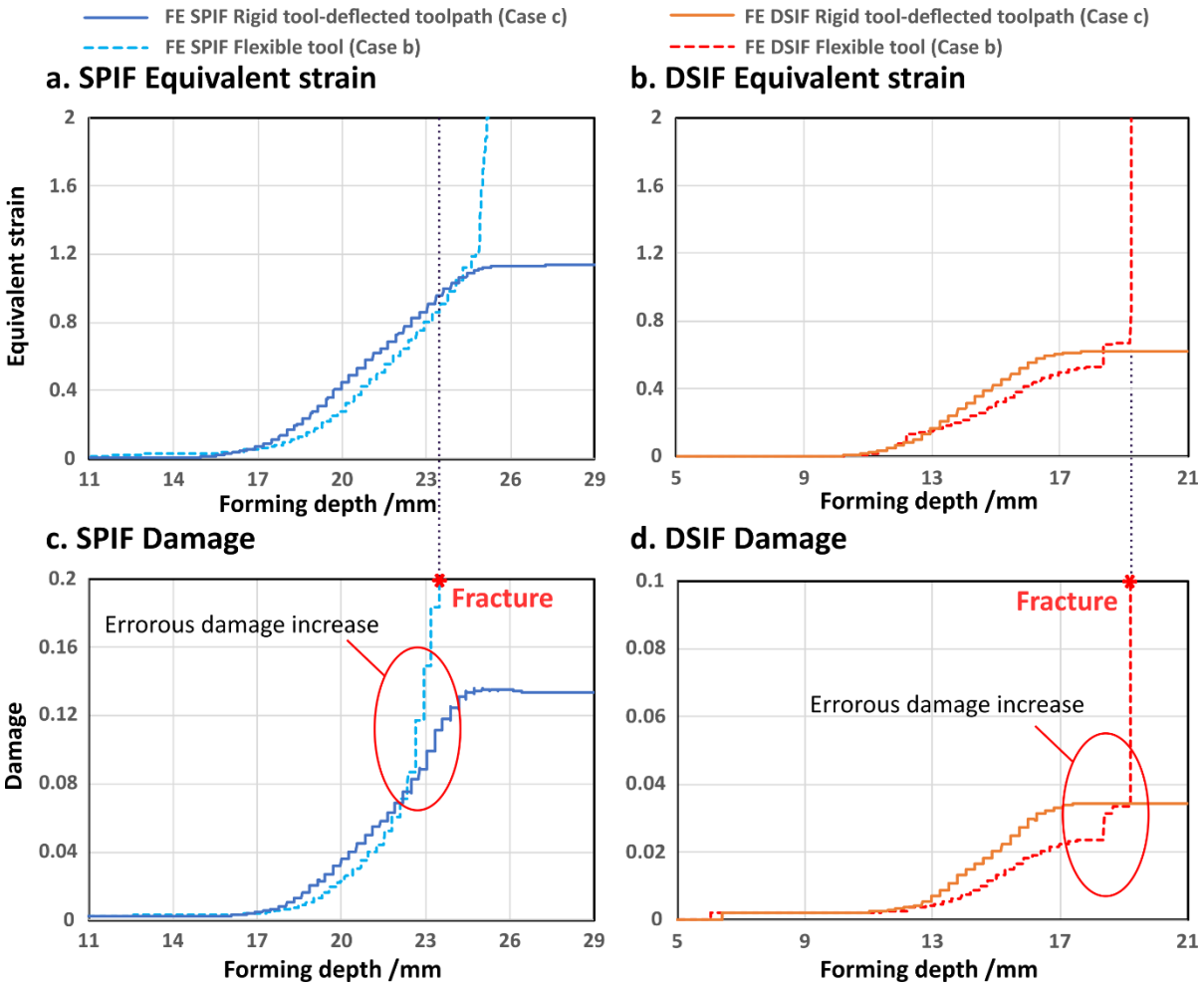


Figure 5.14 Comparison of equivalent strain and damage development from earliest fracture elements in FE models applied with tools with flexibility of machine stiffness (Case B) or the deflected toolpath (Case C) calculated by experimental measured forming forces.

5.4.4. Localised deformation and damage

The local stresses and damage are investigated based on four sections of the formed hyperbolic cone shape on the cross-section of the FE model as shown in Figure 5.15. The four sections are groups of elements selected based on the materials being formed at various forming depths to track the development of equivalent strain, damage and stress states between the SPIF and DSIF processes. There are four elements in each section through-thickness, which represent the "concave", "concave-mid", "convex-mid" and "convex" layers from the contact surface with the master tool. In DSIF simulation, Sections 1-2 are under double-contact and Sections 3-4 lose the contact of the support tool and

hence degenerate the DSIF to SPIF process due to machine deflection. In this chapter, the support tool is defined by the simulated stiffness and conventional toolpath that is calculated based on the sine law. As discussed in Chapter 4, the misposition of the master tool results in insufficient forming, which generates a gap between the desired and practical geometries. Thus the support tool would lose contact with the bottom surface of the part in these simulations.

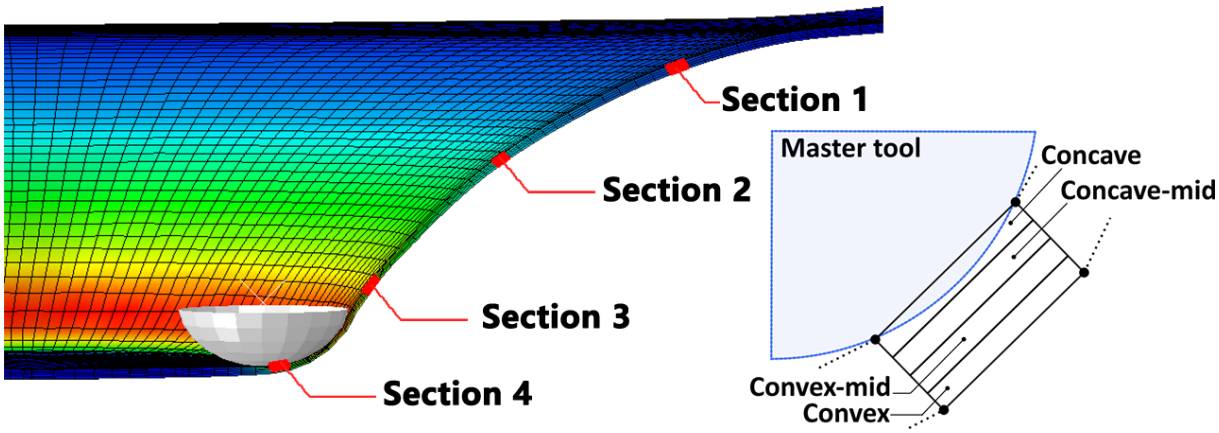


Figure 5.15 Schematic showing investigated element sections along the deformed component wall for sections 1-4.

The equivalent strain variations as a function of forming depth are plotted in Figure 5.16. The equivalent strain is increased in a specific range of forming depth, which indicates the occurrence of local contact when the tool passes on a particular section. In Section 1, the strain in DSIF is larger than in SPIF due to the squeezing effect between the master and support tools in DSIF. In Sections 2 and 3, the final strain values obtained from SPIF and DSIF processes are close. However, there are differences in strain levels between different element layers. In SPIF, the highest equivalent strain occurs on the convex surface elements whilst it is the concave side that has the highest strain in DSIF. It is difficult to solely use the double-contact feature in DSIF to explain the difference with SPIF. One possibility is the finer formed cone flange in DSIF creating solid support, which leads to the larger tension in the concave surface in and after forming stage. The nature of hyperbolic shape requires a larger strain in the concave side. The formation of such inner-convex feature in ISF processes relies on the tension deformation after local contact.

Therefore, the better formed cone flange region in DSIF process is expected to provide a stiffer support which is beneficial to more deformation of this hyperbolic shape (Figures 5.10a and b). As a result, a larger strain in concave side can be observed in DSIF because of this improved forming accuracy to the hyperbolic feature (Figures 5.16c, g, d and h). In section 4, the strain evolutions through layers keeps the similar trend in section 3 till the elements reaching fracture because of elements losing load capability.

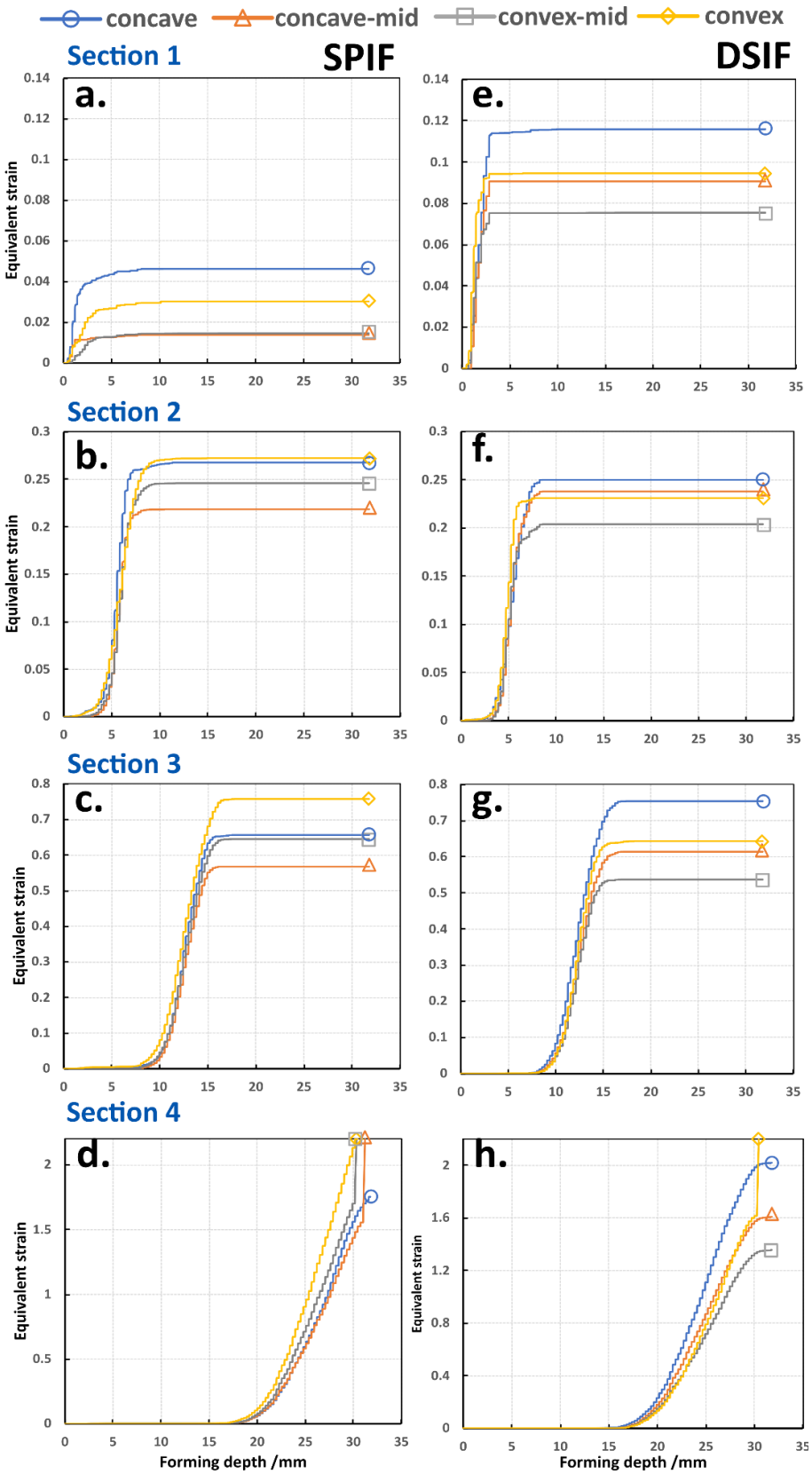


Figure 5.16 The comparison of equivalent plastic strain evolutions for sections 1-4 through 4 element layers

The damage evolutions versus the forming depth increases are shown in Figure 5.17. A high dependency between damage and equivalent plastic strain growth is observed in most elements as shown in Figures 5.17a, b, c, e and g, which present an almost identical trend to the equivalent strain evolution as shown in Figure 5.16. The suppression of damage growth by the support tool in DSIF can still be seen in Section 2 (Figure 5.17b, f). The variation of damage in Section 3 shows a pattern of discrepancy that the damage in the concave and convex elements in DSIF (Figure 5.17g) is much higher than the others. This high level of damage is related to the larger strain evolution in DSIF (Figure 5.16g). In Section 4 (Figure 5.17d, h), the damage evolution indicates the fracture initiates from the convex side of the workpiece in both SPIF and DSIF processes. This is in contrast to the concave side fractures in TCB and TCBC processes as observed in Chapter 3 (Figure 3.28). In comparison to Figures 5.17 d and h, the delay of material fracture in DSIF is also confirmed from the damage evolution results in Section 4. Only the convex element reaches fracture criterion ($D = 1$) in DSIF at the end of forming stage (Figure 5.17h), whilst only the concave element remains undamaged in SPIF at the same forming stage (Figure 5.17d). This leads to a conclusion that the stress states in different processes have a significant impact on the damage evolution although both two processes (SPIF and DSIF) have similar strain histories. From Section 3 and 4, both SPIF and DSIF simulations have been in similar single contact condition. The most discrepancies can be observed in the strain and damage evolution in these sections, especially in concave or convex layers, which may be also related to the formed geometry. This is close to the multi-passes increment sheet forming (M-ISF) to investigate the impact from the formed geometry to local deformation in terms of stress states and strains among depths through-thickness. The effect of through-thickness bending and the formed feature to local strain and damage evolution are topics requiring more experimental and analytical evidence in SPIF and DSIF processes.

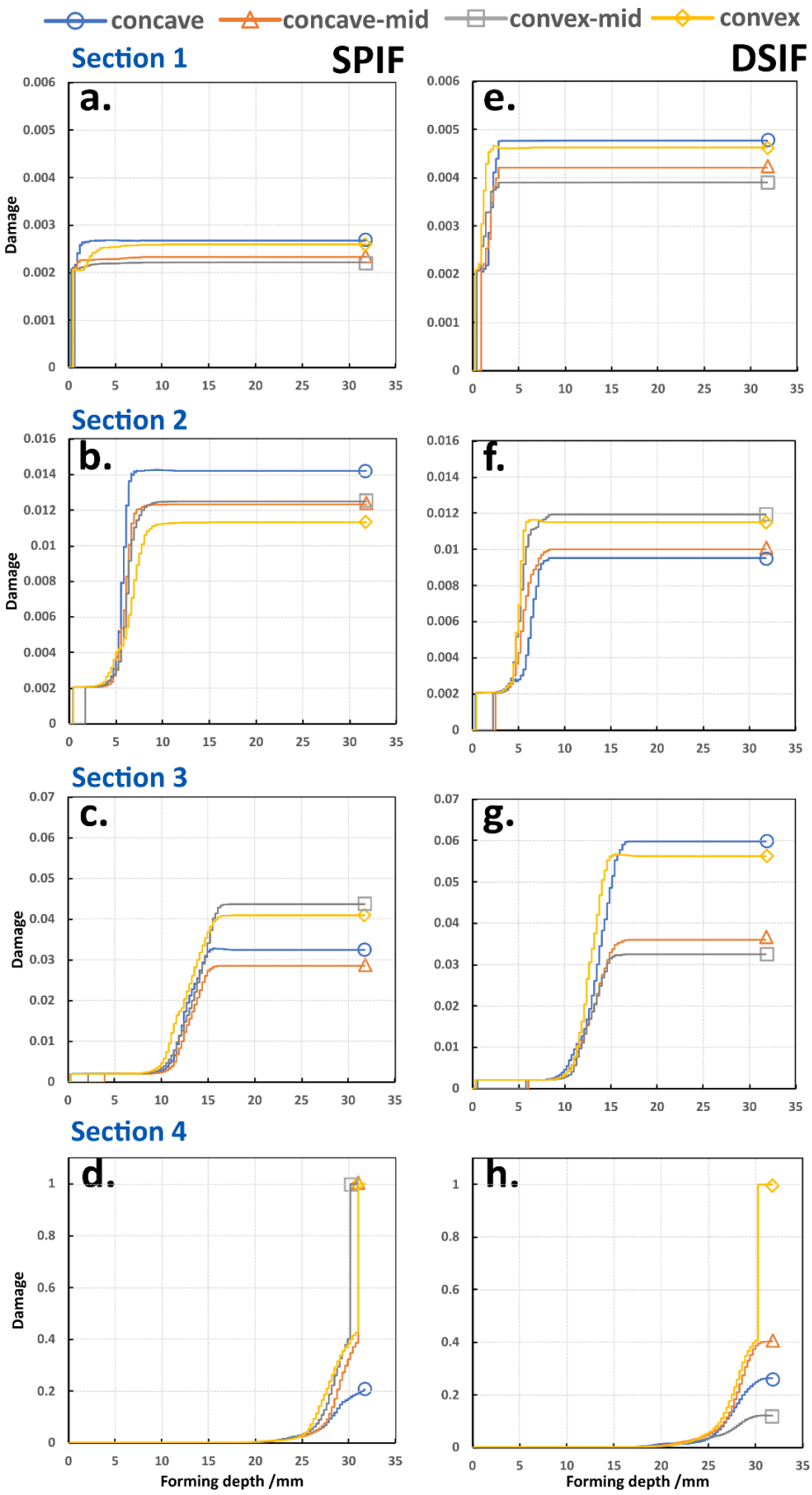


Figure 5.17 The comparison of damage evolution for sections 1-4 through 4 element layers

5.4.5. Local stress state evolution during tool and workpiece contact

To explain the deformation mechanisms of ISF processes, the contact between the tool and workpiece is essential to the local plastic deformation and evolution of damage. The stress triaxiality histories of a typical contact cycle in Section 2, where the support tool is still in contact with the workpiece in DSIF simulation, are extracted and compared through the layers of elements as shown in Figure 5.18. It can be observed that the local stress triaxiality evolutions in ISF processes are comparable to the TCB and TCBC processes (Figure 3.33). The evolution shows a representative bending-unbending deformation behaviour before, during and after the tool and workpiece contact in both SPIF and DSIF processes. Workpiece bending is associated with a notable increase of the stress triaxiality of the convex layer (outer layer) of the workpiece during the tool and workpiece contact. Although such an increase in stress triaxiality happens in both SPIF and DSIF, a higher level of stress triaxiality and changes is captured in SPIF than in DSIF. The same is true for the concave layer to have a higher stress triaxiality before and after the tool and workpiece contact, which may be referred to as unbending deformation. Such an unbending deformation condition sustains a low level of stress triaxiality of the convex layer of the workpiece. The lower level of stress triaxiality and its variation in DSIF than that of SPIF may be considered as an affecting factor to the delayed fracture or improved formability of DSIF over SPIF.

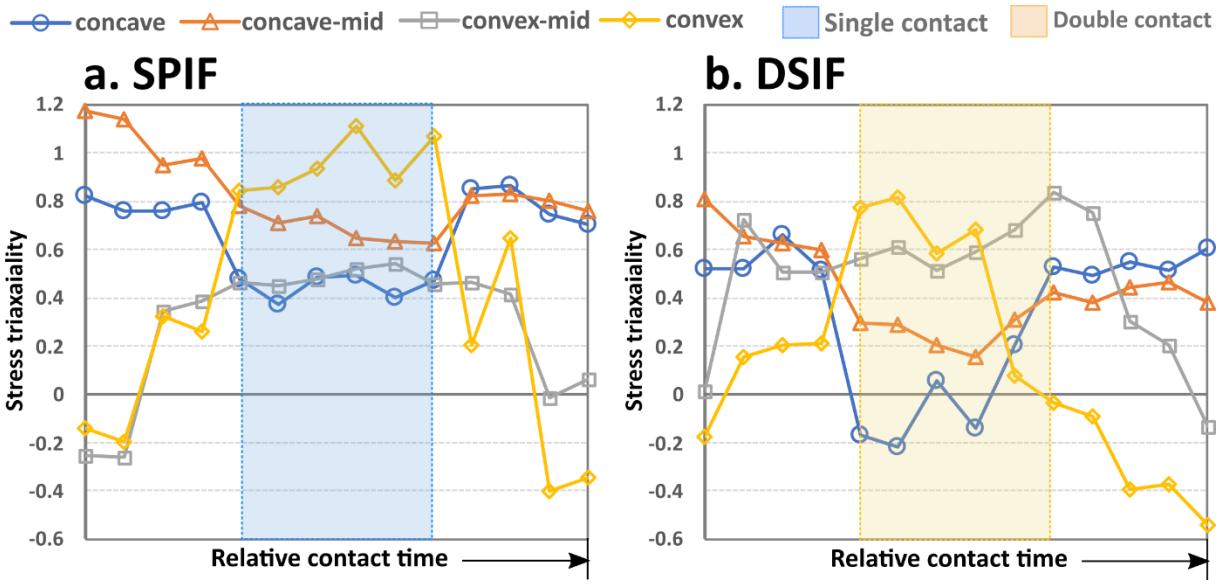


Figure 5.18 Development of local stress triaxiality in a single contact cycle in section 2: (a) SPIF. and (b) DSIF.

The progression of stress triaxiality and damage growth in the last 3 tool contact passes of SPIF and DSIF are plotted against each other in Figure 5.19. The element on the convex side, directly contacting the support tool, is selected to show the impact. The drop of stress triaxiality is clearly demonstrated in the last 2 local deformation cycles, which is under the double-contact condition in the DSIF process. The suppression to damage growth in deformation periods with double contact is also observed and results in less damage increase in the DSIF process, as it plotted in the red shadow area.

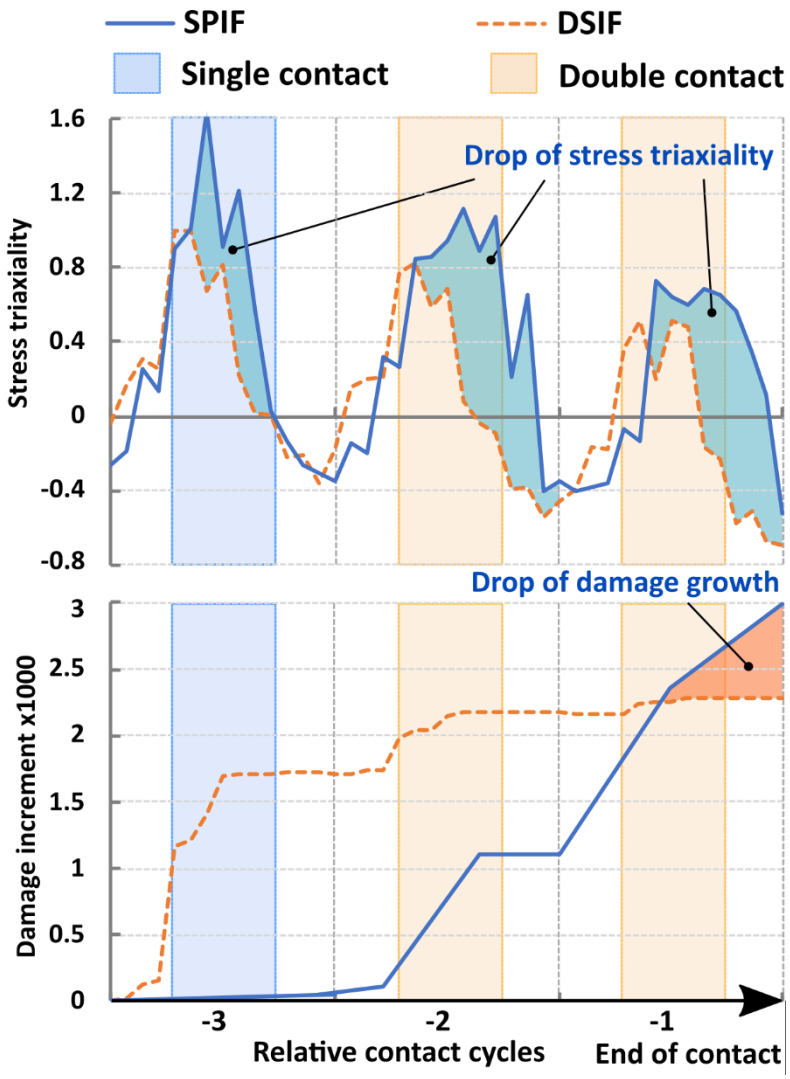


Figure 5.19 The development of stress triaxiality and corresponding damage increment of the concave element in the last 3 local deformation cycles before the end of forming in Section 2.

5.4.6. Deformation mechanisms in SPIF and DSIF

Similar to the cases of TCB and TCBC processes, the stress paths of SPIF and DSIF are drawn in the plane of stress triaxiality and Lode angle parameters. Figure 5.20 shows the stress path of a single local deformation cycle in SPIF and DSIF processes. Four elements through-thickness in section 2 are selected to represent different layers from the proposed FE results successfully predicting the fracture. The dot trend lines with cross starting points and directional arrows are plotted to demonstrate the stress state evolution before, during and after the localised deformation related to the tool contact period. The similarity and differences of deformation modes through thickness are also

compared between the SPIF and DSIF processes.

Unlike the TCB and TCBC processes, the stress paths in both SPIF and DSIF processes exhibit a strong correlation to material position through thickness, which indicates the larger bending effect in the 3D bending case. In the SPIF process (Figure 5.20a), the tool-contacting layers (concave and concave-mid layers) stay at plane strain tension condition before the bending stage. Then the stress state transforms to pure tension with high stress triaxiality along the plane stress path. On the other side, the material away from tool contact (convex-mid and convex layers) is under compression at initial uncontacted stage because of elastic recovery. In this case, the stress state begins with axisymmetric compression and follows a plane strain deformation route, finally reaches to a state between equi-biaxial tension and flat grooved tension. The material in the outer surface is under the equi-biaxial compression condition in the reverse-bending stage.

In DSIF process (Figure 5.20b), the additional tool squeezing reduces the stress triaxiality of the entire forming stage. This leads to increased compression and shear in local deformation in the concave and concave-mid layers. The drop of stress triaxiality also results in more standard equi-biaxial tension deformation on the convex side during contact, which ends at plane strain compression when the bending stage is completed.

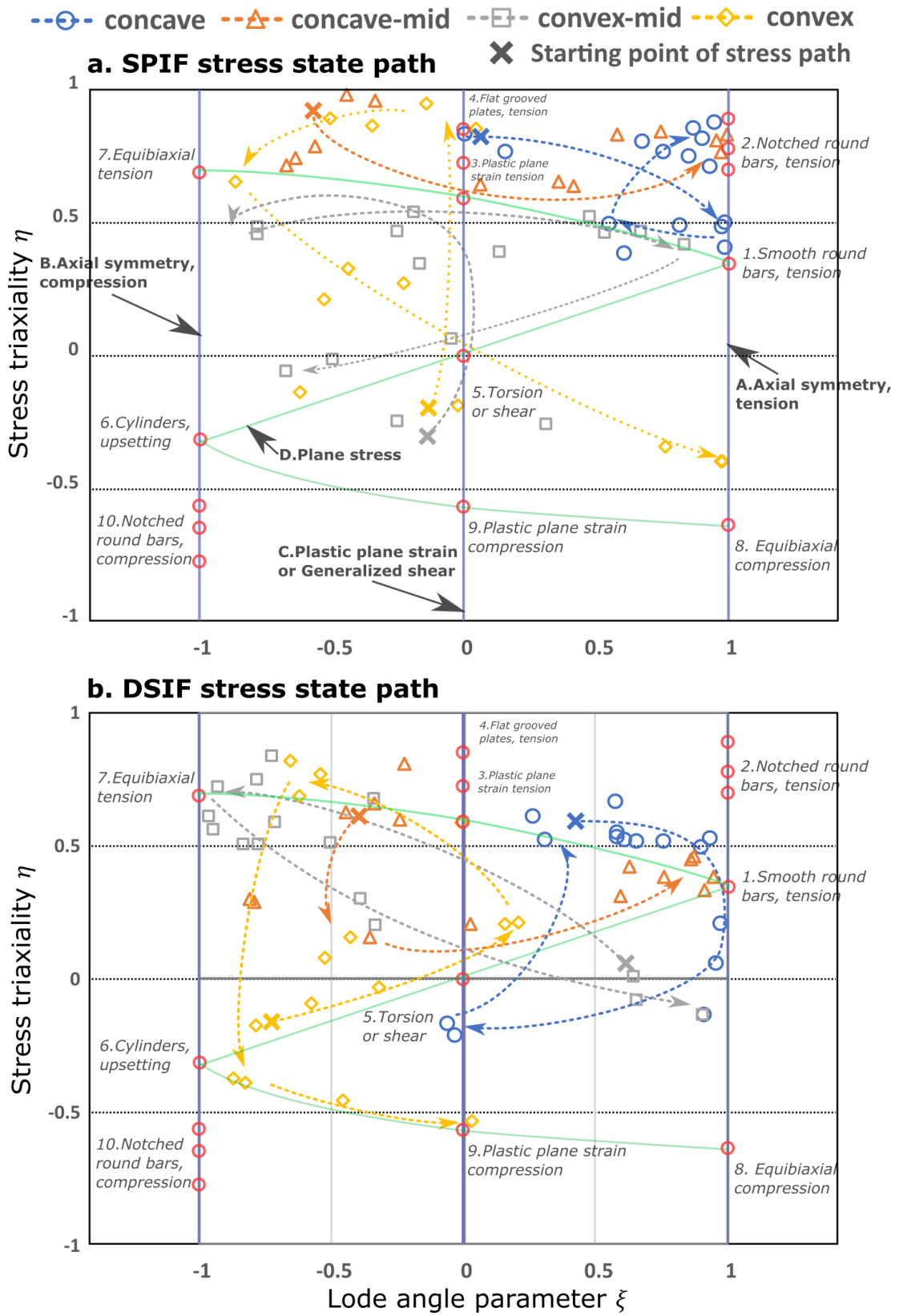


Figure 5.20 Stress paths in a local deformation cycle of (a) SPIF and (b) DSIF in the plane of stress triaxiality and lode angle parameters.

In conclusion, the stresses from FE model indicate that the deformation modes differ at different through thickness positions of material. The deformation modes are crossed over from plane strain tension to equi-biaxial tension conditions from the inner to the outer surface of bending. The additional tool contact in DSIF reduces the stress triaxiality in all layers and causes a shift of stress state on the convex side, the layer where fracture initiated, away from zero Lode angle parameter $\xi = 0$. The formability is benefited from this shift as the deviatoric or shear stresses decrease when the Lode angle parameter ξ approaches ± 1 [183]. The FE stress results confirm the hypothesis of the analytical model and, at the same time, show its limitations. The pure equi-biaxial tension assumption is close to the practical case in DSIF process but underestimates the damage evolution in SPIF. It is still reasonable to use equi-biaxial tension stress state used in analytical fracture prediction because the fracture always initiates on the convex side. However, the implementation of the combined deformation modes through thickness in the analytical model may improve the precision of prediction.

5.5. Discussion

5.5.1. Similarity and differences between TCB/TCBC and SPIF/DSIF

TCB and TCBC tests are similar to SPIF and DSIF processes, particularly in the local deformation features. The local bending introduces the local deformation feature which is created and propagated with tool movement throughout the whole workpiece. This combination of local deformation and tool movement induced local stress modification being beneficial to the whole process formability. The stress triaxiality and shear reduction by additional compression by the support tool can postpone the damage growth during local deformation, hence effectively improves the formability of both TCBC and DSIF processes.

The change from 2D contact in TCB/TCBC processes to 3D spherical contact in SPIF/DSIF processes results in significant differences of stresses in local deformation region. Comparing the stress path graphs (Figures 3.34 and 5.20), the simplification from

biaxial bending in SPIF and DSIF to uniaxial bending in TCB and TCBC causes the reduced stress triaxiality and mirrored Lode angle parameter according to axis $\xi = 0$. The reduced stress triaxiality leads to a larger fracture strain and highlights the dominant role of reverse-bending in the material damage evolution in TCB and TCBC processes, which is also demonstrated on the fracture initiation position. The reason that the fracture initiates on the surface contact to the master tool is because of the relatively high stress triaxiality ($\eta = 1/3$) and plastic strain increase during pure tension deformation in the reverse-bending stage. In the SPIF and DSIF processes, the deformation modes are mainly between biaxial tension ($\eta = 2/3$) and plain stain tension condition (η above 0.6). The change of Lode angle parameter means to obtain the comparative results between TCB/TCBC and SPIF/DISF processes is influenced by Lode dependent material, which has asymmetric fracture strain with Lode angle parameters $\xi = 0$. Therefore, the Nakajima tests would be the closer case to SPIF and DSIF processes than to TCB and TCBC processes from a local stress point of view. This is supported by experimental data from Gatea [98] that the fracture strains from Nakajima tests are close to SPIF test results. The forming limit diagrams of the SPIF process and Nakajima tests were almost identical which may be considered as an evidence of the similar fracture mechanism [98, 184] as shown in Figure 5.21.

However, the improved formability in TCBC tests is complied with the same mechanics of the formability enhancement from SPIF to DSIF. The additional tool compression is beneficial to the delay of ductile fracture for the whole process owing to the local deformation feature. From the aspect of local stress state, the TCBC process can be used as a method of experimental validation to test the effect of stress-related parameters, such as compression force and the relative tool position although there is a degree of uncertainty in contact area changes, which is difficult to predict using either an analytical model or FE simulations. Therefore, the TCBC process, in general, is capable to validate the mechanics of improved formability from SPIF to DSIF, and to verify the effective parameter adjustments. In conclusion, the TCB and TCBC processes are

represented in the mechanics and parametrical investigation of relative formability improvement, but it is a less effective method to predict the fracture strain value or to study the fracture mechanisms of the SPIF and DSIF processes.

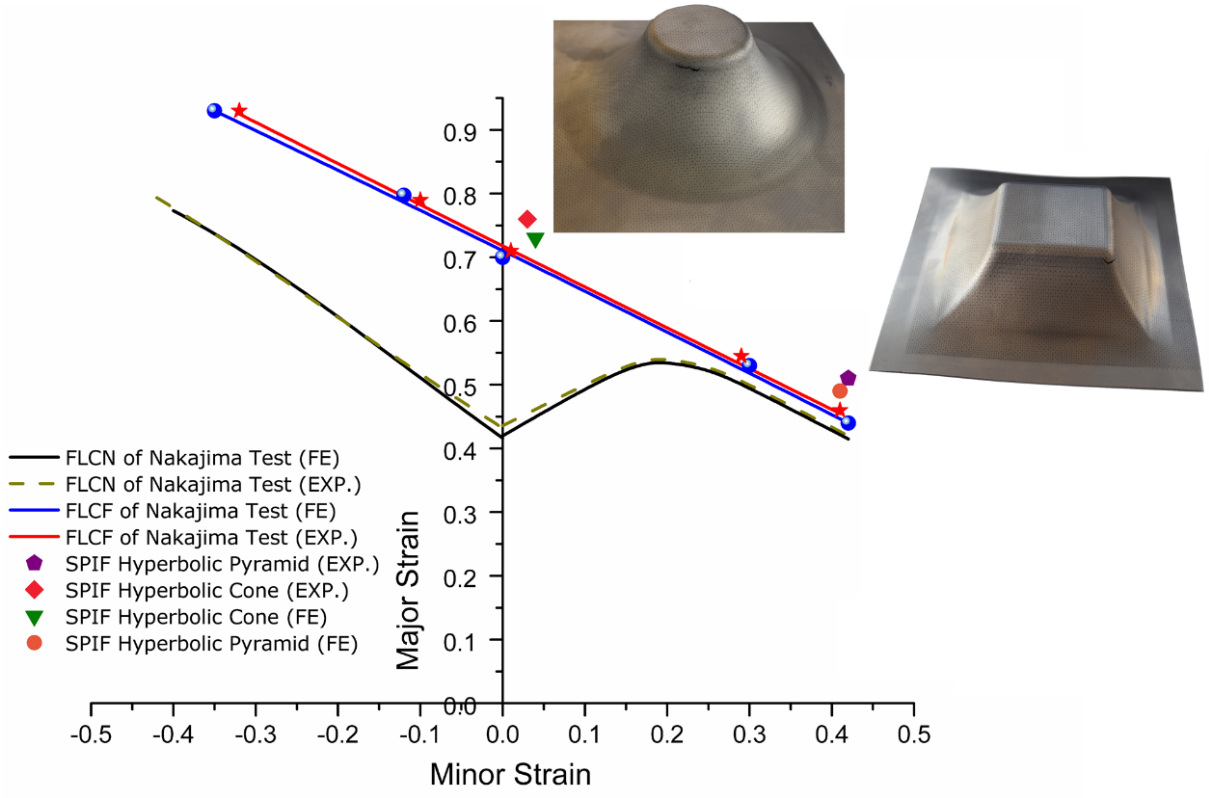


Figure 5.21 Fracture limit curves from numerical and experimental Nakajima and SPIF tests [98].

5.5.2. Influence of tool and workpiece contact in FE simulations

The ISF modelling is a quasi-static process with a significant challenge for a good balance of simulation accuracy and computing efficiency. Because of the local deformation feature under either SPIF or DSIF processing conditions, sufficient number of elements in the contact area are required to achieve stable convergence. On the other hand, the contact algorithm in ABAQUS leads to potentially erroneous results in the calculation of relative sliding between the tool and workpiece. Figure 5.22 shows two contact formulations applied in ABAQUS/Explicit. The finite-sliding formulation (Figure 5.22a) by default uses contact detection per 100 increments frequency. When the mesh density or the contact detection frequency is insufficient, the surface interactions for the instance of node 101 could only be detected between surface 201-202 and surface 501-502. The small jumps

over a part of nodes on the master surface such as nodes 203 and 501 can lead to the deflections of pre-defined toolpath and large reaction force of tools. Using a rigid tool and fully defined toolpath in FE simulation, the inaccurate contact is exhibited with minor fluctuations on tool displacement output. However, when the tool is applied with flexibility, the interaction between deformable bodies is amplified by the small contact jumps, which results in numerical fluctuation for convergence, mesh distortion or exceptional peak of stresses and accelerations as shown in Figure 5.10. This may be the reason why the flexible tool setting was unable to predict the fracture correctly although the defined machine and tool stiffness and the profile prediction was close to practical tests. Theoretically, the small-sliding formulation (Figure 5.22b) using a local tangent plane of the corresponding node on the slave surface can avoid the small contact jumps over nodes and improve computational efficiency. The accuracy of the small-sliding formulation is highly dependent on mesh density on the surfaces of the workpiece. There are still many prior limitations such as element types to implement small-sliding formulation in practice. Therefore, it is valuable to investigate the impact of contact algorithms and tool settings in ISF FE modelling. If suitable modification of contact formulations can be made to improve the accuracy of interaction between the tool and material surfaces, the model with flexible tool setting may be implemented directly in FE simulation without the need for calibration of toolpath according to experimental test data.

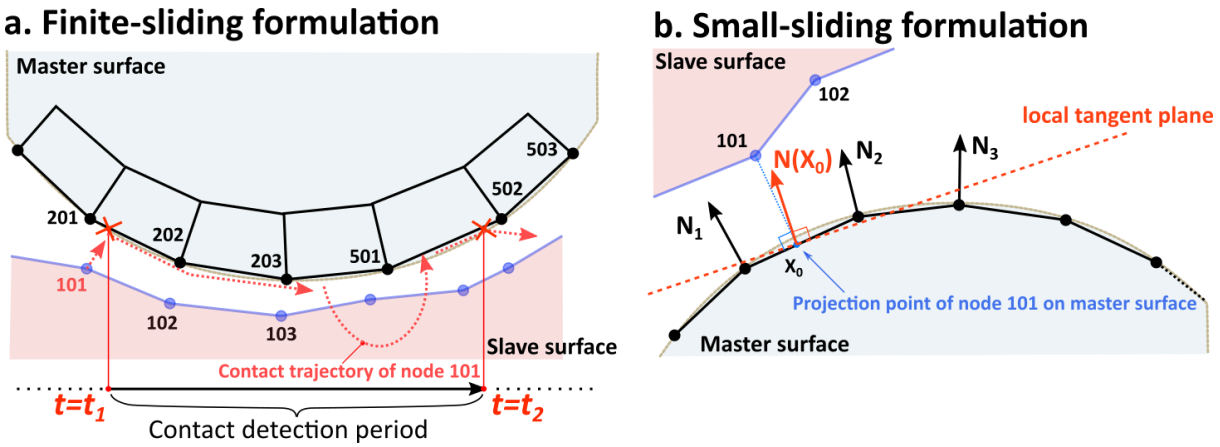


Figure 5.22 Schematics of two contact pair algorithms in ABAQUS/Explicit (a) finite-sliding formulation, and (b) small sliding formulation.

5.5.3. The limitations of the presented analytical model

The fracture strain predictions from the presented analytical model are in an agreement with FE simulations. Figure 5.23 illustrates the damage evolution by equivalent strain increase from the analytical model. The damage corresponding to equivalent strain from the elements through thickness in FE simulations for SPIF and DSIF is superimposed in Figure 5.23. It can be observed that the fracture strain in DSIF, predicted by both the analytical and FE models, is larger than that in SPIF process. Comparing the analytical model to FE simulation, the trend of development and the final fracture estimation are closely matched. One of the reasons is that the identical damage model was used in both the analytical and FE predictions. On the other hand, this agreement also indicates the local strain and stress analysis in the analytical model captures the nature of both the SPIF and DSIF processes.

The differential evolution of damage among elements from FE results at layers in through-thickness direction, due to discrepancies of deformation modes, points out the limitation of this analytical model as well. Though the effect of reverse-bending is taken into consideration, the contact mechanisms, the desired geometry leading to various stress states and the through-thickness effect are not included in the analytical model. The local contact and forming shape may change the local stress states and distribution which

leads to different fracture results. The through-thickness effect is enforced in thick sheet forming. In these conditions, the FE simulation is a more robust tool to give an accurate prediction while the analytical model is efficient when the initial hypothesis is valid.

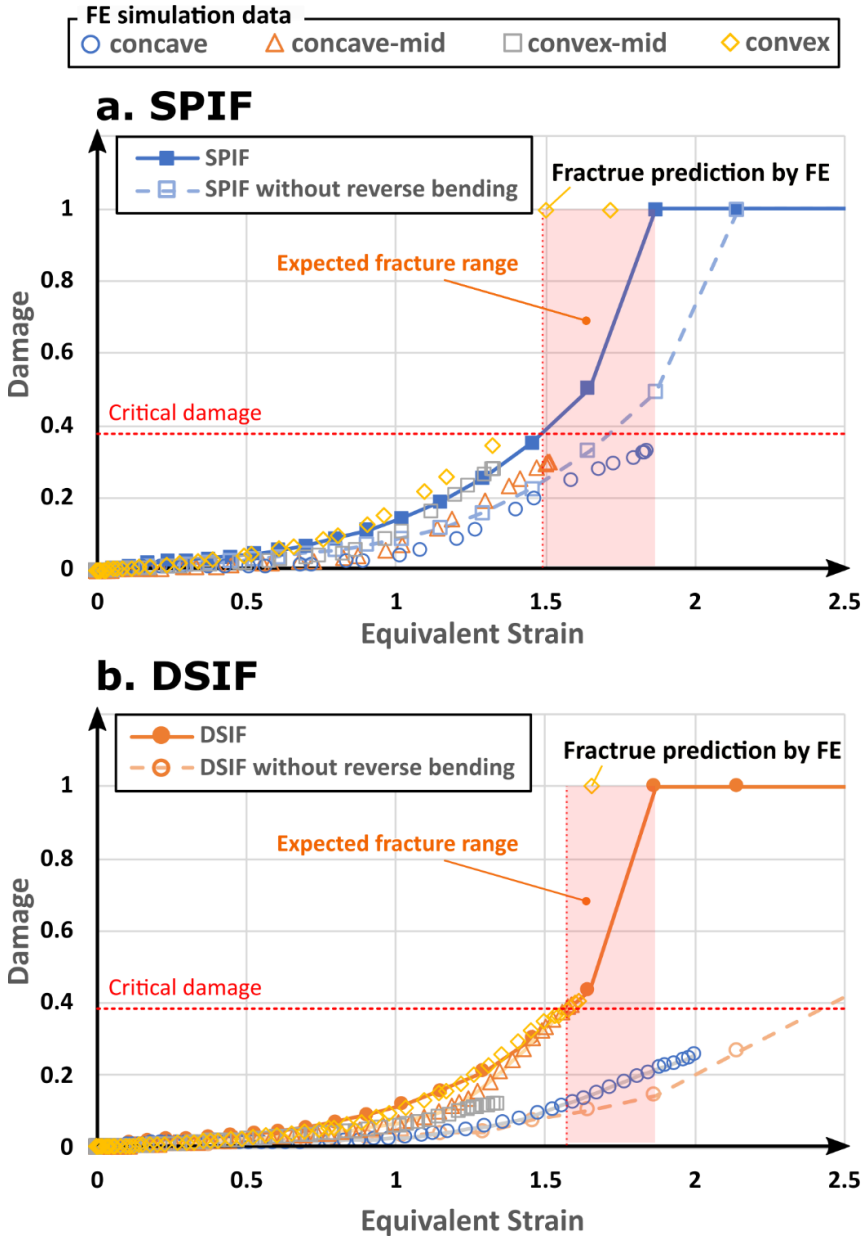


Figure 5.23 The damage development by equivalent strain from analytical model and FE simulations (a) SPIF, and (b) DSIF

5.5.4. The deformation and fracture mechanisms in SPIF and DSIF

The FE model with the deflected toolpath and the shear modified GTN model is able to predict the fracture in both SPIF and DSIF processes. The key is to determine the stress

state changes and quantify its influences on the variation of damage variables defined by void volume fraction and shear damage in the shear modified GTN model.

In the modification of shear mechanisms of the proposed GTN model, the stress description using stress triaxiality and Lode angle parameter is effective in predicting the onset of fracture in TCB and TCBC testing. The stress paths were in agreement with previous studies [26, 185] that the local bending generated high bi-axial tension on the convex surface combined with through-thickness shear. Figure 5.24 indicates that the through-thickness shear in DSIF is smaller than that in SPIF hence leads to a lesser degree of shear damage of DSIF than that of SPIF. This may be explained by the additional squeezing effect between the support tool and workpiece contact to achieve a lower level of through-thickness shear in DSIF.

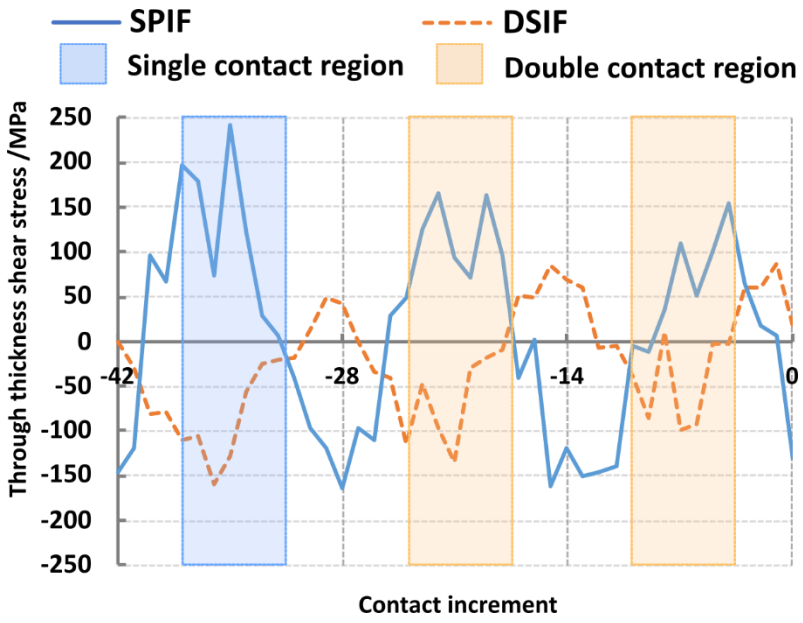


Figure 5.24 Comparison of through thickness shear stress in FE simulations for SPIF and DSIF processes.

Two significant questions about the formability improvement from SPIF to DSIF can be answered from these results: the mechanics of formability improvement and the reason for larger forming depth achieved even with the occurrence of loss of contact of the support tool during DSIF processing. The support tool enables a reduction of stress triaxiality and shear stress, which means the hydrostatic stress takes a dominant role in

deformation and produces a larger strain without fracture. The local stress changes are propagated to the whole forming area by tool travelling and postpone the microstructure damage formed in the workpiece. However, this alone cannot explain the fracture delay after the degeneration from DSIF to SPIF process happens due to loss of contact of the support tool. The material in the latter half of forming process is not benefited by the change of stresses and less damage accumulation from the earlier half of double-contact deformation passes due to the highly localised deformation. The formability improvement after the loss of contact of the support tool might be explained by the increased forming stability in DSIF. In the early forming stage, the tool squeezing results in the steeper transition part (Figure 5.10) and the higher level of strain hardening (Figure 5.16a, e). The strengthened formed region provides enhanced peripheral support that reduces the local deformation instability and improves the formability [30, 64]. This hypothesis needs further investigation with the support of microstructure evidence in future research.

5.6. Conclusions

The deformation and fracture mechanisms of SPIF and DSIF processes are modelled using an analytical model and FE simulation using the shear modified GTN model. The formability in SPIF and DSIF processes was evaluated in terms of fracture strain by loading cycles which suggests that smaller step size and tool diameter are preferable process parameters. For FE damage modelling of SPIF and DSIF processes, three tool modelling strategies were developed and compared in order to capture the effect of machine stiffness in FE simulations. The results showed reasonable predictions of the fracture depths and profiles as compared to experimental results. Finally, the deformation mechanics in SPIF and DSIF are investigated based on the stress and strain evolution relating to damage accumulation from FE simulations. The main conclusions may be drawn in the following:

1. The material in ISF processes is cumulatively deformed by bending and unbending based on tool contact. As the plastic deformation only occurs with

tool contact and propagates by tool travelling, the improvement of local material formability by the modification of local stress states is effective to the whole process.

2. In DSIF process, a part of material is under the double-tool squeezing dependent on the relative tool position. The double-contact results in reduced stress triaxiality and through-thickness shear that leads to the decreased shear damage, delayed fracture and hence improved formability.
3. In comparison with different strategies with the inclusion of machine deflection effect in FE modelling, the strategy to incorporate the deflected toolpath, based on analytical stiffness model and experimental forming forces history, with the rigid tool gives the most accurate prediction to fracture.
4. The FE modelling with the deflected toolpath and the shear modified GTN model are feasible to predict the fracture depth and forming profile with less than 8% discrepancy to the experimental measurement. In agreement with previous studies [26, 186], the results show that the fracture initiates on the outer surface of the transition area between the forming and the formed regions.
5. The stress state paths are evolved in through-thickness direction in both SPIF and DSIF processes. On the concave side, which is under contact with the master tool in DSIF, the plane strain and uniaxial tension are the dominant deformation mode. On the convex side, equi-biaxial tension is the major deformation mode.
6. The process stress paths (Figure 3.34 and 5.19) indicate that the TCB and TCBC process is mainly under plane stress deformation of axial tension. Compared to the plane strain and equi-biaxial tension deformation in SPIF and DSIF processes, the different stress states lead to opposite fracture initiating locations. However, the additional compression applying on the support tool plays a similar role in the formability improvement that the damage growth

reduction is benefited from the reduction of stress triaxiality and through thickness-shear.

CHAPTER 6 CONCLUSIONS AND FUTURE WORK

6.1. Introduction

The key conclusions of deformation and fracture mechanisms in TCB/TCBC and SPIF/DSIF processes are summarised in this chapter. The effect of machine and tool stiffness on the forming accuracy and FE modelling is concluded as a significant phase in progress. This is followed by an outline of recommendations for future work.

6.2. Conclusions

The main objective of this study is to understand the mechanisms of deformation and fracture, especially the reasons for formability improvement brought by the additional compression in DSIF processes. With respect to the forming mechanics and machine errors calibration in FE modelling, the accurate prediction to fracture can be made and the deformation and fracture mechanisms may be presented. The key findings for each of the three main sections are concluded as follows:

6.2.1. TCB and TCBC processes

TCB and TCBC are considered as the representative simplifications of SPIF and DSIF processes. This chapter aims at using analytical analysis and experiments to investigate the effect of process parameters, including the bending depth and compression. A shear modified GTN model was developed with attentions to stress triaxiality and Lode angle parameters. FE simulations were conducted using ABAQUS/Explicit and succeeded in fracture prediction in both TBC and TCBC processes of grade 1 pure Ti with errors under 8%. Based on the results, it can be concluded that:

- The deformation mechanisms in TCB and TCBC processes included local bending deformation and its propagation with cyclic tool movements. The bending effect reduced the required tensile force for material yielding in the bending region which secures the local deformation feature.
- The local bending produces the strain discrepancy through thickness, which would

be balanced in the following reverse-bending stage. In the reverse-bending process, the surface previously in contact with the master tool is under uniaxial tension deformation where the absence of contact pressure results in higher stress triaxiality and more damage accumulation. Therefore, the ductile fracture initiates on the surface contacting the master tool.

- The additional compression in TCBC reduces the stress triaxiality and suppresses the microstructure damage growth during the bending stage. The drop of stress triaxiality and tension-combined-compression deformation mode leads to a delay of final fracture.
- The FE model associated with the shear modified GTN model successfully predict the elongation and initial fracture location in comparisons with TCB and TCBC experimental results. This suggests the different roles that shear and compression play in TCB and TCBC processes determine their descripencies in formability. Such difference can be indicated with the combination of stress triaxiality and Lode angle parameter to give an accurate evaluation to the deformation modes and damage evolution.

6.2.2. Machine and tool stiffness modelling in DSIF

This chapter pays attention to ISF machine and tool stiffness and their impact to DSIF process formability as well as its incorporation in FE simulations. Two goals are achieved: the first is to establish a general approach to construct a stiffness matrix model based on ISF machine structure; the second is to incorporate the stiffness matrix model in FE modelling that simulates the positional errors of ISF tools. The main conclusions may be summarised below:

- The pneumatically supported tool can provide an automatic compensation with consistent backup force to prevent the occurrence of loss of contact in DSIF process. However, it was observed in the experiments that “over-bending” was induced by the support tool proactively squeezing the workpiece due to the master tool mispositioning. The “over-bending” was appeared as inaccuracy in the part profile

especially when forming parts with large wall angle.

- The stiffness matrix model for a Cartesian-structured ISF machine can be established based on HTM methods and reasonable simplifications to beam assembly. The implementation of the stiffness model in FE simulation significantly reduced the geometry differences between the FE predicted and experimentally measured profiles for both SPIF and DSIF processes.
- Compared to the conventional rigid tool configuration in FE simulation, the application of flexible tool configuration with stiffness matrix model reduces the peak strain value and mitigates the strain concentration. These changes may be due to the transition of tool-workpiece interaction from kinematic to kinetic mode.

6.2.3. Deformation and fracture mechanisms in DSIF process

This chapter aims at accurate prediction of fracture in SPIF and DSIF simulations and a better understanding of the deformation and fracture mechanisms. The shear modified GTN model, validated in TCB and TCBC simulations, was implemented in FE modelling incorporated with the conventional rigid tool or the flexible tool configurations involving machine deflections. The conclusions can be made from these studies:

- ISF processes are essentially 3D continuous bending under tension deformation conducted with limited forming cycles. The number of deformation cycles is equal to the tool contact times which is determined by the local wall angle, step size and the master tool radius.
- The derived analytical model predicted the range of equivalent fracture strain and agreed with experimental results of SPIF and DSIF using grade 1 Ti sheets. The model suggested that the larger step size and master tool radius are negative factors for ISF process formability.
- The FE model by using the shear modified GTN model and the toolpath calibrated by machine deflections can predict the fracture depth accurately for both SPIF and DSIF processes with errors less than 8%. The fracture strain obtained in FE model matches the estimation by the analytical model.

- There is no essential difference between the deformation and fracture mechanisms in SPIF and DSIF processes. From the inner surface contacted with the master tool to the outer surface, the dominant deformation modes transfer from the uniaxial to biaxial tension. The formability enhancement is a corollary of the drop of stress triaxiality by additional compression, which delays the void volume fraction and damage accumulation.
- Similar to TCB and TCBC processes, the deformation is localised to the bending around the master tool and propagated with tool travel. The double-tool squeeze reduces the stress triaxiality and through-thickness shear that improves the formability of DSIF process.
- The evolution from 2D bending in TCB/TCBC to the 3D bending in SPIF/DSIF increase the stress triaxiality in the convex side. The biaxial tension in the convex side of the SPIF and DSIF processes outweigh the reverse-bending in the concave side in terms of damage accumulation. This induces the fracture initiated at the convex surface in SPIF and DSIF in contrast to the fracture initiation at the concave surface in TCB and TCBC processes.

6.3. Thesis novelty and contributions to knowledge

The main contributions of this PhD research are summarised in the following:

1. The new shear modified GTN damage model developed is capable of accurate prediction of damage evolution under the effect of both shear and compression. In validation of FE results for TCB and TCBC processes with grade 1 pure Ti, the elongation to fracture has been correctly predicted.
2. For the first time, the GTN model with shear modification has been implemented in DSIF processes and provided accurate forming depth prediction as well as the fracture location. The FE results matched well with the experimental measurement, whereas the fracture location agreed with previous studies [35].
3. Using reliable FE simulation results, the stress state paths during local deformation by

tool contact in TCB/ TCBC and SPIF/ DSIF have been plotted in the plane of stress triaxiality and Lode angle parameters for the first time. The stress triaxiality and Lode angle parameter trace plots clearly illustrate not only the evolution of deformation modes but also the similarities and differences between TCB/TCBC and SPIF/DSIF.

4. The analytical models for TCB/ TCBC and SPIF/ DSIF processes have been developed based on stress analysis and combined with the local strain growth. The analytical results produced formability assessment for various forming parameters in agreement with the experimental test results.
5. A specific "over-bending" phenomenon is reported as a likely reason of formability reduction due to insufficient machine stiffness in pneumatically supported DSIF process. This highlights the need for consideration of the machine stiffness whether to use a dedicated machine or a set of robotic systems in DSIF processes.
6. In the case study of a dedicated DSIF machine, a machine-tool stiffness model is derived using the homogeneous transformation matrices (HTM) method. This machine-tool stiffness model has been implemented via ABAQUS connector elements attached to the forming tools in FE simulations of SPIF and DSIF processes. A significant improvement of prediction accuracy in the formed geometry was observed by comparing the FE results to experimental measurement.

6.4. Future work

The thesis investigates the mechanisms of formability improvement in the incremental sheet forming process via supplementary compression. The FE simulation implemented machine stiffness and the new shear modified GTN model enabled accurate evaluations of damage and deformation mechanisms. Meanwhile, there are also many limitations, which requires further improvement in both experiment and simulation. The areas for future work are classified in different aspects and summarised in the following:

6.4.1. TCB and TCBC testing

- This study validated TCB and TCBC processes as advantageous standardised

testing methods for material to evaluate the material formability and its improvement under compression. The detailed parametric investigations to compression or other parameters such as temperature are still valuable in TCB or TCBC processes. Such results can be used for validation in ISF experiment design

- Theoretically, the material with the larger Lode angle dependence is expected to have the larger elongation-to-fracture improvement from TCB to TCBC tests. The theoretical proof and corresponding experiments need to be conducted with more materials including polymers.

6.4.2. Machine stiffness and tools configuration in FE model

- The need for machine stiffness modelling depends on the practical machine error. The presented machine stiffness method is an analytical solution based on the general structure of the machine. This can be applied to real-time toolpath offset to machine compliance if the experimental calibration is appropriate.
- The current shear modified model focuses on void growth under specific stress states which include limited material soften mechanisms for cyclic load-unload conditions. Recent studies [99, 104] presented the improved force predictions when Bauschinger's effect was involved in the constitutive model. The refinement of material constitutive model is also a direction for improvement in ISF simulation.

6.4.3. DSIF process

- The effect of relative tool position and support force for conventional or pneumatic support DSIF processes are not fully understood. The study to the effect of tool positions, targeted on the further formability improvement, also requires precise determination of local deformation area, a focused research topic but hard to quantify experimentally.
- The microstructure changes in SPIF and DSIF are reported by studies [70, 113, 187]. It is observed that the refined microstructure near the surface contacting with the master tool. In conventional double-contact tension and compression process, such as cryorolling [164, 188] and equal channel angular rolling [166], the

reduction of misorientation of microstructure is presented as evidence of improved ductility of metal material. It is worth examining the microstructure refinement in DSIF and TCBC process from the material point of view.

REFERENCES

[1] Emmens, W. C., Sebastiani, G., and van den Boogaard, A. H., 2010, "The technology of Incremental Sheet Forming—A brief review of the history," Journal of Materials Processing Technology, 210(8), pp. 981-997.

[2] Mason, B., and Applton, E., 1984, "Sheet metal forming for small batches using sacrificial tooling," 3 rd International Conference on Rotary Metalworking Processes(ROMP 3), pp. 495-511.

[3] Silva, M. B., and Martins, P. A. F., 2012, "Two-Point Incremental Forming with Partial Die: Theory and Experimentation," Journal of Materials Engineering and Performance, 22(4), pp. 1018-1027.

[4] Hirt, G., Bambach, M., Bleck, W., Prahl, U., and Stollenwerk, J., 2015, "The Development of Incremental Sheet Forming from Flexible Forming to Fully Integrated Production of Sheet Metal Parts," Advances in Production Technology, C. Brecher, ed., Springer International Publishing, Cham, pp. 117-129.

[5] Kiridena, V., 2017, "Rapid freeform sheet metal forming: Techology development and asystem verification," U. S. D. o. Energy, ed.

[6] Maidagan, E., Zettler, J., Bambach, M., Rodríguez, P. P., and Hirt, G., 2007, "A New Incremental Sheet Forming Process Based on a Flexible Supporting Die System," Key Engineering Materials, 344, pp. 607-614.

[7] Meier, H., Smukala, V., Dewald, O., and Zhang, J., 2007, "Two Point Incremental Forming with Two Moving Forming Tools," Key Engineering Materials, 344, pp. 599-605.

[8] Smith, J., Malhotra, R., Liu, W. K., and Cao, J., 2013, "Deformation mechanics in single-point and accumulative double-sided incremental forming," The International Journal of Advanced Manufacturing Technology, 69(5-8), pp. 1185-1201.

[9] Moser, N., Leem, D., Ehmann, K., and Cao, J., 2021, "A high-fidelity simulation of double-sided incremental forming: Improving the accuracy by incorporating the effects of machine compliance," Journal of Materials Processing Technology, 295, p. 117152.

[10] Moser, N., 2019, "Deformation Mechanisms and Process Planning in Double-Sided Incremental Forming."

[11] Lasunon, O., and Knight, W. A., 2007, "Comparative investigation of single-point and double-point incremental sheet metal forming processes," P I Mech Eng B-J Eng, 221(12), pp. 1725-1732.

[12] Valoppi, B., Sánchez Egea, A. J., Zhang, Z., González Rojas, H. A., Ghiotti, A., Bruschi, S., and Cao, J., 2016, "A hybrid mixed double-sided incremental forming method for forming Ti6Al4V alloy," CIRP Annals - Manufacturing Technology, 65(1), pp. 309-312.

[13] Xu, D. K., Lu, B., Cao, T. T., Zhang, H., Chen, J., Long, H., and Cao, J., 2016, "Enhancement of process capabilities in electrically-assisted double sided incremental forming," Materials & Design, 92, pp. 268-280.

[14] Lu, B., Fang, Y., Xu, D. K., Chen, J., Ai, S., Long, H., Ou, H., and Cao, J., 2015, "Investigation of material deformation mechanism in double side incremental sheet forming," International Journal of Machine Tools and Manufacture, 93, pp. 37-48.

[15] Ndip-Agbor, E. E., Smith, J., Xu, R., Malhotra, R., and Cao, J., 2013, "Effect of relative tool position on the geometric accuracy of accumulative DSIF," AIP Conference Proceedings, 1567(1), pp. 828-831.

[16] Meier, H., Buff, B., Laurischkat, R., and Smukala, V., 2009, "Increasing the part accuracy in dieless robot-based incremental sheet metal forming," CIRP Annals - Manufacturing Technology, 58(1), pp. 233-238.

[17] Meier, H., Magnus, C., and Smukala, V., 2011, "Impact of superimposed pressure on dieless incremental sheet metal forming with two moving tools," CIRP Annals - Manufacturing Technology, 60(1), pp. 327-330.

[18] Praveen, K., Lingam, R., and Venkata Reddy, N., 2020, "Tool path design system to enhance accuracy during double sided incremental forming: An analytical model to predict compensations for small/large components," Journal of Manufacturing Processes, 58, pp. 510-523.

[19] Moser, N., Pritchet, D., Ren, H., Ehmann, K. F., and Cao, J., 2016, "An Efficient and

General Finite Element Model for Double-Sided Incremental Forming," Journal of Manufacturing Science and Engineering, 138(9), p. 091007.

[20] Ai, S., Dai, R., and Long, H., 2020, "Investigating formability enhancement in double side incremental forming by developing a new test method of tension under cyclic bending and compression," Journal of Materials Processing Technology, 275, p. 116349.

[21] Long, H., Ai, S., Tian, F., Lu, B., Chen, J., and Ou, H., 2021, "A New Test Method for Sheet Metal Deformation Subject to Tension Under Cyclic Bending and Compression (TCBC)," Forming the Future, G. Daehn, J. Cao, B. Kinsey, E. Tekkaya, A. Vivek, and Y. Yoshida, eds., Springer International Publishing, Cham, pp. 441-455.

[22] Emmens, W. C., and van den Boogaard, A. H., 2009, "Incremental forming by continuous bending under tension—An experimental investigation," Journal of Materials Processing Technology, 209(14), pp. 5456-5463.

[23] Gatea, S., Ou, H. G., Lu, B., and McCartney, G., 2017, "Modelling of ductile fracture in single point incremental forming using a modified GTN model," Engineering Fracture Mechanics, 186, pp. 59-79.

[24] Gatea, S., Lu, B., Chen, J., Ou, H., and McCartney, G., 2018, "Investigation of the effect of forming parameters in incremental sheet forming using a micromechanics based damage model," International Journal of Material Forming, 12(4), pp. 553-574.

[25] Guzmán, C. F., Yuan, S., Duchêne, L., Saavedra Flores, E. I., and Habraken, A. M., 2018, "Damage prediction in single point incremental forming using an extended Gurson model," International Journal of Solids and Structures, 151, pp. 45-56.

[26] Malhotra, R., Xue, L., Belytschko, T., and Cao, J., 2012, "Mechanics of fracture in single point incremental forming," Journal of Materials Processing Technology, 212(7), pp. 1573-1590.

[27] Bai, Y., and Wierzbicki, T., 2008, "A new model of metal plasticity and fracture with pressure and Lode dependence," International Journal of Plasticity, 24(6), pp. 1071-1096.

[28] Hagan, E., and Jeswiet, J., 2003, "A review of conventional and modern single-point sheet metal forming methods," P I Mech Eng B-J Eng, 217(2), pp. 213-225.

[29] Micari, F., Ambrogio, G., and Filice, L., 2007, "Shape and dimensional accuracy in Single Point Incremental Forming: State of the art and future trends," Journal of Materials Processing Technology, 191(1-3), pp. 390-395.

[30] Duflou, J. R., Habraken, A.-M., Cao, J., Malhotra, R., Bambach, M., Adams, D., Vanhove, H., Mohammadi, A., and Jeswiet, J., 2017, "Single point incremental forming: state-of-the-art and prospects," International Journal of Material Forming.

[31] Gatea, S., Ou, H. G., and McCartney, G., 2016, "Review on the influence of process parameters in incremental sheet forming," Int J Adv Manuf Tech, 87(1-4), pp. 479-499.

[32] Behera, A. K., de Sousa, R. A., Ingarao, G., and Oleksik, V., 2017, "Single point incremental forming: An assessment of the progress and technology trends from 2005 to 2015," Journal of Manufacturing Processes, 27, pp. 37-62.

[33] Jeswiet, J., Micari, F., Hirt, G., Bramley, A., Duflou, J., and Allwood, J., 2005, "Asymmetric Single Point Incremental Forming of Sheet Metal," CIRP Annals - Manufacturing Technology, 54(2), pp. 88-114.

[34] Afonso, D., Alves de Sousa, R., and Torcato, R., 2017, "Integration of design rules and process modelling within SPIF technology-a review on the industrial dissemination of single point incremental forming," The International Journal of Advanced Manufacturing Technology, 94(9-12), pp. 4387-4399.

[35] Fang, Y., Lu, B., Chen, J., Xu, D. K., and Ou, H., 2014, "Analytical and experimental investigations on deformation mechanism and fracture behavior in single point incremental forming," Journal of Materials Processing Technology, 214(8), pp. 1503-1515.

[36] Yamashita, M., Gotoh, M., and Atsumi, S.-Y., 2008, "Numerical simulation of incremental forming of sheet metal," Journal of Materials Processing Technology, 199(1-3), pp. 163-172.

[37] Lu, B., Chen, J., Ou, H., and Cao, J., 2013, "Feature-based tool path generation approach for incremental sheet forming process," Journal of Materials Processing Technology, 213(7), pp. 1221-1233.

[38] Allwood, J. M., Music, O., Raithathna, A., and Duncan, S. R., 2009, "Closed-loop

feedback control of product properties in flexible metal forming processes with mobile tools," Cirp Annals-Manufacturing Technology, 58(1), pp. 287-290.

[39] Azaouzi, M., and Lebaal, N., 2012, "Tool path optimization for single point incremental sheet forming using response surface method," Simulation Modelling Practice and Theory, 24, pp. 49-58.

[40] Matsubara, S., 2001, "A computer numerically controlled dieless incremental forming of a sheet metal," Proceedings of the Institution of Mechanical Engineers, Part B: Journal of Engineering Manufacture, 215(7), pp. 959-966.

[41] Hirt, G., Ames, J., and Bambach, M., 2006, "Basic investigation into the characteristics of dies and support tools used in CNC-incremental sheet forming," Proceedings of the International Deep Drawing Research Group Conference, pp. 341-348.

[42] Malhotra, R., Cao, J., Ren, F., Kiridena, V., Cedric Xia, Z., and Reddy, N. V., 2011, "Improvement of Geometric Accuracy in Incremental Forming by Using a Squeezing Toolpath Strategy With Two Forming Tools," Journal of Manufacturing Science and Engineering, 133(6).

[43] Malhotra, R., Cao, J., Beltran, M., Xu, D., Magargee, J., Kiridena, V., and Xia, Z. C., 2012, "Accumulative-DSIF strategy for enhancing process capabilities in incremental forming," CIRP Annals - Manufacturing Technology, 61(1), pp. 251-254.

[44] Rakesh, L., Amit, S., and Reddy, N. V., 2016, "Deflection Compensations for Tool Path to Enhance Accuracy During Double-Sided Incremental Forming," Journal of Manufacturing Science and Engineering, 138(9), p. 091008.

[45] Wu, J. H., and Wang, Q. C., 2014, "Comparison of the Geometric Accuracy by DSIF Toolpath with SPIF Toolpath," Appl Mech Mater, 494-495, pp. 497-501.

[46] Jeswiet, J., and Young, D., 2005, "Forming limit diagrams for single-point incremental forming of aluminium sheet," Proceedings of the Institution of Mechanical Engineers, Part B: Journal of Engineering Manufacture, 219(4), pp. 359-364.

[47] Duflou, J. R., Callebaut, B., Verbert, J., and De Baerdemaeker, H., 2007, "Laser assisted incremental forming: Formability and accuracy improvement," Cirp Annals-

Manufacturing Technology, 56(1), pp. 273-276.

[48] Duflou, J. R., Verbert, J., Belkassem, B., Gu, J., Sol, H., Henrard, C., and Habraken, A. M., 2008, "Process window enhancement for single point incremental forming through multi-step toolpaths," CIRP Annals, 57(1), pp. 253-256.

[49] Reddy, N. V., and Lingam, R., 2018, "Double Sided Incremental Forming: Capabilities and Challenges," Journal of Physics: Conference Series, 1063, p. 012170.

[50] Wang, Y., Huang, Y., Cao, J., and Reddy, N. V., 2008, "Experimental Study on a New Method of Double Side Incremental Forming," ASME 2008 International Manufacturing Science and Engineering Conference collocated with the 3rd JSME/ASME International Conference on Materials and Processing, pp. 601-607.

[51] Meier, H., Dewald, O., and Zhang, J., 2005, "Development of a Robot-Based Sheet Metal Forming Process," steel research international, 76(2-3), pp. 167-170.

[52] Lingam, R., Prakash, O., Belk, J. H., and Reddy, N. V., 2016, "Automatic feature recognition and tool path strategies for enhancing accuracy in double sided incremental forming," The International Journal of Advanced Manufacturing Technology, 88(5-8), pp. 1639-1655.

[53] Störkle, D. D., Möllensiep, D., Thyssen, L., and Kuhlenkötter, B., 2018, "Geometry-dependent parameterization of local support in robot-based incremental sheet forming," Procedia Manufacturing, 15, pp. 1164-1169.

[54] Konka, P., Lingam, R., Singh, U. A., Shivaprasad, C. H., and Reddy, N. V., 2020, "Enhancement of accuracy in double sided incremental forming by compensating tool path for machine tool errors," The International Journal of Advanced Manufacturing Technology, 111(3-4), pp. 1187-1199.

[55] Zeng, Q., Ehmann, K. F., and Cao, J., 2014, "Tri-pyramid Robot: Design and kinematic analysis of a 3-DOF translational parallel manipulator," Robotics and Computer-Integrated Manufacturing, 30(6), pp. 648-657.

[56] Liao, S., Ehmann, K., and Cao, J., 2020, "Kinematic Calibration and Data-Based Error Compensation of a Parallel Robot-Based Incremental Sheet Forming Machine," 2020

International Symposium on Flexible Automation.

[57] Kreimeier, D., Buff, B., Magnus, C., Smukala, V., and Zhu, J., 2011, "Robot-Based Incremental Sheet Metal Forming – Increasing the Geometrical Accuracy of Complex Parts," Key Engineering Materials, 473, pp. 853-860.

[58] Wang, H., Zhang, R., Zhang, H., Hu, Q., and Chen, J., 2018, "Novel strategies to reduce the springback for double-sided incremental forming," The International Journal of Advanced Manufacturing Technology, 96(1-4), pp. 973-979.

[59] Paniti, I., 2014, "A novel, single-robot based two sided incremental sheet forming system," ISR/Robotik 2014; 41st International Symposium on Robotics, pp. 1-7.

[60] Sortais, H. C., Kobayashi, S., and Thomsen, E., 1962, "Mechanics of conventional spinning," University of California, Berkeley.

[61] Ren, H., Moser, N., Zhang, Z., Ndip-Agbor, E., Smith, J., Ehmann, K. F., and Cao, J., 2015, "Effects of Tool Positions in Accumulated Double-Sided Incremental Forming on Part Geometry," Journal of Manufacturing Science and Engineering, 137(5), p. 051008.

[62] Ndip-Agbor, E., Smith, J., Ren, H., Jiang, Z., Xu, J., Moser, N., Chen, W., Xia, Z. C., and Cao, J., 2015, "Optimization of relative tool position in accumulative double sided incremental forming using finite element analysis and model bias correction," International Journal of Material Forming, 9(3), pp. 371-382.

[63] Allwood, J. M., and Shouler, D. R., 2009, "Generalised forming limit diagrams showing increased forming limits with non-planar stress states," International Journal of Plasticity, 25(7), pp. 1207-1230.

[64] Lu, B., Xu, D. K., Liu, R. Z., Ou, H. A., Long, H., and Chen, J., 2015, "Cranial Reconstruction Using Double Side Incremental Forming," Key Engineering Materials, 639, pp. 535-542.

[65] Davarpanah, M. A., Mirkouei, A., Yu, X., Malhotra, R., and Pilla, S., 2015, "Effects of incremental depth and tool rotation on failure modes and microstructural properties in Single Point Incremental Forming of polymers," Journal of Materials Processing Technology, 222, pp. 287-300.

[66] Davarpanah, M. A., and Malhotra, R., 2018, "Formability and failure modes in Single Point Incremental Forming of Metal-Polymer Laminates," Procedia Manufacturing, 26, pp. 343-348.

[67] Jackson, K. P., Allwood, J. M., and Landert, M., 2008, "Incremental forming of sandwich panels," Journal of Materials Processing Technology, 204(1-3), pp. 290-303.

[68] Fiorotto, M., Sorgente, M., and Lucchetta, G., 2010, "Preliminary Studies on Single Point Incremental Forming for Composite Materials," International Journal of Material Forming, 3(S1), pp. 951-954.

[69] Yang, Z., Chen, F., Gatea, S., and Ou, H., 2020, "Design of the novel hot incremental sheet forming experimental setup, characterization of formability behavior of polyether-ether-ketone (PEEK)," The International Journal of Advanced Manufacturing Technology, 106(11), pp. 5365-5381.

[70] Davarpanah, M. A., Zhang, Z., Bansal, S., Cao, J., and Malhotra, R., 2016, "Preliminary investigations on Double Sided Incremental Forming of thermoplastics," Manufacturing Letters, 8, pp. 21-26.

[71] Ji, Y. H., and Park, J. J., 2008, "Formability of magnesium AZ31 sheet in the incremental forming at warm temperature," Journal of Materials Processing Technology, 201(1-3), pp. 354-358.

[72] Ambrogio, G., Filice, L., and Manco, G. L., 2008, "Warm incremental forming of magnesium alloy AZ31," Cirp Annals-Manufacturing Technology, 57(1), pp. 257-260.

[73] Otsu, M., Yasunaga, M., Matsuda, M., and Takashima, K., 2014, "Friction stir incremental forming of A2017 aluminum sheets," Procedia Engineer, 81, pp. 2318-2323.

[74] Xu, D., Wu, W., Malhotra, R., Chen, J., Lu, B., and Cao, J., 2013, "Mechanism investigation for the influence of tool rotation and laser surface texturing (LST) on formability in single point incremental forming," International Journal of Machine Tools and Manufacture, 73, pp. 37-46.

[75] Göttmann, A., Bailly, D., Bergweiler, G., Bambach, M., Stollenwerk, J., Hirt, G., and Loosen, P., 2012, "A novel approach for temperature control in ISF supported by laser and

resistance heating," The International Journal of Advanced Manufacturing Technology, 67(9-12), pp. 2195-2205.

[76] Palumbo, G., and Brandizzi, M., 2012, "Experimental investigations on the single point incremental forming of a titanium alloy component combining static heating with high tool rotation speed," Materials & Design, 40, pp. 43-51.

[77] Zhang, Z. X., Ren, H. Q., Xu, R., Moser, N., Smith, J., Ndip-Agbor, E., Malhotra, R., Xia, Z. C., Ehmann, K. F., and Cao, J., 2015, "A Mixed Double-Sided Incremental Forming Toolpath Strategy for Improved Geometric Accuracy," Journal of Manufacturing Science and Engineering, 137(5), p. 051007.

[78] Belchior, J., Guillo, M., Courteille, E., Maurine, P., Leotoing, L., and Guines, D., 2013, "Off-line compensation of the tool path deviations on robotic machining: Application to incremental sheet forming," Robotics and Computer-Integrated Manufacturing, 29(4), pp. 58-69.

[79] Stoerkle, D. D., Seim, P., Thyssen, L., and Kuhlenkoetter, B., 2016, "Machine Learning In Incremental Sheet Forming," Proceedings of ISR 2016: 47st International Symposium on Robotics, pp. 1-7.

[80] Ambrogio, G., Cozza, V., Filice, L., and Micari, F., 2007, "An analytical model for improving precision in single point incremental forming," Journal of Materials Processing Technology, 191(1), pp. 92-95.

[81] Asghar, J., Lingam, R., Shibin, E., and Reddy, N. V., 2013, "Tool path design for enhancement of accuracy in single-point incremental forming," Proceedings of the Institution of Mechanical Engineers, Part B: Journal of Engineering Manufacture, 228(9), pp. 1027-1035.

[82] Lu, H., Kearney, M., Li, Y., Liu, S., Daniel, W. J. T., and Meehan, P. A., 2016, "Model predictive control of incremental sheet forming for geometric accuracy improvement," The International Journal of Advanced Manufacturing Technology, 82(9), pp. 1781-1794.

[83] Fiorentino, A., Feriti, G. C., Ceretti, E., Giardini, C., Bort, C. M. G., and Bosetti, P., 2014, "Development of Tool Path Correction Algorithm in Incremental Sheet Forming," Key

Engineering Materials, 622-623, pp. 382-389.

[84] Zhu, H., Han, F., and Liu, Y., 2018, "The effect of the extrusion direction on the incremental forming quality considering tool deformation," The International Journal of Advanced Manufacturing Technology, 97(5-8), pp. 1835-1846.

[85] Decultot, N., Robert, L., Velay, V., and Bernhart, G., 2010, "Single point incremental sheet forming investigated by in-process 3D digital image correlation," EPJ Web of Conferences, 6, p. 11001.

[86] Eyckens, P., Belkassem, B., Henrard, C., Gu, J., Sol, H., Habraken, A. M., Duflou, J. R., Van Bael, A., and Van Houtte, P., 2011, "Strain evolution in the single point incremental forming process: digital image correlation measurement and finite element prediction," International journal of material forming, 4(1), pp. 55-71.

[87] Fiorentino, A., Ceretti, E., Feriti, G. C., and Giardini, C., 2015, "Improving Accuracy in Aluminum Incremental Sheet Forming of Complex Geometries Using Iterative Learning Control," Key Engineering Materials, 651-653, pp. 1096-1102.

[88] Ambrogio, G., Filice, L., Guerriero, F., Guido, R., and Umbrello, D., 2011, "Prediction of incremental sheet forming process performance by using a neural network approach," The International Journal of Advanced Manufacturing Technology, 54(9-12), pp. 921-930.

[89] Hartmann, C., Opritescu, D., and Volk, W., 2019, "An artificial neural network approach for tool path generation in incremental sheet metal free-forming," Journal of Intelligent Manufacturing, 30(2), pp. 757-770.

[90] Ren, H., Li, F., Moser, N., Leem, D., Li, T., Ehmann, K., and Cao, J., 2018, "General contact force control algorithm in double-sided incremental forming," CIRP Annals, 67(1), pp. 381-384.

[91] Peng, W., Li, M., Lu, B., Chen, J., Becker, A., and Ou, H., 2019, "Experimental and finite element investigation of over-bending phenomenon in Double-Sided Incremental Forming (DSIF) of aluminium sheets," Procedia Manufacturing, 29, pp. 59-66.

[92] Verbert, J., Duflou, J. R., and Lauwers, B., 2007, "Feature Based Approach for Increasing the Accuracy of the SPIF Process," Key Engineering Materials, 344, pp. 527-534.

[93] Behera, A., Vanhove, H., Lauwers, B., and Duflou, J., 2011, "Accuracy Improvement in Single Point Incremental Forming Through Systematic Study of Feature Interactions," Key Engineering Materials, 473, pp. 881-888.

[94] Behera, A. K., Verbert, J., Lauwers, B., and Duflou, J. R., 2013, "Tool path compensation strategies for single point incremental sheet forming using multivariate adaptive regression splines," Computer-Aided Design, 45(3), pp. 575-590.

[95] Malhotra, R., Reddy, N., and Cao, J., 2010, "Automatic 3D spiral toolpath generation for single point incremental forming," Journal of manufacturing science and engineering, 132(6), p. 061003.

[96] Ndip-Agbor, E., Ehmann, K., and Cao, J., 2017, "Automated Flexible Forming Strategy for Geometries With Multiple Features in Double-Sided Incremental Forming," Journal of Manufacturing Science and Engineering, 140(3), p. 031004.

[97] Moser, N., Zhang, Z., Ren, H., Zhang, H., Shi, Y., Ndip-Agbor, E. E., Lu, B., Chen, J., Ehmann, K. F., and Cao, J., 2016, "Effective forming strategy for double-sided incremental forming considering in-plane curvature and tool direction," CIRP Annals - Manufacturing Technology, 65(1), pp. 265-268.

[98] Gatea, S., 2017, "Experimental and Numerical Investigation of Formability and Ductile Fracture in Incremental Sheet Forming," University of Nottingham, Nottingham, UK.

[99] Leem, D., Moser, N., Ren, H., Mozaffar, M., Ehmann, K. F., and Cao, J., 2019, "Improving the accuracy of double-sided incremental forming simulations by considering kinematic hardening and machine compliance," Procedia Manufacturing, 29, pp. 88-95.

[100] Moser, N., Leem, D., Liao, S., Ehmann, K., and Cao, J., 2021, "Advancing the Accuracy of Computational Models for Double-Sided Incremental Forming," Springer International Publishing, Cham, pp. 271-281.

[101] Subrahmanyam, A., Lingam, R., Hayakawa, K., Tanaka, S., and Nallagundla, V. R., 2019, "Experimental and Numerical Investigation of Residual Stresses in Incremental Forming," MATERIALS TRANSACTIONS, 61.

[102] de Sena, J. I. V., Guzmán, C. F., Duchêne, L., Habraken, A. M., Behera, A. K., Duflou, J., Valente, R. A. F., and de Sousa, R. J. A., 2015, "Simulation of a two-slope pyramid made by SPIF using an adaptive remeshing method with solid-shell finite element," International Journal of Material Forming, 9(3), pp. 383-394.

[103] Sena José, I. V., Lequesne, C., Duchene, L., Habraken, A.-M., Valente Robertt, A. F., and Alves de Sousa Ricardo, J., 2016, "Single point incremental forming simulation with adaptive remeshing technique using solid-shell elements," Engineering Computations, 33(5), pp. 1388-1421.

[104] Barrett, T. J., Takagi, S., Islam, N., Kuwabara, T., Hassan, T., Kinsey, B. L., Knezevic, M., and Korkolis, Y. P., 2020, "Material modeling and simulation of continuous-bending-under-tension of AA6022-T4," Journal of Materials Processing Technology, p. 116658.

[105] Martins, P. A. F., Bay, N., Skjoedt, M., and Silva, M. B., 2008, "Theory of single point incremental forming," CIRP Annals, 57(1), pp. 247-252.

[106] Lu, B., Fang, Y., Xu, D. K., Chen, J., Ou, H., Moser, N. H., and Cao, J., 2014, "Mechanism investigation of friction-related effects in single point incremental forming using a developed oblique roller-ball tool," International Journal of Machine Tools and Manufacture, 85, pp. 14-29.

[107] Gatea, S., Xu, D., Ou, H., and McCartney, G., 2017, "Evaluation of formability and fracture of pure titanium in incremental sheet forming," The International Journal of Advanced Manufacturing Technology, 95(1-4), pp. 625-641.

[108] Wang, C., Daniel, W. J. T., Lu, H., Liu, S., and Meehan, P. A., 2017, "FEM Investigation of Ductile Fracture Prediction in Two-Point Incremental Sheet Metal Forming process," International Conference on the Technology of Plasticity, Procedia Engineering, Cambridge, United Kingdom.

[109] Emmens, W. C., and van den Boogaard, A. H., 2011, "Cyclic stretch-bending: Mechanics, stability and formability," Journal of Materials Processing Technology, 211(12), pp. 1965-1981.

[110] Roemer, T. J., Barrett, T. J., Knezevic, M., Kinsey, B. L., and Korkolis, Y. P., 2019,

"Experimental study of continuous-bending-under-tension of AA6022-T4," Journal of Materials Processing Technology, 266, pp. 707-714.

[111] Zecevic, M., Roemer, T. J., Knezevic, M., Korkolis, Y. P., and Kinsey, B. L., 2016, "Residual Ductility and Microstructural Evolution in Continuous-Bending-under-Tension of AA-6022-T4," Materials (Basel), 9(3).

[112] Knezevic, M., Poulin, C. M., Zheng, X., Zheng, S., and Beyerlein, I. J., 2019, "Strengthening of alloy AA6022-T4 by continuous bending under tension," Materials Science and Engineering: A, 758, pp. 47-55.

[113] Valoppi, B., Zhang, Z., Deng, M., Ghiotti, A., Bruschi, S., Ehmann, K. F., and Cao, J., 2017, "On the Fracture Characterization in Double-Sided Incremental Forming of Ti6Al4V Sheets at Elevated Temperatures," Procedia Manufacturing, 10, pp. 407-416.

[114] Benedyk, J. C., Kinsey, B. L., Korkolis, Y. P., and Roemer, T. J., 2015, "Fundamental Studies of Continuous Bending under Tension (CBT) and Potential Automotive Forming Applications," Materials Today: Proceedings, 2(10), pp. 4998-5005.

[115] Allwood, J. M., Shouler, D. R., and Tekkaya, A. E., 2007, "The Increased Forming Limits of Incremental Sheet Forming Processes," Key Engineering Materials, 344, pp. 621-628.

[116] Ai, S., and Long, H., 2019, "Finite element modelling of material deformation and damage by tension under cyclic bending and compression test," 2113, p. 180012.

[117] McClintock, F. A., 1968, "A Criterion for Ductile Fracture by the Growth of Holes," Journal of Applied Mechanics, 35(2), pp. 363-371.

[118] Rice, J. R., and Tracey, D. M., 1969, "On the ductile enlargement of voids in triaxial stress fields*," Journal of the Mechanics and Physics of Solids, 17(3), pp. 201-217.

[119] Gurson, A. L., 1977, "Continuum Theory of Ductile Rupture by Void Nucleation and Growth: Part I—Yield Criteria and Flow Rules for Porous Ductile Media," Journal of Engineering Materials and Technology, 99(1), pp. 2-15.

[120] Tvergaard, V., 1981, "Influence of voids on shear band instabilities under plane strain conditions," International Journal of fracture, 17(4), pp. 389-407.

[121] Nahshon, K., and Hutchinson, J. W., 2008, "Modification of the Gurson Model for shear failure," European Journal of Mechanics - A/Solids, 27(1), pp. 1-17.

[122] Xue, L., 2008, "Constitutive modeling of void shearing effect in ductile fracture of porous materials," Engineering Fracture Mechanics, 75(11), pp. 3343-3366.

[123] Zhou, J., Gao, X., Sobotka, J. C., Webler, B. A., and Cockeram, B. V., 2014, "On the extension of the Gurson-type porous plasticity models for prediction of ductile fracture under shear-dominated conditions," International Journal of Solids and Structures, 51(18), pp. 3273-3291.

[124] Chen, Y., Zhang, C., and Varé, C., 2017, "An extended GTN model for indentation-induced damage," Computational Materials Science, 128, pp. 229-235.

[125] Kailasam, M., and Castaneda, P. P., 1997, "The evolution of anisotropy in porous materials and its implications for shear localization," IUTAM symposium on mechanics of granular and porous materials, Springer, pp. 365-376.

[126] Castañeda, P. P., and Zaidman, M., 1994, "Constitutive models for porous materials with evolving microstructure," Journal of the Mechanics and Physics of Solids, 42(9), pp. 1459-1497.

[127] Kailasam, M., Aravas, N., Casta, ntilde, and eda, P.-P., 2000, "Porous Metals with Developing Anisotropy: Constitutive Models, Computational Issues and Applications to Deformation Processing," Computer Modeling in Engineering \& Sciences, 1(2), pp. 105--118.

[128] Aravas, N., and Castañeda, P. P., 2004, "Numerical methods for porous metals with deformation-induced anisotropy," Computer methods in applied mechanics and engineering, 193(36-38), pp. 3767-3805.

[129] Ponte Castañeda, P., 2002, "Second-order homogenization estimates for nonlinear composites incorporating field fluctuations: I—theory," Journal of the Mechanics and Physics of Solids, 50(4), pp. 737-757.

[130] Ponte Castañeda, P., 2002, "Second-order homogenization estimates for nonlinear composites incorporating field fluctuations: II—applications," Journal of the Mechanics

and Physics of Solids, 50(4), pp. 759-782.

[131] Bao, Y., and Wierzbicki, T., 2004, "On fracture locus in the equivalent strain and stress triaxiality space," International Journal of Mechanical Sciences, 46(1), pp. 81-98.

[132] Xiaosheng, G., Guihua, Z., and Roe, C., 2009, "A Study on the Effect of the Stress State on Ductile Fracture," International Journal of Damage Mechanics, 19(1), pp. 75-94.

[133] Barsoum, I., and Faleskog, J., 2007, "Rupture mechanisms in combined tension and shear—Experiments," International Journal of Solids and Structures, 44(6), pp. 1768-1786.

[134] Wierzbicki, T., Bao, Y., and Bai, Y., 2005, "A New Experimental Technique for Constructing a Fracture Envelope of Metals under Multi-axial loading," Proceedings of the 2005 SEM Annual Conference and Exposition on Experimental and Applied Mechanics.

[135] Liu, Z. G., Wong, W. H., and Guo, T. F., 2016, "Void behaviors from low to high triaxialities: Transition from void collapse to void coalescence," International Journal of Plasticity, 84, pp. 183-202.

[136] Tekoğlu, C., Leblond, J. B., and Pardoen, T., 2012, "A criterion for the onset of void coalescence under combined tension and shear," Journal of the Mechanics and Physics of Solids, 60(7), pp. 1363-1381.

[137] Seppala, E. T., Belak, J., and Rudd, R. E., 2004, "Onset of void coalescence during dynamic fracture of ductile metals," Phys Rev Lett, 93(24), p. 245503.

[138] Park, J.-J., 2013, "Finite-Element Analysis of Cylindrical-Void Closure by Flat-Die Forging," ISIJ International, 53(8), pp. 1420-1426.

[139] Feng, C., and Cui, Z., 2015, "A 3-D model for void evolution in viscous materials under large compressive deformation," International Journal of Plasticity, 74, pp. 192-212.

[140] Chen, F., Cui, Z., Ou, H., and Long, H., 2016, "Mesoscale modeling and simulation of microstructure evolution during dynamic recrystallization of a Ni-based superalloy," Applied Physics A, 122(10).

[141] Wang, X., and Dong, X., 2020, "A void evolution model accounting for stress triaxiality, Lode parameter and effective strain for hot metal forming," International

Journal of Mechanical Sciences, 168, p. 105309.

[142] Saby, M., Bernacki, M., Roux, E., and Bouchard, P. O., 2013, "Three-dimensional analysis of real void closure at the meso-scale during hot metal forming processes," Computational Materials Science, 77, pp. 194-201.

[143] Zhang, X.-X., Cui, Z.-S., Chen, W., and Li, Y., 2009, "A criterion for void closure in large ingots during hot forging," Journal of Materials Processing Technology, 209(4), pp. 1950-1959.

[144] Zhang, X.-x., and Cui, Z.-s., 2009, "Theoretical study of void closure in nonlinear plastic materials," Applied Mathematics and Mechanics, 30(5), pp. 631-642.

[145] Srivastava, A., and Needleman, A., 2013, "Void growth versus void collapse in a creeping single crystal," Journal of the Mechanics and Physics of Solids, 61(5), pp. 1169-1184.

[146] Bao, Y., and Wierzbicki, T., 2004, "A Comparative Study on Various Ductile Crack Formation Criteria," Journal of Engineering Materials and Technology, 126(3), p. 314.

[147] Dæhli, L. E., Morin, D., Børvik, T., and Hopperstad, O. S., 2018, "A Lode-dependent Gurson model motivated by unit cell analyses," Engineering Fracture Mechanics, 190, pp. 299-318.

[148] Danas, K., and Ponte Castañeda, P., 2012, "Influence of the Lode parameter and the stress triaxiality on the failure of elasto-plastic porous materials," International Journal of Solids and Structures, 49(11-12), pp. 1325-1342.

[149] Kiran, R., and Khandelwal, K., 2014, "A triaxiality and Lode parameter dependent ductile fracture criterion," Engineering Fracture Mechanics, 128, pp. 121-138.

[150] Tekoğlu, C., 2014, "Representative volume element calculations under constant stress triaxiality, Lode parameter, and shear ratio," International Journal of Solids and Structures, 51(25-26), pp. 4544-4553.

[151] Tvergaard, V., 1982, "On localization in ductile materials containing spherical voids," International Journal of fracture, 18(4), pp. 237-252.

[152] Tvergaard, V., Needleman, A., DCAMM., and DTH., 1983, Analysis of the Cup-cone

Fracture in a Round Tensile Bar, Technical University of Denmark.

[153] Malcher, L., Andrade Pires, F. M., and César de Sá, J. M. A., 2014, "An extended GTN model for ductile fracture under high and low stress triaxiality," International Journal of Plasticity, 54, pp. 193-228.

[154] Jiang, W., Li, Y., and Su, J., 2016, "Modified GTN model for a broad range of stress states and application to ductile fracture," European Journal of Mechanics - A/Solids, 57, pp. 132-148.

[155] Malcher, L., Andrade Pires, F. M., and César de Sá, J. M. A., 2012, "An assessment of isotropic constitutive models for ductile fracture under high and low stress triaxiality," International Journal of Plasticity, 30-31, pp. 81-115.

[156] Wierzbicki, T., Bao, Y., Lee, Y.-W., and Bai, Y., 2005, "Calibration and evaluation of seven fracture models," International Journal of Mechanical Sciences, 47(4-5), pp. 719-743.

[157] Bai, Y., and Wierzbicki, T., 2015, "A comparative study of three groups of ductile fracture loci in the 3D space," Engineering Fracture Mechanics, 135, pp. 147-167.

[158] Johnson, G. R., and Cook, W. H., 1985, "Fracture characteristics of three metals subjected to various strains, strain rates, temperatures and pressures," Engineering Fracture Mechanics, 21(1), pp. 31-48.

[159] Lou, Y., Yoon, J. W., and Huh, H., 2014, "Modeling of shear ductile fracture considering a changeable cut-off value for stress triaxiality," International Journal of Plasticity, 54, pp. 56-80.

[160] Zhai, J., Luo, T., Gao, X., Graham, S. M., Baral, M., Korkolis, Y. P., and Knudsen, E., 2016, "Modeling the ductile damage process in commercially pure titanium," International Journal of Solids and Structures, 91, pp. 26-45.

[161] Ortiz, M., and Simo, J. C., 1986, "An analysis of a new class of integration algorithms for elastoplastic constitutive relations," International Journal for Numerical Methods in Engineering, 23(3), pp. 353-366.

[162] Engelmann, B. E., and Whirley, R. G., 1992, "Recent developments in NIKE2D for

metalforming analysis and low rate impact," Nuclear engineering and design, 138(1), pp. 23-35.

[163] Popov, V. L., Heß, M., and Willert, E., 2019, Handbook of Contact Mechanics, Springer-Verlag Berlin Heidelberg.

[164] Zherebtsov, S. V., Dyakonov, G. S., Salem, A. A., Malysheva, S. P., Salishchev, G. A., and Semiatin, S. L., 2011, "Evolution of grain and subgrain structure during cold rolling of commercial-purity titanium," Materials Science and Engineering: A, 528(9), pp. 3474-3479.

[165] Pushkareva, M., Sket, F., Segurado, J., Llorca, J., Yandouzi, M., and Weck, A., 2019, "Effect of grain orientation and local strains on void growth and coalescence in titanium," Materials Science and Engineering: A, 760, pp. 258-266.

[166] Rahimi, H. R., Sedighi, M., and Hashemi, R., 2016, "Forming limit diagrams of fine-grained Al 5083 produced by equal channel angular rolling process," Proceedings of the Institution of Mechanical Engineers, Part L: Journal of Materials: Design and Applications, 232(11), pp. 922-930.

[167] Bozcheloei, J. E., Sedighi, M., and Hashemi, R., 2019, "The effect of temperature on the mechanical properties and forming limit diagram of Al 5083 produced by equal channel angular rolling," The International Journal of Advanced Manufacturing Technology, 105(10), pp. 4389-4400.

[168] Yoshida, F., Uemori, T., and Fujiwara, K., 2002, "Elastic–plastic behavior of steel sheets under in-plane cyclic tension–compression at large strain," International Journal of Plasticity, 18(5-6), pp. 633-659.

[169] Marcadet, S. J., and Mohr, D., 2015, "Effect of compression–tension loading reversal on the strain to fracture of dual phase steel sheets," International Journal of Plasticity, 72, pp. 21-43.

[170] Uemori, T., Okada, T., and Yoshida, F., 1998, "Simulation of Springback in V-bending Process by Elasto-Plastic Finite Element Method with Consideration of Bauschinger Effect," Metals and Materials, 4(3), pp. 311-314.

[171] Wang, Z., Cai, S., and Chen, J., 2020, "Experimental investigations on friction stir assisted single point incremental forming of low-ductility aluminum alloy sheet for higher formability with reasonable surface quality," Journal of Materials Processing Technology, 277, p. 116488.

[172] Bambach, M., 2010, "A geometrical model of the kinematics of incremental sheet forming for the prediction of membrane strains and sheet thickness," Journal of Materials Processing Technology, 210(12), pp. 1562-1573.

[173] Lingam, R., Bhattacharya, A., Asghar, J., and Reddy, N. V., 2015, "Compensations for tool path to enhance accuracy during double sided incremental forming," ASME 2015 International Manufacturing Science and Engineering Conference, American Society of Mechanical Engineers, pp. V001T002A094-V001T002A094.

[174] Kopac, J., and Kampus, Z., 2005, "Incremental sheet metal forming on CNC milling machine-tool," Journal of Materials Processing Technology, 162-163, pp. 622-628.

[175] Reshetov, D. N., and Portman, V. T., 1988, Accuracy of machine tools, Amer Society of Mechanical.

[176] Lu, H. B., Li, Y. L., Liu, Z. B., Liu, S., and Meehan, P. A., 2014, "Study on Step Depth for Part Accuracy Improvement in Incremental Sheet Forming Process," Advanced Materials Research, 939, pp. 274-280.

[177] Silva, M. B., Nielsen, P. S., Bay, N., and Martins, P. A. F., 2011, "Failure mechanisms in single-point incremental forming of metals," The International Journal of Advanced Manufacturing Technology, 56(9-12), pp. 893-903.

[178] Malhotra, R., Xue, L., Cao, J., and Belytschko, T., 2011, "Identification of Deformation Mechanisms Responsible for Failure in Incremental Forming using a Damage Based Fracture Model," AIP Conference Proceedings, 1383(1), pp. 469-476.

[179] Malhotra, R., Xue, L., Cao, J., and Belytschko, T., 2011, "Identification of Deformation Mechanisms Responsible for Failure in Incremental Forming using a Damage Based Fracture Model," AIP Conference Proceedings, AIP, pp. 469-476.

[180] Mirnia, M. J., and Shamsari, M., 2017, "Numerical prediction of failure in single

point incremental forming using a phenomenological ductile fracture criterion," Journal of Materials Processing Technology, 244, pp. 17-43.

[181] Silva, M. B., Skjoedt, M., Martins, P. A. F., and Bay, N., 2008, "Revisiting the fundamentals of single point incremental forming by means of membrane analysis," International Journal of Machine Tools and Manufacture, 48(1), pp. 73-83.

[182] Ai, S., Lu, B., and Long, H., 2017, "An analytical study of new material test method for tension under bending and compression in double side incremental forming," Procedia Engineering, 207, pp. 1982-1987.

[183] Dunand, M., and Mohr, D., 2011, "On the predictive capabilities of the shear modified Gurson and the modified Mohr–Coulomb fracture models over a wide range of stress triaxialities and Lode angles," Journal of the Mechanics and Physics of Solids, 59(7), pp. 1374-1394.

[184] Kami, A., Dariani, B. M., Sadough Vanini, A., Comsa, D. S., and Banabic, D., 2015, "Numerical determination of the forming limit curves of anisotropic sheet metals using GTN damage model," Journal of Materials Processing Technology, 216, pp. 472-483.

[185] Jackson, K. P., 2008, "The Mechanics of Incremental Sheet Forming," University of Cambridge.

[186] Jackson, K., and Allwood, J., 2009, "The mechanics of incremental sheet forming," Journal of materials processing technology, 209(3), pp. 1158-1174.

[187] Lu, B., Li, Z., Long, H., Chen, F., Chen, J., and Ou, H., 2017, "Microstructure refinement by tool rotation-induced vibration in incremental sheet forming," Procedia Engineering, 207, pp. 795-800.

[188] Zherebtsov, S. V., Dyakonov, G. S., Salem, A. A., Sokolenko, V. I., Salishchev, G. A., and Semiatin, S. L., 2013, "Formation of nanostructures in commercial-purity titanium via cryorolling," Acta Materialia, 61(4), pp. 1167-1178.